

Simultaneous EEG-fMRI at ultra-high field for the study of human brain function

THÈSE N° 6969 (2016)

PRÉSENTÉE LE 22 AVRIL 2016

À L'ÉCOLE POLYTECHNIQUE FÉDÉRALE DE LAUSANNE

À LA FACULTÉ DES SCIENCES DE BASE

LABORATOIRE LEENAARDS-JEANTET D'IMAGERIE FONCTIONNELLE ET MÉTABOLIQUE

ET

À L'INSTITUTO SUPERIOR TÉCNICO (IST) DA UNIVERSIDADE DE LISBOA

PROGRAMME DOCTORAL EN PHYSIQUE

ET

DOUTORAMENTO EM ENGENHARIA BIOMÉDICA

POUR L'OBTENTION DU GRADE DE DOCTEUR ÈS SCIENCES (PhD)

PAR

João Pedro FORJACO JORGE

acceptée sur proposition du jury:

Prof. M. Q. Tran, président du jury

Prof. R. Gruetter, Prof. P. Figueiredo, directeurs de thèse

Prof. L. Lemieux, rapporteur

Prof. K. Mullinger, rapporteuse

Prof. M. Herzog, rapporteur



Suisse
2016

E anda sempre alguém por lá
junto à tempestade...

— Jorge Palma

To sis, mom, dad

Acknowledgements

Despite coming at the start, the acknowledgements were the last part of this thesis to be written. I was hoping to come up with just the right words to thank all the great people who were part of this 4-year-and-a-bit journey. I'm now pretty sure I won't even come close to perfect – that's just how awesome you guys are! But here's an honest attempt.

I have to start with the person who got me into this whole MRI-EEG-Neuroscience adventure, some 5 years ago – Prof. Patrícia Figueiredo. You gave me an initial opportunity for my Master's project, introduced me to many concepts, and to bright people in the MR community; motivated me to pursue a PhD and guided me along. I've quite enjoyed the balance you achieve with us students, with some guidelines to keep us on track but also some space to try out new (and sometimes rather far-out) ideas – always with a friendly approach and genuine interest. My second thanks go to Prof. Rolf Gruetter, who kindly received me in his group at EPFL, where the major part of this work was done. You've created a fantastic lab here, both with excellent conditions for research, and an excellent group of people to conduct it. I've also learned a lot with your approach to problems – simplifying, focusing on the fundamentals; it really applies to pretty much every problem in science, engineering, and beyond!

A very special thanks goes to Wietske van der Zwaag, the person with whom I worked most closely throughout this PhD. I don't think I can possibly say how much (f)MRI know-how I've learned from you during this time. You set the bases for this project before I even arrived in Lausanne, making for a much smoother start, and your help was crucial at many points thereafter – I've really come to admire the ease with which you grasp new problems and propose solutions. The second person with whom I worked most closely was Frédéric Grouiller, the EEG side of this story. You've taught me a lot on EEG recording (those neat tips that don't come in the books), and we've spent many hours together recording phantoms, patients and undergrad students, pondering on interesting results, tackling mysterious technical issues... The outcomes of this project were initially somewhat uncertain, but this didn't demotivate you from making the Geneva-Lausanne trip as often as needed. I believe that really made a difference. A third special thanks goes to Özlem Ipek, who also made very important contributions to this work, at a later stage. Your friendly, knowledgeable and very efficient working approach made it really enjoyable to work with you, and very valuable for this project.

The larger part of this PhD was done in Lausanne, where I got to know many fantastic people.

Acknowledgements

I won't attempt to name you all! I thank everyone at the LIFMET/CIBM, current and previous members, for their joyful attitude, readily available to discuss this and that problem, scientific or else-wise, happy to share some interesting story, go out for a beer, get some sun at the lake or some powder at the slopes. My current and previous office-mates Diana, Andrea, Alberto, Pavel, Emine, Jérémie, Frédéric, Yohan and Emma for being such great, helpful, joyful company, and twice again to Yohan who also undertook the considerable challenge of revising my abstract en français. My buddies Tom, Francisca, João and Pınar from "Available", the greatest band in the world. The awesome "old-school crew", Tobi, Benoît, Ruud, Rajika, Simo and Gabri, who made me feel at home since the first days in Lausanne. Masoumeh, for sharing great stories and introducing us to the wonders of Iranian cuisine. Daniel and José, for all the valuable discussions and lessons in MR imaging, your interest and passion for cool ideas. Florent for your unbreakable good-mood, readiness to go in the scanner for us for "just a quick test", the epic movie editing sessions and parties at your house. Mélanie, Sarah, Elise, Matthieu, Olivier, Ileana, Veronika, Guillaume, Antoine, Arthur, Hikari, Nico, Hongxia, Domenica, Blanka, Lali, Mayur, Lijing, for the fun coffee-breaks, lunch-breaks and Satellite-breaks. Cédric, Tanja and Lillian for the efficient and joyful help with all the "admin stuff". Many others who I've come to meet during my stay, from Lausanne, the EPFL, the cardiac and brain groups at the CHUV, and the HUG in Geneva.

While this "emigrant" has been abroad for a while, a part of his heart hasn't left the sunny shores and pastry shops of Portugal. I thank everyone at Prof. Patrícia's group and ISR for their warm, welcoming attitude when we see each other now and then, their bright ideas and dedication, with which we've built some great long-distance ventures. My friends from Biomedical Engineering, it's always great to see you, have a chat, laugh about something, occasionally notice how swiftly time does fly by – it's now been more than 10 years since we first met at IST. A special holler to Miguel, Marco, André and Diogo from "Sins'05", the other greatest band on the planet. Ricardo and Michel, with whom I lived during the first six months of this PhD; those times were unforgettable! Great thanks as well to my friends back in the glorious town of Barreiro and outskirts, some of which I've known since kindergarten... It's always a special, sort of cozy pleasure to be back home, have a coffee or a beer, hear how you've been doing.

A very special thanks goes, of course, to Jessica – my greatest (non-scientific) finding over this PhD! Your love and support means a lot to me; having you around has made me a better (certainly more proactive) person. For last, but certainly not least, I thank the love and unconditional support of my family, and especially my mom, dad, sister, grandmothers Amélia and Lucília, my aunts Zé and Cristina. My late granddads David and Henrique, true inspirations, who were happy to hear of my soldering adventures, and how one can actually have fun repeatedly going up and down steep hills under freezing conditions (also known as "skiing"). The journey to where I am today would certainly not have been possible without all your support over these 28 years. You have my deepest thanks.

Lausanne, January 11st, 2016

João

Abstract

Scalp electroencephalography (EEG) and functional magnetic resonance imaging (fMRI) have proved to be valuable tools for the study of human brain function. Furthermore, the two techniques have highly complementary substrates, strengths and limitations, and their combination has been actively sought within neuroscience research. The important gains in fMRI sensitivity achieved with higher field strengths open exciting perspectives for combined EEG-fMRI. However, simultaneous EEG-fMRI acquisitions are subject to highly undesirable interactions between the two modalities, which can strongly compromise data quality, and raise concerns on subject safety. Most of these interactions are field strength-dependent, and can become very problematic at higher field strengths such as 7 T. Despite continued research efforts, many of these challenges remain open problems in the field, compromising the applicability and reliability of this approach, especially at higher field strengths.

The work described in this thesis was centered on the development of simultaneous EEG-fMRI in humans at 7 T, covering aspects of subject safety, signal quality assessment, and quality improvement. Additionally, given the potential value of high-field EEG-fMRI to study the neuronal correlates of so-called negative blood oxygenation level-dependent (BOLD) responses, an initial fMRI study was dedicated to these phenomena, providing a starting point for future investigations with EEG-fMRI.

The initial, pure-fMRI study aimed to characterize, in humans, positive (PBRs) and negative BOLD responses (NBRs) to visual checkerboard stimulation of varying contrast and duration, at 7 T, focusing on NBRs occurring in visual and in auditory cortical regions. Results showed that visual PBRs and both visual and auditory NBRs significantly depend on stimulus contrast and duration. Response amplitudes increased with stimulus contrast, with both visual and auditory NBR amplitudes linearly correlated with the visual PBR. For stimuli up to 10–16 s, all response durations remained linearly correlated. For longer stimulation periods, however, both NBRs exhibited earlier returns to baseline than the PBR. These findings suggested a highly dynamic system of visual-auditory interactions, sensitive to stimulus contrast and duration. The neuronal correlates of these interactions could not be addressed in higher detail with fMRI alone, yet could potentially be clarified in future work with combined EEG-fMRI.

Moving on to simultaneous EEG-fMRI implementation, the first stage comprised an assessment of potential safety concerns for simultaneous acquisitions at 7 T, using the particular setup intended to be applied in future studies. The safety tests comprised numerical simula-

tions of RF power distribution and real temperature measurements on a phantom during fMRI acquisition. Two distinct head RF coils were tested – a volume and an occipital surface coil. Overall, no significant safety concerns were found for the setup tested. Simulations predicted a moderate decrease in average power deposition with the introduction of the EEG system (4.9% for the surface coil, 7.9% for the volume coil), with peak values also decreasing for the surface coil (12.5%), and slightly increasing with the volume coil (10.2%). Temperature increases in the monitored EEG electrodes remained below 1°C. Having found no significant safety concerns, a characterization of artifacts induced on MRI data due to the presence of EEG components was then performed. Image quality was assessed in both functional and anatomical human data, and the underlying degradation mechanisms were investigated via \vec{B}_0 and \vec{B}_1^+ field mapping. With the introduction of the EEG system, functional and anatomical images exhibited general losses in spatial SNR (37% and 29%, respectively), with a more moderate loss in temporal SNR (23%) in fMRI data. \vec{B}_0 inhomogeneity increases were essentially limited to extra-cerebral tissue. In contrast, \vec{B}_1^+ maps evinced a general loss in amplitude across the head, along with more accentuated local effects in central-superior regions. These results pointed towards RF pulse disruption as the major degradation mechanism affecting MRI data. Nevertheless, the resulting losses in functional sensitivity were found to be acceptable for fMRI applications, particularly when addressing the visual cortex.

The main part of this work focused on EEG artifacts arising from the combination with MRI, which can surpass the signals of interest by several orders of magnitude, especially at 7 T. The first step focused on optimizing signal transmission between the EEG cap and amplifiers, to minimize artifact contamination at this important stage of the setup. The effects of EEG cable length and geometry were assessed in a phantom model, with specific attention to He coldhead contributions. Adequate cable shortening and bundling effectively reduced environment noise by up to 84% in average power and 91% in inter-channel variability. Simultaneous acquisitions were then performed on human volunteers, using the optimized setup. EEG data exhibited clear eyes-closing alpha modulation and average visual evoked potentials (VEP), with concomitant BOLD signal changes. On a single-trial level, alpha power variations could be observed with relative confidence; VEP detection was more limited. In the second step, a novel approach for head motion artifact detection was developed, based on a simple modification of the EEG cap in which four electrodes were adapted to record only electromagnetic induction effects. Simultaneous acquisitions were performed in volunteers undergoing reversing-checkerboard visual stimulation. Data analysis assisted by the motion sensors revealed that, after gradient artifact correction, EEG signal variance was largely dominated by pulse artifacts, but contributions from spontaneous motion were still comparable to or even larger than those of neuronal activity. Multiple approaches were tested to optimize the denoising approach, and optimal results were obtained when applying an initial pulse artifact correction step, followed by motion artifact correction, and finally ICA denoising. On average, motion artifact correction yielded a 61% reduction in signal power and a 62% increase in VEP trial-by-trial consistency. Combined with ICA, these improvements rose to a 74% power reduction and an 86% increase in trial consistency.

Overall, the results obtained offer optimistic perspectives for the implementation of EEG-

fMRI at ultra-high fields. No significant safety concerns were found for the setups tested. Although MRI data quality was significantly affected by RF disruption effects, their impact was found acceptable for studies of visual function, and could still potentially be reduced. The improvements achieved in EEG data quality were well appreciable at single-subject as well as single-trial levels, and set encouraging perspectives for future studies at 7 T, which may still be further improved by additional future efforts, namely targeting gradient and pulse artifacts.

Keywords: EEG; fMRI; ultra-high field; negative BOLD; simultaneous EEG-fMRI; RF safety; RF field disruption; environment noise; head motion

Resumo

A electroencefalografia de escalpe (EEG) e a imagiologia por ressonância magnética funcional (fMRI) são ferramentas valiosas para o estudo do funcionamento do cérebro humano. Para além disto, as duas técnicas são altamente complementares ao nível dos processos biofísicos que medem, vantagens e limitações, e a sua combinação tem sido activamente procurada em áreas de investigação em Neurociências. Os importantes ganhos em sensibilidade para fMRI que podem ser obtidos a campos magnéticos mais elevados abrem perspectivas motivadoras para aplicações de EEG-fMRI. No entanto, as aquisições simultâneas de EEG-fMRI são também afectadas por interacções altamente prejudiciais entre as duas modalidades, que podem comprometer severamente a qualidade dos dados adquiridos, bem como levantar questões a nível de segurança para os sujeitos submetidos às aquisições. Grande parte destas interacções depende da intensidade do campo magnético aplicado, e pode tornar-se altamente problemática a campos mais elevados como 7 T. Apesar de serem objecto de esforços contínuos de investigação, muitos destes problemas permanecem em aberto, comprometendo a aplicabilidade e fiabilidade dos dados adquiridos, especialmente a campos mais elevados.

O trabalho descrito nesta tese centrou-se no desenvolvimento da técnica de EEG-fMRI simultâneo para humanos a 7 T, englobando aspectos de segurança, avaliação da qualidade dos sinais, e sua melhoria. Adicionalmente, dado o potencial desta técnica para o estudo das origens neuronais das chamadas respostas de sinal BOLD negativas, um estudo inicial de fMRI foi dedicado a este fenómeno, providenciando um ponto de partida para estudos futuros de EEG-fMRI.

Neste estudo inicial, exclusivamente de fMRI, procurou caracterizar-se, em humanos, as respostas BOLD positivas (PBRs) e negativas (NBRs) a um estímulo visual de xadrez alternado de contraste e duração variável, a 7 T, com principal atenção para as NBRs que ocorrem em regiões corticais visuais e auditivas. Os resultados obtidos mostraram que as PBRs visuais e tanto as NBRs visuais como auditivas dependem significativamente do contraste e da duração de estímulo. A amplitude das respostas aumentou com o contraste, e tanto a amplitude das NBRs visuais como das auditivas exibiu uma correlação linear com a amplitude da PBR visual. Para estímulos até 10–16 s, as durações de todos os tipos de resposta mantiveram-se linearmente correlacionadas. No entanto, para períodos de estímulo mais longos, ambos os tipos de NBR mostraram retornos mais precoces para o nível de repouso do que a PBR. Estas observações sugeriram a presença de um sistema altamente dinâmico de interacções

visual-auditivas, que depende de propriedades do estímulo como o contraste e a duração. Os processos neuronais envolvidos nestas interações não puderam ser isolados em maior detalhe apenas com fMRI, mas poderão ser clarificados em estudos futuros com a combinação de EEG e fMRI.

Passando ao EEG-fMRI simultâneo, a primeira fase de implementação consistiu num estudo de possíveis riscos de segurança associados às aquisições simultâneas a 7 T, para o caso particular do sistema adoptado para este estudo, e estudos futuros. Os testes de segurança incluíram simulações numéricas da distribuição de potência dos pulsos de RF, bem como medições reais de temperatura num fantoma durante aquisições de EEG-fMRI. Foram testados dois modelos distintos de antenas de RF – uma antena de volume, e uma antena de superfície occipital. De um modo geral, não foram encontrados riscos de segurança para os sistemas estudados. As simulações previram reduções moderadas na potência média transmitida aos tecidos da cabeça aquando da introdução do sistema de EEG (de 4.9% para a antena de superfície, e 7.9% para a antena de volume), com os valores de pico também a decrescer para a antena de superfície (12.5%) e a aumentar ligeiramente para a antena de volume (10.2%). Os aumentos de temperatura nos eléctrodos de EEG medidos permaneceram abaixo de 1°C. Não tendo encontrado riscos de segurança para o sistema estudado, passou-se seguidamente à caracterização dos artefactos induzidos nos dados de MRI devido à presença das componentes de EEG. A qualidade das imagens foi avaliada em dados humanos, tanto funcionais como anatómicos, e os mecanismos de degradação subjacentes foram investigados através do mapeamento dos campos \vec{B}_0 e \vec{B}_1^+ . Com a introdução do sistema de EEG, tanto as imagens funcionais como anatómicas exibiram perdas gerais de SNR espacial (de 37% e 29%, respectivamente), com uma perda mais moderada de SNR temporal (23%) nos dados de fMRI. Perdas na homogeneidade do campo \vec{B}_0 mostraram-se essencialmente limitadas a tecidos extra-cerebrais. Por outro lado, os mapas de \vec{B}_1^+ evidenciaram uma perda geral de amplitude em toda a região da cabeça, aliada a efeitos locais mais acentuados em regiões centro-superiores. Estes resultados apontam para a disrupção dos pulsos de RF como principal mecanismo de degradação dos dados de MRI. Todavia, as perdas em sensibilidade funcional resultantes mostraram-se aceitáveis para aplicações de fMRI, particularmente quando dedicadas ao córtex visual.

A componente principal deste trabalho focou-se efectivamente nos artefactos de EEG resultantes da combinação com MRI, que podem ultrapassar os sinais de interesse em várias ordens de magnitude, especialmente a 7 T. A primeira fase centrou-se na optimização da transmissão de sinal entre a touca de EEG e os amplificadores, de forma a minimizar a contaminação por artefactos desta importante componente do sistema de aquisição. A influência do comprimento e geometria dos cabos de transmissão foi estudada num fantoma, com especial atenção dedicada a contribuições dos compressores de He. Observou-se que a redução do comprimento dos cabos e a sua compressão levaram a reduções de ruído ambiente de até 84% em valor médio de potência, e até 91% na variabilidade entre canais. Foram seguidamente efectuadas aquisições de EEG-fMRI simultâneo em voluntários humanos, utilizando o sistema optimizado. Os dados de EEG resultantes exibiram padrões claros de modulação de ritmos alfa aquando do abrir/fechar de olhos, e potenciais visuais evocados (VEP), bem como as correspondentes alterações no sinal BOLD esperadas para estes estímulos. Ao nível

de repetições individuais, as variações na potência de ritmos alfa puderam ser robustamente observadas; a detecção de VEPs foi mais limitada. Na segunda fase, desenvolveu-se um novo método para detecção de artefactos induzidos por movimentos da cabeça, baseado numa modificação simples da touca de EEG segundo a qual quatro eléctrodos são adaptados para captar apenas efeitos de indução electromagnética. Aquisições simultâneas foram conduzidas em voluntários durante estimulação visual com padrões de xadrez alternados. A análise dos dados adquiridos assistida por informação dos sensores de movimento revelou que, após remoção dos artefactos de gradiente, a variância do sinal de EEG foi fortemente dominada pelos artefactos de pulso, mas as contribuições resultantes de movimentos espontâneos foram ainda assim comparáveis ou até superiores às da actividade neuronal. Foram testadas múltiplas abordagens para otimizar o procedimento de redução de artefactos, tendo-se obtido os resultados mais favoráveis mediante a aplicação de um passo inicial de correcção de artefactos de pulso, seguido da correcção de artefactos de movimento, e finalmente um último passo baseado em ICA. Em média, a correcção de artefactos de movimento resultou em reduções na potência de sinal de 61%, e aumentos de 62% na consistência de VEPs de repetição para repetição. Em combinação com ICA, estas melhorias cresceram para uma redução de 74% na potência de sinal e um aumento de 86% na consistência dos VEPs.

De um modo geral, os resultados obtidos ao longo deste trabalho oferecem boas perspectivas para a implementação da técnica de EEG-fMRI simultâneo a campos ultra-elevados. Não foram encontrados riscos de segurança para os sistemas testados. Ainda que a qualidade dos dados de MRI tenha sido significativamente afectada por efeitos de disrupção dos pulsos de RF, o impacto destes efeitos foi considerado aceitável para estudos de função visual, e poderá ainda potencialmente vir a ser reduzido. As melhorias obtidas na qualidade dos dados de EEG foram evidentes tanto ao nível de sujeitos como de repetições individuais, e oferecem perspectivas encorajadoras para estudos futuros a 7 T, que poderão ainda ser continuamente melhoradas por desenvolvimentos futuros, nomeadamente focados nos artefactos de gradiente e artefactos cardíacos.

Palavras-chave: EEG; fMRI; campo magnético ultra-elevado; resposta BOLD negativa; EEG-fMRI simultâneo; segurança em RF; disrupção de campos de RF; ruído ambiente; artefactos de movimento

Résumé

L'électroencéphalographie (EEG) et l'imagerie par résonance magnétique fonctionnelle (fMRI) sont des outils de grande valeur pour l'étude du fonctionnement du cerveau humain. En outre, les deux techniques sont très complémentaires en termes de substrats, d'avantages et de limites, et leur combinaison a été activement recherchée dans les neurosciences. Les gains importants en sensibilité de la fMRI obtenus à très haut champ magnétique ouvrent des perspectives intéressantes pour la combinaison de l'EEG et de la fMRI. Cependant, les acquisitions simultanées EEG-fMRI sont soumises à des interactions hautement indésirables entre les deux modalités, qui peuvent compromettre fortement la qualité des données, et soulever des préoccupations sur la sécurité des sujets. La plupart de ces interactions sont dépendantes de l'intensité du champ magnétique, et peuvent devenir très problématiques à des plus hauts champs tel que 7 T. Malgré des efforts de recherche continus, ces défis demeurent des problèmes ouverts dans ce domaine d'étude, et compromettent l'applicabilité et la fiabilité de la technique, en particulier à intensités de champ plus élevées.

Le travail décrit dans cette thèse a été centré sur le développement de la technique de l'EEG-fMRI simultanée pour les sujets humains à 7 T, couvrant les aspects de sécurité des sujets, l'évaluation de la qualité du signal et l'amélioration de celle-ci. En outre, compte tenu de la valeur potentielle de l'EEG-fMRI à haut champ pour étudier les corrélats neuronaux des soi-disant réponses BOLD négatives, une première étude fMRI a été consacrée à ces phénomènes, offrant un point de départ pour des futures enquêtes avec EEG-fMRI.

L'étude initiale de fMRI visait à caractériser, chez les sujets humains, les réponses BOLD positives (PBR) et négatives (NBR) à la stimulation visuelle en damier de contraste et durée variables, à 7 T, en se concentrant sur les NBR des régions corticales visuelles et auditives. Les résultats ont montré que les PBR visuelles et les NBR visuelles et auditives dépendent de manière significative du contraste et de la durée des stimuli. Les amplitudes de réponse ont augmenté avec le contraste, avec les amplitudes des NBR visuelles et auditives linéairement corrélées avec la PBR visuelle. Pour des stimuli allant jusqu'à 10–16 s, toutes les durées de réponse sont restées linéairement corrélées. Cependant, pour les périodes de stimulation plus longues, les deux NBR ont montré un retour au niveau de repos plus rapide que la PBR. Ces résultats suggèrent un système très dynamique d'interactions visuelles et auditives, sensibles au contraste et à la durée de stimulation. Les corrélats neuronaux de ces interactions ne peuvent pas être abordés avec plus de détails en utilisant la fMRI seul, mais pourraient être

clarifiées dans des travaux futurs avec l'EEG-fMRI.

Passant au développement de la technique de l'EEG-fMRI simultanée, la première étape a été consacrée à l'évaluation des potentiels problèmes de sécurité pour les acquisitions simultanées à 7 T, en utilisant la configuration particulière destinée à être appliquée dans des études futures. Les tests de sécurité comprirent des simulations numériques de distribution de puissance RF, et des mesures de température réelles sur un fantôme lors de l'acquisition fMRI. Deux antennes de RF pour la tête ont été testées - une antenne de volume et une antenne de surface occipital. Dans l'ensemble, aucun problème de sécurité important n'a été trouvé pour les configurations testées. Les simulations prédirent une baisse modérée de dépôt de puissance moyenne avec l'introduction du système de l'EEG (4.9% pour l'antenne de surface, et 7.9% pour l'antenne de volume), avec des valeurs maximales également en baisse pour l'antenne de surface (12.5%) et en légère augmentation avec l'antenne de volume (10.2%). Les hausses de température dans les électrodes de l'EEG surveillés sont restées en dessous de 1°C. N'ayant trouvé aucun problème de sécurité important, une caractérisation des artefacts induits sur des images de la fMRI en raison de la présence des composants de l'EEG a ensuite été effectuée. La qualité d'image a été évaluée avec des données humaines anatomiques et fonctionnelles, et les mécanismes de dégradation sous-jacents ont été étudiés par la cartographie des champs \vec{B}_0 et \vec{B}_1^+ . Avec l'introduction du système de l'EEG, les images fonctionnelles et anatomiques ont révélé des pertes générales de SNR spatial (37% et 29%, respectivement), avec une perte plus modérée de SNR temporel (23%) dans les données de la fMRI. Les hausses d'inhomogénéité du champ \vec{B}_0 ont été essentiellement limitées aux tissus extra-cérébrales. En revanche, le champ \vec{B}_1^+ a manifesté une perte générale d'amplitude sur la tête, avec des effets locaux plus accentués dans les régions central-supérieures. Ces résultats indiquent que la perturbation du champ \vec{B}_1^+ est le mécanisme de dégradation majeure affectant les données de la MRI. Toutefois, les pertes résultantes sur la sensibilité fonctionnelle ont été jugées acceptables pour des applications de la fMRI, en particulier lorsqu'on aborde le cortex visuel.

La partie principale de ce travail a été consacrée aux artefacts de l'EEG découlant de la combinaison avec la MRI, qui peuvent dépasser les signaux d'intérêt par plusieurs ordres de grandeur, en particulier à 7 T. La première étape a été centrée sur l'optimisation de la transmission du signal entre le casque et les amplificateurs de l'EEG, pour minimiser la contamination par artefacts à ce stade important de la configuration. Les effets de la longueur et de la géométrie des câbles de l'EEG ont été évalués dans un fantôme, avec une attention particulière aux contributions des compresseurs d'He. Le raccourcissement des câbles et son regroupement ont produit des réductions dans le bruit de l'environnement jusqu'à 84% en puissance moyenne et de 91% pour la variabilité inter-canal. Des acquisitions simultanées ont ensuite été effectuées sur des volontaires humains, en utilisant la configuration optimisée. Les données de EEG ont clairement montré des modulations des rythmes alpha avec la fermeture des yeux, et des potentiels évoqués visuels (VEP) en moyenne, avec des changements de signal BOLD concomitants. Au niveau des essais individuels, les variations de puissance d'alpha ont pu être observées avec confiance ; la détection de VEP individuels a été plus limitée. Dans la deuxième étape, une nouvelle approche pour la détection d'artefacts de mouvement de la tête a été dé-

veloppée, basée sur une modification simple du casque de l'EEG dans lequel quatre électrodes ont été adaptés pour enregistrer seulement des effets d'induction électromagnétique. Des acquisitions simultanées ont été effectuées sur des volontaires humains, durant stimulation visuelle en damier. L'analyse des données assistée par les détecteurs de mouvement a révélé que, après correction de l'artefact de gradient, la variance du signal de l'EEG a été largement dominée par des artefacts cardiaques, mais les contributions de mouvement spontané ont été toujours comparables ou même plus grandes que celles de l'activité neuronale. Plusieurs approches ont été testées afin d'optimiser l'approche de réduction d'artefacts, et des résultats optimaux ont été obtenus lors de l'application d'une étape initiale de correction d'artefacts cardiaques, suivie par la correction d'artefacts de mouvement et enfin par correction avec l'ICA. En moyenne, la correction d'artefacts de mouvement a conduit à une réduction de 61% de la puissance de signal et une augmentation de 62% de la cohérence de VEP entre essais. Combiné avec l'ICA, ces améliorations ont réduit la puissance de 74% et augmenté de 86% la cohérence entre essais.

Dans l'ensemble, les résultats obtenus offrent des bonnes perspectives pour la mise en œuvre de la technique de l'EEG-fMRI à champ ultra-élevé. Aucun problème de sécurité important n'a été trouvé pour les configurations testées. Bien que la qualité des données de la MRI a été significativement affectée par des effets de perturbation de RF, leur impact a été jugée acceptable pour les études de la fonction visuelle, et pourrait encore être potentiellement réduite. Les améliorations apportées dans la qualité des données de l'EEG ont été bien appréciables au niveau des sujets, ainsi que pour des essais individuels, et définissent des perspectives encourageantes pour des études futures à 7 T, qui peut encore être améliorée par des efforts futurs additionnels, comme par exemple dédiés aux artefacts de gradient et aux artefacts cardiaques.

Mots-clefs : EEG ; fMRI ; champ magnétique ultra-élevé ; BOLD négative ; EEG-fMRI simultanée ; sécurité en RF ; perturbation des champs de RF ; bruit d'environnement ; artefacts de mouvement de la tête

Contents

Acknowledgements	i
Abstract (English/Português/Français)	iii
Introduction	1
Thesis outline	2
1 Fundamentals of EEG and fMRI	3
1.1 Fundamentals of EEG	3
1.1.1 Neuronal substrates of EEG	4
1.1.2 Scalp potential generation and source estimation	6
1.1.3 Scalp EEG recording	8
1.1.4 Rhythmic and transient activity	10
1.1.5 Limitations of scalp EEG	13
1.2 Fundamentals of fMRI	14
1.2.1 Nuclear magnetic resonance	15
1.2.2 Magnetic resonance imaging	21
1.2.3 The BOLD contrast	23
1.2.4 BOLD fMRI acquisition	25
1.2.5 Limitations of BOLD fMRI	28
1.3 EEG-fMRI integration	30
1.3.1 Substrates of EEG, fMRI and behavior	31
1.3.2 Experimental design	31
1.3.3 Generic data processing	33
1.3.4 Data integration: comparison approaches	34
1.3.5 Data integration: asymmetrical approaches	35
1.3.6 Data integration: symmetrical approaches	37
2 The negative BOLD response to visual stimulation	41
2.1 Introduction	41
2.2 Methods	44
2.2.1 Data acquisition	44
2.2.2 Functional paradigms	44
2.2.3 Data analysis	45

Contents

2.3	Results	47
2.3.1	Positive and negative BOLD stimulus dependence	47
2.3.2	Grey matter – vein separation	50
2.3.3	ICA-assisted denoising	52
2.4	Discussion	54
2.4.1	Positive and negative BOLD stimulus dependence	55
2.4.2	Grey matter – vein separation	57
2.4.3	ICA-assisted denoising	58
2.4.4	Conclusion	59
3	EEG-fMRI at 7T: subject safety	61
3.1	Introduction	61
3.2	Methods	64
3.2.1	EEG-(f)MRI acquisition setup	64
3.2.2	Electromagnetic simulations	64
3.2.3	Temperature measurements	66
3.3	Results	67
3.3.1	Electromagnetic simulations	67
3.3.2	Temperature measurements	68
3.4	Discussion	71
3.4.1	Conclusion	73
4	EEG-fMRI at 7T: MRI data quality	75
4.1	Introduction	75
4.2	Methods	77
4.2.1	MRI data acquisition	77
4.2.2	MRI data analysis	77
4.3	Results	78
4.4	Discussion	79
4.4.1	Conclusion	81
5	EEG-fMRI at 7T: EEG data quality	83
5.1	Introduction	84
5.1.1	Gradient and pulse artifacts	84
5.1.2	Environment noise	85
5.1.3	Head motion artifacts	86
5.2	Theory	88
5.2.1	EEG artifact generation	88
5.2.2	Motion artifact generation	88
5.2.3	Motion artifact correction	90
5.3	Methods: signal transmission	91
5.3.1	MRI system	91
5.3.2	Signal transmission optimization	91

5.3.3	Optimized EEG setup	92
5.3.4	Human acquisitions	93
5.4	Methods: head motion	95
5.4.1	Data acquisition	95
5.4.2	fMRI data analysis	96
5.4.3	EEG data analysis	96
5.5	Results: signal transmission	100
5.5.1	EEG cable noise contributions	100
5.5.2	Simultaneous acquisitions in humans	102
5.6	Results: head motion	105
5.6.1	Part I: pulse and motion artifact correction	107
5.6.2	Part II: optimization of motion artifact correction	110
5.6.3	Part III: motion artifact correction and ICA	112
5.7	Discussion	113
5.7.1	EEG signal transmission optimization	115
5.7.2	Optimized EEG-fMRI acquisitions	116
5.7.3	Motion artifact detection	118
5.7.4	Motion artifact correction	119
5.7.5	Motion artifacts and ICA	121
5.7.6	Conclusion	121
6	Conclusions	123
6.1	Outlook	124
	Bibliography	127
	List of figures	151
	Publications arising from this thesis	155
	Curriculum Vitae	157

Introduction

The human brain is a remarkably intricate organ, capable of a wide range of cognitive and analytical operations, interlaced with complex emotions and motivations. Investigating the mechanisms and interactions underlying brain function is no easy task, yet its contributions can be tremendous, not only for the understanding of human nature and physiology per se, but also for the development of more effective treatments for life-impairing diseases, as well as inspiring technological advances in distinct scientific fields such as artificial intelligence. With such goals in mind, Mankind has devoted remarkable scientific efforts to the study of brain function over the last centuries.

To face the complex challenges of studying the brain, many techniques have been developed and continually improved, each with its specific substrates, strengths and limitations. The brain can be decomposed into basic units – the neurons, each of which a complex structure that can provide valuable information about the whole. Nevertheless, it is in its function as a dynamic, organized arrangement of neurons, influencing and influenced by internal and external factors, including sensory information and a rich variety of metabolites flowing throughout the body, that the brain attains its remarkable capabilities. For this reason, techniques that can monitor aspects of the human brain as a whole, without affecting its natural function – i.e. minimally invasive, are extremely valuable. Two such examples are scalp electroencephalography (EEG) and functional magnetic resonance imaging (fMRI).

While both EEG and fMRI have proven to be valuable tools on their own for neuroscience research, with numerous contributions for basic research and clinical studies alike, considerable interest has also been devoted to their combined application, motivated by a strong degree of complementarity between the two modalities. While EEG measures the electric potential fluctuations generated by post-synaptic activity of neuronal populations, with high temporal resolution but poor spatial specificity, fMRI is sensitive to a combination of metabolic and hemodynamic changes induced by such neuronal activity, with lower temporal resolution but higher spatial specificity. The two techniques can thus provide highly complementary measures of brain function – like two pieces of a common "neuroimaging puzzle" (Babiloni et al., 2004).

The combination of EEG and fMRI has been actively pursued for more than two decades, both in basic neuroscience and clinical contexts, with continued technical improvements. In

particular, a fundamental line of development for fMRI has been the pursuit of higher magnetic field strengths, which leads to super-linear gains in functional sensitivity. These gains can be valuable for numerous applications, and have likewise raised considerable interest in the combination of EEG and fMRI at higher fields. Unfortunately, however, simultaneous EEG-fMRI acquisitions are also subject to highly undesirable interactions occurring between the two modalities, which can strongly compromise data quality, as well as raise concerns on subject safety. Crucially, many of these deleterious interactions are field strength-dependent, and can become very problematic at ultra-high field strengths such as 7 Tesla. For this reason, before the benefits of ultra-high field imaging can be effectively explored in simultaneous EEG-fMRI, important challenges must be addressed and overcome. With this purpose in mind, the work described in this thesis was centered on the development of simultaneous EEG-fMRI in humans at 7 T, covering aspects of subject safety, signal quality assessment, and quality improvement. The findings here reported contribute to a recent, and still fairly unexplored line of research focused on EEG-fMRI at ultra-high field, seeking to improve the applicability and effectiveness of this approach, and ultimately helping to expand our current understanding of human brain function, in both health and disease.

Thesis outline

This thesis is organized in six interrelated chapters. *Chapter 1* provides a theoretical overview of the biophysical principles underlying EEG and fMRI, followed by a review of the most important aspects to consider in the integration of the two techniques for the study of brain function. In *Chapter 2*, a purely fMRI-based study is reported, investigating both positive and negative brain responses to visual stimulation, in visual and auditory regions. *Chapters 3–5* cover technical aspects of the development of simultaneous EEG-fMRI at 7 T. *Chapter 3* reports on the assessment of subject safety, an aspect of primary importance for human experimentation, and includes both numerical simulations performed with realistic computational models and real temperature measurements conducted in phantom models. *Chapter 4* provides a comprehensive evaluation of the impact of EEG equipment on MRI data quality, with a particular focus on fMRI data. *Chapter 5*, the largest and possibly most important of this thesis, addresses MRI-induced artifacts on EEG recordings, and presents a number of novel modifications developed to reduce these highly-compromising artifact contributions. Finally, *Chapter 6* summarizes the main conclusions derived from this work, followed by an outlook on relevant potential lines of future development.

1 Fundamentals of EEG and fMRI

Electroencephalography (EEG) and **functional magnetic resonance imaging** (fMRI) are valuable tools for neuroscience, each with a remarkable record of contributions to the study of brain function. Furthermore, beyond their individual value, the two techniques are highly complementary to each other, and their combined application can yield improved descriptions of the neurological, vascular and metabolic processes underlying brain function. This chapter provides a theoretical overview of the biophysical principles underlying EEG and fMRI, followed by a review of the aspects of most importance for the integration of the two techniques.

1.1 Fundamentals of EEG

As a general definition, EEG is a technique that measures fluctuations in **electric potentials** generated by brain activity. It is most commonly performed by placing electrodes in physical contact with the scalp, with minimum invasiveness for the subject under study. The first human scalp EEG recordings were performed by the neuropsychiatrist Hans Berger in 1925. Berger, who coined the term "electroencephalogram", was the first to observe several important features of the human EEG such as alpha oscillations, sleep spindles, and even hints of epileptic activity (Niedermeyer and Lopes da Silva, 2005). Since then, the technique has undergone remarkable technological improvements to enhance its sensitivity and temporal resolution, accompanied by continuous developments in data analysis methodologies. In parallel, widespread efforts using a variety of other techniques, both in vivo and in vitro, have helped to form a better, and still growing understanding of what is exactly measured by EEG, and how this information can provide insights into the underlying brain activity.

Parts of this chapter were adapted from:

EEG-fMRI integration for the study of human brain function, J. Jorge, W. van der Zwaag, P. Figueiredo, 2014, Neuroimage 102 (1), p.24–34.

1.1.1 Neuronal substrates of EEG

It is currently well known that brain activity is accomplished through a complex network of interactions carried by fundamental functional units – the **neurons**, assisted by supporting units generally termed **glia cells**. Each neuron receives input from upstream neurons via synaptic interactions, and its output is produced in the form of traveling action potentials (also termed "spiking") that are sent to other neurons. When at rest, neurons typically maintain a difference in electric potential between the intra and extracellular spaces of -70 to -90 mV. This is achieved by maintaining a different concentration of ions such as Na^+ and K^+ inside the cellular space, compared to the outside medium, achieved with active transport systems at the cost of energy. When the transmembrane potential is raised above a threshold of approximately -50 mV, in a specific point of the cell, it triggers the opening of voltage-gated ion channels in the membrane, allowing ion fluxes that can reverse, and raise the potential difference to approximately +35 mV – and thereby an **action potential** is formed. This event tends to be quickly counteracted by other ion fluxes, leading to a return to the baseline state after only a few milliseconds. Nevertheless, the depolarization of a certain point leads to potential increases in neighboring regions, which can likewise trigger local action potentials. This phenomenon allows the generation of traveling waves, which can propagate the action potential along the cell membrane, typically from the cell dendrites down its axon, without any decay in amplitude (Guyton and Hall, 2006).

In a typical **neuronal synapse** (Fig. 1.1a), action potentials arriving from the upstream or presynaptic neuron to a presynaptic terminal can trigger the release of neurotransmitter molecules to a narrow extracellular space termed synaptic cleft. Presynaptic terminals lie close to the surface of post-synaptic neurons, along various regions such as the dendrites, cell body, and even the axon. When released, the neurotransmitters can couple to highly specific receptors in the cell membrane of the postsynaptic neuron, and either modulate the excitability of the cell or directly change its transmembrane potential. The second effect is mediated by ligand-dependent ion channels, and can be excitatory, inducing depolarization, or inhibitory, inducing hyperpolarization. The ion fluxes across the cell membrane induced by neurotransmitter reception are known as **postsynaptic activity**. These fluctuations create differences in electric potential between the stimulated dendrites and sub-synaptic regions, which in turn generate both intra and extracellular currents *along* the cell membrane (Fig. 1.1b). The latter currents generate the so-called **local field potentials** (LFPs), and can be seen as equivalent electric dipoles formed between the dendrites and downstream regions (Niedermeyer and Lopes da Silva, 2005). Because the brain is a conductive medium, the extracellular currents generated near the neuron propagate almost virtually instantaneously across its space, and thereby these LFPs can be detected at the surface of the head (Dale and Halgren, 2001).

Besides LFPs, the generation and propagation of action potentials also causes extracellular currents along the cell surface, which can be measured by electrodes placed close to the originating neurons. On the other hand, electrodes placed in farther regions, particularly at

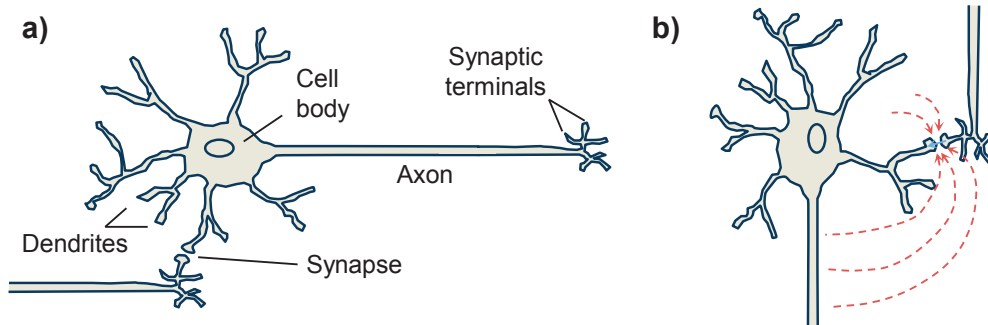


Figure 1.1: Neuronal substrates of EEG. **a)** Representation of a neuron, with a neuronal synapse. Synapses can typically be observed in every dendritic terminal, as well as in other regions of the cell surface. **b)** Extracellular current generation (represented by red dashed arrows) due to an excitatory synaptic interaction (blue arrow). Far from the neuron, the created potential field can be approximated by that of a localized current dipole. If several neurons, aligned in parallel with each other, are excited in synchrony, the resulting potentials are favorably summed, facilitating detection.

the scalp, are considerably less sensitive, and can only detect the net dipole potentials created by large neuronal populations functioning in synchrony. LFPs occur in a timescale that allows favorable summation of group activity; on the other hand, fluctuations created by neuronal spiking, also termed **multi-unit activity** (MUA), have considerably shorter timescales, and do not achieve sufficient synchrony to be measurable at the scalp. The main neuronal substrate of scalp EEG is, therefore, the LFP fluctuations created by synchronized postsynaptic activity of large neuronal populations (Nunez and Silberstein, 2000).

Besides temporal constraints, the **geometry** of neuronal cell arrangements in the brain is likewise a crucial factor for the sensitivity of scalp EEG. The cortex can be described in terms of distinct layers, conventionally numbered I–VI, from the outside (pial surface) to the inside (white matter). Each layer is characterized by a particular distribution of neuronal cell types and connections; nevertheless, extensive connections can be observed between cells from the different layers, often spanning the entire cortical depth. In the somatosensory cortex, for example, incoming sensory signals typically excite layer IV neurons first, and then extend towards more superficial and deeper layers; neurons from layers II and III send signals to related cortical areas in the opposite hemisphere, while neurons in layers V and VI send axons to deeper parts of the nervous system (Guyton and Hall, 2006). Along with its layer differentiation, the cortex can also be described as a columnar structure, composed of basic units denominated **minicolumns**, each with a cross-section diameter of approximately 50 μm , and main axis oriented perpendicularly to the pial surface. Each minicolumn comprises a narrow chain of neurons extending vertically from the deeper to the more superficial layers. Minicolumns can then form groups, linked together by short-range horizontal connections, designated **cortical columns** – each including several dozens of minicolumns (several thousands of neurons), with a cross-sectional diameter of several hundred μm . Minicolumns and cortical columns have been proposed to form the basic units of cortical processing, under-

going different dynamic states with high specificity and cooperating with each other in a context-dependent manner. This columnar organization of cortical function is highly important, and advantageous, for scalp EEG; in particular, a strong flow of information is created vertically along each column, carried in great part by **pyramidal cortical neurons**. These cells have the main axes of the dendritic trees parallel to each other and perpendicular to the pial surface, and long axons that are similarly vertically-oriented – a "palisade" arrangement. Extracellular currents created by post-synaptic activity in these neurons will thus have fairly regular orientations, and the corresponding equivalent dipoles are favorably summed. The (postsynaptic) activity of pyramidal cortical cells, arranged in functionally-specific columns, forms thereby the major substrate of scalp EEG (Mulert and Lemieux, 2010).

1.1.2 Scalp potential generation and source estimation

In order to interpret the electric potential fluctuations measured at the scalp and draw inferences regarding the underlying neuronal sources, particularly their strength and spatial distribution, it is essential to design adequate biophysical models that can relate the LFPs generated by neuronal activity with the fluctuations measured at the scalp. When studying neurons at a microscopic scale, the local electric potential fields induced by postsynaptic stimuli are considerably challenging to model, because the associated ion currents are typically formed from specific dendritic regions (near the activated synaptic receptors) to a more distributed volume along the subsynaptic regions, which depends on the conductivities of intra and extracellular fluids, as well as on the conductivity and capacitive properties of the cell membrane. Fortunately, however, at the considerably larger spatial scale of EEG measurements, these distributions can be adequately modeled as simpler "sink-source" configurations, or **equivalent current dipoles** (Nunez and Srinivasan, 2006).

In empty space, the electric potential ϕ created by a static point charge q at a distance r from the charge can be derived from Coulomb's law, and is given by:

$$\phi(r) = \frac{1}{4\pi\epsilon_0} \frac{q}{r} \quad (1.1)$$

where ϵ_0 is the electric permittivity of empty space. A current dipole can be seen as a pair of opposite monopoles (current "source" and current "sink"). While physically distinct from static charges in an empty space or dielectric medium, current monopoles obey an analogous form of Poisson's equation, and their electric potential can be described by a mathematically-equivalent form of Eq.1.1. In particular, for an infinitely-large, homogeneous, isotropic and purely resistive conductive medium, the electric potential created by a current monopole pair is equal to:

$$\phi(r_1, r_2) = \frac{I}{4\pi\sigma} \left(\frac{1}{r_1} - \frac{1}{r_2} \right) \quad (1.2)$$

where I is the magnitude of the current source (in units of electric current), σ is the electric

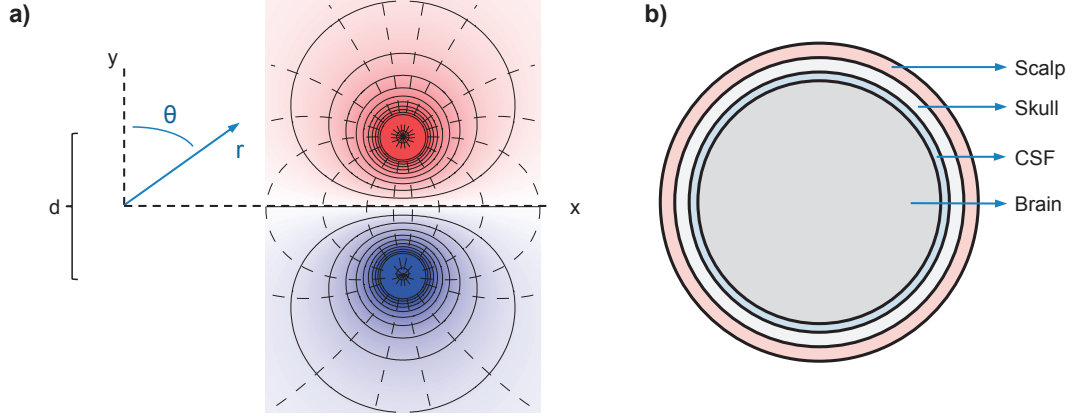


Figure 1.2: Potential generation and source modeling. **a)** Electric potential distribution created by a current source-sink pair in a homogeneous and isotropic conductive medium. **b)** A schematic example of a simple concentric conductive shell model for EEG source estimation in the head, differentiating scalp, skull, cerebrospinal fluid (CSF) and brain tissues.

conductivity of the medium, and r_1 and r_2 are the distances from the measuring point to each of the two poles (Fig. 1.2a). If the measurement is performed far from the source compared to the distance between the two poles (as is the case in scalp EEG), ϕ can be approximated by:

$$\phi(r, \theta) \approx \frac{I}{4\pi\sigma} \frac{d \cos \theta}{r^2} \quad (1.3)$$

where r is the distance from the dipole center to the measuring point, θ is the angle formed between the dipole axis and the measuring position \vec{r} relative to the dipole center, and d is the spatial extent of the dipole (i.e. the distance between monopoles). This is a suitable approximation considering, for instance, that equivalent source-sink separations in pyramidal cells are smaller than 1 mm, while the closest point at the scalp may be more than 1 cm away. Considering the particular, fairly "vertical" geometry of pyramidal neurons, a more appropriate model for postsynaptic excitatory potentials would, in fact, be that of a uniform source distribution along a vertical segment of length d , with a point sink at the top (or vice-versa, for inhibitory activity). The electric potential field created by this geometry can be approximated by:

$$\phi(r, \theta) \approx \frac{I}{8\pi\sigma} \frac{d \cos \theta}{r^2} \quad (1.4)$$

which can be seen as an extension of Eq. 1.3 where the effective distance is now $d/2$, owing to the spatial dispersion of the sources (Nunez and Srinivasan, 2006).

Having established a suitable relationship between neuronal sources and electric potential distributions – the **forward model**, one can then attempt to estimate current dipole magnitudes and orientations based on a series of electric potential measurements – a process known as **inverse modeling**. Multiple dipolar sources can be considered and estimated from the same

measurement set, as a linear combination of electric potentials, following the principle of superposition. The homogeneous medium simplification provides insights into important aspects of neuronal potential propagation: first, the signal amplitude decays with the square of the distance to the source; second, the amplitude depends on the orientation of the dipole relative to the position of the measurements (Nunez and Silberstein, 2000). Moving on to real brain signals measured at the scalp, it is then necessary to improve the basic model to account for important properties of this medium. The head is not an infinite volume, and its conductivity varies across different types of tissues, which include grey and white matter, cerebrospinal fluid (CSF), various membranes, skull, and scalp – the skull, in particular, is considerably less conductive than the other tissues (Mulert and Lemieux, 2010). A commonly-used model to account for these differences is that of a set of concentric conductive shells approximating the different head layers (Fig. 1.2b). Given approximated values for layer conductivity and thickness, this model can be solved analytically for dipole estimation (Nunez and Srinivasan, 2006).

Although practical, the choice of a spherical geometry yields a poor approximation to model the human head. To overcome this and other limitations, more elaborate (and typically iterative) approaches have been proposed and continuously improved. Subject-specific models can be estimated from real anatomical data (obtained with MRI or computed tomography, for example), using numerical discretization approaches such as **boundary element methods** (BEM) (Fuchs et al., 2002) or **finite element methods** (FEM) (Awada et al., 1997). The latter class can additionally incorporate the effects of anisotropic conductivity (Wolters et al., 2006), at the cost of increased computational demands. It is important to note that the challenge of source estimation from scalp EEG is a very ill-posed problem – mathematically, a given potential distribution measured at the surface has an infinite number of possible solutions within the volume. For this reason, estimation approaches require heavy **regularization**, with more or less biophysically-inspired constraints (Michel et al., 2004). In applications where a few particularly dominant sources are expected, the number and/or orientation of source dipoles can be restricted (down to a single dipole). In more elaborate variants of this approach, the entire cortical tissue is segmented from anatomical data and parcellated into surface patches; each patch is then given a dipole of fixed orientation (perpendicular to the cortical surface), and only dipole magnitudes remain to be estimated (Hillebrand and Barnes, 2003). Overall, however, even with strong regularization constraints, source estimation from scalp EEG remains a challenging problem, and solutions typically have poor spatial specificity.

1.1.3 Scalp EEG recording

The fluctuations measurable by scalp EEG during normal brain function are typically below 100 μV , and mainly occupy a range of 0–100 Hz in the spectral domain (although interesting features have been identified at higher frequencies as well (Andrade-Valenca et al., 2011)). In order to capture these fluctuations, EEG recording systems must ensure good electrical conductivity with the scalp, effective signal amplification, adequate temporal sampling, and

shielding from potential artifact sources such as power line noise (50/60 Hz) (Mulert and Lemieux, 2010). The first stage comprises a set of **electrodes** that are placed on the scalp, built of a conductive material such as copper or gold. For some electrode types, an electrolyte paste or gel is applied between the skin and the electrode, forming an electrolyte bridge to improve conductivity between the two media. Electric potentials can be transmitted between these media via redox reactions, using interface materials such as Ag/AgCl to coat the electrodes. These interfaces must be adequately designed to ensure that the kinetics and efficiency of the transmission processes do not alter the temporal properties of the measured signals. It is also fundamental to ensure a good overall conductivity through the interface, since any additional impedance elements in the circuit will lead to an attenuation of the signal measured at the amplifiers (Fig. 1.3a) – to prevent significant attenuation, amplifier input impedances are usually designed to reach several M Ω , whereas electrode impedances in the order of k Ω are usually sought during cap preparation (Niedermeyer and Lopes da Silva, 2005). EEG systems vary considerably in the number of electrodes used for recording (from as little as 2 to as many as 512); higher numbers provide richer information and are especially beneficial for source localization purposes, but are also less practical and require longer preparation times. Electrode positions typically follow well-established standards such as the international 10–20 system.

In most recording setups, the electrodes are passive elements that simply detect and transmit the electric potentials to a central **amplification** stage. Transmission is carried through conductive **leads**. At the amplifiers, reference signals are subtracted from individual electrode potentials, and these difference signals are then amplified. The two most common types of systems employ either bipolar amplification, where each amplified signal is the difference between a given electrode and its previous neighbor, in succession, or unipolar amplification, where amplified signals are the difference between each electrode and one common reference electrode. In either case, the signals that are common to both channels in each pair are thereby excluded – a useful feature known as common-mode rejection. Following amplification, modern EEG systems employ a **digitization** step to convert the measured analog signals into digital format, for subsequent storing and numerical analysis. Before digitization, it is also common to apply some form of **temporal filtering** to remove the DC component and slow drifts, as well as to prevent spectral aliasing (Mulert and Lemieux, 2010).

It is important to note that electric potential is not an absolute quantity, and EEG signals are always recorded as **potential differences** between pairs of electrodes. This aspect must be kept in mind when interpreting fluctuations measured at a given channel, and for certain purposes, it becomes convenient to work with reference-independent features extracted from the measured signals, or to bring the measurements into alternative, reference-free representations (such as the space of neuronal sources, obtained via inverse modeling). Another important consequence is that in order to detect any measurable differences between two electrodes, they must be placed at some distance from each other (Fig. 1.3b). This spatial separation imposes the formation of a non-negligible area within the **circuit loop** formed by the electrodes, leads, amplifier and the subject head, which is exposed to any interfering

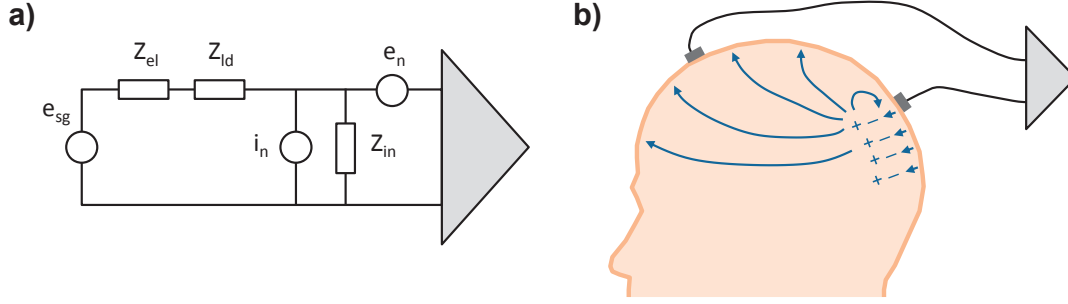


Figure 1.3: Schematics of scalp EEG recording. **a)** Simplified diagram of the input circuit of an EEG recording channel. Z_{el} represents the electrode impedance, Z_{ld} the lead impedance and Z_{in} the amplifier input impedance; e_{sg} represents the EEG signal, i_n and e_n the noise current and voltage sources, respectively, inherent to the amplifier. **b)** Signals are measured as differences in electric potential between pairs of electrodes, requiring a certain degree of spatial separation between the measuring points.

electromagnetic (EM) fields that may exist in the surrounding space. In particular, for a given wire loop l , the presence of a temporally-varying magnetic field \vec{B} will induce an electromotive force ξ_l in the loop according to Faraday's law of induction, as follows:

$$\xi_l(t) = -\frac{d\Phi_\Sigma}{dt}(t) = -\frac{d}{dt} \int_\Sigma \vec{B}(\vec{r}, t) \cdot \vec{N}(\vec{r}, t) d\Sigma \quad (1.5)$$

where Φ_Σ is the magnetic flux through the surface Σ enclosed by the loop, and \vec{N} is the unitary normal vector to the surface, at each position \vec{r} and instant t . In the case of an actual EEG loop, this expression must be modified to account for the presence of the head, where current paths are considerably more complex to describe (Yan et al., 2009). Nevertheless, its fundamental aspects remain: the stronger the temporal variation of Φ_Σ , or the larger the exposed surface Σ , the stronger will be the contribution ξ_l . Also importantly, any such contribution will linearly add to, and be amplified together with, the EEG signals of interest. It is therefore crucial to minimize noise contamination at this stage. A common approach is to place both subject and recording system inside a Faraday cage, or at least an isolated room, to minimize interfering fields from surrounding sources; when this is not possible, careful analysis and design of the transmission lead configuration should be considered instead, in order to minimize the exposed loop areas.

1.1.4 Rhythmic and transient activity

EEG features can be grouped in two main categories: rhythmic and transient. Each feature exhibits specific temporal properties, and is associated with a particular electric potential topology across the scalp. When several neuronal sources are involved, this characteristic topology may vary in time as well, provided the temporal resolution is sufficiently high.

Rhythmic activity comprises signal oscillations of specific frequency that vary in power across time. They reflect concomitant neuronal LFP fluctuations that are generated and regulated by an interplay of several factors, both at cellular and at network levels. EEG signals can exhibit rich spectral profiles, and different aspects of brain function have consistently been associated with oscillations at particular frequency ranges. This has motivated a subdivision of the EEG spectrum into a set of empirically-defined frequency bands, which include the delta band (1–4 Hz), the theta band (4–8 Hz), the alpha band (8–12 Hz), the beta band (12–30 Hz) and the gamma band (above 30 Hz). In practice, the specified frequency intervals should be regarded only as reference guidelines, with important deviations occurring due to various factors such as age and species (Buzsáki, 2006). Oscillations in the **delta** band are commonly found in adults during deep stages of the sleep cycle; they reflect various interactions arising from the cortex or from the thalamus (Niedermeyer and Lopes da Silva, 2005). The **theta** range has been prominently observed in the hippocampus of numerous animal species, and associated with various cognitive features such as orientation, attention and active motor behavior (Buzsáki, 2006); in the human cortex, theta oscillations have been observed, albeit with some difficulty, in processes related with problem-solving, learning and memory, and have also been associated with drowsiness, as well as relaxed and meditative states (Schacter, 1977). Oscillations in the **alpha** range can be observed in a wide variety of cognitive states and functions, and have been extensively studied with EEG. Alpha waves become prominent in subjects at rest, and can be enhanced specifically in posterior regions upon closing of the eyes. These oscillations appear to play a major role in thalamocortical interactions, particularly in less active cognitive states (Niedermeyer and Lopes da Silva, 2005). Idleness of the arms and legs can also potentiate a specific type of rhythm, putatively analogous to visual alpha, termed **mu** rhythm (Buzsáki, 2006). Oscillations observed at higher frequencies have generally been associated with active processes requiring increased attention and cognitive demands. Generators of these waves can be traced to superficial layers of the cortex (Roopun et al., 2006), although not excluding possible interactions with the thalamus (Steriade et al., 1996). Waves in the **beta** range can be modulated by motor behavior and demanding tasks or concentration, and **gamma**-band oscillations tend to be amplified during a large variety of active cognitive or motor functions (Mulert and Lemieux, 2010).

While the different bands can express very specific modulations for particular cognitive functions and states, the lower frequency rhythms, namely alpha, tend to be more typically associated with large-scale, resting activity, while higher frequency rhythms such as gamma are more associated with focal, active function. Crucially, while oscillatory patterns can be observed with EEG at any ongoing state of the subject, they can also be enhanced or suppressed by specific stimuli or tasks – a phenomenon termed **event-related synchronization** (ERS) or **desynchronization** (ERD), respectively (Pfurtscheller and Lopes da Silva, 1999).

Transient activity comprises particular fluctuations in electric potential of diverse morphology, appearing in specific points of the EEG timecourse. Certain types of activity can occur spontaneously, while others appear in response to external stimuli or during cognitive and motor actions – generally termed **event-related potentials** (ERPs). Both types can contain highly

relevant information regarding the underlying neuronal function. Examples of spontaneous transient activity include **sleep spindles** and **K-complexes**, which occur during normal sleep and are thought to reflect important processes of arousal suppression, learning, and memory consolidation (Dang-Vu et al., 2010; Tamminen et al., 2010). Fluctuations observed during seizures in **epilepsy** patients also form an important example of spontaneous (pathological) transient activity (Gotman and Gloor, 1976). Another important class of transient states and patterns comprises the so-called **EEG microstates**, commonly found during wakeful rest. Microstates are observed as particular electric potential topologies that occur spontaneously and briefly, and are thought to reflect the activation of specific functional networks in ongoing mental activity (Lehmann et al., 1987). Microstate properties have shown alterations across wakefulness and sleep stages (Cantero et al., 1999), as well as in schizophrenia (Koenig et al., 1999). Event-related microstate occurrences have also been observed and studied.

In the ERP domain, various types of fluctuations have been found and systematically studied, a prime example being the **visual evoked potential** (VEP), which can be elicited by presentation of an image or visual pattern to the subject (ACNS, 2006). VEP fluctuations are more accentuated in occipital regions, given their proximity to the visual cortex, and usually show an anterior-posterior dipolar distribution across the scalp. This dipole arises most prominently at approximately 100 ms from stimulus onset, with two additional relevant occurrences around 70 and 140 ms, with reversed polarity (Fig. 1.4). The three components are commonly designated P100, N70 and N140, respectively (Skrandies, 2005). As with any other ERP, VEPs are a manifestation of the underlying neuronal processes elicited or modulated by the stimulus. In this case, the primary network at play is the visual pathway, including the retina, the lateral geniculate nucleus (LGN) of the thalamus, and the visual cortex (Felleman and Van Essen, 1991) – the latter being the main contributor for scalp EEG signals. Variations in certain properties of the stimulus, such as intensity, frequency or field-of-view (FOV), will create differences in the neuronal response, and consequently affect the properties of the measured VEP. Similarly, anomalies in the visual pathway may also produce detectable alterations at the VEP level (ACNS, 2006).

It should be noted that typical EEG recordings are performed with a high-pass filter time constant of 1–10 s, or lower, and as such very slow oscillations, also known as **slow cortical potentials**, can be suppressed by the high-pass filtering stage. Such fluctuations do carry relevant information on the state of activity of neuronal cells. Important examples may include the contingent negative variation, associated with stimulus anticipation and sensorimotor integration (Walter et al., 1964), and altered physiological conditions such as hypercapnia and asphyxia can also produce observable changes at long timescales (Niedermeyer and Lopes da Silva, 2005). Unfortunately, while relevant in various contexts, these fluctuations are technically challenging to measure due to spurious contributions introduced by sweat and the galvanic skin response, for example, and are thereby less often studied (Niedermeyer and Lopes da Silva, 2005).

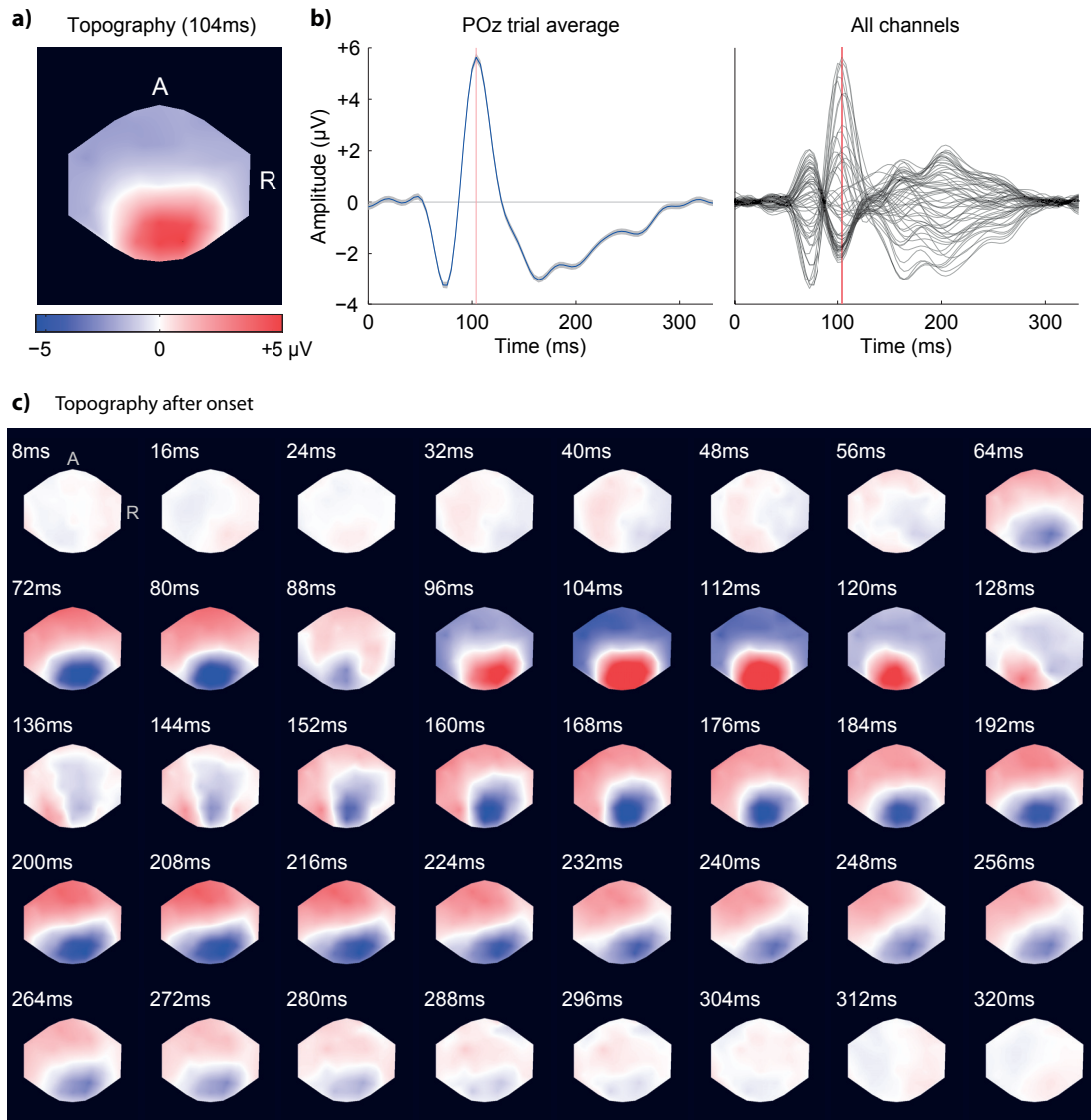


Figure 1.4: Human visual evoked potential elicited by flickering-checkerboard stimuli. The responses shown correspond to an average over 340 trials, with re-referencing to the mean scalp timecourse. The instant $t = 0$ corresponds to stimulus delivery. **a)** Average scalp topography at $t = 104$ ms, corresponding to the P100 component of the VEP. **b)** Average response timecourses for an occipital channel where the response is most prominent (POz), and for all channels together. **c)** Evolution of the scalp topography after stimulus delivery (averaged across trials). The P100, N70 and N140 components are well visible in occipital channel responses.

1.1.5 Limitations of scalp EEG

For almost a century, scalp EEG has yielded countless contributions to both basic and clinical neuroscience. Nevertheless, the technique carries important limitations that must be taken into consideration. For instance, because the signals are measured at the surface of the head,

their **signal-to-noise ratio** (SNR) and **spatial specificity** are relatively poor, compromised by the presence of intermediate tissues separating the electrodes from the neuronal cells. The skull is the most deleterious of these components, its very low conductivity producing a strong reduction and spatial dispersion of volume currents arising from the brain to the scalp (Mulert and Lemieux, 2010). This effect results in a spatial blurring of the signals measured at the scalp, and a strong decrease in SNR, and thereby sensitivity. In practice, while post-synaptic activity creates fluctuations of cell membrane potentials in the order of mV, the signals measured at the scalp are limited to a range of a few hundreds of μV , even during large-scale synchronous activity of thousands or millions of neurons.

Added to its low sensitivity and spatial resolution, scalp EEG is prone to various biasing factors that have an important impact on the signals measured. First, since the electric potential of a dipole falls with the square of the distance to the probe, the sensitivity of EEG is **depth-dependent**, with more superficial sources such as cortical neurons dominating the signal, and deeper structures such as thalamic nuclei being considerably harder to detect. Second, because electric dipoles are vector quantities, favorable summation of individual neuronal fluctuations must be attained not only in time but also in **spatial orientation** (Nunez and Silberstein, 2000). As a result, a strong sensitivity bias exists towards more regularly-oriented cells such as the pyramidal cortical neurons, while other cell types such as interneurons cannot produce significant net dipoles due to field cancellation.

Finally, although scalp EEG is often regarded as a relatively direct measure of neuronal activity, a complete understanding of its neurophysiological substrates has in fact not yet been achieved. While postsynaptic activity is thought to be the main source of scalp fluctuations, additional contributions can be captured as well; in particular, membrane potential oscillations and after-potentials following spike propagation share the frequency domain of postsynaptic activity (altogether termed **perisynaptic activity**), and will also contribute to LFPs (Logothetis, 2008). Evidence suggests that the faster nature of **action potentials** prevents a favorable summation of large population activity; nevertheless, recent studies have shown that features from certain scalp EEG frequency bands can be used to infer spiking activity as well (Whittingstall and Logothetis, 2009). Furthermore, besides neurons, **glial cells** also possess a polarized intracellular medium; despite not exhibiting postsynaptic activity or action potentials, these cells can be depolarized when the extracellular K^+ concentration exceeds certain thresholds (namely during repetitive neuronal firing), giving rise to local ion fluxes that will contribute to existing LFPs (Niedermeyer and Lopes da Silva, 2005).

1.2 Fundamentals of fMRI

MRI is a technique that explores the **magnetic spin** properties of certain atomic nuclei, most often hydrogen, to obtain high-contrast images of living tissues non-invasively and without ionizing radiation. The spin of the proton and its interactions with applied magnetic fields were first explored in the 1920's by Rabi and colleagues, and extended by Bloch and Purcell

in the 1930's with a highly practical macroscopic description. Nevertheless, it was only later on, in the 1970's, that MR-based imaging effectively began, with the revolutionary ideas of Lauterbur and Mansfield: these authors proposed the use of spatially-varying magnetic fields to encode magnetic spins with space-dependent properties, and thereby obtain information regarding their distribution in living tissues – and ultimately, images (Haacke et al., 1999). Despite its relatively recent origins, the advantages of MRI over other imaging modalities were soon recognized by the scientific and medical communities, and massive technological and scientific efforts were devoted to its development, and widespread implementation in clinical practice.

The fundamental laws at play in MRI make it an extremely versatile approach, and its original focus on static anatomical imaging soon branched into various other applications. The major breakthrough for the application of MRI to the study of brain function was achieved in the early 1990's by Ogawa and colleagues, with the discovery of the **blood oxygenation level-dependent (BOLD) contrast** (Ogawa et al., 1990). This technique, sensitive to local fluctuations in the metabolic and vascular properties of living tissues, allowed for the non-invasive monitoring of human brain function with unprecedented spatial resolution, and has since offered tremendous contributions to modern neuroscience. As MR technology continues to improve, BOLD fMRI progressively reaches ever higher levels of sensitivity, which allow the study of more subtle features of brain function, and can also be traded for increased spatial resolution or higher temporal sampling rates. At the same time, fundamental studies combining fMRI with additional modalities, such as EEG and positron emission tomography (PET), continually contribute towards our understanding of the neurovascular substrates of the BOLD response.

1.2.1 Nuclear magnetic resonance

MRI is fundamentally based on the phenomenon of nuclear magnetic resonance (NMR), displayed by the nuclei of certain atomic species. Protons and neutrons are known to possess a property designated **intrinsic angular momentum** (or "spin"), \vec{P} ; this can be seen as the quantum equivalent of the classical angular momentum displayed by rotating macroscopic bodies, in the sense that it is quantized (only specific discrete values are measured). Depending on the number of protons and neutrons in a certain atomic nucleus, it too can have a net angular momentum different from zero, and as nuclei are by nature positively charged particles, this angular momentum will be associated to a corresponding **nuclear magnetic moment**, $\vec{\mu}$. The angular momentum and magnetic moment of a given atomic nucleus are related by a simple expression:

$$\vec{\mu} = \gamma \vec{P} \tag{1.6}$$

where γ is the **gyromagnetic ratio**, a nucleus-specific empirical constant. In a sample of nuclei with non-zero magnetic moments, in the absence of external magnetic fields, these moments are randomly oriented, and the summed magnetic moment of the sample equals

zero (Fig. 1.5a). However, if a **static magnetic field** \vec{B}_0 is applied to the sample, for instance along the z -direction, each nucleus will adopt one of $2I + 1$ distinct, discrete energy levels, with I being the nuclear spin number, which depends on the composition of the nucleus. Each energy level corresponds to a specific orientation of the nuclear magnetic moment with respect to \vec{B}_0 (Fig. 1.5b), with its projection along z given by:

$$\mu_z = \gamma \frac{h}{2\pi} m_I \quad (1.7)$$

where h is the Planck constant, and m_I takes one of $2I + 1$ possible values. Examples of naturally-abundant nuclei with non-zero magnetic moments include ^1H , ^{19}F and ^{23}Na . Of these, **hydrogen** is undoubtedly the most important for biological applications – its presence in water molecules, which make up a large fraction of living tissues such as the human body, make it an ideal substrate for MRI. Other biologically-relevant elements such as carbon and oxygen can also provide important insights into function and metabolism, but typically require "artificial" increases of the rarer isotopes ^{13}C and ^{17}O , respectively, since the more abundant forms (^{12}C and ^{16}O) have a null magnetic moment.

The ^1H nucleus is essentially a single proton and has a spin number of $1/2$. Its two energy levels correspond to two opposite orientations: one of lowest energy, parallel to \vec{B}_0 , and another of highest energy, antiparallel to \vec{B}_0 . The difference in energy between the two states is proportional to the magnitude of \vec{B}_0 , and given by:

$$\Delta E_H = \gamma_H \frac{h}{2\pi} B_0 \quad (1.8)$$

which is analogous to the classical description of a magnetic dipole placed in a magnetic field, $E = -\vec{\mu} \cdot \vec{B}_0 = -\mu_z B_0$. In the absence of thermal agitation, all nuclei would acquire the parallel conformation, leading the system to its minimum energy state. However, at typical physiological temperatures, the energy involved in thermal agitation is significant and dominates the energy difference ΔE_H . The expected balance between the number of antiparallel (N_1) and parallel ^1H nuclei (N_2) can be estimated from Boltzmann's equation, as:

$$\frac{N_1}{N_2} = e^{-\frac{\Delta E_H}{kT}} \quad (1.9)$$

where k is Boltzmann's constant and T is the temperature. In the MRI context, this proportion is typically very close to 1; for example, for an applied field of 1.5 T at room temperature, Boltzmann's equation predicts that only 10 nuclei in 1 million are expected to contribute for a non-zero net magnetization (with the remaining nuclei canceling each other out) – this minute but essential difference is, in fact, what is measured in typical MRI acquisitions (Jezzard et al., 2001). Also importantly, the stronger the applied \vec{B}_0 , the larger the net magnetization available.

A proton in the lowest energy state can be excited to the higher energy state by radiation of specific frequency ν , such that the photon energy $E = h\nu$ matches ΔE_H . This interaction, which typically involves energies in the radiofrequency (RF) band (hundreds of MHz), is

fundamental for NMR, and subsequently for MRI. For a sample of ^1H nuclei in a static magnetic field \vec{B}_0 , the **net magnetization** \vec{M} of the sample, comprising the sum of all the individual magnetic moments, can be described as a vector parallel to \vec{B}_0 (since all contributions cancel each other out, except for the exceeding parallel component) (Fig. 1.5c). Although the nuclear magnetic moment and its interactions with radiation are inherently quantum properties, it has been shown that these phenomena can be treated in a classical framework, equivalent to that of macroscopic magnetic dipoles. In particular, the magnetic moments can be regarded as if precessing around \vec{B}_0 at the so-called **Larmor frequency**, ω_L , related to the field strength by:

$$\omega_L = \gamma B_0 \quad (1.10)$$

and thereby proportional to ΔE_H as well. If a second, **oscillatory field** \vec{B}_1 , transverse to \vec{B}_0 , is applied at a frequency similar to the Larmor frequency, it is said to be on resonance with the precessing nuclei, and can then interact with the net magnetization \vec{M} and change its equilibrium orientation (Fig. 1.5d). The process can be described analogously to its classical equivalent, a macroscopic magnetic dipole, by:

$$\frac{d\vec{M}}{dt} = -\gamma \vec{B} \times \vec{M} \quad (1.11)$$

where \vec{B} , in this context, is the sum of \vec{B}_0 and \vec{B}_1 . An interaction of particular interest is that achieved with a circularly-polarized field \vec{B}_1 , precessing in the xy -plane at the Larmor frequency, perpendicular to \vec{B}_0 (which remains constant along the z -axis). It can be shown that such a pulse, applied for period of time τ , can rotate \vec{M} towards the xy -plane by a certain angle α , called the **flip angle**, equal to:

$$\alpha = \gamma B_1 \tau \quad (1.12)$$

(given in radians). Except for the special cases of full excitation ($\alpha = 90^\circ$) or inversion ($\alpha = 180^\circ$), \vec{M} will now have a **longitudinal** component \vec{M}_z , of magnitude $M \cos(\alpha)$, and a **transverse** component \vec{M}_{xy} , of magnitude $M \sin(\alpha)$ and rotating about the z -axis at the Larmor frequency. Because of this precession in time, the transverse component can be detected by an adequately-placed **receiver coil**, by means of EM induction (based on Faraday's law). An important aspect of this process is its frequency-selectivity: if the precession frequency of \vec{B}_1 differs from the Larmor frequency of the sample under \vec{B}_0 , the probability of energy state transition by individual nuclei is reduced. In the classical framework, this effect can be described as the two magnetic fields acting together in a less efficient combination, and the resulting α will typically be considerably smaller, or effectively negligible (Fig. 1.6c).

Once excited away from its equilibrium, the magnitude of \vec{M}_z and \vec{M}_{xy} will not remain constant in time. In fact, the energy absorbed from \vec{B}_1 by the sample is gradually dissipated, and the net magnetization eventually returns to its equilibrium \vec{M}_0 , parallel to \vec{B}_0 , with \vec{M}_{xy} becoming once again null. This process is termed **spin relaxation**, and includes various mech-

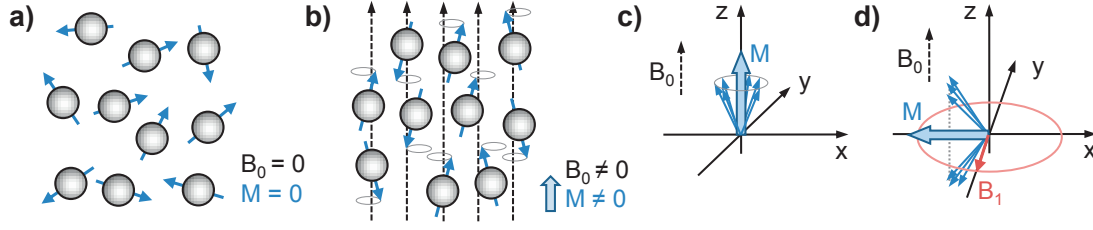


Figure 1.5: Behavior of a nuclei sample (with $I = 1/2$) when placed in a strong magnetic field along z . **a)** Nuclear magnetic moments are randomly oriented prior to the application of a magnetic field. **b)** Gradually, the moments align either with the field or against it; the slight preferential alignment along the direction of the field acts as a single net magnetization vector \vec{M} . An oscillating magnetic field \vec{B}_1 can change the orientation of some of the nuclear moments from equilibrium **(c)**, until there is a net magnetization vector in the xy -plane **(d)**.

anisms that are of utmost importance for tissue differentiation, or in other words, for image contrast in MRI. In biological tissues such as the human body, when the nuclei of interest are excited, they undergo a complex process of energy dissipation by means of EM interactions with surrounding particles. These interactions can be grouped into three distinct mechanisms:

a) A mechanism known as **T_1 relaxation** or **spin-lattice relaxation**, by which the excited nuclei dissipate their energy in interactions with surrounding molecules mediated by randomly-fluctuating magnetic fields. The relevant fields for T_1 relaxation, including contributions from random molecular motion (translational, rotational and vibrational), are those occurring at frequencies close to the Larmor frequency, to achieve the necessary transition energy. The effectiveness of this mechanism depends, therefore, on both the strength of \vec{B}_0 and the motion characteristics of the medium. An important property governing the dynamics of fluctuating magnetic fields is the so-called correlation time (τ_c), defined as the expected time taken by a molecule to rotate by one radian. The correlation time increases with the viscosity of the medium and the size of the molecule, and decreases with temperature; T_1 relaxation is maximally accentuated when $\omega_L \tau_c \approx 1$. The T_1 relaxation process governs the regeneration of \vec{M} along the z -axis, as described for each instant t after excitation by:

$$\frac{dM_z}{dt}(t) = \frac{M_0 - M_z(t)}{T_1} \Rightarrow M_z(t) = M_0 - (M_0 - M_z(0))e^{-t/T_1} \quad (1.13)$$

b) A mechanism known as **T_2 relaxation** or **spin-spin relaxation**, by which the excited nuclei experience small variations in their Larmor frequency, due to low-frequency, microscopic random fluctuations of the local magnetic field. These random field fluctuations, experienced at a molecular level, are generated by tumbling with neighboring nuclei, and therefore the process depends mainly on the motion characteristics of the medium. These small individual variations in the Larmor frequency lead to a general loss of phase coherence for the individual magnetic moments, resulting in a decrease of the magnitude of the transverse magnetization,

\vec{M}_{xy} , as described by:

$$\frac{dM_{xy}}{dt}(t) = -\frac{M_{xy}(t)}{T_2} \Rightarrow M_{xy}(t) = M_{xy}(0)e^{-t/T_2} \quad (1.14)$$

c) Finally, a mechanism known as **T_2' relaxation** is also of great importance, especially for BOLD-fMRI. Despite sharing similar principles to those of T_2 relaxation, T_2' mechanisms are associated with differences in Larmor frequency across a sample of nuclei due to "external", macroscopic magnetic field inhomogeneities. These inhomogeneities can be caused by imperfections in the applied \vec{B}_0 field, or by differences in magnetic susceptibility between structures in the sample – at the proximity of air/tissue interfaces, for example, or in blood vessels. As with T_2 relaxation, these processes result in an exponential decrease of the transverse net magnetization with time. The combination of the two types is commonly referred to as **T_2^* relaxation**, with a time constant T_2^* given by:

$$\frac{1}{T_2^*} = \frac{1}{T_2} + \frac{1}{T_2'} \quad (1.15)$$

It is worth mentioning that given their systematic (non-random) origins, T_2' contributions can be countered by applying 180° pulses in the xy -plane (also called refocusing pulses). This technique, known as spin echo, renders the transverse relaxation sensitive mainly to T_2 mechanisms, and contrasts with so-called gradient-echo approaches, which retain the full T_2^* weighting.

The characteristic relaxation times T_1 , T_2 and T_2' are intrinsic properties of each sample, which depend on the various molecular species that exist together with the water protons, and the microscopic architectures in which they are arranged. In the human body, different tissues such as blood, fat deposits, grey matter and white matter, as well as various other tissue types, display particular and considerably distinct time constants that differentiate them apart – this property contributes to the excellent **soft-tissue contrast** that can be achieved with MRI.

The processes of excitation and relaxation can be jointly described by combining Eqs.1.11, 1.13 and 1.14 into a set of fundamental equations, also known as **Bloch equations** (Bloch, 1946):

$$\begin{aligned} \frac{dM_x}{dt}(t) &= \gamma(M_y(t)B_z(t) - M_z(t)B_y(t)) - \frac{M_x(t)}{T_2} \\ \frac{dM_y}{dt}(t) &= \gamma(M_z(t)B_x(t) - M_x(t)B_z(t)) - \frac{M_y(t)}{T_2} \\ \frac{dM_z}{dt}(t) &= \gamma(M_x(t)B_y(t) - M_y(t)B_x(t)) - \frac{M_z(t) - M_0}{T_1} \end{aligned} \quad (1.16)$$

These equations can be solved numerically for any pattern of applied magnetic fields, and are useful to predict the behavior of nuclear magnetization throughout complex excitation sequences. For certain applications, a commonly-used approach to simplify the system is

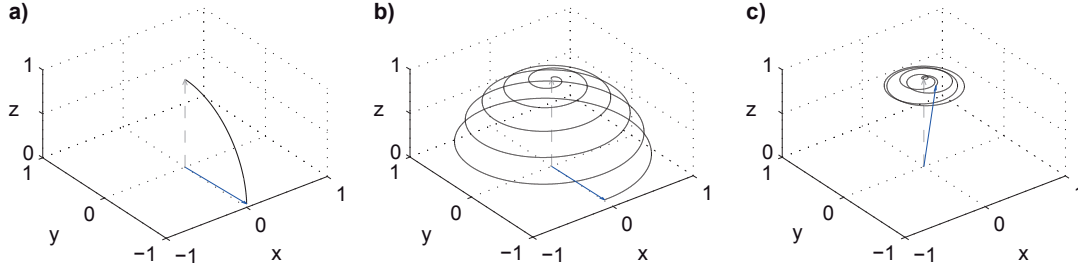


Figure 1.6: A 90° pulse for spin excitation with a precessing magnetic field \vec{B}_1 , either on-resonance (**a,b**) or off-resonance, at $0.8 \omega_L$ (**c**). The magnetization vector \vec{M} before excitation is shown in grey (dashed line), and after excitation in blue. The magnetization trajectory throughout the pulse is shown in black. **a**) excitation as seen from a reference frame rotating at the Larmor frequency; the effective field \vec{B}_{eff} is static, along the x -direction. **b,c**) excitation as seen from a static reference frame.

through the use of a **rotating reference frame**, particularly matching the rotation about the z -axis at the Larmor frequency – with this reference change, the precession of \vec{M} due to \vec{B}_0 is excluded, as is that of \vec{B}_1 when applied on-resonance (Fig. 1.6a).

A series of pulses with specific timings can be designed so as to highlight the effects of certain relaxation mechanisms relative to others. For instance, if a 90° pulse is repeatedly applied to the sample with a period TR (called **repetition time**), the longitudinal magnetization M_z available just before each new pulse will obey:

$$M_z(TR^-) \propto M_0(1 - e^{-TR/T_1}) \quad (1.17)$$

assuming that $T_2^* \ll TR$, and thereby no transverse contributions remain to be tipped back to the z -direction with the next pulse. With each 90° pulse, the longitudinal component is fully transferred to the transverse component, M_{xy} . After a time TE following excitation (called **echo time**), M_{xy} will have relaxed according to:

$$M_{xy}(TE) \propto M_0(1 - e^{-TR/T_1})e^{-TE/T_2^*} \quad (1.18)$$

The corresponding signal, if picked up by a nearby coil, will thus be weighted by contributions from both T_1 and T_2^* (or T_2 , if a refocusing pulse is included). Crucially, by appropriately manipulating the acquisition parameters TR and TE , each of these contributions can be given more or less emphasis, and the resulting signal will then be more sensitive to differences in the associated time constant. This offers the user a certain degree of control over the contrast achieved between different tissues.

1.2.2 Magnetic resonance imaging

As previously discussed, NMR phenomena are highly frequency-specific, with resonant frequencies being established by the externally applied fields. MRI techniques cleverly exploit this property to be able to discriminate nuclear densities and medium properties across the three dimensions of space. In practice, this is accomplished by superimposing **magnetic field gradients** to the applied field \vec{B}_0 , so as to vary the Larmor frequency across a given sample. Gradient forms are typically linear, leading to a field distribution of the form:

$$\vec{B}(x, y, z) = \vec{B}_0 + (G_x x + G_y y + G_z z) \vec{e}_z \quad (1.19)$$

where G_x , G_y and G_z are the gradient slopes along the x , y and z direction, respectively, and \vec{e}_z is a unitary vector parallel to the z -axis.

One of the most elementary frameworks for image generation combines three types of spatial encoding, one for each spatial dimension (Fig. 1.7). The first stage, designated **slice selection**, comprises the excitation of a thin, planar slice across the object, at a certain orientation. For example, to obtain an axial slice (perpendicular to the z -axis), centered at a well-defined height z_s , a gradient G_z is established (with $G_x = G_y = 0$), and an RF pulse \vec{B}_1 is applied at frequency ω_s , such that:

$$\omega_s = \gamma(B_0 + G_z z_s) \quad (1.20)$$

In practice, the RF pulse excites a range of frequencies centered at ω_s , which will correspond to a certain slice thickness in the image. In the time domain, the pulse can be modulated by an approximation to a *sinc* function, for example, which corresponds to a square function in the frequency domain, centered at ω_s and spanning the desired frequency (thickness) interval.

After excitation of a slice, the magnetization of the corresponding nuclei acquires a non-zero \vec{M}_{xy} component. In a macroscopic description, \vec{M}_{xy} can be considered a magnetization density, continuous in space. It is also useful to describe \vec{M}_{xy} as a complex number, with the x and y components forming the real and imaginary part, respectively. The complex equivalent can then be treated in terms of its **magnitude** M_{xy} and **phase** ϕ , as:

$$\vec{M}_{xy}(x, y, z, t) \rightarrow M_{xy}(x, y, z, t) e^{j\phi(x, y, z, t)} \quad (1.21)$$

where the magnitude decreases in time with relaxation while the phase varies with precession. After excitation, the resulting \vec{M}_{xy} can be detected by a nearby RF coil. For example, for an axial slice at a height z_s , the signal measured S_{z_s} , after demodulation from the reference frequency and for the moment neglecting relaxation effects, will be described by:

$$S_{z_s} \propto \int_X \int_Y M_{xy}(x, y, z_s) dy dx \quad (1.22)$$

S_{z_s} provides a measure of the total signal content of the slice, but cannot offer information on

its distribution along the x and y directions. That discrimination is achieved with further use of gradient fields, in two stages designated **phase encoding** and **frequency encoding** (Fig. 1.7). The phase-encoding step, employed in the y direction, for example, consists in the application of a gradient G_y during a time period τ_{PE} prior to data acquisition. This will introduce a spatially-dependent phase shift ϕ_y of the form:

$$\phi_y(y, G_y, \tau_{PE}) = \gamma G_y y \tau_{PE} \quad (1.23)$$

After the application of G_y , frequency encoding (in the remaining x direction) is mediated by a third gradient G_x applied simultaneously with signal acquisition ("**readout**") itself. Differentiating the precession frequencies along the x direction, the presence of G_x results in a second, space and time-dependent phase shift ϕ_x , of the form:

$$\phi_x(x, G_x, t) = \gamma G_x x t \quad (1.24)$$

With the combination of the two encoding processes, the ω_s -demodulated signal S_{zs} , acquired during frequency encoding, can be expressed as:

$$\begin{aligned} S_{zs}(t, G_x, G_y, \tau_{PE}) &\propto \int_X \int_Y M_{xy}(x, y, z_s) e^{-j\phi_x(x, G_x, t)} e^{-j\phi_y(y, G_y, \tau_{PE})} dy dx \\ S_{zs}(t, G_x, G_y, \tau_{PE}) &\propto \int_X \int_Y M_{xy}(x, y, z_s) e^{-j\gamma G_x x t} e^{-j\gamma G_y y \tau_{PE}} dy dx \\ S_{zs}(k_x, k_y) &\propto \int_X \int_Y M_{xy}(x, y, z_s) e^{-2\pi j(k_x x + k_y y)} dy dx \end{aligned} \quad (1.25)$$

with $k_x = \gamma G_x t / 2\pi$ and $k_y = \gamma G_y \tau_{PE} / 2\pi$. This last formulation highlights the analogy of S_{zs} with the **spatial Fourier transform** of M_{xy} . Indeed, the acquisition process here described can be regarded as the sampling of the Fourier transform of M_{xy} for a specific domain of values of k_x and k_y , adequately named the **k-space**. Each phase-encoding stage sets a specific k_y , and the following frequency-encoding stage allows for the acquisition of a series of k_x (increasing in time under G_x) for that k_y – which can be regarded as a line of elements in k-space. By repeating the process for several different values of k_y , different lines are acquired, and when the k-space is filled, a map of $M_{xy}(x, y, z_s)$ can be recovered via an inverse Fourier transform. The whole process can likewise be repeated for a series of slices, yielding a full 3D image of the object.

As would be expected, there is a close reciprocity between k-space and image-space properties: the image FOV is inversely proportional to the resolution in k-space (Δk), and the image resolution ($\Delta x, \Delta y$) is inversely proportional to the maximum range of sampled k-values (given by $k_x = \gamma G_x t_{RO} / 2\pi$ and $k_y = \gamma G_{y_{max}} \tau_{PE} / 2\pi$, respectively, with t_{RO} corresponding to the readout duration). It is important to note that the basic acquisition protocol presented above is considered a 2D acquisition method, in the sense that multiple 2D slices are separately acquired. Nevertheless, 3D extensions have also been developed, in which a single, thick slab is excited by the RF pulse, and the slice direction is taken as a second phase-encoding direction.

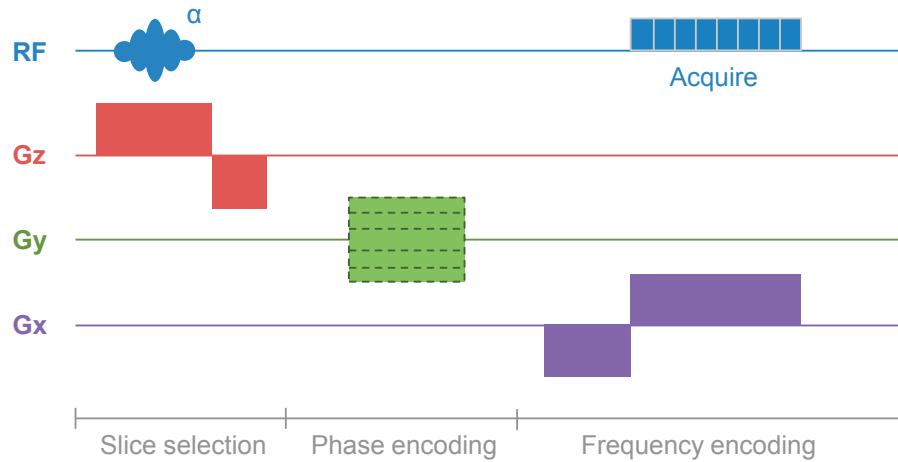


Figure 1.7: Block diagram representing the basic 2D gradient-recalled echo acquisition sequence, with slice selection along z , phase encoding along y and frequency encoding along x . Phase-encoding and readout sections are repeated for several values of G_y , in order to sample several phase-encoding lines in k -space. Refocusing gradients are included to compensate for finite slice thickness and dephasing effects, balancing the phase evolution throughout the sequence.

1.2.3 The BOLD contrast

Despite a number of limitations, the BOLD contrast has been the workhorse of fMRI since its discovery in the early 1990's. Normal blood can be regarded as a concentrated solution of hemoglobin. As discovered by Pauling and Coryell in 1936, hemoglobin (Hb) behaves as a **diamagnetic** substance when bound to oxygen (interacting with external magnetic fields in a repulsive way), and as a **paramagnetic** substance when deoxygenated (interacting with external magnetic fields in an attractive way) (Pauling and Coryell, 1936). Therefore, changes in Hb oxygenation will influence the magnetic susceptibility of the blood, which in turn defines how it will interact with, and distort, an applied magnetic field. In 1990, Ogawa et al. reported gradient-echo MRI signal loss around blood vessels of cat brains under hypoxia, an effect which would be reversed with normoxia. This was attributed to changes in the magnetic susceptibility of the blood associated with deoxygenation: since both oxyhemoglobin and brain tissues in general are diamagnetic, while **deoxyhemoglobin** (dHb) is paramagnetic, the presence of the latter will generate local field gradients between the blood vessels and adjacent tissues, locally decreasing T_2^* (Ogawa et al., 1990). The measured signal, given a T_2^* weighting to enhance sensitivity to these effects, was baptized **BOLD** signal.

In fact, both T_2 and T_2^* mechanisms are thought to be associated with the BOLD effect: inside blood vessels, water protons diffuse freely in and out of red blood cells in the time scale of TE, experiencing rapidly-changing magnetic fields around their vicinity, which induce shifts in their Larmor frequency. As blood oxygenation is decreased, the field gradients between red

blood cells and their surroundings become stronger, boosting the shift effects in water protons – this can be regarded as a **T_2 relaxation** process. On the other hand, in the tissues adjacent to blood vessels, extravascular water protons experience significant local field gradients with respect to the vessels (depending on proximity and relative orientation), which increase with blood deoxygenation. The resulting effect can be considered a **T_2^* relaxation** process.

With the discovery of the BOLD effect, the association of changes in blood oxygenation with neuronal activity, and therefore with brain function, was an intuitive leap that soon followed, marking the birth of fMRI (Ogawa et al., 1992, 1993). In the brain, the local concentration of dHB varies essentially with three factors: **cerebral blood flow** (CBF), **cerebral blood volume** (CBV), and the **cerebral metabolic rate of oxygen consumption** (CMRO₂) (Davis et al., 1998; Buxton et al., 1998). Neuronal activity is tightly linked to metabolic pathways of ATP production, which drive CMRO₂ fluctuations, but is also known to exert a more direct influence on local CBF (Logothetis, 2002; Attwell et al., 2010). Overall, a local increase in neuronal activity will raise CMRO₂, leading to an *increase* in [dHB], but also typically induce a strong increase in CBF, mediated by local autoregulation mechanisms, resulting in a net *decrease* in [dHB], and thereby a positive BOLD response (Buxton, 2012).

Given the combination of vascular and metabolic mechanisms generating the BOLD response, its temporal dynamics are considerably slower than the underlying neuronal activity, and tend to exhibit a more complex morphology. The typical BOLD response to a short visual stimulus exhibits a main positive peak occurring 5–8 s after stimulus onset; if the stimulus has stopped, the BOLD signal again decreases over a few seconds, reaching a level below the initial baseline, often termed **post-stimulus undershoot**; a slow recovery to baseline level then follows, lasting for 12–18 s (Fig. 1.8). The overall response can last for more than 20 s after stimulus cessation. In a number of studies, with adequate temporal sampling, a negative inflection of the BOLD signal has also been observed immediately after stimulus onset, lasting until the response increase begins – this is usually referred to as **initial dip** (Ernst and Hennig, 1994).

The BOLD response here described for a short stimulus can be regarded as a **hemodynamic response function** (HRF). Several studies have investigated the conditions under which an analogy with impulse response functions of linear time-invariant systems is acceptable for BOLD response prediction. Such a property is highly convenient, since it would allow complex BOLD response patterns to be modeled by a timecourse of the stimulation or task paradigm linearly convolved with a fixed impulse response function – defined, for example, as a standard, **canonical HRF** (Friston et al., 1998) (Fig. 1.8a,b). Important studies have suggested that, while this approach is inadequate to model responses to long-duration stimuli, where phenomena such as habituation, for example, may become significant (Bandettini et al., 1997), it should provide a reasonable approximation in cases where the stimulus duration is sufficiently close to what is considered an "impulse" (Logothetis and Wandell, 2004).

An important feature of the BOLD contrast is its dependence on the applied **field strength**. The SNR of MRI signals has been shown to increase linearly with B_0 (Edelstein et al., 1986). Yet,

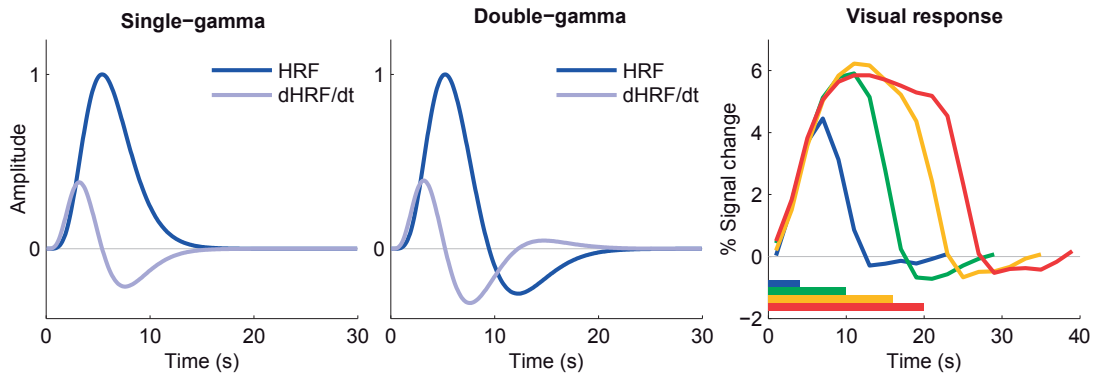


Figure 1.8: Models and observations of the BOLD response timecourse. **Left, center:** Canonical HRFs used in statistical analysis of the BOLD response, along with their temporal derivatives (often included to account for small temporal shifts). These curves are intended to model the response to brief stimuli of unit amplitude. **Right:** Real BOLD responses observed in the visual cortex, for visual stimuli of varying duration: 4 s (blue), 10 s (green), 16 s (yellow) and 20 s (red).

while this linear increase is important per se, the BOLD contrast is still further enhanced by additional field strength-dependent factors. First, the effects due to **magnetic susceptibility** differences between tissues increase with B_0 ; while this is a source of important artifacts, it is also the origin of the BOLD effect, which relies on bulk magnetic susceptibility differences between blood containing dHb and the surrounding tissues. The added effect leads to super-linear gains in sensitivity (Turner et al., 1993; van der Zwaag et al., 2009a). Second, because the T_2 and T_2^* of venous blood are considerably shorter at higher field strengths such as 7 T, the measured signal at typical TEs becomes strongly dominated by grey matter contributions relative to **draining vein** contributions, resulting in a higher spatial specificity for functional localization (Gati et al., 1997; Yacoub et al., 2001). This synergistic combination of benefits to sensitivity and specificity has been a strong motivation for the pursuit of higher field strengths for BOLD fMRI. Trading the added sensitivity for a higher spatial resolution, fMRI studies conducted at ultra-high fields such as 7 T have achieved sub-millimeter voxel widths (Yacoub et al., 2008), and higher field strengths continue to be pursued (Deelchand et al., 2010; Duyn, 2012).

1.2.4 BOLD fMRI acquisition

NMR-based interactions, as well as the techniques devised for imaging, require the application of (electro)magnetic fields with extremely precise frequency, timing, amplitude and spatial distribution. This is accomplished through highly sophisticated technology assembled together as an **MRI scanner**, with an associated control room (Fig. 1.9).

A typical human scanner possesses a permanent static field \vec{B}_0 , maintained by a cylindrical **superconducting magnet**, containing the volume of interest for imaging. This magnet is

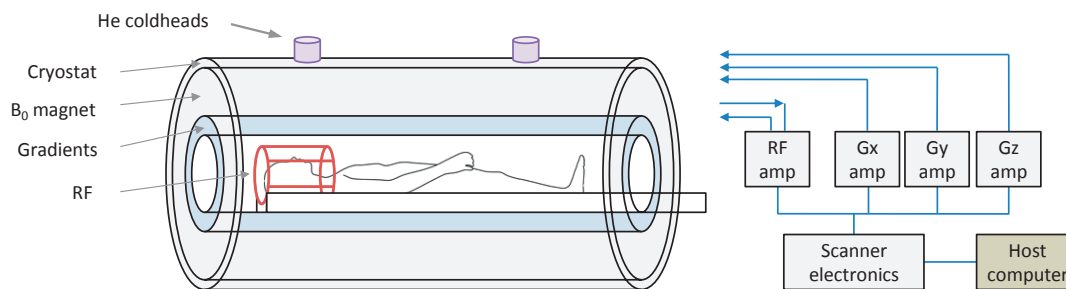


Figure 1.9: Simplified schematics of an MRI scanner. The scanner electronics produce signals that are amplified before being sent to the gradient or RF coils. The detected signal is then digitized for processing and image reconstruction.

kept at low temperatures to preserve its superconducting state, typically in a bath of liquid helium (He), which has a boiling point below 4.3 K. In order to maintain this state, thermal insulation layers are added to the bore, and one or more **He coldheads** (or equivalent systems) are set on the top and work permanently to recover evaporating He. The coldheads work in repeated thermodynamic cycles that apply mechanical energy to extract heat from the medium, leading to the recondensation of ascending He gas. The resulting field \vec{B}_0 is typically in the order of 1–10 T (for human applications), constant in time, and made to be as spatially homogeneous as possible within the volume of interest. This property can be further improved through a process called **\vec{B}_0 shimming**, which uses superimposed field components created by additional coils, adjusted specifically to increase the field homogeneity in the desired FOV, for a specific sample (Gruetter, 1993). The \vec{B}_0 field naturally extends beyond the volume of interest, and certain **magnetic shielding** measures must be adopted to limit its range, for safety reasons. Passive shielding relies on reinforcing the magnet room walls with heavy ferromagnetic layers, to confine the field; active shielding, developed more recently, employs a second set of superconducting windings, outside of the main magnet and with opposite current, to reduce the outer field. The latter approach results in a fast decay in field amplitude with the distance from the magnet; reciprocally, a considerably steep field rise is created at the entrance of the bore.

The gradient fields used for spatial encoding are generated by three sets of **gradient coils** with orthogonal contributions (x, y, z) , fed by high-power current sources. They are designed to generate spatially homogeneous field slopes with extremely fast rise-times, in order to meet the demanding slew-rate requirements of fast spatial encoding schemes in MRI, and particularly those used in fMRI acquisition. An important issue that must be well dealt with, to allow for fast field switching, is the impact of opposing fields generated by eddy currents.

Nuclear spin excitation and detection is performed with **RF coils**, which can be designed with various sizes, numbers of elements and geometries, for optimal performance in specific applications and body regions. Transmission and detection can be performed by the same, or by separate coils. The generated \vec{B}_1 fields in MRI are typically in the radiofrequency range,

and thus constitute non-ionizing radiation. Nevertheless, the power deposited in biological tissues leads to heating, and may eventually cause injuries. For this reason, RF safety is an important aspect of coil design, and determines the specific limits for power transmission allowed for MRI acquisition. The distribution of power deposition in biological tissues is highly dependent on the properties of both coil and sample, and can be estimated either with computational simulations or through temperature measurements in phantom models – this will be discussed in more detail in Chapter 3.

The generation of images requires a suitable, well-timed application of RF pulses and field gradients, in predefined sequences. For BOLD fMRI, the main workhorse for image acquisition has been the **echo-planar imaging** (EPI) technique. This sequence employs a rapid gradient-encoding scheme that allows for the sampling of several k-space lines in a single excitation. This is accomplished with a rectilinear "zig-zag" trajectory where several line readout blocks are included, separated by short phase-encoding blips, which correspond to k-space line shifts in the phase-encoding direction (Fig. 1.10). In its most common form, **multislice 2D EPI**, a full k-space plane is sampled following each RF excitation, yielding an image slice per excitation, and a full volume can be obtained within a few seconds. This temporal resolution is essential for proper sampling of BOLD fluctuations. The TE of an EPI sequence is defined as the time from excitation until the center of the readout train, at which point the k-space origin is sampled. In order to minimize gradient-induced spin dephasing effects at $t = TE$, additional gradients can be placed before the readout train (a gradient-echo approach), or instead, a refocusing 180° pulse can be used (a spin-echo approach). It can be shown that the TE offering optimal sensitivity for BOLD signal changes lies between the T_2^* values of the activated and baseline states – typically close to 30 ms at 3 T, and 25 ms at 7 T (Yacoub et al., 2001). This rather short duration requires a fast sampling of k-space planes, and for higher spatial resolutions (which involve more sampling points) acceleration schemes based on **k-space undersampling** are often employed (McGibney et al., 1993; Griswold et al., 2002).

Despite their obvious advantages in terms of acquisition speed, EPI techniques are particularly sensitive to certain artifact types, mainly due to their rather long readouts, which result in a low bandwidth for the phase-encoding direction. For instance, the resonance frequency of 1H protons in fat tissues have a **chemical shift** that accumulates throughout spatial encoding, resulting in substantial displacements of the fat signal in the phase-encoding direction. **\vec{B}_0 inhomogeneities**, especially strong at air-tissue boundaries such as in the nasal cavities, generate off-resonance artifacts and phase slopes during encoding that arise as geometric distortions in the images. The successive switching of the readout gradient polarity between successive k-space lines produces an alternation in the direction of phase shifts, resulting in **Nyquist ghosting** artifacts in the phase-encoding direction, shifted by half of the image FOV. Numerous approaches have been devised to minimize each particular artifact type, and may be advantageous for studies targeting particularly problematic brain regions. Despite these artifacts, in general, given their high sampling speed, adequate spatial resolution and functional sensitivity, EPI methods have remained the most widely used techniques for BOLD fMRI data acquisition.

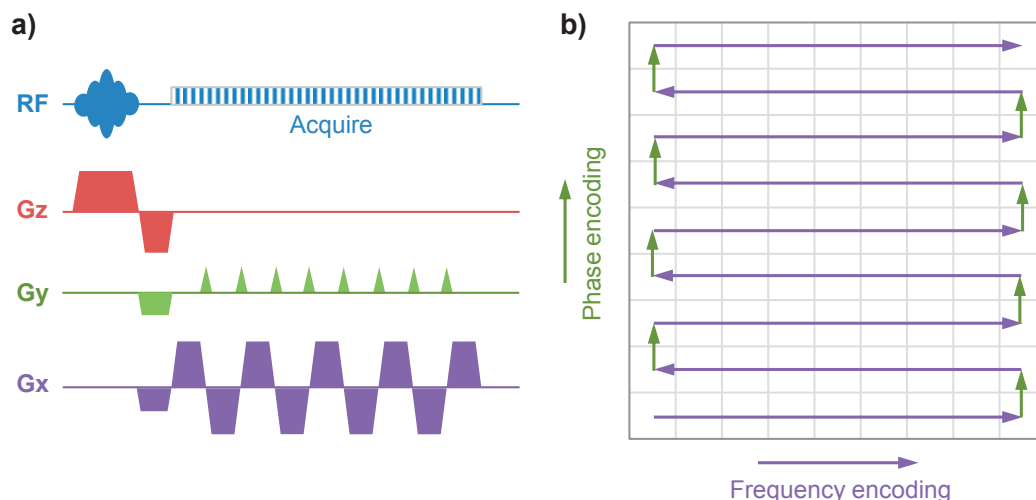


Figure 1.10: A 2D gradient-echo EPI pulse sequence (a) and its k-space traversal diagram (b) for a 9×9 -point image. The initial phase gradient moves the acquisition to the edge of k-space in the phase-encoding direction. The alternating read gradient then causes a train of gradient echoes to be formed and the subsequent gradient "blips" on the phase axis serve to step the acquisition through k-space in the phase-encoding direction. The combination of frequency and phase-encoding gradients yields a rectilinear trajectory of data points in k-space with the direction of the readout gradient being switched for alternate lines.

1.2.5 Limitations of BOLD fMRI

Despite the tremendous impact of BOLD fMRI in modern neuroscience, the technique contains a number of caveats that must be taken into consideration, and which introduce important limitations to its applicability and the interpretation of results. Due to the slower nature of vascular and metabolic processes compared to neuronal activity, BOLD responses have a relatively poor **temporal resolution**. Even with extremely fast acquisition sequences, capable of sampling entire brain volumes in only a few hundreds of milliseconds, the limitations introduced by physiology cannot be avoided, and strongly hinder the estimation of response timings and causal relationships in neuronal interactions.

While its poor temporal specificity is a limiting aspect, the strongest drawback of the BOLD effect is in fact its interpretability. The coupling between neuronal activity and BOLD fluctuations, resulting from an interplay of CBF, CBV and $CMRO_2$, has proved to be highly complex and still remains poorly understood (Logothetis, 2008). The vascular and metabolic processes underlying the BOLD response throughout its various stages have been extensively studied, and some points of consensus have been reached, yet many aspects remain unclear. For instance, observations of the rather elusive **initial dip** have varied widely across studies, depending on factors such as the acquisition parameters, stimulus type and animal species. This feature has been hypothesized to reflect a rapid deoxygenation of capillary blood caused by suddenly-increased synaptic activity, but evidence has also suggested it may instead be due to

a local, rapid increase in capillary CBV (Uludag, 2010; Hu and Yacoub, 2012).

A few seconds after activity onset (with or without an observable initial dip), it is well accepted that CBF displays an increase of about 50–70%, outweighing the CMRO₂ increase, which is only of 2–5% (Jezzard et al., 2001) – resulting in a main positive response peak. Although very consistently observed, the rise in blood flow following increases in neuronal activity is mediated by highly complex mechanisms involving both neurons and neighboring **astrocytes**. Neurotransmitter-mediated signaling, particularly by **glutamate**, is currently thought to play a major role in this process, although other regulation factors such as nitric oxide, arachidonic acid and K⁺ are also involved, and the local concentration of O₂ seems to modulate these processes significantly (Attwell et al., 2010). The hierarchical level of the **vascular structures** affected by these processes, as well as the propagation and timing of the alterations, are also a subject of active debate (Hillman, 2014).

Following the main BOLD peak, the **post-stimulus undershoot** has also proved considerably challenging to understand. Initial studies associated this effect to a slowly-resolving, passive increase in CBV that lasts for a longer period than changes in CBF and CMRO₂ – as described by the so-called balloon model (Buxton et al., 1998). Although fairly well-accepted, alternatives to this mechanism have been proposed, namely a prolonged high-CMRO₂ state that outlasts the CBF response (Lu et al., 2004), or a strong decrease in CBF accompanied by a small drop in CMRO₂, below baseline (an inverse mechanism to that of the main peak). The latter hypothesis suggests an actual influence from ongoing neuronal activity in the generation of the undershoot, and has received increasing support in recent years (Sadaghiani et al., 2009; Mullinger et al., 2013b).

Given the complexity of **neurovascular coupling** mechanisms, BOLD fluctuations must be carefully interpreted. For instance, while deactivated populations may express negative BOLD responses (Shmuel et al., 2006), complex arrangements of competing excitatory and inhibitory activity can have unpredictable outcomes (Lauritzen and Gold, 2003). Neurovascular coupling has been found to vary across brain regions (de Munck et al., 2007; Goense et al., 2012), and alterations have also been identified in certain pathological conditions such as epilepsy (Grouiller et al., 2010), cortical spreading depression, brain ischemia and Alzheimer's disease (Attwell et al., 2010). Given these various sources of variability, the linear time-invariant modeling approach based on a canonical HRF can thus be expected to perform inaccurately.

Finally, the **neuronal substrates** of BOLD are also a point of important debate. Although not undisputedly (Mukamel et al., 2005), evidence suggests that LFPs are more tightly correlated with BOLD than MUA (Logothetis, 2002; Rauch et al., 2008). While this points to perisynaptic activity as the best correlate of BOLD fluctuations, the problem becomes even more complex as different LFP frequency bands tend to show distinct, context-dependent correlations with BOLD (Niessing et al., 2005; Whitman et al., 2013). Finally, besides neurons, other cell types such as astrocytes can influence hemodynamic fluctuations significantly (Schummers et al., 2008). Moreover, ongoing **physiological processes** such as the cardiac and respiratory cycles

can also introduce important confounds (Kruger et al., 2001; Jorge et al., 2013).

Given the limitations of the BOLD contrast, other MRI-based approaches have been proposed and explored for functional imaging. An important alternative is **arterial spin labeling** (ASL), which relies on the transient magnetic "labeling" of water protons traveling in proximal blood vessels (using inversion RF pulses), yielding a signal which is directly proportional to cerebral perfusion (Detre et al., 1994). Furthermore, if complemented by appropriate calibration data, and following a number of assumptions, simultaneous ASL perfusion and BOLD measurements can yield estimates of CMRO₂ responses, a considerably more direct measure of neuronal activity (Leontiev and Buxton, 2007). Other alternatives to BOLD include the direct measurement of changes in CBV, based on approaches such as **vascular space occupancy** (VASO) imaging (Lu et al., 2003). Unfortunately, in general, despite providing more direct, quantitative measures of neuronal activity than BOLD fMRI, the currently-existing alternatives still remain inferior in terms of image SNR and temporal resolution, among other constraints, limiting their applicability.

1.3 EEG-fMRI integration

Having considered the physiological substrates, strengths and limitations of EEG and fMRI, it is straightforward to recognize the potential benefits of combining the two techniques for the study of brain function (Babiloni et al., 2004). Indeed, the first EEG recordings performed inside an MRI scanner were accomplished shortly after fMRI started being applied to humans (Ives et al., 1993), and aimed for a better spatial localization of **epileptic networks** in patients undergoing presurgical evaluation (Patel et al., 1999). These initial localization attempts were performed in an interleaved scheme, with the EEG recordings allowing for the identification of seizure onsets in real time, and these being used to start fMRI acquisition. BOLD data from these periods were then compared to "event-free" intervals, allowing for the identification of brain regions with significant signal variation between the two states.

Importantly, due to their strong static magnetic field, rapidly-varying gradients and RF pulses, MRI scanners impose a harsh environment for EEG recording, raising important issues in both patient safety and data quality (Laufs, 2012). **Safety concerns** arise from the possible generation of electric currents along the EEG wires and through biological tissues, induced by the MRI gradients or RF pulses (Dempsey et al., 2001), as well as the disruption of \vec{B}_1 field distributions due to the presence of the conductive EEG components, possibly leading to important changes in power deposition within the head (Angelone et al., 2004). Regarding **data quality**, when EEG and fMRI are acquired simultaneously, both modalities can be affected by severe artifacts. On the one hand, the presence of EEG materials can lead to MR image degradation, caused by magnetic susceptibility effects between the head tissues and the EEG components (Krakow et al., 2000), as well as \vec{B}_1 disruption or shielding effects caused by the EEG materials. On the other hand, the EEG recordings are affected by strong artifacts essentially generated by EM induction, mainly caused by the MRI gradients (Allen et al.,

2000), followed by various effects related to the cardiac cycle (Mullinger et al., 2013a), as well as head motion in \vec{B}_0 , and vibrations propagated from the He coldheads (Mullinger et al., 2008a) and ventilation systems (Nierhaus et al., 2013). These important challenges encouraged a remarkable course of technological advancements in EEG system design and fMRI acquisition protocols (Allen et al., 1998; Goldman et al., 2000; Mandelkow et al., 2006), which mitigated many of the initial problems, and eventually allowed for a transition from **interleaved acquisitions**, where "silent periods" are included in the fMRI protocol to allow the recording of gradient artifact-free EEG intervals (Bonmassar et al., 1999; Kruggel et al., 2000), to truly **simultaneous acquisitions** (Lemieux et al., 2001; Goldman et al., 2002; Moosmann et al., 2003). Likewise, EEG-fMRI applications were rapidly extended from epilepsy to the study of healthy brain function, with important contributions to its understanding (Debener et al., 2006; Herrmann and Debener, 2008).

Despite these technological advances, combined studies still involve important conceptual and methodological questions at the level of experimental design, data acquisition, modality-specific data processing and multimodal data integration (Mullinger and Bowtell, 2011). These aspects are introduced in this section, with some being discussed in greater detail later on in Chapters 3–5.

1.3.1 Substrates of EEG, fMRI and behavior

While strongly dependent on the underlying neuronal activity, the signals captured by either **EEG** or **fMRI** form a complex, biased expression of only part of that activity. Indeed, their neuronal substrates can be schematized as two partially-overlapping domains contained inside the larger pool of neuronal activity (Rosa et al., 2010a), which can itself be divided into an event-related domain, comprising evoked activity associated to an experimental paradigm, and an event-unrelated domain, comprising spontaneous activity (Debener et al., 2006). **Behavior** can also be considered as a third domain of observation (Laufs, 2012) (Fig. 1.11). These representations highlight the subtleties of multimodal integration – for example, a behavioral change may be accompanied by measurable changes in EEG, fMRI, or both, but the underlying sources may differ (Nunez and Silberstein, 2000). Likewise, different integration approaches involve different assumptions regarding this uncertainty, and thus carry specific vulnerabilities when applied to the complex dynamics of brain function, which must not be neglected (Martinez et al., 1999; Daunizeau et al., 2005; Im et al., 2005; Laufs et al., 2006; Regenbogen et al., 2012).

1.3.2 Experimental design

A fundamental question regarding the combination of EEG and fMRI is whether the two modalities should be acquired separately – in different sessions with similar experimental paradigms, or simultaneously. More specifically, this relates to whether the scientific question in hand can be answered satisfactorily from separately-acquired data (Debener et al., 2006).

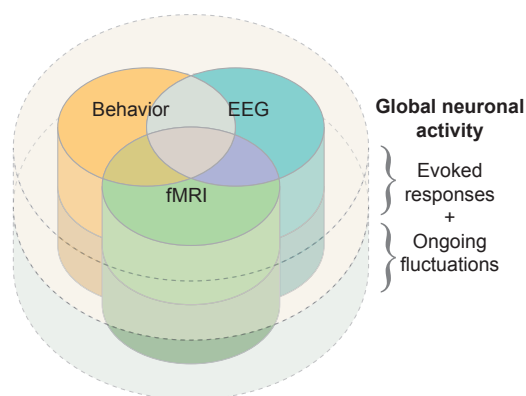


Figure 1.11: EEG, fMRI and behavior can be seen as separate measures of distinct, only partially overlapping, substrates of the whole domain of brain activity. This larger domain can be divided into externally-evoked activity, associated to an experimental protocol, and spontaneous activity, comprising ongoing fluctuations.

Separate acquisitions carry two main advantages. First, due to the different temporal scales of electrophysiology and hemodynamics, most stimulation or task designs cannot be optimized for both modalities simultaneously. For example, while the maximum-amplitude responses to alternating visual checkerboards have been identified at a reversing frequency of 8 Hz for both EEG and fMRI, the full duration of a typical VEP cannot be resolved at such a high frequency (Singh et al., 2003; Wan et al., 2006). Additionally, in interleaved acquisitions, the inclusion of "MR-silent" periods affects the choice of TR and may further constrain stimulation timings (Garreffa et al., 2004). Furthermore, a second, and often more important advantage, is that separate acquisitions are not susceptible to the specific artifacts of simultaneous EEG-fMRI.

Despite the advantages of separate recordings, certain experimental confounds and applicability limitations can only be overcome with **simultaneous acquisitions**. The distinct environments in which EEG and fMRI are typically acquired can present very different and potentially confounding spurious stimuli (Novitski et al., 2003; Sammer et al., 2005). Separate sessions can also introduce training or habituation effects (Debener et al., 2002), along with different subjective impressions and experiences, as well as emotional and motivational states (Raichle and Gusnard, 2005; Boly et al., 2007; Busch et al., 2009). Regarding applicability, the study of spontaneous activity, such as in epilepsy (Tyvaert et al., 2008; Gotman and Pittau, 2011) and in resting state (Mantini et al., 2007a; Scheeringa et al., 2008), simply cannot be accomplished in separate sessions. The same applies to the study of trial-by-trial fluctuations, which have been found to predict additional variability across modalities (Debener et al., 2005; Becker et al., 2011). Given the distinct timescales of EEG and fMRI responses, experimental paradigms must be carefully designed to highlight the phenomena of interest in each modality (Garreffa et al., 2004), while dealing with potential sensitivity and specificity compromises (Liu et al., 2001). Along this line, parametric designs, where stimuli are presented with controlled variations of a specific parameter, have proved to be particularly insightful (Horovitz et al., 2004; Mulert et al.,

2005; Schicke et al., 2006; Liu et al., 2010).

1.3.3 Generic data processing

Before integrated analysis, both EEG and fMRI data are usually subjected to a number of modality-specific preprocessing stages (Fig. 1.12). For **fMRI**, typical steps include image reconstruction from sampled k-space data, motion and slice-timing correction, spatial smoothing and normalization, and slow-drift removal (Smith et al., 2004b; Strother, 2006). On the **EEG** side, common steps are temporal filtering, epoch extraction, electrode re-referencing and data resampling (Delorme and Makeig, 2004). Additionally, when acquired simultaneously with fMRI, highly compromising artifacts are imposed on EEG data, and must be adequately addressed in data preprocessing as well – this is investigated and discussed in more detail in Chapter 4.

A few other techniques are worthy of mention given their frequent use in EEG-fMRI studies. For instance, frequency-specific EEG power fluctuations, particularly in the alpha and gamma bands, have been extensively analyzed. Such information is associated with a **time-frequency representation** or "spectrogram", which can be obtained by segmenting the EEG timecourses into small epochs and Fourier-transforming each individual epoch (Goldman et al., 2002). This approach can be further improved with multi-tapering methods (Thomson, 1982), which minimize the variance of higher-frequency estimates (Martuzzi et al., 2009; Scheeringa et al., 2011). Also, instead of Fourier transforms, some authors have opted for wavelet-based analysis (Moosmann et al., 2003; Mizuhara et al., 2005; Mulert et al., 2010), which allows a versatile trade-off between time and frequency resolution (Tallon-Baudry et al., 1998).

As for fMRI, the identification of brain regions displaying significant signal changes in association with an external stimulus or task is often performed by **general linear model** (GLM) analysis. Here, a model of the activity of interest is typically convolved with a suitable HRF and used for voxel-by-voxel regression analysis, yielding statistical maps of associated BOLD changes (Worsley and Friston, 1995). The adopted HRF, representing the transfer function assumed to link neuronal activity to the BOLD signal, can be based on a commonly-established canonical form (Friston et al., 1998), or specifically adapted to the data and context at hand (Logothetis et al., 2001; de Munck et al., 2007; Grouiller et al., 2010).

Finally, in both EEG and fMRI alike, a growing number of studies have adopted the use of **independent component analysis** (ICA), a fully data-based technique that aims to decompose the data into a set of statistically-independent sources (Eichele et al., 2008; Marques et al., 2009; Masterton et al., 2013). Both for EEG (Brown et al., 2001) and fMRI (McKeown and Sejnowski, 1998), ICA typically generates a set of timecourses associated to particular spatial distributions in the brain or on the scalp. These sources can then be selected or excluded from further analysis based on their spatial, temporal and/or spectral properties (Scheeringa et al., 2008). As an example, EEG data are sometimes contaminated by line noise affecting individual channels, which is often well separated by ICA as a component with a focal distribution centered on

the affected channel(s) and a strong power peak at 50/60 Hz. Artifacts due to eye blinking are also often well identified as a component with stronger incidence on frontal channels, and a characteristic timecourse with sparse, large signal deflections. After having identified such components, the decomposed EEG data can typically be reconstructed by back-projection from the independent component space, using only the components of interest. Given the different nature of the data from each modality, temporal ICA is usually applied to EEG data, while spatial ICA is a more common choice for fMRI (Calhoun et al., 2009).

1.3.4 Data integration: comparison approaches

Many EEG-fMRI studies investigating neurovascular coupling have employed purely comparative approaches, analyzing which measures of each modality yield the closest similarities between the two (Fig. 1.12). Certain seminal studies involved the implantation of **cortical microelectrodes** in experimental animals, allowing for the direct comparison of LFP and MUA measures with the local BOLD response (Logothetis et al., 2001; Niessing et al., 2005). From such recordings, LFP and MUA fluctuations can be estimated from lower and higher frequency bands, respectively, convolved with suitable HRFs, and compared to local BOLD responses.

More recently, a few groups have also compared fMRI with **intracranial EEG** (icEEG, or "electrocorticography", ECoG), in human patients undergoing presurgical evaluation. The few simultaneous studies published so far have investigated responses to motor tasks, focusing on time-frequency fluctuations of cortical activity and their BOLD correlates (Carmichael et al., 2011), and interictal epileptiform activity, analyzing the propagation dynamics and hemodynamic correlates of occurring discharges (Vulliemoz et al., 2011; Cunningham et al., 2012). Separate fMRI and icEEG acquisitions have also been explored in a few cognitive studies (Lachaux et al., 2007), allowing for more optimized experimental approaches such as the use of ultra-high field strengths (Harvey et al., 2012). Although highly invasive, and limited in brain coverage and applicability, the higher specificity and SNR of intracranial recordings are sparking a rapidly-growing interest in their integration with fMRI (Hermes et al., 2012).

Despite their limitations compared to invasive electrophysiology, whole-brain approaches integrating **scalp EEG** and fMRI have proven to be powerful tools for comparative analysis. For instance, in event-related studies, EEG information from pre- and post-stimulus onset periods can be statistically tested for task-related variations, and mapped across the brain with source estimation techniques. These source maps can then be directly compared to the corresponding task-related BOLD response maps, highlighting region- and feature-specific couplings (Martuzzi et al., 2009; Yuan et al., 2010). Important work has also been dedicated to the study of resting-state networks (RSNs), which comprise spontaneous but spatially-correlated fluctuations in brain activity (Biswal et al., 1995; Fox and Raichle, 2007). Decomposition techniques such as ICA can be used to identify prominent patterns of spontaneous activity in EEG signals, often frequency-specific, and can also detect networks of coherent resting-state fluctuations in BOLD data. The two types of patterns can then be compared and analyzed for significant

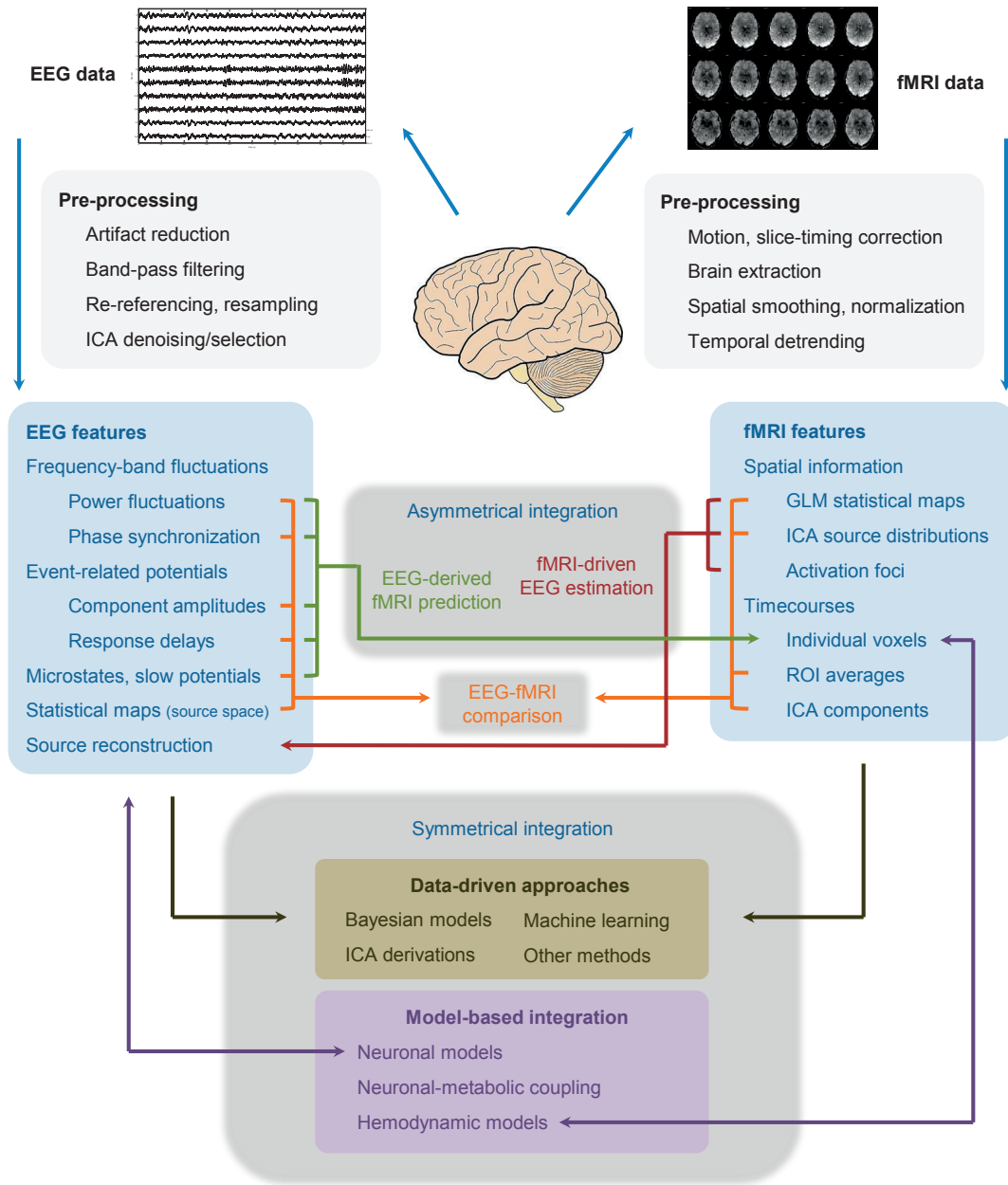


Figure 1.12: A general scheme of the main EEG-fMRI data integration approaches proposed in the literature, including purely comparative, asymmetrical and symmetrical techniques.

covariations in time (Mantini et al., 2007b; Meyer et al., 2013).

1.3.5 Data integration: asymmetrical approaches

In general, asymmetrical integration approaches rely on information extracted from one of the two modalities to drive or constrain the analysis of the other (Fig. 1.12), aiming to complement

its specific spatiotemporal limitations and yield better estimates. This idea has motivated a wide variety of methods (Herrmann and Debener, 2008), which can be grouped into two main categories: fMRI-driven EEG estimation, and EEG-derived BOLD prediction. In either case, however, results must be interpreted carefully, as these approaches tend to rely heavily on the assumption that the neuronal substrates of EEG and fMRI are coincident.

In **fMRI-driven EEG estimation** approaches, statistical maps of paradigm-related BOLD signal changes are used to guide or constrain EEG source reconstruction. The ill-posed nature of the EEG source estimation problem forcibly leads to the incorporation of spatial constraints and regularization terms (Michel et al., 2004). Techniques such as MRI can provide useful information for this purpose, namely with high-resolution, subject-specific head volume conductance maps (Dale and Sereno, 1993; Wolters et al., 2006). In a further step, *functional* information given by fMRI and PET has also been found useful to provide spatial constraints and better-informed regularization criteria (Heinze et al., 1994). For instance, electric dipole positions can be restricted to the cortical regions displaying significant BOLD responses, thereby considerably reducing the number of unknown variables (Ullsperger and von Cramon, 2001; Bledowski et al., 2004). Dipole "seeds" are placed in the regions of interest, defined with high spatial resolution, and source estimation can then be performed for each instant of the EEG response, with high temporal resolution. This approach can yield very informative descriptions of how different stationary brain sources interact and contribute to the observed ERPs (Brass et al., 2005; Meyer et al., 2012).

Alternative approaches have also been proposed where fMRI is used not to specify source locations but, instead, to guide the optimization of distributed source models, through the inclusion of a priori information in their cost function. For instance, in a Bayesian formulation seeking the solution that is most consistent with a given set of EEG and fMRI observations, the fMRI-derived maps can be used to model the spatial covariance of source dipole strength (Dale et al., 2000), and the introduced bias can be made adjustable to avoid over-regularization (Babiloni et al., 2004, 2005). These models can then be taken even further by incorporating constraints on the relationship between BOLD fluctuations and (integrated) EEG response power, based on prior assumptions regarding neurovascular coupling (Liu and He, 2008).

EEG-derived BOLD prediction, a somewhat reciprocal approach to fMRI-driven EEG estimation, opts for the extraction of meaningful activity timecourses from EEG data to model certain contributions to BOLD signal variance ("integration by prediction"). Typically, EEG-derived timecourses are HRF-convolved, down-sampled to match fMRI acquisition timings, and then used as regressors in voxel-wise GLM analyses. While these stages are relatively common, the selection of relevant EEG features can itself rely on very diverse assumptions and hypotheses regarding the EEG-BOLD coupling, and various options have been explored. Frequency band-specific power fluctuations are possibly the most extensively analyzed EEG feature for fMRI prediction, including studies focused on specific frequency bands, especially alpha (Goldman et al., 2002; Goncalves et al., 2006), and more expanded analyses exploring multiple-band interactions (de Munck et al., 2009; Scholvinck et al., 2010; Scheeringa et al., 2011).

Although meaningful correlations between BOLD and EEG power timecourses have often been reported, these carry strong assumptions regarding the EEG-BOLD coupling, and must be considered carefully. Supporting the approach, it has been suggested that, while both neuronal and hemodynamic responses behave in a highly nonlinear manner with stimulus strength and duration (Logothetis, 2002), the relationship between EEG source power and BOLD amplitude remains itself close to linear, both in positive (Wan et al., 2006; Liu et al., 2010) and negative responses (Arthurs et al., 2007). Nonetheless, recent studies have identified particularly informative new metrics, such as the EEG "root-mean-squared frequency" (Kilner et al., 2005). This heuristic measure has been found superior to power-weighted metrics for BOLD prediction, highlighting the importance of relative power redistribution across the spectrum, over absolute power fluctuations, in the modulation of BOLD amplitude (Rosa et al., 2010b; Leite et al., 2013).

While power fluctuations have been the most extensively explored EEG features, other measures have proved meaningful as well. Long-range phase synchronization, thought to reflect the functional integration of distributed neuronal units, is one such example (Mizuhara et al., 2005; Jann et al., 2009). In event-related studies, certain ERP components can be associated to activity in specific cortical regions. In agreement with this, the trial-by-trial fluctuations in amplitude, as well as latency, of ERP components have proved to explain some of the inter-trial variability of BOLD responses, aiding the localization of the associated sources (Eichele et al., 2005; Benar et al., 2007). Slow cortical potentials have also been explored following this approach (Khader et al., 2008). Other EEG features have been considered within the study of spontaneous activity, including brief sleep phenomena (Laufs et al., 2007) and EEG microstates (Britz et al., 2010; Yuan et al., 2012). Epilepsy studies, where concurrent EEG-fMRI has its roots, have strongly benefited from EEG-based prediction approaches, and a substantial amount of work has been dedicated to this application (Gotman and Pittau, 2011). As has been found, the temporal dynamics of epileptic activity can often be captured with EEG and converted into meaningful BOLD predictors, allowing for a more precise spatial localization of neuronal generators and propagation networks (Tyvaert et al., 2008; Grouiller et al., 2011).

1.3.6 Data integration: symmetrical approaches

In contrast with asymmetrical approaches, which tend to rely on the assumption that the two modalities probe coincident neuronal substrates, symmetrical approaches explicitly recognize EEG and fMRI signals as measures of distinct, only partially overlapping substrates of neuronal activity. These methodologies seek to establish a bilateral dependence between EEG and fMRI (Rosa et al., 2010a), and can be grouped into two main categories: data-driven and model-based (Fig. 1.12).

Data-driven symmetrical approaches typically rely on blind estimation methods that avoid the need to explicitly model the complex neuronal population and neurovascular coupling dynamics. A considerable variety of approaches have been explored. For example, some

authors have proposed a finite parcelling of the cortical surface into a set of functionally homogeneous clusters, and modeled EEG and BOLD signals as linear systems with respect to the distributed cortical dipoles and HRF. Spatial and temporal smoothness priors are specified for this multimodal hierarchical model, and its posterior probability density function is then iteratively estimated (Daunizeau et al., 2007; Luessi et al., 2011). Others have used Bayesian-formulated criteria to match functional networks obtained separately from each modality by spatial ICA, whereby fMRI networks are introduced as covariance priors to reconstruct the sources of EEG networks (Lei et al., 2011).

Another approach of growing interest is that of joint ICA, where individual fMRI and ERP data are merged and analyzed with ICA on a multi-subject scale. It is assumed that EEG independent temporal components and the associated fMRI independent spatial components are linearly combined across subjects by the same mixing matrix, and ICA can decompose the global observation matrix to yield the underlying BOLD-ERP components that were combined to form individual subject responses (Calhoun et al., 2009; Mijovic et al., 2012). In recent years, various other heuristic methods have been proposed, for example exploring information theory concepts, such as mutual information and synergy (Ostwald et al., 2011; Caballero-Gaudes et al., 2013), combinations of EEG-based fMRI prediction with fMRI-driven EEG estimation (Yang et al., 2010), canonical correlation analysis (Correa et al., 2010), and machine learning concepts (De Martino et al., 2011a).

Model-based symmetrical approaches have addressed the integration problem through the development of increasingly more realistic biophysical models describing the neuronal, metabolic, and hemodynamic processes underlying EEG and BOLD signals, continuously improved with information from brain architecture and function at diverse spatial scales (Rosa et al., 2010a). The full modeling challenge can be decomposed into interacting stages, including: (1) the neuronal response to external stimulation, neuronal population dynamics and interactions; (2) the propagation of EM fluctuations to the scalp; and (3) the coupling between neuronal activity, CMRO₂ and CBF, the vascular mechanisms relating dHb concentration, CBF and CBV, and the BOLD signal dependence thereon (Riera et al., 2006).

Neuronal population responses and interactions pose a remarkable modeling challenge (Lauritzen and Gold, 2003). Earlier studies proposed to recreate neuronal and hemodynamic responses to stimulation with a simple inhibitory feedback system, describing the local neuronal response as a balance between excitatory and inhibitory inputs (Buxton et al., 2004). Subsequently, more biophysically-inspired approaches were continuously developed, first with models of single cortical columns, receiving excitatory input and including inhibitory feedback (Jansen and Rit, 1995), later on with multiple cortical columns, introducing anatomically-plausible interactions between neighboring columns (Babajani and Soltanian-Zadeh, 2006), and finally with multiple cortical areas, interacting via long-range connections (Babajani-Feremi and Soltanian-Zadeh, 2010). Following neuronal response modeling, the link to measurable scalp EEG fluctuations can then be established through a forward model of head volume conduction (Dale and Sereno, 1993; Lenz et al., 2011).

For BOLD signals, the link to neuronal activity is mediated by a complex cascade of metabolic and hemodynamic processes governing CMRO_2 , CBF and CBV changes, of which many aspects remain unclear (Riera and Sumiyoshi, 2010; Hillman, 2014). Earlier studies proposed a linear relationship between synaptic activity and CBF, described by a set of differential equations that included coupling efficacy, signal decay and auto-regulatory feedback effects (Friston et al., 2000). Later models introduced more elaborate interactions, such as differences in the metabolic and vascular effects of excitatory, relative to inhibitory synaptic activity (Sotero and Trujillo-Barreto, 2007), and multiple-area interactions (Sotero and Trujillo-Barreto, 2008). CBV changes in response to CBF and CMRO_2 have also been addressed, especially through the so-called balloon model, which assumes CBV changes to occur primarily in the venous compartment, modeled as a balloon fed by the capillary bed output (Buxton et al., 1998). This model was further extended with a resistive description of brain vasculature, to model capillary and venous compliance (Mandeville et al., 1999), and has since been integrated in numerous studies.

Overall, approaches for the integration of EEG and fMRI have been continually improved over the last two decades, guided by insights arising from their application to various contexts, as well as from parallel neuroscience investigations relying on complementary modalities. With a better understanding of the substrates and limitations of each technique, as well as the dynamics of coupling between synaptic activity, metabolic and hemodynamic mechanisms, increasingly richer and more accurate predictions can be drawn with combined EEG-fMRI. Many questions still remain to be clarified, such as, for example, the nature of ultra-high frequency oscillations observed in EEG, and of negative BOLD responses observed in fMRI. In parallel, widespread efforts continue to be dedicated to the improvement of data quality in simultaneous acquisitions, which plays a vital role in subsequent data integration. Altogether, these efforts continue to drive the development of data acquisition, analysis, multimodal integration and interpretation, so as to explore the full potential of combined EEG-fMRI.

2 The negative BOLD response to visual stimulation

In fMRI studies, external stimulation often elicits **negative BOLD responses** in various brain regions, and growing evidence supports their association with local neuronal deactivation, giving functional meaning to this phenomenon. The fMRI study presented in this chapter aimed to characterize, in humans, positive (PBRs) and negative BOLD responses (NBRs) to visual checkerboard stimulation of varying contrast and duration, focusing on NBRs occurring in visual and in auditory cortical regions. Response estimation was improved by excluding large draining vein contributions and via ICA-assisted denoising, particularly important for auditory NBRs. Results showed that visual PBRs and both visual and auditory NBRs significantly depend on stimulus contrast ($p < 0.01$) and duration ($p < 0.05$). Response amplitudes increased monotonically with stimulus contrast, with both visual and auditory NBR amplitudes linearly correlated with the visual PBR amplitude. For stimuli up to 10–16 s, the areas under the response curves increased with stimulus duration and all response areas remained linearly correlated. For longer stimulation periods, however, both NBRs exhibited earlier returns to baseline than the PBR. Under the hypothesis of neuronal deactivation, these findings suggest a highly dynamic system of visual-auditory interactions, sensitive to stimulus contrast and duration, which can occur even for the passive observation of basic visual stimuli.

2.1 Introduction

Since the discovery of the BOLD contrast, fMRI has been widely used for in vivo neuroscience. The BOLD contrast is sensitive to the local concentration of deoxyhemoglobin, which in the brain varies according to changes in CBF, CBV and CMRO₂. The coupling mechanisms linking neuronal activity with vascular and metabolic processes are still a topic of intense research and debate (Hillman, 2014). Nevertheless, it is generally accepted that a local increase in neuronal activity will raise CMRO₂, but also typically induce a strong increase in CBF, resulting in a net **positive BOLD response** (PBR).

Parts of this chapter were adapted from:

Stimulus dependence of the negative BOLD response to visual stimulation in visual and auditory cortical regions at 7 T, J. Jorge, P. Figueiredo, R. Gruetter, W. van der Zwaag, under review.

Chapter 2. The negative BOLD response to visual stimulation

While positive responses to a stimulation paradigm or task are the most commonly sought, sustained paradigm-locked BOLD signal decreases are also often found in various brain regions, and have captured considerable interest (Lauritzen et al., 2012). This effect, termed **negative BOLD response** (NBR), has been robustly observed in humans during, for example, visual stimulation (Shmuel et al., 2002; Smith et al., 2004a), tactile stimulation (Hlushchuk and Hari, 2006; Kastrup et al., 2008; Klingner et al., 2010), and motor tasks (Hamzei et al., 2002; Stefanovic et al., 2004). Cortical areas exhibiting NBRs are often found in close proximity to positively-responding regions (Shmuel et al., 2002), or symmetrically in the opposite hemisphere, such as in somatosensory stimulation or motor tasks (Hlushchuk and Hari, 2006; Mullinger et al., 2014b). In addition, NBRs have been reported in cortical regions not directly related to the stimulus modality, namely in auditory areas during visual stimulation, as well as in visual areas during auditory stimulation (Laurienti et al., 2002), and also in regions coinciding with the default-mode network (DMN) (van der Zwaag et al., 2009b).

Due to the complex nature of the BOLD contrast, NBR interpretation has motivated intense debate, with several hypotheses being proposed: (1) a pure decrease in CBF with no changes in CMRO₂, caused by "vascular steal" effects from activated neighboring regions, or by hypothetical long-range CBF control mechanisms; (2) a decrease in CMRO₂, with CBF reductions that overcome the decreased CMRO₂; (3) an increase in CMRO₂ that is not compensated by increased CBF (Wade, 2002; Mullinger et al., 2014b). While a number of studies have identified vascular steal effects or suggested the existence of central mechanisms for CBF regulation, competing with local demands (Smith et al., 2004a; Vafaei and Gjedde, 2004), considerable evidence suggests a dominant influence of **local neuronal activity** in the generation of NBRs. Negative responses have been found strongly coupled with decreased CMRO₂ in the visual cortex (Shmuel et al., 2002; Pasley et al., 2007), primary motor cortex (Stefanovic et al., 2004) and DMN (Lin et al., 2011), and with psychophysiological measures of functional inhibition in somatosensory (Kastrup et al., 2008) and motor studies (Hamzei et al., 2002). Studies combining fMRI with local electrophysiology measures have provided additional, more direct evidence of a neuronal origin for NBRs, including the observation of local field potential and spiking decreases in primate visual cortex (Shmuel et al., 2006) and rat somatosensory cortex (Boorman et al., 2010), as well as inhibitory activity (neuronal hyperpolarization) increases in rat somatosensory cortex (Devor et al., 2007). Furthermore, in human studies using scalp electroencephalography, NBR amplitudes in the visual cortex, auditory cortex and DMN have been found to correlate with pre-stimulus alpha-band power (Mayhew et al., 2013), and NBRs in the sensorimotor cortex have been related to increased mu oscillation power and evoked potential amplitudes (Mullinger et al., 2014b). Overall, these observations suggest that NBRs can be driven by decreases in excitatory activity, increases in inhibitory activity, or both; the combination of these processes, as a whole, is hereafter referred to as "neuronal deactivation".

The association of NBRs with local neuronal deactivation, even without fully excluding hemodynamic contributions, is an important landmark for fMRI. Under visual stimulation, results from large single-subject datasets have unveiled widespread sustained NBRs in more than 50% of all grey matter (Gonzalez-Castillo et al., 2014). With both positive and negative BOLD

responses demonstrating functional significance, their joint characterization is thus likely to yield richer descriptions of brain function, including interactions within specific functional regions, as well as across regions with distinct functional nature (also termed cross-modal interactions). Relevant insights include not only response localization, but also their **temporal dynamics** and **stimulus dependence**. Studies focused on the visual cortex, using visual stimuli of varying intensity and duration, have reported a tight covariation between PBRs and NBRs, in both amplitude and temporal evolution (Shmuel et al., 2002). In the somatosensory cortex, ipsilateral NBRs to median nerve stimulation were also found to intensify monotonically with stimulus strength (Klingner et al., 2010). On the other hand, ipsilateral NBRs to prolonged (20 s) tactile stimulation have been shown to decay faster than contralateral PBRs (Hlushchuk and Hari, 2006), and NBRs to median nerve stimulation revealed relevant differences in onset and peak timing relative to the PBR (Klingner et al., 2011), contrasting with the "mirror-like" behavior observed in visual responses (Shmuel et al., 2002). This suggests differences in the temporal dynamics of neuronal activations and deactivations, or different hemodynamic coupling properties (Mullinger et al., 2014b), which may be modality-specific or become more evident with prolonged stimulation. Numerous questions thus remain to be addressed. While visual NBRs to visual stimulation have been shown to vary with stimulus contrast and duration (Shmuel et al., 2002), it is currently unknown whether the accompanying auditory NBR (Laurienti et al., 2002) may exhibit similar stimulus dependence. It is also unknown whether more prolonged visual stimuli may reveal differences in temporal profile between PBRs and NBRs, as observed for tactile and median nerve stimulation, which were not evident at shorter stimulus durations.

The study of NBRs is often limited by their inherently low amplitude when compared to PBRs, and can thus greatly benefit from the use of stronger **static magnetic fields** for fMRI acquisition, yielding super-linear gains in functional sensitivity (van der Zwaag et al., 2009a). In addition to this, the shorter venous T_2^* at higher field strengths such as 7 T (Yacoub et al., 2001) grants a lower sensitivity to contributions from **draining veins**, which can introduce undesirable biases in response localization (Turner, 2002; Barth and Norris, 2007) and characterization, including NBR-specific confounding effects (Bianciardi et al., 2011).

The aim of the work presented in this chapter was to study the positive and negative BOLD responses to visual stimulation, in humans, focusing on NBRs occurring in the visual cortex and the primary auditory cortex. Visual and auditory NBRs were jointly elicited by visual stimuli consisting of flickering checkerboards of varying contrast (2–80%) and an extended range of durations (4–20 s). BOLD data were acquired at 7 T, to obtain NBR as well as PBR estimates at fine spatial resolution (1.5 mm), especially relevant for auditory NBRs. Furthermore, the high spatial resolution and short venous T_2^* allowed us to identify and separate large draining veins from grey matter voxels, thereby being able to assess and reduce their potential confounding effects. Response estimation was also improved by removing selected confounds obtained from ICA decomposition of the data.

2.2 Methods

This study was approved by the institutional review board of the local ethics committee (Commission d'Éthique de la Recherche sur l'Être Humain du Canton de Vaud), and involved the participation of 10 healthy volunteers (aged 23 ± 4 years old, 5 male/5 female), who provided written informed consent.

2.2.1 Data acquisition

Functional data were acquired on a Magnetom 7 T head scanner (Siemens, Erlangen, Germany) equipped with a 32-channel receive/single-channel quadrature transmit head coil (Nova Medical, MA, USA). Functional images were acquired using a 2D multi-slice GE-EPI sequence with $TR/TE = 2000/25$ ms, $\alpha = 78^\circ$, $2\times$ -GRAPPA acceleration, $7/8$ partial Fourier sampling (McGibney et al., 1993) and sinusoidal readout. EPI volumes comprised 30 slices with $1.5 \times 1.5 \times 1.5$ mm³ spatial resolution (22.2×22.2 cm² in-plane FOV, interleaved acquisition, 5% inter-slice gaps), and were placed in an axial-oblique orientation to cover both the primary visual cortex and primary auditory cortex.

2.2.2 Functional paradigms

All functional runs employed a repetition of blocks consisting of a visual stimulation period followed by a baseline period (fixation). Stimulus delivery was set with an LCD projector placed outside the scanner room, transmitting images through a small waveguide to a screen placed at the back of the bore. Visual stimulation was performed with grey-scale checkerboards reversing at 8 Hz (15° FOV central-field presentation, 12 segments across the diameter); the total luminance was kept equal to baseline periods. A red cross was shown at the center of the FOV at all times, with slight changes in color occurring twice per block at random times. Subjects were instructed to remain focused on the cross and report color changes via a button press, in order to ensure attention.

All subjects underwent 3 distinct paradigms: a functional localizer (*FLoc*), a contrast-varying run (*FCont*), and a duration-varying run (*FDur*, Fig. 2.1). The localizer run was used to unbiasedly identify regions of interest (ROIs) with significant responses to visual checkerboard stimulation, which were then used for response averaging in *FCont* and *FDur* data. *FLoc* runs comprised 8 blocks of 10 s stimulation separated by 20 s rest; checkerboards were presented at 20% contrast. *FCont* runs comprised 32 blocks of 10 s stimulation separated by 20 s rest, with each block of stimuli presented at one of 4 different contrast levels: 2%, 5%, 20% or 80%; each level was applied in 8 blocks throughout the run, in randomized order. These contrast levels were chosen based on preliminary tests, aiming to cover a well-distributed range of (positive) response amplitudes in the visual cortex. *FDur* runs comprised 32 blocks of variable-length stimulation, at 20% contrast, separated by 20 s rest; each block employed one of 4 different stimulus durations: 4 s, 10 s, 16 s or 20 s; each duration was likewise applied

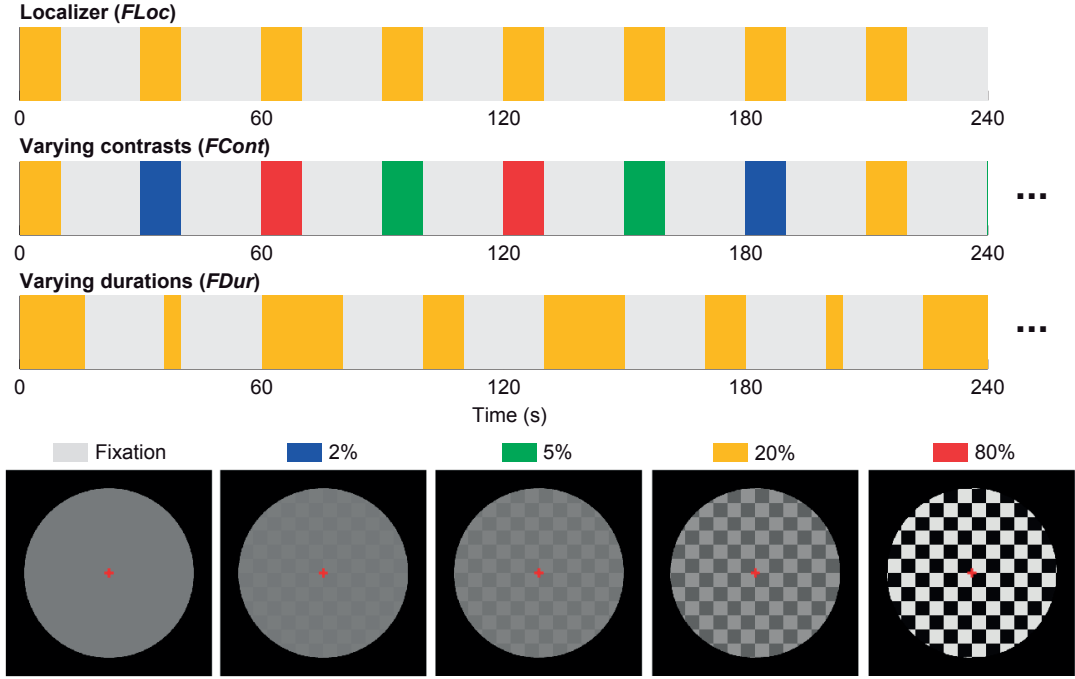


Figure 2.1: Functional paradigms employed for checkerboard-based visual stimulation. **Upper:** Stimulation timecourses of the functional localizer (*FLoc*), varying-contrast (*FCont*) and varying-duration (*FDur*) paradigms; for easier visualization, only the first 4 mins of *FCont* and *FDur* are shown (of a total of 16 min each). **Lower:** Visual patterns employed during fixation (baseline) and stimulation periods.

in 8 blocks throughout the run, in randomized order. Each subject underwent one of each run type, separated by pauses of several minutes. The three run types were conducted in counter-balanced order across subjects.

2.2.3 Data analysis

In order to estimate and characterize PBRs and NBRs to the applied stimuli, functional data underwent a set of processing stages as outlined in Fig. 2.2. All steps were executed in Matlab (Mathworks, Natick MA, USA) using routines developed in-house.

Pre-processing: Analysis started with a pre-processing stage consisting of motion correction (6 degrees of freedom, referenced to the middle volume of the series) (Jenkinson et al., 2002), slice-timing adjustment (set to the middle of each TR, via linear interpolation), brain segmentation (Smith, 2002), and Gaussian spatial smoothing (FWHM = 2mm). For each subject, the unsmoothed middle volume of each timecourse (coincident with the reference volume for motion correction) was used to estimate the spatial registration parameters from *FLoc* to *FCont* and to *FDur* (linear transformation, 9 degrees of freedom (Jenkinson et al., 2002)).

Large vein segmentation: The unsmoothed reference volume of each timecourse was also

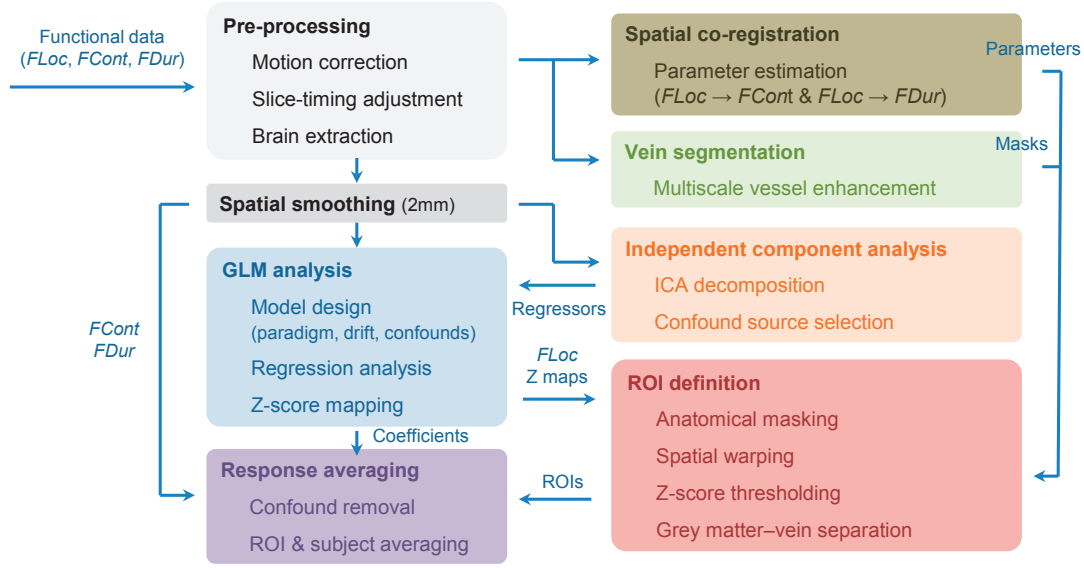


Figure 2.2: Schematic outline of the processing steps adopted for data analysis in this chapter, with the goal of estimating positive and negative BOLD responses to the various stimulus conditions applied during data acquisition.

used for the semi-automatic segmentation of large draining veins. This was performed via multiscale vessel enhancement filtering (Frangi et al., 1998), an image-based technique which uses second-order (curvature) information to highlight vessel-like structures. Originally proposed for more dedicated angiography modalities, variants of this approach have been successfully adapted for high-spatial resolution gradient-echo fMRI data, at 3 T (Koopmans et al., 2010). For our GE-EPI, 1.5 mm-resolution 7 T images, the original filter (Frangi et al., 1998) was found to perform well, with parameters $\alpha = \beta = 0.5$, $\gamma = 0.02$, and covering spatial scales of 0.5–3.0 mm (in 0.5 mm steps). These values were defined empirically for optimal performance on the acquired dataset.

ICA-based confound extraction: For each subject and paradigm, the pre-processed functional data were decomposed by ICA using the extended infomax algorithm (Lee et al., 1999), imposing statistical independence in the spatial dimension. Data decomposition was preceded by a dimensionality reduction step based on principal component analysis, where the most important components explaining 95% of total data variance were kept. Following ICA, the resulting sources were manually reviewed in search for relevant confounds, mainly related to subject motion (Kelly et al., 2010), physiological noise (Bianciardi et al., 2009) and spontaneous brain activity, and avoiding any sources with temporal periodicities close to that of the applied stimulation paradigm. For each dataset, a total of 0–6 task-irrelevant sources were selected (3 on average), and the corresponding timecourses were included as confounds in subsequent regression analyses.

General linear model analysis: All pre-processed functional datasets underwent GLM analy-

sis (Worsley and Friston, 1995), for the purpose of response localization (*FLoc*) and timecourse denoising (*FCont* and *FDur*). Functional paradigms were modeled as boxcar functions, convolved with a canonical HRF defined by a double-gamma curve. In *FCont* and *FDur* runs, each contrast/duration level was modeled as a separate regressor. Each full model comprised the set of paradigm regressors (convolved boxcars and their 1st order temporal derivatives), 4 slow-drift regressors (1st–3rd order polynomials), 6 motion confounds (the motion correction parameters, consisting of 3 translation and 3 rotation timecourses), and the ICA-derived confounds.

ROI definition and averaging: Following GLM analysis, for each subject, a Z-score map was estimated from *FLoc* to quantify the statistical significance of BOLD responses to checkerboard stimulation across the brain. This map was subsequently warped to *FCont* and *FDur* spaces based on the previously estimated co-registration parameters. From each map, three ROIs were then defined: a visual PBR ROI, a visual NBR ROI, and an auditory NBR ROI. Visual PBR and visual NBR ROIs were restricted to the occipital lobe and comprised all voxels with $Z \geq +8.0$ and $Z \leq -2.5$, respectively; the auditory NBR ROI was restricted to the auditory cortex (Brodmann areas 41 and 42) and included all voxels with $Z \leq -1.5$. Based on the masks obtained from vein segmentation, each of the 3 regions was finally split into 2 ROIs, one containing grey matter (and non-detected vessels) and the other comprising large draining veins. Anatomical ROI masking was based on the direct identification of landmarks such as the lateral fissure and Heschl's gyrus on individual functional images, a manual approach that proved more accurate than alternatives based on spatial co-registration to standard atlases. The three adopted Z-score thresholds were the same for all subjects, chosen empirically so that every subject kept no less than 20 voxels in any of the 6 ROIs. No information from *FCont* or *FDur* was used in ROI definition, except for the vein segmentation masks.

Prior to response averaging, *FCont* and *FDur* data were denoised by removing slow-drift, motion and ICA confounds, appropriately weighted by the corresponding GLM fit coefficients. The denoised voxel timecourses were then baseline-corrected on a block-by-block basis by subtracting the mean value of the last two timepoints of the block, and divided by the mean BOLD signal of the timecourse for normalization to a % signal change scale. The normalized timecourses were finally averaged across repetitions, ROIs, and subjects.

2.3 Results

2.3.1 Positive and negative BOLD stimulus dependence

To characterize the stimulus dependence of PBRs and NBRs, response ROIs were obtained from the *FLoc* paradigm, and applied to *FCont* and *FDur* data for spatial averaging of responses to each contrast level and duration. Consistently across subjects, Z-score maps from the *FLoc* paradigm exhibited several brain regions within the FOV with statistically significant BOLD responses to checkerboard stimulation. Clusters with large positive scores were found

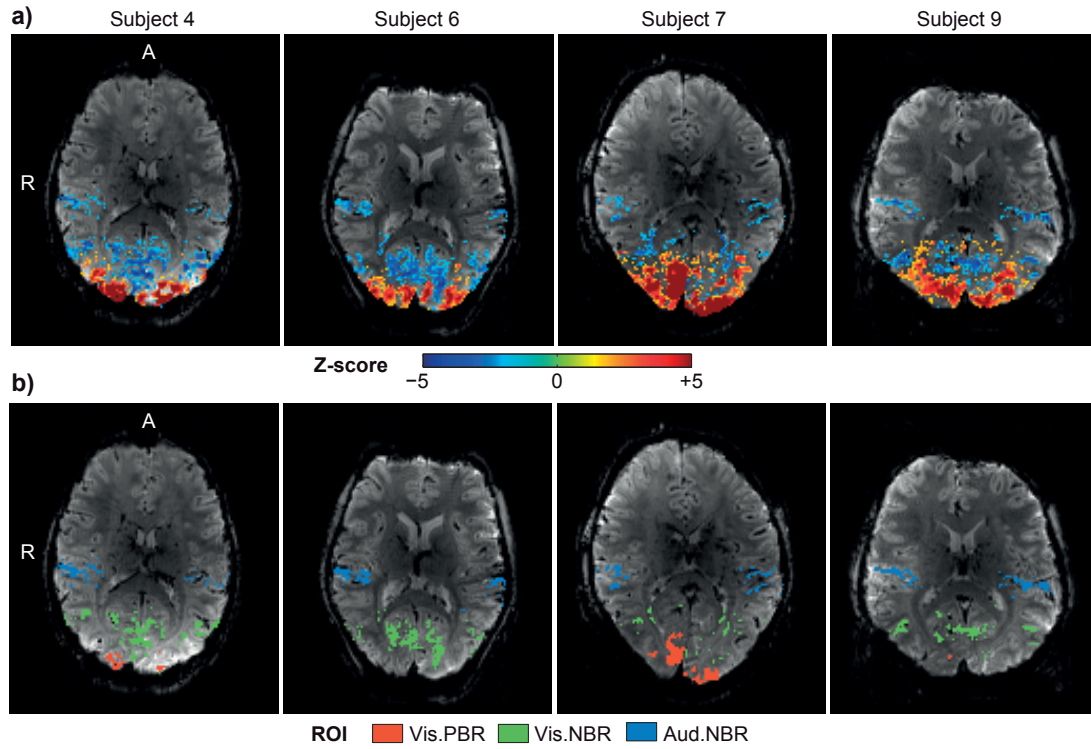


Figure 2.3: BOLD response localization for the functional localizer paradigm (*FLoc*), in four of the ten participating subjects. These subjects were chosen for having a slice orientation favorable for displaying all three response types in the same slice. **a)** Z-score maps quantifying the statistical significance of BOLD responses to checkerboard stimulation; these maps have been anatomically masked and thresholded ($|Z| > 1.5$) to evince occipital regions with positive and negative BOLD responses, and temporal regions (primary auditory cortex) with negative BOLD responses; the color bar range was manually restricted for clearer visualization. **b)** ROIs defined for response estimation, using more specific Z-thresholds (+8.0 for visual PBR ROIs, -2.5 for visual NBR ROIs, and -1.5 for auditory NBR ROIs); visual PBR ROIs were more widely distributed across slices than NBR ROIs, in some cases being more evident in lower slices than the ones shown.

mainly within the visual cortex, while clusters with negative scores could be found both in the visual and in the primary auditory cortex (Fig. 2.3), as well as in other areas such as the somatosensory/motor cortex. Across subjects, the ROIs selected as visual PBR areas included 696 ± 191 voxels (already excluding detected veins) and displayed ROI-average Z-scores of +8.76 to +9.86, with peak scores ranging from +9.44 to +14.71. NBR ROIs in visual areas included 1629 ± 340 voxels, with average Z-scores of -2.88 to -3.38 and peak scores of -4.57 to -9.46. ROIs in auditory regions included 580 ± 94 voxels and exhibited average Z-scores of -1.92 to -2.18, with peak scores ranging from -3.48 to -4.86. No systematic inter-hemispheric differences were found across subjects for any of the three ROIs.

Contrast dependence: Under contrast-varying stimulation (*FCont* paradigm), group average

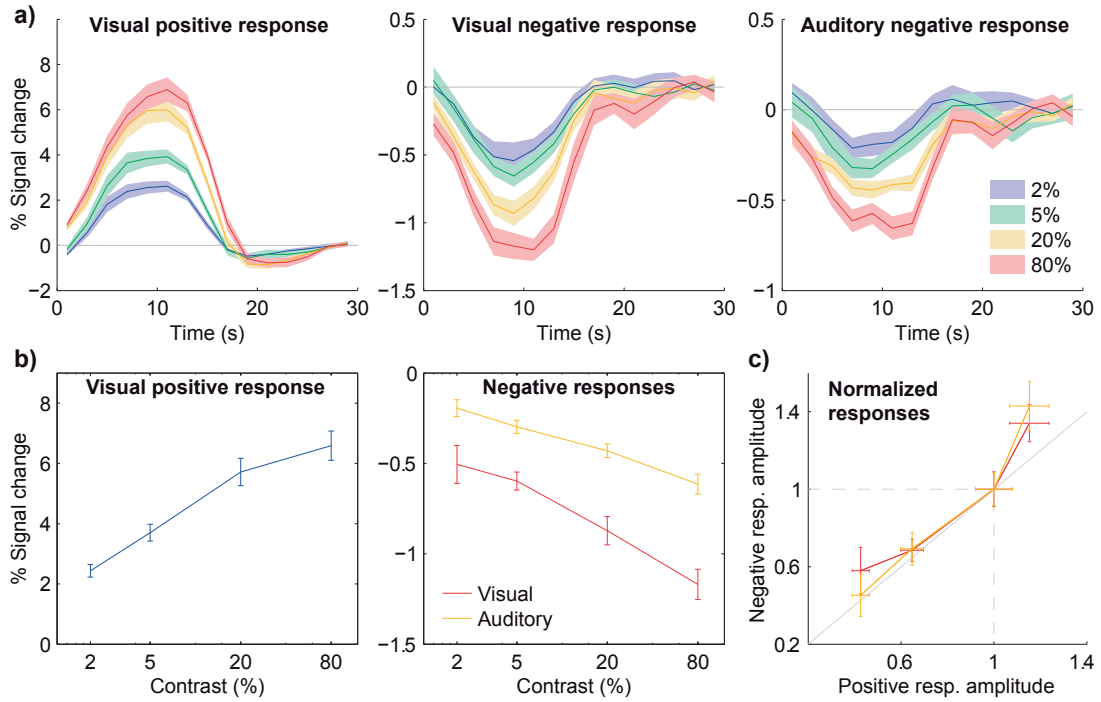


Figure 2.4: Group average BOLD responses to 10s-checkerboard stimulation with varying contrast ($FCont$), in grey matter. **a)** Visual PBRs (left), visual NBRs (center) and auditory NBRs (right) to 4 different contrast levels (note the different amplitude scales for each response type). **b)** Peak response amplitudes for each contrast level. **c)** Visual and auditory NBR amplitude as a function of visual PBR amplitude, after normalization of each response to the amplitude at 20% contrast; the diagonal grey line marks the identity function. All response curves and amplitudes represent averages across stimulation blocks and subjects, with error margins and bars representing the standard error across subjects.

BOLD responses exhibited clear stimulus dependence in all three grey matter ROIs (Fig. 2.4a), with response peak amplitudes increasing monotonically with checkerboard contrast (Fig. 2.4b). The contrast dependence of response amplitudes was statistically significant for all ROIs ($p < 0.01$ for the effect of stimulus contrast, balanced one-way ANOVA). NBRs were then compared to the visual PBR by normalizing each set relative to its 20% contrast response amplitude. This procedure revealed a linear correlation between both visual and auditory NBR amplitudes and the visual PBR amplitude, at least for contrast levels up to 20% (Fig. 2.4c). Within this range, pooling together the response amplitudes from all subjects and three (lower) contrast levels, without normalization, a linear relationship was observed between the visual PBR amplitude and both visual NBR (Pearson coefficient $r = -0.50$, with $p < 0.01$) and auditory NBR amplitudes ($r = -0.55$, with $p < 0.01$). At 80% contrast, both normalized NBRs displayed a comparable deviation from the PBR, with stronger relative increases in amplitude (Fig. 2.4c). Overall, the two NBR types exhibited a similar dependence on stimulus contrast, although with the visual NBR achieving larger amplitudes in general.

Duration dependence: Under varying stimulus duration (*FDur* paradigm), group average BOLD responses also exhibited a clear stimulus dependence, with response duration increasing monotonically with stimulus duration in all grey matter ROIs (Fig. 2.5a). When comparing the response timecourses from the three ROIs after amplitude normalization (Fig. 2.5b), positive and negative responses exhibited comparable temporal properties for shorter stimuli (4 s and 10 s), but for longer stimuli an earlier decay was observed in both visual and auditory NBRs, compared to the visual PBR – although reaching the baseline at a similar time. This was especially evident at the longest stimulation level (20 s). Response duration was quantified by estimating the area under the normalized response curve for each stimulus level, excluding the under/overshoot and subsequent periods (Fig. 2.5c). Duration dependence of the PBR was statistically significant for all levels ($p < 0.01$ for the effect of stimulus duration, balanced one-way ANOVA), while NBRs were only significantly stimulus-dependent ($p < 0.05$) for the two shorter durations. A comparison between positive and negative response areas (normalized to the respective 10 s values) suggested a linear correlation between both NBRs and the visual PBR for shorter stimuli up to 10 s (Fig. 2.5d). This trend was also observed by pooling together the response areas from all subjects for the two shorter stimulus durations, without normalization, and comparing visual PBR areas with visual NBR ($r = 0.53$ with $p < 0.01$) and auditory NBR areas ($r = 0.33$ with $p = 0.07$). Growing deviations to this linear correlation were evident for longer stimuli (16 s, 20 s), where smaller relative increases in area were observed for both visual and auditory NBRs compared to the visual PBR (Fig. 2.5d). This effect tended to be more accentuated for auditory NBRs, and at 20 s duration the areas of the two normalized NBR types did significantly differ from each other ($p = 0.02$, paired t-test).

2.3.2 Grey matter – vein separation

To assess the impact of vein contributions to BOLD response characterization, the voxels identified as large draining veins (Fig. 2.6) were analyzed separately and compared to those attributed to grey matter. Visual inspection of *FLoc* Z-score maps across subjects identified several small clusters (1.5–4.5 mm diameter) dominated by a central Z-score peak, spatially coincident with a large draining vein, as previously detected by the multiscale filtering approach (Fig. 2.7a). In general, responses to visual stimulation from vein-identified regions were considerably stronger than in grey matter – approximately $3\times$ higher in amplitude in both positive and negative responses, for the ROIs defined in this work. Furthermore, visual PBRs were visibly delayed in veins relative to grey matter (Fig. 2.7b). While the available temporal resolution did not allow for proper quantification of the temporal delay, this effect was robustly observed in visual PBRs at all contrast levels and durations, as well as in NBRs to higher contrast levels. Finally, although roughly expressing similar trends, the stimulus dependence of venous responses was considerably more irregular than in grey matter, especially for NBRs (Fig. 2.7c). Upon merging vein and grey matter ROIs for each response type (as would happen if no vein separation had been applied), response amplitudes and durations remained roughly similar to those of "pure" grey matter for visual PBRs and NBRs, but showed relevant perturbations for auditory NBRs (results not shown). Concordantly, in these merged ROIs, the

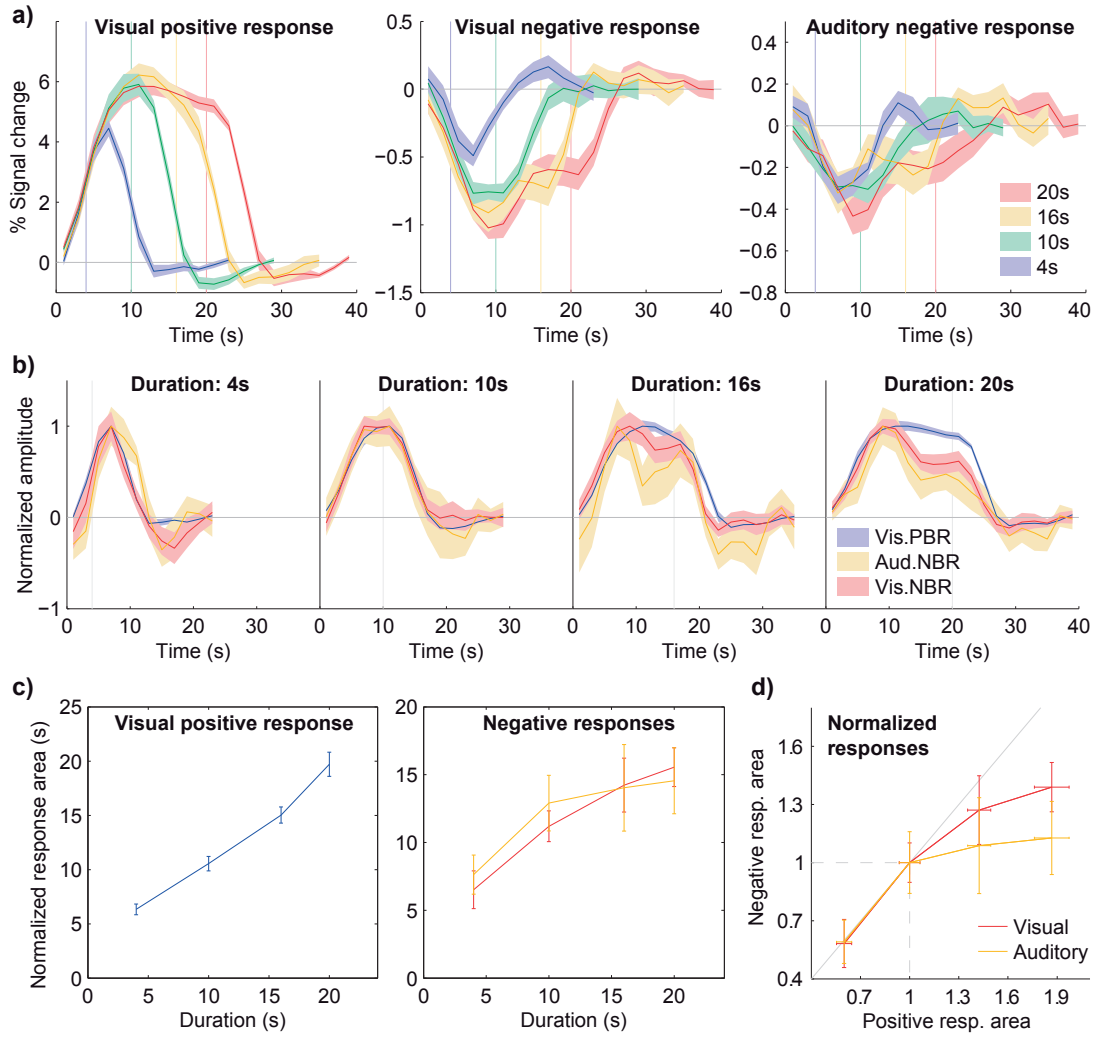


Figure 2.5: Group average BOLD responses to 20% contrast-checkerboard stimulation with varying duration ($FDur$), in grey matter. **a)** Visual PBRs (left), visual NBRs (center) and auditory NBRs (right) to 4 different stimulus durations (note the different amplitude scales for each response type). **b)** Comparison between positive and negative response shapes for each duration level, after normalization of each response curve to its peak amplitude. **c)** Response areas for each duration level, estimated as the area under the response curve, after amplitude normalization. **d)** Visual and auditory NBR area as a function of visual PBR area, after normalization of each response to the area at 10s stimulus duration; the diagonal grey line marks the identity function. All response curves and areas represent averages across stimulation blocks and subjects, with error margins and bars representing the standard error across subjects; vertical lines mark the instant of stimulus cessation for each duration level.

effects of stimulus contrast and duration became less statistically significant in general, with particular importance for the NBRs to varying stimulus duration (from $p \approx 0.02$ to $p \approx 0.04$ for the visual NBR, and from $p \approx 0.05$ to $p \approx 0.07$ for the auditory NBR).

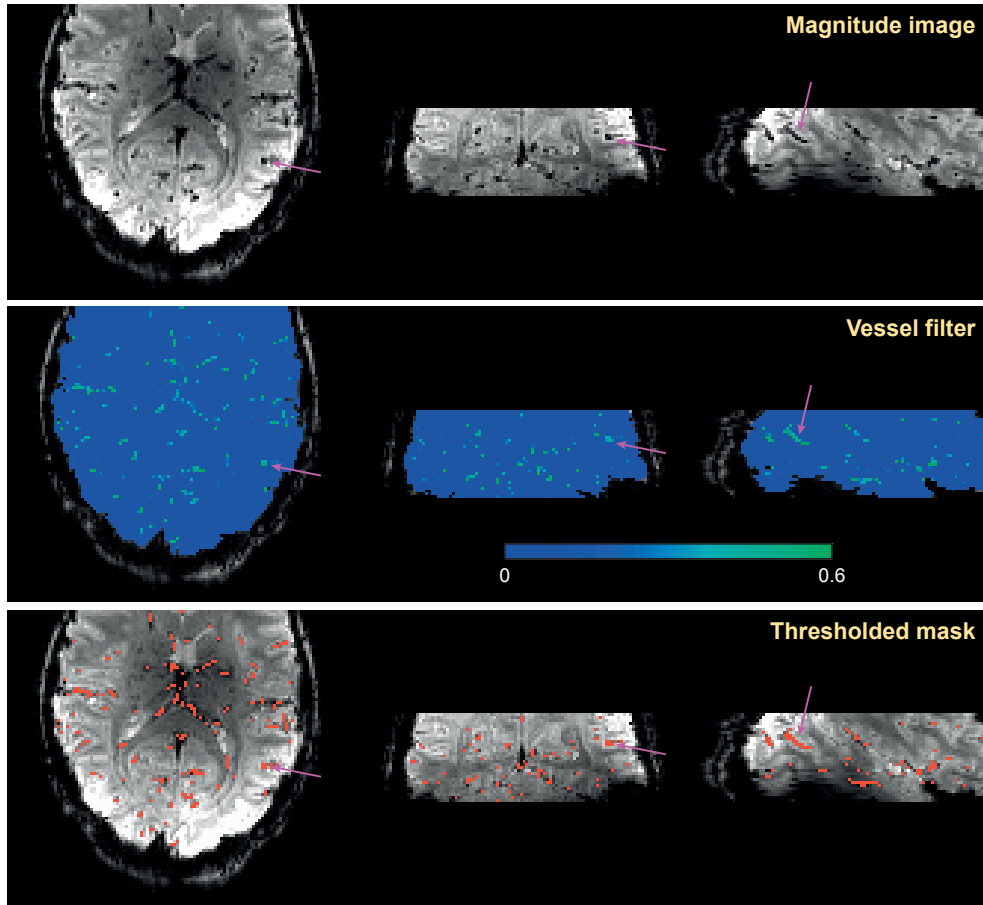


Figure 2.6: Large draining vein segmentation performed on GE-EPI magnitude data, from a representative subject. **Top:** Original magnitude image. **Middle:** "Vesselness" filter output – higher values indicate a local morphology that is closer to a tubular structure. **Bottom:** Vein segmentation obtained via thresholding of the vessel filter output map.

2.3.3 ICA-assisted denoising

The impact of ICA-assisted denoising on data quality was assessed based on both the variance explained by ICA confounds and their effect on block-by-block response variability. Systematically across subjects, ICA decomposition of the functional data produced a number of components that could be clearly identified based on their spatial distribution and/or temporal properties, such as paradigm-related sources, DMN sources, and physiological noise sources related to cardiac or respiratory processes (Fig. 2.8).

Variance explained by ICA: the proportions of data variance explained by ICA confounds were estimated based on the adjusted coefficient of determination (R_{adj}^2) obtained from GLM analyses performed with and without including those regressors (Jorge et al., 2013). A similar estimation procedure was also applied to the paradigm regressors, for comparison. Across ROI voxels and subjects (excluding three cases from *FLoc* and *FCont* data where no confounds

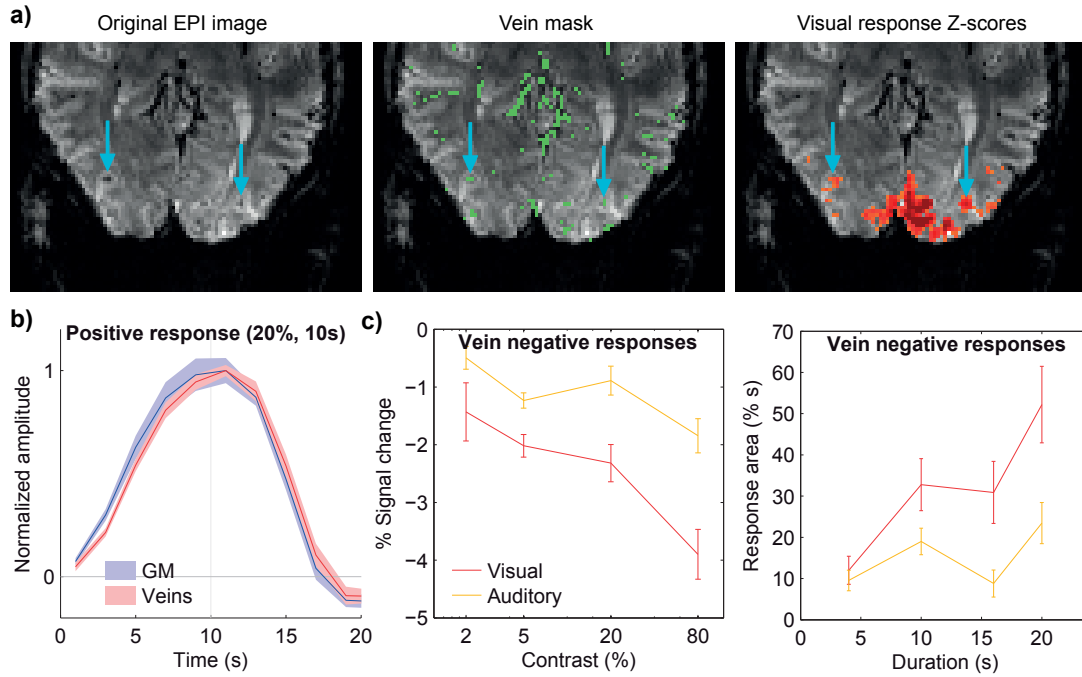


Figure 2.7: The influence of large draining veins in response localization and temporal characterization. **a)** GE-EPI data from a single subject (left), the respective vein mask obtained with multiscale vessel enhancement filtering (center), and the thresholded Z-score map for positive visual responses to the functional localizer; the blue arrows indicate two detected veins which are positioned in the center of activation clusters, exhibiting large Z-scores. **b)** Group average visual PBRs to checkerboard stimuli of 20% contrast and 10 s duration, in grey matter (blue) and segmented vein voxels (red). **c)** Group average peak amplitude (left) and response area (right) of visual and auditory NBRs to varying contrast level (left) and duration (right), in segmented veins. All response curves and amplitudes/areas represent averages across stimulation blocks and subjects, with error margins and bars representing the standard error across subjects.

were included), the selected ICA confounds proved to explain significant amounts of data variance, ranging from approximately 5% in visual PBR ROIs to 10% in visual and auditory NBR ROIs (Fig. 2.9a). Conversely, the paradigm regressors were found to explain approximately 40% of data variance in visual PBR ROIs, and only approximately 4% in visual and auditory NBR ROIs, confirming the lower contrast-to-noise ratio of negative, compared to positive, BOLD responses. The proportions of variance explained by ICA confounds tended to be higher in *FCont* than in *FDur* data, but were nevertheless statistically significant in both cases ($p < 0.01$, one-sample t-tests).

Impact on response variability: To assess block-by-block response variability, for each subject and stimulus level, considering ROI-averaged BOLD timecourses, the standard deviation across blocks was computed for each instant of the response window, and then averaged across instants, stimulus levels, and subjects. In this sense, on average, ICA denoising reduced

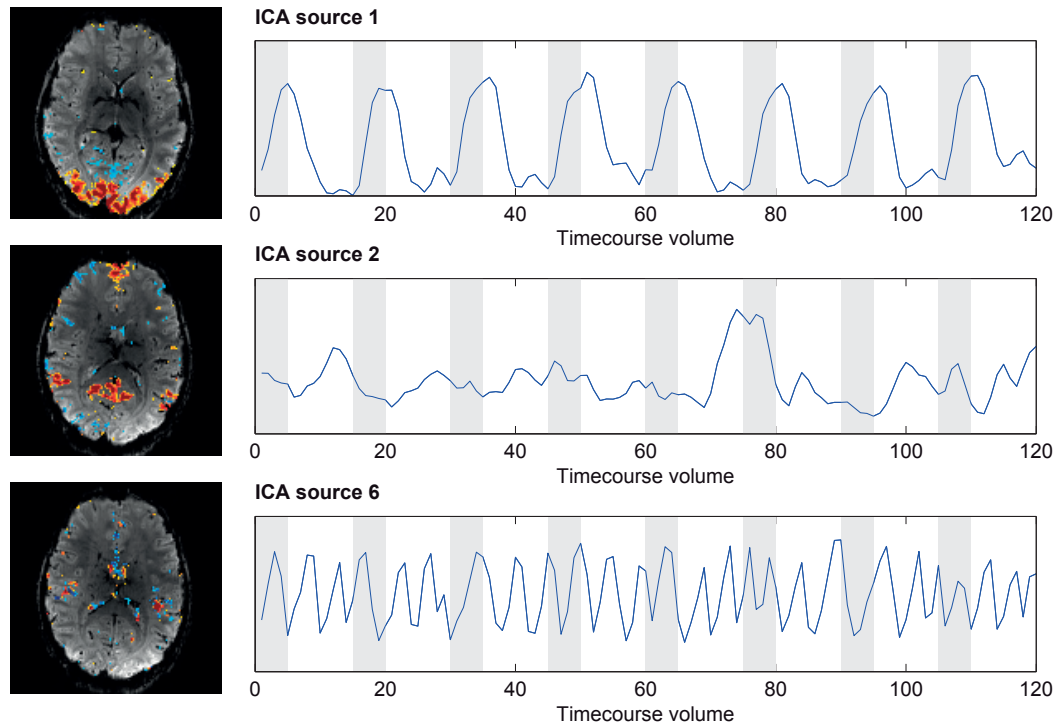


Figure 2.8: Maps and timecourses of typical independent components obtained from ICA decomposition in one of the ten participating subjects. The examples shown correspond to a paradigm-related (top), default mode network (middle) and physiological noise source, probably of cardiac origin (bottom). These components were systematically encountered across subjects, with the lower two being typical candidates for use as confound regressors. Component maps (left) have been thresholded and overlaid on the reference EPI volume for clearer visualization.

block-by-block response variability by approximately 35% in visual PBR ROIs and by almost 50% in visual and auditory NBR ROIs, similarly in both *FCont* and *FDur* data (Fig. 2.9b). The effect of ICA denoising on response variability was statistically significant in both paradigms ($p < 0.01$, balanced one-way ANOVA).

2.4 Discussion

This study shows that, under visual stimulation, the visual positive BOLD response and both visual and auditory negative BOLD responses significantly depend on stimulus intensity and duration. Response amplitudes increase monotonically with stimulus intensity and, below response saturation levels, both visual and auditory NBRs are linearly correlated with each other and with the PBR. For stimuli up to 10–16 s, response durations increase with stimulus duration and are likewise linearly correlated, while for longer stimulation periods both visual and auditory NBRs exhibit earlier decays to baseline than the corresponding visual PBR. Regarding methodology, the performance of the adopted vein separation and

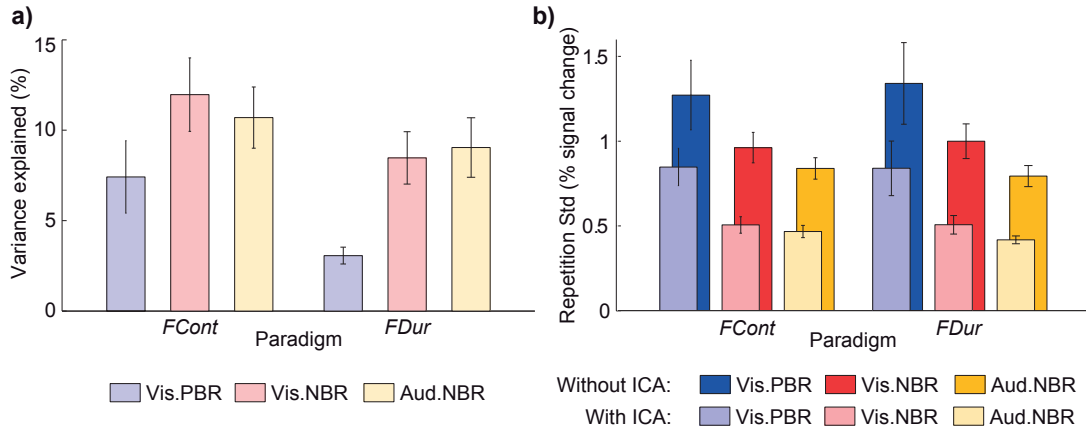


Figure 2.9: The impact of ICA-assisted denoising on contrast- and duration-varying data (*FCont* and *FDur*). **a)** Average percentages of data variance explained by ICA confounds in the GLM analyses for visual PBR, visual NBR and auditory NBR ROIs. **b)** Block-by-block response variability with and without previous ICA denoising. Bar heights indicate averages across subjects, with error margins representing the standard error across subjects.

ICA-assisted denoising techniques indicates that both approaches can be highly valuable to improve response estimation.

2.4.1 Positive and negative BOLD stimulus dependence

The stimulus dependence of visual negative BOLD to visual stimuli, often termed intra-modal NBR, has been previously shown for both stimulus intensity and duration (Shmuel et al., 2002). As for the auditory NBR to visual stimulation, although its occurrence has been robustly observed in previous work (Laurienti et al., 2002), the stimulus dependence of this cross-modal response remains largely unexplored, and is here shown for the first time. This finding carries relevant implications: as with ipsilateral NBRs to tactile stimulation (Hlushchuk and Hari, 2006; Kastrup et al., 2008; Klingner et al., 2010) and motor tasks (Hamzei et al., 2002; Stefanovic et al., 2004), the auditory NBR to visual stimulation is spatially well separated from the visual PBR region, and thus unlikely to be caused by passive "vascular steal" effects. This strengthens the hypothesis of true local neuronal deactivation (Shmuel et al., 2006), or alternatively of the existence of active, long-range vascular control mechanisms that affect CBF in auditory regions (Smith et al., 2004a; Vafaei and Gjedde, 2004). Given the robust stimulus dependence of the observed responses, the first hypothesis would hence imply that auditory neuronal deactivation increases with visual stimulus intensity and is more prolonged with longer stimuli. The second hypothesis could either imply a stimulus-dependent CBF modulation (without changes in auditory neuronal activity), or an unvarying suppression of CBF changes with stimulus-dependent increases in auditory neuronal activity (Wade, 2002). Given the steadily-growing body of evidence associating negative BOLD with true neuronal deactivation (Shmuel et al., 2006; Pasley et al., 2007; Boorman et al., 2010; Mullinger et al.,

Chapter 2. The negative BOLD response to visual stimulation

2014b), including electrophysiology data specifically showing that visual stimuli can modulate the firing of neurons in the auditory cortex (Kayser et al., 2008), the hypothesis of neuronal deactivation in the primary auditory cortex constitutes the strongest candidate to explain the observed NBRs. Under this hypothesis, the results here obtained expose the existence of highly dynamic visual-auditory interactions that depend on stimulus intensity and duration, even under passive observation of basic, low attention-demanding visual stimuli.

Under contrast-varying checkerboard stimulation, the observed response amplitudes showed a tight correlation between the visual NBR and the visual PBR, for contrast levels up to 20% (Fig. 2.4c). This is consistent with previous observations at similar contrast ranges, up to 40% (Shmuel et al., 2002). Notably, the auditory NBR was also strongly correlated to the visual PBR, suggesting similar underlying neuronal interactions for both NBR instances, and possibly analogous hemodynamic coupling dynamics relative to the visual PBR. At 80% contrast, the visual PBR showed signs of possible saturation, with a lower relative increase (Fig. 2.4b). This effect was not evinced by either visual or auditory NBRs, which maintained a steady relative increase, and thus appeared to deviate from the PBR – although remaining well correlated to each other. This is a potentially interesting behavior to be explored in future work, possibly with new parameter combinations to boost stimulus intensity, which may push both positive and negative responses to saturation. Another potentially interesting variable to explore would be the stimulus frequency, which is known to exert a non-linear and non-monotonous effect on visual PBR amplitude.

With varying stimulus duration, both visual and auditory NBR results suggested a linear correlation with the visual PBR, for stimulus durations up to 10–16 s (Fig. 2.5d). For longer stimuli, however, both NBR instances exhibited increasingly earlier decays to baseline relative to the PBR (Fig. 2.5b), leading to growing deviations from linear covariation. This phenomenon has not been observed in previous work focused on the visual NBR, which explored stimulus durations only up to 16s (Shmuel et al., 2002). On the other hand, in tactile stimulation studies using longer stimuli (20s), ipsilateral somatosensory NBRs have likewise been found to decay faster than contralateral PBRs (Hlushchuk and Hari, 2006). This effect suggests either the existence of differences between the hemodynamic coupling mechanisms of positive and negative BOLD responses, which become more evident for sufficiently long stimuli, or the possibility that neuronal deactivation may not be maintained as steadily in time as activation. In the first case, the possibility of hemodynamic coupling differences between positive and negative responses has been previously suggested by work in both visual (Shmuel et al., 2002) and median nerve stimulation (Mullinger et al., 2014b), arising as differences in the ratio of ΔCMRO_2 to ΔCBF . Such differences, however, have not been found in the motor cortex (Stefanovic et al., 2004) or DMN (Lin et al., 2011). These diverging observations could be related to the time-dependent properties of the underlying coupling mechanisms, a topic which is still under intense research and debate, even for the PBR per se (Hillman, 2014). In fact, for longer periods of visual stimulation (several minutes), ΔCBF has been observed to decrease with time, while ΔCMRO_2 eventually starts to rise. This has been hypothesized to reflect a local transition from non-oxidative to oxidative metabolism, with the latter process not eliciting increases in

Δ CBF (Lin et al., 2009). If present, in some measure, at shorter timescales, this effect could potentially have a different impact on NBR, relative to PBR regions, due to different metabolic dynamics of neuronal activation and deactivation.

Following the second hypothesis, an attenuation of neuronal deactivation for longer stimuli could suggest the existence of mechanisms which downplay the importance of visual stimuli once these have been presented for sufficiently long periods of time, possibly acquiring some form of "stationary character". Positive BOLD responses are known to suffer from habituation effects for sufficiently long stimuli (Hoge et al., 1999), as is the underlying neuronal activity (Janz et al., 2001). Here, however, an earlier response decay of NBRs was observed relative to the PBR itself, suggesting that the hypothetical adaptation mechanisms involved in releasing neuronal inhibition in NBR regions could be faster than those attenuating neuronal excitation in PBR regions. Overall, future studies monitoring both BOLD and electrophysiological activity in positive and negative BOLD regions could be highly relevant to address this question, with potentially valuable contributions to the study of the nature of the NBR, and the neurovascular coupling mechanisms underlying the BOLD signal in general. Another relevant question regards the relationship between the different response types for stimulus durations below 4 s, which were not covered in this study. Previous work has shown that the visual NBR amplitude maintains a linear covariation with the visual PBR down to 2 s duration (Shmuel et al., 2002). In our work, the auditory NBR has shown a comparable behavior to the visual NBR for all tested stimulus durations and contrast levels (even when deviating from the PBR), which suggests that this cross-modal response may similarly maintain its linear covariation with the visual PBR for shorter stimulus durations. Nevertheless, it would be interesting to test this in future experiments.

2.4.2 Grey matter – vein separation

To improve response estimation, large draining vein contributions were isolated and excluded from ROI averaging. Draining veins are well known to influence response localization (Barth and Norris, 2007) and have been shown to propagate activity-related changes in blood oxygenation for several millimeters downstream from activation sites (Turner, 2002). Furthermore, as vein-propagated responses are delayed in time relative to the original activation site, their contributions for response averaging can affect the temporal properties of the responses of interest. Thus, although less influential at 7 T than at lower field strengths (Yacoub et al., 2001; van der Zwaag et al., 2009a), venous contributions are highly undesirable, especially for the characterization of typically lower-contrast responses, such as NBRs.

Various approaches for vein identification in fMRI have been proposed (Menon, 2002; Barth and Norris, 2007; Koopmans et al., 2010). Given the high spatial resolution available at 7 T, along with a decreased venous T_2^* (Yacoub et al., 2001), large veins are clearly discernible as low-intensity, focal susceptibility artifacts in functional images, motivating the use of image-based approaches for vein segmentation. To our knowledge, this is the first study applying

multiscale vessel-enhancement filtering directly on GE-EPI data, an approach which presents several advantages: first, it avoids the acquisition of separate "vein-sensitized" images, and the necessary co-registration steps to fMRI data space, which need to be highly accurate for correct vessel localization; second, being an image-based segmentation method, the procedure can be easily verified and tuned through visual inspection; third, this approach imposed no requirements on the sequence and parameters used for fMRI acquisition, and could similarly be applied to other existing BOLD-sensitive GE-EPI datasets without additional scans. Naturally, the sensitivity of the method will depend crucially on the discernibility of veins in each dataset, which does constitute a disadvantage compared to the use of separate acquisitions designed for optimal vein visualization, often with higher spatial resolution.

It should be noted that this segmentation approach does not yield actual venograms, as it is based on the susceptibility artifacts created by veins, which expand beyond the vessels and include adjacent tissues. While lowering the specificity of segmentation, this effect is actually advantageous as it allows the detection of vessels thinner than the available spatial resolution. Furthermore, it renders more accurate response estimations in grey matter, as tissues with T_2^* perturbations due to the proximity of veins are likewise excluded. In this work, the confounding effects of veins in both response localization and characterization could be clearly observed (Fig. 2.7a,b). Moreover, the stimulus dependence of venous ROIs, segmented as described above, was considerably less regular than that of grey matter ROIs (Fig. 2.7c), potentially due to their inherently poorer response specificity and/or to a higher sensitivity to subject motion and physiological noise. The impact of this behavior on response estimation was further assessed by combining venous and grey matter responses as if no vein separation had been performed. While maintaining the general trends observed in grey matter alone, the stimulus dependence of merged responses did become less regular, especially for auditory NBRs. This outcome is not surprising given the lower contrast-to-noise ratio (CNR) of the auditory NBR, and suggests that vein separation was beneficial for the purpose of this work, and may likewise be highly desirable for other studies targeting responses with similar properties.

2.4.3 ICA-assisted denoising

The use of ICA for fMRI data analysis has been extensively explored for more than a decade. Various ICA-based denoising approaches have been proposed, with distinguishing features in mainly two aspects: source selection and noise removal. Source selection can be performed in semi-automated ways based on temporal, spectral, and spatial properties of the sources (Salimi-Khorshidi et al., 2014). Here, we opted instead for manual source selection performed under fixed criteria, in line with previous works (van der Zwaag et al., 2009b; Kelly et al., 2010), to ensure that no paradigm-related sources were taken as confounds. As for noise removal, while many approaches rely on simply reconstructing the decomposed data without the selected sources, we opted to include their timecourses as confounds in the regression models, as often performed for motion and physiological noise reduction (Bianciardi et al.,

2009), thus unifying response detection and noise modeling in the GLM analysis stage. This allowed us to benefit from the model-free exploratory capabilities of ICA integrated in the well-established framework of GLM analysis, and led to a more accurate statistical analysis as the loss in degrees of freedom due to denoising was inherently accounted for in the models. It should further be noted that, alternatively to noise source removal, ICA could be used to select the paradigm-related sources instead (Fig. 2.8), excluding all others. This approach was likewise avoided due to the danger of neglecting less evident paradigm-related sources in the data, potentially affecting response properties.

As with vein exclusion, the motivation for ICA-assisted denoising in this work was the improvement of BOLD response detection and characterization. The performance of this approach was assessed with two complementary measures: the data variance explained by ICA confounds in GLM analyses, and their impact on block-by-block response variability. The first measure is well-suited to quantify the relevance of specific regressor sets, as it relies on R^2_{adj} , which is independent of the number of degrees of freedom in the linear regression, and thus allows for an unbiased comparison between models with different numbers of regressors. The second measure is not independent of the number of degrees of freedom (always decreasing as more regressors are added), but provides a more direct indication of improvements in response denoising. In this work, both measures suggested benefits in including selected ICA-based confounds. These regressors were found to explain significant proportions of data variance in all three ROIs, and especially for NBR ROIs, potentially due to the lower CNR of the negative responses (comprising smaller fractions of total data variance). Concordantly, reductions in block-by-block variability were significant for all estimated responses, and were also relatively stronger in NBR ROIs than for the PBR. As previously mentioned, and illustrated in Fig. 2.8, the ICA decompositions revealed a number of important components that were consistent across the subjects and paradigms included in this study, in terms of spatial and time-frequency profile. This suggests a suitable level of reproducibility of the method, at least within a subject group undergoing the same experimental protocol, which is an important feature for consistent denoising across subjects. Overall, the use of ICA-derived confounds for BOLD data denoising arises as a valuable approach, which can complement or even replace other techniques targeting correlated noise sources, such as physiological noise modeling based on external monitoring.

2.4.4 Conclusion

The results here obtained show that, under visual stimulation, the visual PBR and both visual and auditory NBRs significantly depend on stimulus intensity and duration. Response amplitudes increase monotonically with stimulus intensity, and both visual and auditory NBRs are linearly correlated with the PBR. For stimuli up to 10–16 s, response durations increase with stimulus duration and all responses remain linearly correlated, while for longer stimulation periods both visual and auditory NBRs decay to baseline earlier than the corresponding visual PBR. In light of the growing evidence associating the NBR with local neuronal deactivation,

Chapter 2. The negative BOLD response to visual stimulation

these findings suggest the existence of a highly dynamic system of visual-auditory interactions which are sensitive to stimulus intensity and duration, even for the passive observation of basic visual stimuli. The deviations from linear covariation observed with longer stimuli suggest either that neuronal deactivation may be more quickly attenuated in time than neuronal activation, or that the neurovascular coupling properties of NBRs may differ from those of the PBR. Overall, future studies monitoring both BOLD and electrophysiological activity, such as with EEG-fMRI, could be highly relevant to clarify the mechanisms underlying these dynamics, with potentially valuable contributions to the study of the nature of the NBR, and the neurovascular coupling mechanisms underlying the BOLD signal in general. Regarding methodology, the performance of the vein separation and ICA-assisted denoising techniques adopted in this work indicates that both approaches can be highly valuable to improve response estimation, especially for the study of lower-CNR features such as negative BOLD responses.

3 EEG-fMRI at 7T: subject safety

Simultaneous EEG-fMRI can provide unique insights into the dynamics of human brain function, and could greatly benefit from the increased functional sensitivity offered by ultra-high field fMRI. Unfortunately, the combination of the two modalities is subject to highly undesirable interactions that can compromise **subject safety**, especially at higher field strengths such as 7 T. Here, a series of preliminary tests were conducted to assess the presence of any potential safety concerns for simultaneous EEG-fMRI in humans at 7 T, using the particular acquisition setup intended to be applied in future studies. The safety tests comprised numerical simulations of EM field distribution on a realistic computational model, and real temperature measurements on a phantom model during two 8 min-long, SAR-intensive fMRI acquisitions. The tests were performed for two distinct RF coils: a single-channel transmit/8-channel receive head loop array, and an in-house-built single-channel transmit/receive surface quadrature coil for occipital head regions. Overall, no significant safety concerns were found for the setup tested. For both RF coils, EM simulations predicted a decrease in average SAR with the introduction of the EEG system (4.9% for the surface coil, 7.9% for the volume coil), with the peak SAR also decreasing for the surface coil (12.5%), and slightly increasing (10.2%) with the volume coil. Temperature increases in the EEG electrodes during the fMRI runs remained below 1°C for both RF coils. The EEG amplifiers exhibited more significant heating effects (up to 6.5°C), albeit still remaining well within the respective operating range.

3.1 Introduction

In simultaneous EEG-fMRI acquisitions, safety concerns arise from the possible generation of electric currents along the EEG wires and through biological tissues, created by the fast-switching MRI gradients used for spatial encoding, or by the RF pulses used for spin excitation. These interactions can be associated with two distinct mechanisms: EM induction, and RF antenna effects. **EM induction** occurs when the magnetic flux within the loops formed by EEG

Parts of this chapter were adapted from:

Simultaneous EEG-fMRI at ultra-high field: artifact prevention and safety assessment, J. Jorge, E. Grouiller, Ö. Ipek, R. Stoermer, C. M. Michel, P. Figueiredo, W. van der Zwaag, R. Gruetter, 2015, *Neuroimage* 105, p.132–144.

leads and the head changes in time, causing electromotive forces that can generate currents along the leads (as described by Eq. 1.5) (Dempsey and Condon, 2001). The currents created along the EEG leads can be dissipated by ohmic heating, causing temperature increases. Furthermore, because the leads terminate in electrodes that are in physical contact with the head, the induced currents can flow through the biological tissues (also designated "contact currents"), and potentially cause damage. Electric currents are expected to be induced in the human body under normal scanning conditions; however, conducting loops provide a low-impedance component for concentration of currents, which can generate a high current density in the tissue under an electrode, thus constituting an important safety hazard. Finally, additional heating can also arise due to **eddy currents** generated within the electrodes or the gel (Lemieux et al., 1997).

RF antenna effects occur when EEG leads act as antenna wires that are sensitive to the electric component of the RF field. Importantly, when the wire length approximately matches half the radiation wavelength λ , resonant standing waves can be created, with electric field maxima at the tips of the wire (Dempsey and Condon, 2001). This property makes antenna effects especially relevant at higher field strengths, where the corresponding RF wavelengths become fairly comparable to EEG wire lengths – at 7 T, for instance, the wavelength of ^1H excitation pulses in water is approximately 11 cm (Schick, 2005). Unlike EM induction effects, antenna effects do not require the existence of loops to be generated. Additionally, the associated currents remain confined to the EEG wires, and neither create measurable signals at the amplifiers nor contact currents through the head. The main hazard associated with these effects is the heating and possible damage of the conducting wires, and of resistors that may be included at their extremities, where energy deposition is maximal (Lemieux et al., 1997).

To assure subject safety, the various interaction mechanisms described above must be carefully studied and accounted for. A straightforward measure to reduce EM induction is to avoid forming any unnecessary loops along the EEG leads (leaving only the "main" loops passing through the head and amplifiers), and to electrically insulate each lead, from the others as well as from the head tissues. In 1997, Lemieux and colleagues presented a comprehensive assessment of all the aforementioned deleterious interactions, comprising both theoretical predictions and experimental measurements. The authors considered worst-case scenarios regarding gradient slew-rate and temporal shape, loop geometry and position, and RF pulse power, duration and repetition time, and determined the RF fields to be the main source of potential safety concerns for EEG-fMRI. The inclusion of **current-limiting resistors** near the electrodes, in the order of 10 k Ω per electrode, was proposed as a general measure to constrain the potential safety hazards, and has since been widely adopted by hardware manufacturers. Additionally, manufacturers have recommended a careful selection of **low-RF power MRI sequences** for both functional and structural acquisitions (Noth et al., 2012).

The proposed modifications and guidelines have provided a reliable framework for safe EEG-fMRI acquisitions. Nevertheless, with the constant pursuit of higher field strengths, optimized RF coils and novel fMRI sequences, continued attention must be given to maintain EM

interactions under suitable safety limits. Particularly, if the \vec{B}_0 field strength is increased, the interference mechanisms tend to become more problematic, as RF pulse frequency, and therefore energy, increases linearly with \vec{B}_0 , and gradient slew-rates tend to be increased as well, to achieve higher spatial resolutions. Moreover, at 7 T, RF pulse wavelengths in water become smaller than the typical sample size, and the risk of resonant antenna effects along the EEG leads is also increased (Dempsey et al., 2001). Another aspect of great importance is that the presence of the conductive EEG materials may alter the **transmit** \vec{B}_1 (\vec{B}_1^+) field distribution across the head, introducing unpredicted changes in local power deposition (Angelone et al., 2004). This problem also becomes more relevant for the shorter wavelengths created at 7 T, which lead to decreased RF penetration (Roschmann, 1987) and considerably more heterogeneous \vec{B}_1 distributions across the head (Eggenschwiler et al., 2012).

Given the prime importance of subject safety for human studies, considerable efforts have been dedicated to the assessment of potential injury risks for particular EEG-MRI setups, especially at higher field strengths. **Temperature** is the most direct measure for risk assessment, and as such temperature measurements during EEG-fMRI acquisition, in phantoms and humans, are often performed. However, these measurements typically have a limited coverage, with only a few points monitored simultaneously, and restricted to the surface when testing with human subjects. MRI itself can be used to obtain 3D maps of the (\vec{B}_1^+) field distribution across the head; however, it is the electric component \vec{E} of the RF field that determines power deposition, and this component cannot currently be measured with a similar approach. Nevertheless, **EM simulations** can be performed with realistic models of the acquisition setup and the acquired sample, applying Maxwell's equations to predict both the \vec{B}_1^+ and \vec{E} field distributions across the head (Angelone et al., 2006). In general, these simulations are highly relevant for RF coil design and calibration, and can likewise be applied to study the effects of introducing EEG components in the sample (Angelone et al., 2006). A standard measure of power deposition, widely used in MR safety analyses, is the **specific absorption ratio** (SAR), which is related to the electric field as follows:

$$SAR = \frac{1}{V} \int_V \frac{\sigma(\vec{r}) |\vec{E}(\vec{r})|^2}{\rho(\vec{r})} d\vec{r} \quad (3.1)$$

where V is the volume of interest, and σ and ρ are respectively the electric conductivity and density of the tissue at each position \vec{r} . SAR is therefore expressed in units of power per mass; a typical choice for V is the volume corresponding to 10g of tissue, for local SAR calculation and mapping. Naturally, power deposition in living tissues, and therefore SAR, is closely linked to temperature increases. Although the dynamics of this relationship depend on various aspects such as tissue type and dimensions, as well as the effectiveness of physiological mechanisms of heat dissipation, computational simulations and animal studies have allowed for the evaluation and establishment of general guidelines for RF-induced SAR increases (Hirata et al., 2009). These guidelines determine the maximum SAR values allowed to be imposed on different human tissues, and are currently defined by International Electrotechnical Commission (IEC) standards; for MRI, these limits are described in IEC 60601-2-33 (2010). Together with EM

simulation results, these guidelines determine the maximum power that can be fed to a given RF coil for acquisitions on a given body region, which in turn will limit the RF pulse amplitude and duty cycle (which are then closely related to sequence parameters such as the flip angle and TR). These limits may or may not need to be adjusted in the presence of EEG components.

The present chapter reports on a series of EM simulations and phantom temperature measurements conducted to assess the presence of any potential safety concerns for simultaneous EEG-fMRI at 7 T, using the particular acquisition setup intended to be applied in future studies. Both a volume and a surface head RF coil were tested for MRI acquisition.

3.2 Methods

Safety tests comprised EM simulations with a realistic computational model and real temperature measurements performed on a phantom. To assess the validity of EM simulations, B_1^+ measurements were also performed on a human volunteer, with and without EEG.

3.2.1 EEG-(f)MRI acquisition setup

For both temperature and B_1^+ measurements, the EEG-(f)MRI acquisition system was set as similar as possible to the optimized setup intended to be used in future human studies. The MRI system consisted of an actively-shielded Magnetom 7 T head-only scanner (Siemens, Erlangen, Germany), equipped with an AC84 head gradient set (max. slew-rate 333 T/m/s) and using either a single-channel transmit/8-channel receive head loop array (Rapid Biomedical, Rimpf, Germany) or a single-channel quadrature transmit/receive occipital coil (home-built). EEG data were recorded using two 32-channel BrainAmp MR Plus amplifiers (Brain Products, Munich, Germany) and a customized BrainCap MR model (EasyCap, Herrsching, Germany) with 64 Ag/AgCl ring-type electrodes ("multitrodes"), arranged according to the international 10–20 system, and fitted with 5 k Ω resistors to limit induced currents. One of the 64 electrodes was placed on the back of the subject for electrocardiogram (ECG) recording. The two amplifiers rested on top of each other, close to the head, placed on the RF gateway box. In both phantom and human recordings, Abralyte gel (EasyCap) was used to reduce electrode impedances. A more detailed description of the setup, including modifications at the level of signal transmission, can be found in Chapter 5, section 5.3.

3.2.2 Electromagnetic simulations

EM simulations were performed to evaluate the impact of the custom EEG setup on B_1^+ and SAR distributions across the head. The measurement setup was simulated with the finite difference time domain (FDTD) package SEMCAD X (SPEAG, Zürich, Switzerland), using the realistic human meshed model Duke from the Virtual Family (Christ et al., 2010). For the RF coils, the copper strips of the loops were modeled as perfect electric conductors (PEC), with

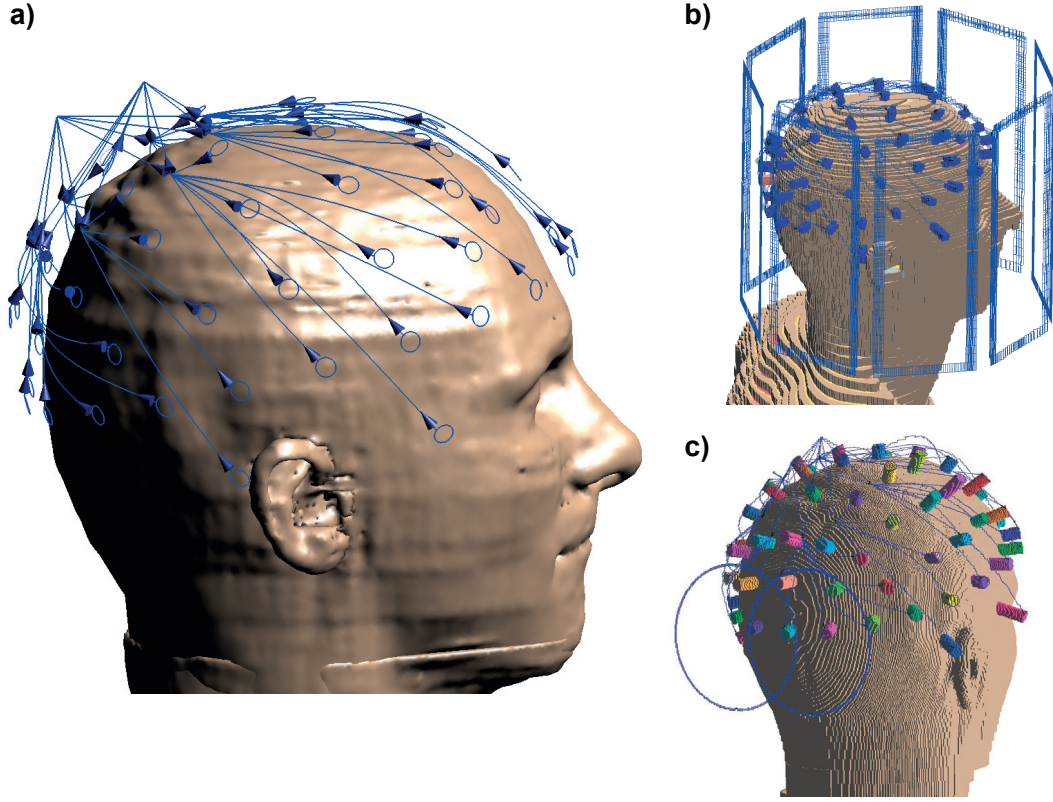


Figure 3.1: Computational models developed for EM simulations assessing the impact of an EEG cap on B_1^+ and SAR distributions, using either a volume or a surface head RF coil, at 7 T. **a)** Geometric model consisting of a realistic human head and a set of 66 ring electrodes, safety resistors and leads simulating the EEG cap used in this work; the wire branching was designed according to the real cap, terminating in two connectors close to the head; the electrolyte gel and head array are not displayed. **b),c)** Voxel mesh obtained with either coil from the full geometric model, including the electrolyte gel components.

capacitors and voltage sources inserted on each loop to ensure excitation of the circularly polarized mode. For the EEG cap, ring electrodes were designed as a set of 66 PEC loops, connected to PEC leads via $5\text{ k}\Omega$ resistors. The leads converged in 8 branches towards the 2 connectors, standing approximately 2 cm above the scalp. Wire branching and connector positions were modeled according to the real cap (Fig. 3.1a), with specific care to ensure that no wires/electrodes were in physical contact with each other or the skin. Contact with the scalp was modeled with small cylinders mimicking the Abralyte gel (Fig. 3.1b,c), with dielectric properties $\epsilon_r = 68$ and $\sigma = 4.7\text{ S/m}$, measured from a real gel sample using a dielectric probe (DAKS, SPEAG, Zürich, Switzerland).

The simulation model was meshed in a non-uniform grid of approximately 8 MCells, with voxeling steps ranging from $0.26 \times 0.40 \times 0.29\text{ mm}^3$ to $69 \times 78 \times 85\text{ mm}^3$, for the volume coil (Fig. 3.1b), and from $0.4 \times 0.2 \times 0.1\text{ mm}^3$ to $38 \times 50 \times 42\text{ mm}^3$ for the surface coil (Fig. 3.1c). A harmonic

excitation at 297.2 MHz was applied, and steady-state conditions were achieved within 30 periods of simulation time. Perfectly matched layers in medium strength were used at the edges of the FDTD domain. The B_1^+ and SAR maps obtained for each coil, with and without the cap, were normalized to a 1 W delivered power and then exported to Matlab (Mathworks, Natick MA, USA) to be resampled into a uniform grid.²

The B_1^+ maps obtained from a human volunteer for comparison with EM simulations were acquired with a SA2RAGE sequence (64 sagittal slices, $2.0 \times 2.5 \times 2.0 \text{ mm}^3$ resolution, TR/TE = 2400/1.4 ms, $TI_1/TI_2 = 65/1800$ ms, $\alpha_1/\alpha_2 = 4^\circ/11^\circ$) (Eggenschwiler et al., 2012). These tests were conducted after confirming adequate safety conditions with both EM simulations and temperature measurements on a phantom (described in the following section), and were approved by the institutional review board of the local ethics committee (Commission d'Éthique de la Recherche sur l'Être Humain du Canton de Vaud). The volunteer provided written informed consent prior to the acquisition.

3.2.3 Temperature measurements

Temperature monitoring was conducted on an agar gel phantom contained in a realistic head shape, which was covered with an Abralyte gel layer and fitted with the EEG cap. Measurements were performed using a 4-channel fiber optic temperature sensor (Neoptix, Québec, Canada). For both RF coils, two probes were placed on electrodes AF8 and FT9 (directly in the gel within the ring electrodes), one probe was placed in between the two EEG amplifiers, and another was suspended above the phantom, for reference. This choice of electrodes was motivated by the large loop area relative to \vec{B}_0 formed by channel FT9, and by the position of channel AF8, which was situated relatively close to a region of SAR increase predicted by the EM simulations for the volume coil (see section 3.3.1 for details). For the surface coil, a second measurement was also performed with probes placed on electrodes O1, P1 and FT9, and the fourth probe suspended above the phantom. This choice was motivated by the particular transmission profile of the surface coil, which is more focused in occipital head regions.

Temperature fluctuations were measured during 16 min-long sessions where two fMRI runs were applied sequentially, for 8 min each: a sinusoidal gradient-echo (GE) EPI sequence (25 slices, $1.5 \times 1.5 \times 1.5 \text{ mm}^3$ spatial resolution with 1.5 mm interslice gaps, TR/TE = 2000/25 ms, $\alpha = 78^\circ$, 69% of SAR limit), followed by a spin-echo (SE) EPI sequence (20 slices, $1.5 \times 1.5 \times 1.5 \text{ mm}^3$ spatial resolution, TR/TE = 5000/44 ms, $\alpha = 90^\circ$, 91% of SAR limit). For the volume coil tests, the slices were set with axial orientation, whereas a coronal orientation was employed with the surface coil. The two functional runs were separated by approximately 2 min, which included shimming and other adjustment procedures for the second run. The patient ventilation system, room and bore lights remained switched off at all times. No MRI acquisitions had been performed on the scanner for several hours prior to each session.

²The model discretization and EM simulation steps were performed by Dr. Özlem Ipek (email: ozlem.ipek@epfl.ch), who provided the resulting B_1^+ and SAR maps in matrix format, for further analysis.

3.3 Results

3.3.1 Electromagnetic simulations

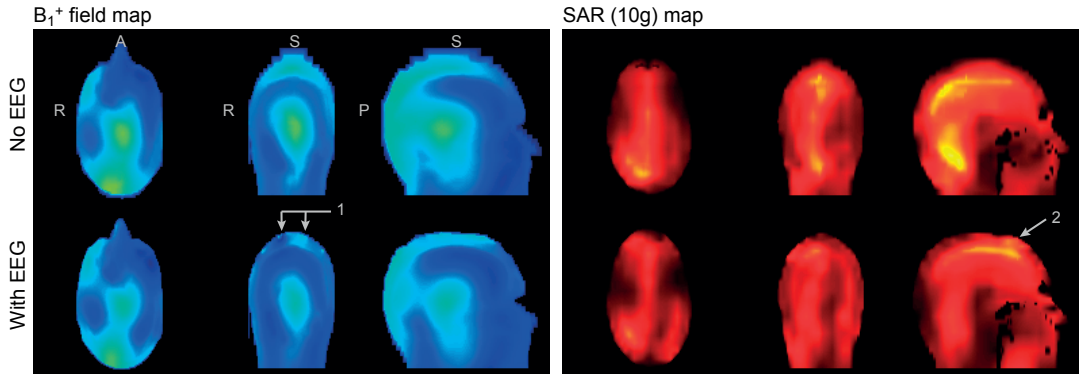
To assess the impact of the custom EEG cap on B_1^+ and SAR distributions across the head, EM simulations performed with and without the cap in place were compared (Fig. 3.2).

Volume RF coil: For the volume coil, the presence of the EEG materials led to a general loss in B_1^+ amplitude – approximately 8.0% over the head region. The general properties of the field distribution, with higher amplitude in the center and in occipital regions, were roughly maintained with the inclusion of the EEG cap. Nevertheless, a number of local, more accentuated effects were observed in superior regions, mostly restricted to the scalp, especially in the vicinity of EEG leads (Fig. 3.2, arrow 1). These local effects included both field decreases and increases, in some voxels up to $1.7\times$ the nominal flip angle. SAR maps (averaged over 10g of tissue) expressed similar trends, with the introduction of the EEG cap leading to an overall decrease of approximately 7.9% over the whole head. A few local increases could be observed in superior-anterior regions, close to the skin (Fig. 3.2, arrow 2), pushing the peak 10g-average SAR value from 0.39 W/Kg without EEG to 0.43 W/Kg with the cap (normalized to 1 W power).

Surface RF coil: With the surface coil, a general reduction in B_1^+ amplitude was also observed, albeit more moderate – approximately 4.5% over the occipital region. As observed for the volume array, the general properties of the field distribution obtained with the surface coil, with higher amplitude in occipital regions and a steady decay with the distance to the elements, were roughly maintained with the inclusion of the EEG cap. A subtle shift of the field distribution in the upward direction could be noticed, although no local increases were found; the peak amplitude actually decreased from 1.8 to $1.7\times$ the nominal flip angle with the introduction of the EEG cap. The estimated SAR distributions exhibited similar trends, with an overall decrease of approximately 4.9% over the head. A slight upward shift in power deposition could be observed (Fig. 3.2, arrow 3), albeit without any significant focal increases. The peak 10g-average SAR value was reduced from 0.72 W/Kg to 0.63 W/Kg with the EEG cap.

Validation: The validity of the EM simulations was assessed by comparing the estimated B_1^+ maps with real measurements performed on human subjects, with and without the EEG cap in place (Fig. 3.3). In general, the in vivo measurements exhibited similar field distributions to the simulated maps, with higher B_1^+ in the center and occipital regions for the volume array, or more concentrated in the occipital area for the surface coil. In the volume coil measurement, a 12.8% overall decrease in B_1^+ strength was observed upon introduction of the EEG cap. Local B_1^+ deviations occurring closer to the skin effectively differed in location and shape, but expressed similar intensity variations, with in vivo measurements showing decreases down to near-complete B_1^+ loss and increases up to approximately $1.8\times$ the nominal flip angle. With the surface coil, B_1^+ measurements showed an average amplitude reduction of 9.1% in the occipital region. Similar to the volume coil, local B_1^+ deviations occurring closer to the skin effectively differed in location and shape; a peak amplitude of $1.5\times$ the nominal flip angle was

Volume coil



Surface coil

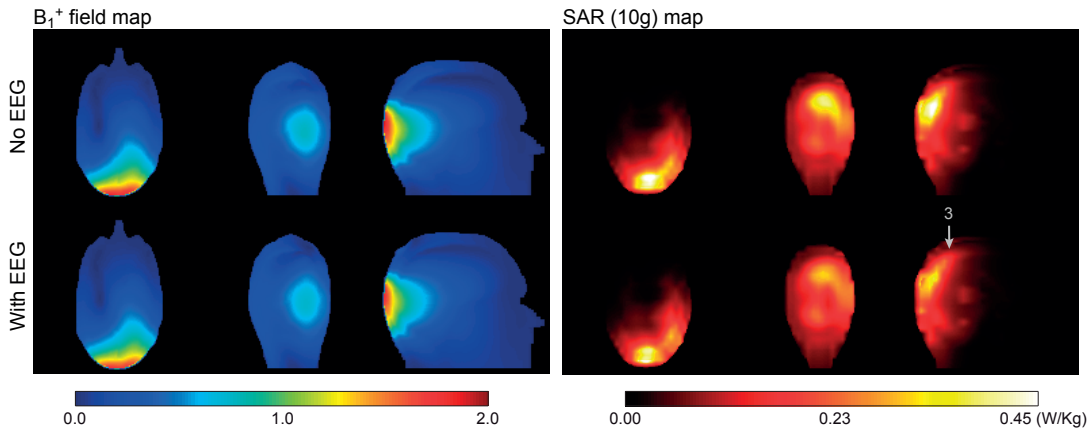


Figure 3.2: EM simulation results obtained with and without the EEG cap in place, using either a volume or a surface RF coil. The slices presented contain the most relevant differences between the two conditions. **Left:** B_1^+ field distribution, expressed as a fraction of the nominal flip angle; accentuated local field variations near the skin are indicated by arrow 1. **Right:** SAR distribution, expressed as the average value over 10 g of tissue; for the volume coil, a moderate increase in SAR in superior-anterior regions, near the scalp, is indicated by arrow 2; for the surface coil, arrow 3 indicates a subtle upward shift in the SAR distribution.

found both with and without EEG.

3.3.2 Temperature measurements

Complementary to EM simulations, local heating effects due to the EEG system were assessed by temperature monitoring on a phantom during a GE-EPI followed by a SE-EPI acquisition.

Volume RF coil: With the volume coil, during both 8 min runs, no significant temperature increases were found in any of the monitored locations apart from the EEG amplifiers (Fig. 3.4, top). In the reference probe suspended above the phantom, temperature increased from 19.7 to 20.0°C in the GE run and then up to 20.3°C during the SE run. The 2 probes placed on EEG

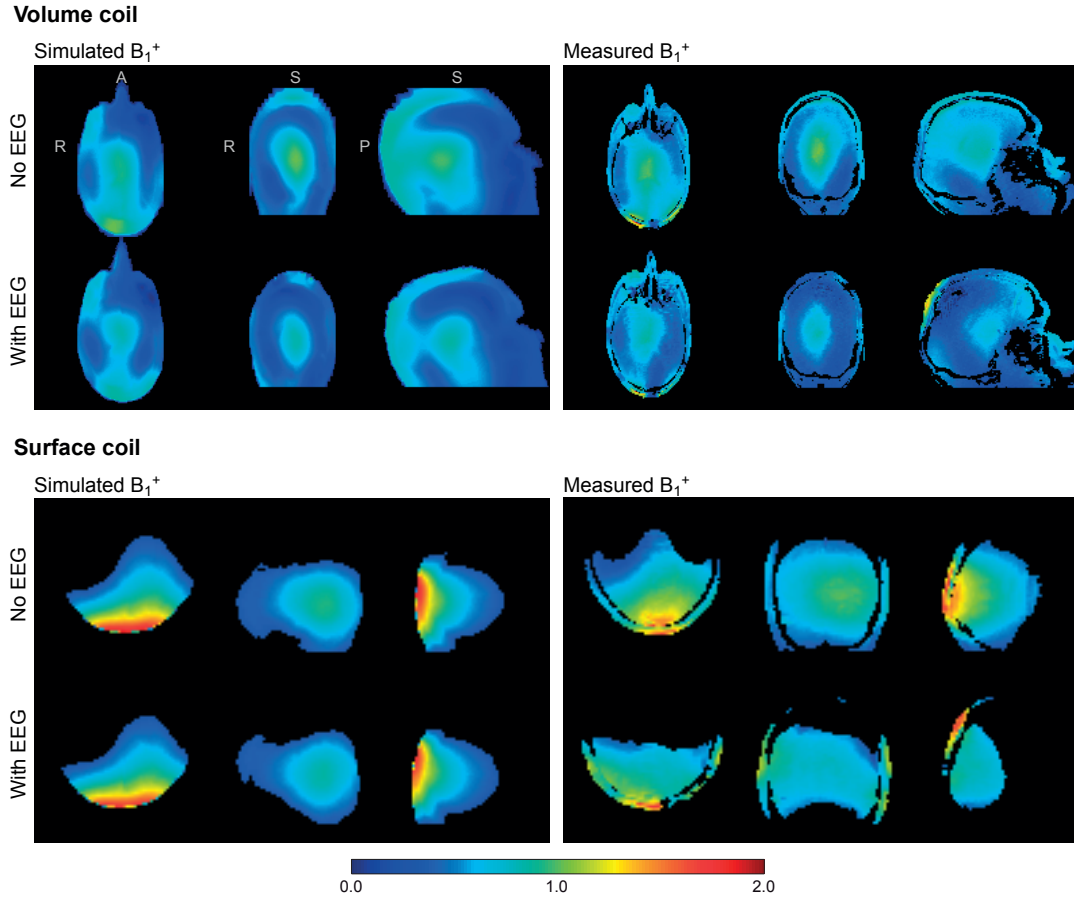


Figure 3.3: Comparison of B_1^+ field maps obtained from EM simulations, using a volume or a surface RF coil, with real measurements performed on human volunteers. The field distributions are expressed as a fraction of the nominal flip angle.

electrode sites exhibited similar trends, at slightly lower temperatures, with total increases below 1°C – on AF8, temperature rose from 18.2 to 18.7°C (GE) and then up to 19.1°C (SE); FT9 showed an increase from 17.8 to 18.1°C (GE) and then up to 18.4°C (SE). The sensor placed on the EEG amplifiers did measure stronger heating effects: from 21.4 to 25.8°C in the GE run, and then up to 27.9°C during the SE run.

Surface RF coil: Regarding the surface coil, in the first experiment, focused on the same locations as with the volume coil, similar trends were observed: the reference probe exhibited a temperature increase from 18.7 to 19.1°C in the GE run and then up to 19.3°C during the SE run. The 2 probes placed on EEG electrode sites remained at approximately 19.9°C (AF8) and 19.3°C (FT9) during both acquisition sequences, with fluctuations within a range of 0.2°C . Also as before, the sensor placed on the EEG amplifiers measured stronger heating effects: from 21.4 to 24.0°C in the GE run, and then up to 26.8°C during the SE run (Fig. 3.4, bottom).

In the second measurement performed with the surface coil, monitoring more occipital

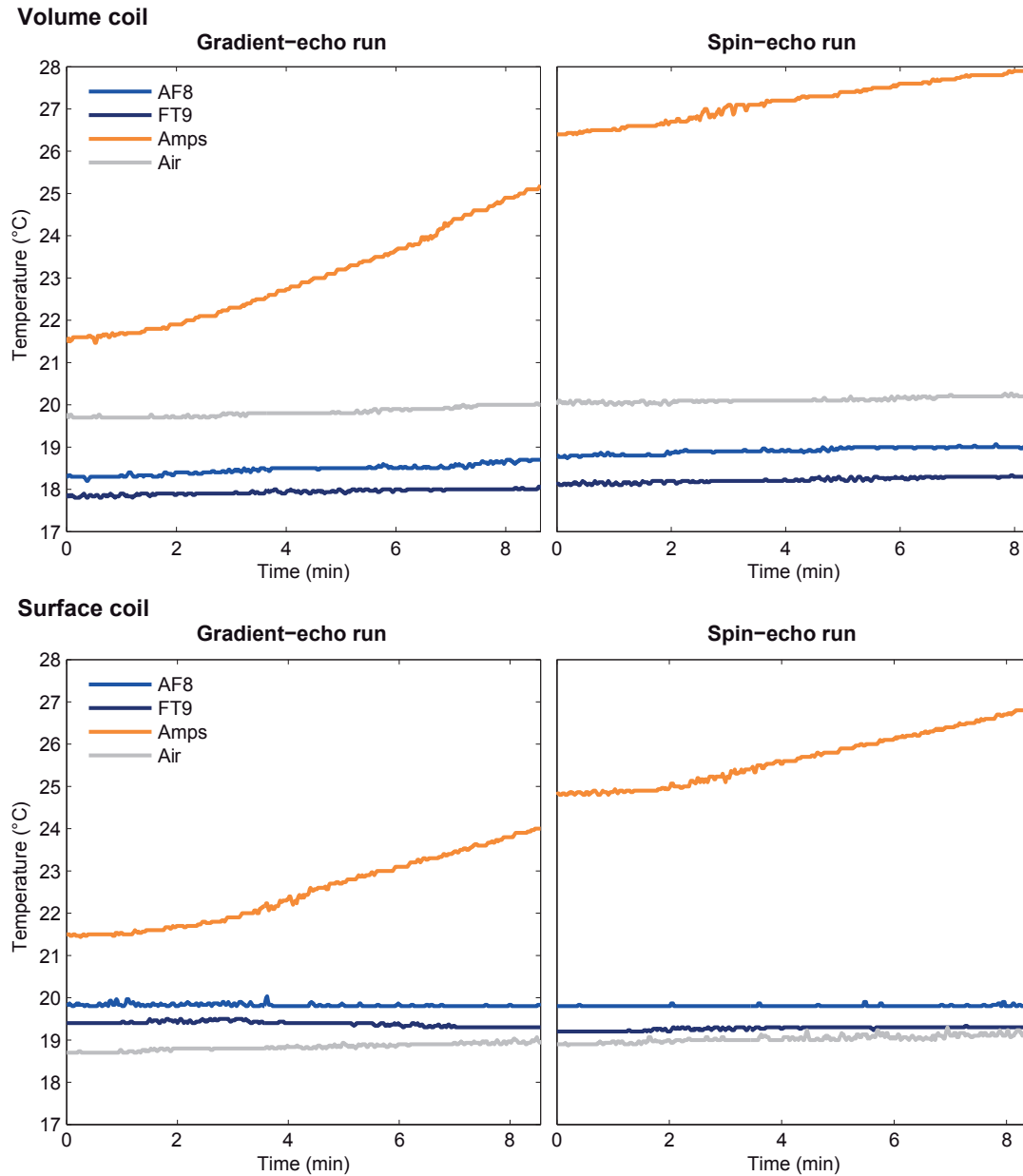


Figure 3.4: Temperature fluctuations during an 8 min-long GE-EPI acquisition followed by an 8 min-long SE-EPI run, using either a volume or a surface RF coil. The two runs were separated by approximately 2 min, which included shimming and adjustment procedures for the SE run. Temperature monitoring was performed in two cap electrodes (AF8 and FT9, blue), in between the two EEG amplifiers (orange), and suspended inside the bore above the phantom (grey).

electrodes, the reference probe remained at approximately 18.4°C, with fluctuations within a range of 0.2°C throughout both EPI runs. The probe placed at FT9 showed a fairly stable temperature value of approximately 17.1°C, with fluctuations in the range of 0.1°C. The probes

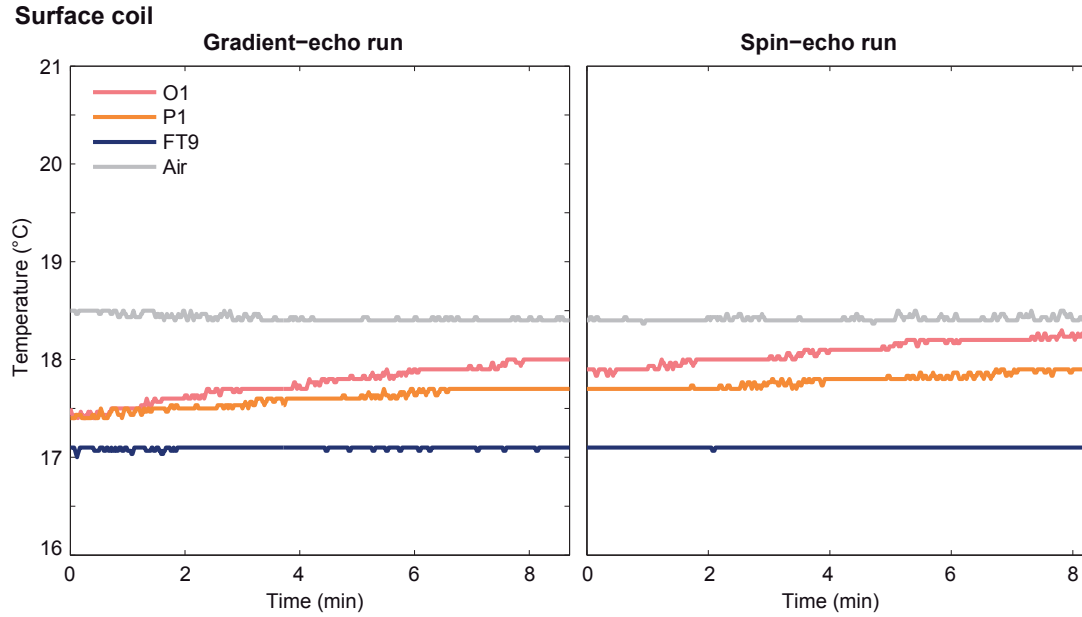


Figure 3.5: Temperature fluctuations during an 8 min-long GE-EPI acquisition followed by an 8 min-long SE-EPI run, using a surface RF coil. The two runs were separated by approximately 2 min, which included shimming and adjustment procedures for the SE run. Temperature monitoring was performed in three cap electrodes (O1 in red, P1 in orange, and FT9 in blue), and suspended inside the bore above the phantom (grey).

placed at P1 and O1 exhibited moderate, but steady temperature increases: both started at 17.4°C, then rose to 17.7°C (P1) and 18.0°C (O1) in the GE-EPI run, and finally to 17.9°C (P1) and 18.3°C (O1) in the SE-EPI run (Fig. 3.5).

3.4 Discussion

Given the interactions that can occur between EEG materials and RF waves (Lemieux et al., 1997), subject safety has always been a major point of concern with simultaneous EEG-fMRI (Laufs, 2012). While safety guidelines do exist, the pursuit of increasingly higher field strengths, higher EEG channel densities, and various custom modifications (coil designs, MR sequences), has continuously demanded site-specific safety assessments for setup validation. Temperature measurements in phantoms and humans have been extensively adopted for this purpose (Lemieux et al., 1997; Lazeyras et al., 2001; Mullinger et al., 2008a). While useful and practical, these tests are limited in spatial coverage, and cannot assess local SAR variations occurring in vivo within the brain. As a valuable complement, EM simulations using realistic head models allow for the estimation of high-resolution SAR distributions across the head, but only a small number of studies have presented results from such approaches (Angelone et al., 2004, 2006).

In this work, we relied on both EM simulations and surface temperature measurements for safety assessment, with neither approach raising significant concerns. In both tested RF

coils, the introduction of the EEG cap led to a small overall decrease in SAR, which is in fact contrasting with results from previous simulations conducted at 7 T, reporting overall increases around 32% (Angelone et al., 2006). This may be related to various differences existing between the two models, including electrode density, lead geometry, RF coil configuration, and the electromagnetic properties of the human model. In our particular implementation, for the volume coil, a number of areas exhibiting SAR increases did appear with the introduction of the EEG cap (Fig. 3.2, top), notably in skin/skull regions, but the overall range of the SAR distribution remained practically unaltered. It could be proposed that, in cases where peak SAR values are steadily reduced in the presence of EEG, the established hardware limits could be adjusted (increased), to counter B_1^+ losses with higher RF transmission power. In particular, this option could be considered for the surface coil tested in this work, where the peak SAR (as well as the average SAR) was reduced upon introducing the EEG system. Such adjustments could prove decisive for certain applications such as MR spectroscopy, where B_1^+ efficiency often plays a major role in acquisition. Nevertheless, given its crucial impact on subject safety, the modification of transmit power limits should only be considered in cases of absolute confidence regarding the effects of EEG on SAR.

The relevance and reliability of EM simulation results is, naturally, highly dependent on how accurately they model the characteristics of the real system. To assess this, the estimated B_1^+ distributions were compared to real measurements performed on a human volunteer. In general, the observed B_1^+ distributions were remarkably similar to those predicted by simulations, both before and after introduction of the EEG system. With EEG, general losses in B_1^+ amplitude were observed, as well as a number of more accentuated local effects, especially in more peripheral regions close to the skin (Fig. 3.3). Interestingly, for both coils, the average B_1^+ losses predicted by simulations (8.0% and 4.5% for the volume and surface coil, respectively) tended to underestimate the measurements obtained from this particular volunteer (12.8% and 9.1%). This may be better clarified in future work by collecting B_1^+ measurements with and without EEG from a larger number of subjects, along with simulations from a range of human head models (varying with age and gender, for example). Nevertheless, the high degree of similarity between simulations and measurements already observed in this work confirms that EM simulations can be a highly valuable tool for EEG-fMRI development, on the one hand for safety assessment, to predict SAR distributions as well as to guide the placement of temperature probes (as performed here with electrode AF8), and on the other hand to predict alterations in B_1^+ distribution. As will be further discussed in Chapter 4, B_1^+ disruption stands as the main contributor for MR image degradation in EEG-fMRI, and therefore, the ability to predict such effects for a given setup improvement, before its actual implementation, may prove highly useful for development and optimization purposes.

Regarding the temperature measurements, in all tests conducted with both RF coils, the fluctuations observed in EEG electrodes over the two 8-minute acquisitions were below 1°C, in good agreement with previous reports at 7 T (Angelone et al., 2006; Mullinger et al., 2008a). Although our measurements were conducted over a relatively short period, compared to a more common duration of approximately 1 hour for such sessions, the individual 8-minute

runs were comparable to typical fMRI runs, and there were no reasons to expect any significant changes in the observed trends for subsequent runs. As predicted by theoretical considerations and confirmed by EM simulations, the B_1^+ and SAR fields created by the surface coil were both concentrated in the occipital region, closest to the coil itself. Consistent with this, temperature measurements exhibited progressively stronger increases in the electrodes closest to this region (P1, then O1), while farther electrodes such as FT9 and AF8 remained practically unperturbed (Fig. 3.4, 3.5). In contrast, using the volume coil, both AF8 and FT9 exhibited steadier, albeit moderate, temperature increases during the EPI acquisitions. This is likely due to the more widely-distributed energy deposition created by this coil (Fig. 3.2, top).

The EEG amplifiers did experience considerably larger temperature increases than the electrodes (6.5°C with the volume coil and 5.4°C with the surface coil, over 16 min of EPI acquisition), although it was not possible to conclude how much of this heating was propagated from the RF gateway box (on which the amplifiers were standing and which by itself warms up during operation), or truly related to MR gradient or RF pulse effects. The slightly lower temperature increase observed with the surface coil could indeed suggest a contribution from RF transmission, since the volume coil can excite a considerably larger FOV than the surface coil, which is more restricted to occipital areas, and thereby may impose a larger energy deposition on the nearby amplifiers. Nevertheless, as each coil has a different RF gateway box, differences in this component could likewise play a role in the different heating trends observed. In any case, despite these increases, the observed values were still well within the normal operating range of the amplifiers (10–40°C), thus raising no cause for concern.

3.4.1 Conclusion

In conclusion, under the conditions of typical functional acquisitions, the temperature measurements and EM simulations conducted in this study showed no significant safety concerns for this particular EEG-fMRI setup, using either a volume or a surface head RF coil. The EM simulations proved valuable to predict the impact of these acquisition setups on B_1^+ and SAR distributions, and may become a useful tool to aid the design and optimization of future setup developments.

4 EEG-fMRI at 7T: MRI data quality

The presence of EEG components and materials in the MRI scanner can create important deleterious effects that result in **image quality** degradation and reductions in **functional sensitivity**. This chapter describes an extensive characterization of EEG-induced MRI data artifacts, for the particular setup implemented in this thesis, at 7 T. Functional sensitivity was assessed based on human fMRI acquisitions, performed with and without the EEG system in place. Image quality was characterized in both functional and anatomical images, and the underlying mechanisms of degradation were investigated via \vec{B}_0 and \vec{B}_1^+ field mapping. Overall, both functional and anatomical images exhibited general losses in spatial SNR, of approximately 37% and 29%, respectively. In fMRI data, white matter temporal SNR exhibited a more moderate loss of $23 \pm 6\%$ across subjects. \vec{B}_0 inhomogeneities introduced by the EEG system were in general limited to extra-cerebral tissue, with the distribution in the brain remaining comparable to the no-EEG situation. In contrast, \vec{B}_1^+ maps evinced a general loss of 12.8% in amplitude over the whole head, along with a number of more accentuated local effects, particularly at superior regions, coinciding with areas of more focal SNR loss. Hence, these results point towards **RF pulse disruption** as the major degradation mechanism affecting MRI data acquired simultaneously with EEG.

4.1 Introduction

In addition to safety concerns, simultaneous recordings from both EEG and fMRI can be affected by severe artifacts, many of which are field strength-dependent. On the fMRI side, the presence of EEG components and materials can lead to MR image degradation through two distinct mechanisms: magnetic susceptibility effects, and RF field disruption.

Magnetic susceptibility effects can arise due to differences in magnetic susceptibility between the head tissues and the added EEG components, including the leads, safety resistors, elec-

Parts of this chapter were adapted from:

Simultaneous EEG-fMRI at ultra-high field: artifact prevention and safety assessment, J. Jorge, E. Grouiller, Ö. Ipek, R. Stoermer, C. M. Michel, P. Figueiredo, W. van der Zwaag, R. Gruetter, 2015, Neuroimage 105, p.132–144.

trodes and electrolyte gel. When placed in \vec{B}_0 , a material with a certain magnetic susceptibility χ will cause a disturbance in the field of the order of $\chi|\vec{B}_0|$. Consequently, when materials with different susceptibilities are brought together, inhomogeneities arise in the resulting static field, with most pronounced field gradients at the boundary between the materials. These inhomogeneities can have an important impact on image properties: on the one hand, T_2^* relaxation effects are accentuated on spins traveling through the field inhomogeneities, leading to increased signal loss in these areas; on the other hand, if the variations in Larmor frequency become similar in size to the frequency separation of voxels in the image, these can interfere with the spatial encoding scheme, originating geometric distortions in the acquired image (Jezzard et al., 2001). These effects are particularly problematic for EPI sequences, which typically have a low bandwidth in the phase encoding direction. Even without EEG hardware, air-tissue boundary regions such as in the nasal cavity are usually strongly affected by signal loss and distortions. Likewise, the introduction of EEG materials has been observed to introduce localized signal drops (Krakow et al., 2000; Mullinger et al., 2008b).

\vec{B}_1 field disruption or shielding effects can be introduced due to the presence of EEG components between the RF coil and the head. When submitted to RF fields, the electrically-conductive EEG materials will promptly generate surface currents to screen the fields from their interior volume, creating field distortions that extend to nearby regions. The resulting \vec{B}_1 field inhomogeneities, already introduced in the previous chapter in the context of subject safety, can likewise become an important degradation mechanism for the acquired images, since both transmit and receive fields are affected. The resulting effects typically arise as SNR losses, more accentuated in regions closer to the EEG components. Additionally, the power lost in the interactions between the RF coil and the conductive EEG materials increases the effective resistance of the RF coil, acting as a source of additional noise, and thereby also leading to a global reduction in image SNR (Scarff et al., 2004; Mullinger et al., 2008b).

MRI data degradation effects during concurrent EEG recordings have been frequently observed in previous methodological studies. A number of improvements to mitigate these effects have been proposed, essentially through the use of certain alternative materials for the EEG wires and electrodes, such as conductive ink (Vasios et al., 2006) or carbon (Negishi et al., 2008). Fortunately, with modern EEG systems, even the more conventional silver- or copper-based components have actually been found to have an acceptable impact on fMRI data quality at fields up to 3 T (Bonmassar et al., 2001; Lazeyras et al., 2001). It has further been proposed that functional sensitivity in fMRI is relatively well-preserved, since with any loss in image SNR, physiological noise is also reduced (because it scales with image signal (Kruger et al., 2001)), resulting in a more moderate reduction in temporal SNR (Luo and Glover, 2012). Nevertheless, the acceptable reductions observed at lower fields may become considerably more compromising as higher field strengths are pursued. Both magnetic susceptibility and RF disruption effects are expected to worsen with field strength, and this trend has been experimentally confirmed (Mullinger et al., 2008b). The report of Mullinger et al., covering field strengths up to 7 T, is currently the only comprehensive assessment of fMRI data degradation effects due to EEG available in the literature (Mullinger et al., 2008b). As such, additional

studies of these effects at other centers, with particular differences in magnet characteristics, gradients, RF coils and EEG setup, may prove valuable to complement the currently-limited existing literature, especially at ultra-high field, and consolidate previous observations.

This chapter presents an extensive characterization of MRI data artifacts induced by EEG components, for the particular setup implemented in this thesis, at 7 T. To evaluate changes in functional sensitivity, GE-EPI data were acquired from a group of healthy volunteers with concurrent EEG recording, and from a similar group without EEG. Additionally, from the first group, one of the volunteers was scanned both with and without the EEG system in place. For this subject, changes in data quality were assessed in both functional and anatomical images, and the underlying mechanisms were investigated via \vec{B}_0 and \vec{B}_1^+ field mapping.

4.2 Methods

A total of 9 human volunteers (20 ± 2 years old) participated in this study, 5 of which underwent concurrent EEG-fMRI acquisitions, whereas 4 were only subjected to fMRI. The study was approved by the institutional review board of the local ethics committee (Commission d'Éthique de la Recherche sur l'Être Humain du Canton de Vaud), and all volunteers provided written informed consent.

4.2.1 MRI data acquisition

MRI data were acquired both with and without concurrent EEG recording, using the setup previously introduced in Chapter 3, section 3.2.1, and further detailed in Chapter 5, section 5.3. When present, the EEG setup was kept operating similarly to a normal recording. For the fMRI acquisitions, a GE-EPI sequence was used (25 axial slices, $1.5 \times 1.5 \times 1.5 \text{ mm}^3$ spatial resolution with 1.5 mm interslice gaps, $\text{TR}/\text{TE} = 2000/25 \text{ ms}$, $\alpha = 78^\circ$, sinusoidal readout). A timecourse of 120 volumes were acquired from each subject, corresponding to a duration of 4 minutes. Subjects were asked to simply lie still throughout the acquisition.

One subject was scanned with and without the EEG setup in place. For both cases, a set of four MRI sequences was applied: a single GE-EPI volume (same parameters as described above), a gradient-recalled echo (GRE) anatomical image (176 sagittal slices, $1.0 \times 1.0 \times 1.0 \text{ mm}^3$ spatial resolution, $\text{TR}/\text{TE} = 6.5/2.8 \text{ ms}$, $\alpha = 4^\circ$), a GRE-based \vec{B}_0 field map (30 slices, $3.0 \times 3.0 \times 3.0 \text{ mm}^3$ resolution, $\text{TR}/\text{TE}_1/\text{TE}_2 = 1050/4/5 \text{ ms}$, $\alpha = 40^\circ$), and a SA2RAGE image (64 sagittal slices, $2.0 \times 2.5 \times 2.0 \text{ mm}^3$ resolution, $\text{TR}/\text{TE} = 2400/1.4 \text{ ms}$, $\text{TI}_1/\text{TI}_2 = 65/1800 \text{ ms}$, $\alpha_1/\alpha_2 = 4^\circ/11^\circ$) for \vec{B}_1^+ field mapping (Eggenchwiler et al., 2012).

4.2.2 MRI data analysis

Data quality assessment and comparison were performed through direct visual inspection, and additionally, for functional and anatomical images, through the estimation of SNR losses.

Spatial SNR: Spatial, or image SNR, was estimated as the mean amplitude in a specific region within the head divided by the standard deviation of signal amplitudes outside the head (avoiding areas potentially affected by Nyquist ghosting). Two head regions were considered: one comprising more inferior areas not visibly affected by accentuated signal drops, for a general measure of SNR loss, and another comprising more superior regions affected by pronounced signal losses.

Temporal SNR: Given the importance of temporal, rather than spatial SNR for fMRI (Luo and Glover, 2012), temporal SNR values were estimated from the EPI timecourses acquired from the two subject groups. For each run, temporal SNR was calculated for each voxel as the mean timecourse amplitude divided by the timecourse standard deviation, and then averaged within a frontal white matter region ($7 \times 7 \times 7$ voxels) not affected by accentuated signal loss. All estimated spatial and temporal SNR values were above 10, and therefore a compensation for the Rician distribution of the noise was not necessary (Triantafyllou et al., 2005). The effect of GRAPPA acceleration on background noise was present, but similar on both conditions.

4.3 Results

The impact of the EEG system on MRI data quality was assessed in functional and anatomical images acquired with and without the EEG system, and its underlying mechanisms were investigated via \vec{B}_0 and \vec{B}_1^+ mapping.

SNR: In the single-subject dataset, both functional (GE-EPI) and anatomical (GRE) images exhibited general losses in spatial SNR of approximately 37% and 29%, respectively. Central-superior regions were particularly affected (arrows 1–2 in Fig. 4.1), with SNR losses rising to 62% (functional) and 44% (anatomical) in the top-most axial slices. In the group acquisitions, similar degradation effects could be observed when comparing with-EEG and without-EEG EPI images, with both general losses in SNR and more accentuated losses in central-superior regions (Fig. 4.2). On average across subjects, white matter temporal SNR values decreased from 22 ± 1 in fMRI-only runs to 17 ± 1 in EEG-fMRI runs, corresponding to an average loss of $23 \pm 6\%$.

Field mapping: in the single-subject dataset, with the EEG system in place, the \vec{B}_0 distribution did evince a number of local inhomogeneities along the scalp (arrow 3 in Fig. 4.1), likely corresponding to individual electrodes and gel. However, these inhomogeneities were in general limited to extra-cerebral tissue, whereas in the brain the \vec{B}_0 distribution remained comparable to the no-EEG situation. This is in agreement with the observation that no geometric deformations were found in GE-EPI or GRE images with the introduction of the EEG cap. In contrast, \vec{B}_1^+ maps evinced clear differences between the two conditions, including both a general 12.8% loss in amplitude over the whole head and a number of more accentuated local effects (arrow 4 in Fig. 4.1), as predicted by previous EM simulations (Chapter 3). Relevant increases were mainly located outside the brain, while accentuated local decreases could also be seen in deeper regions.

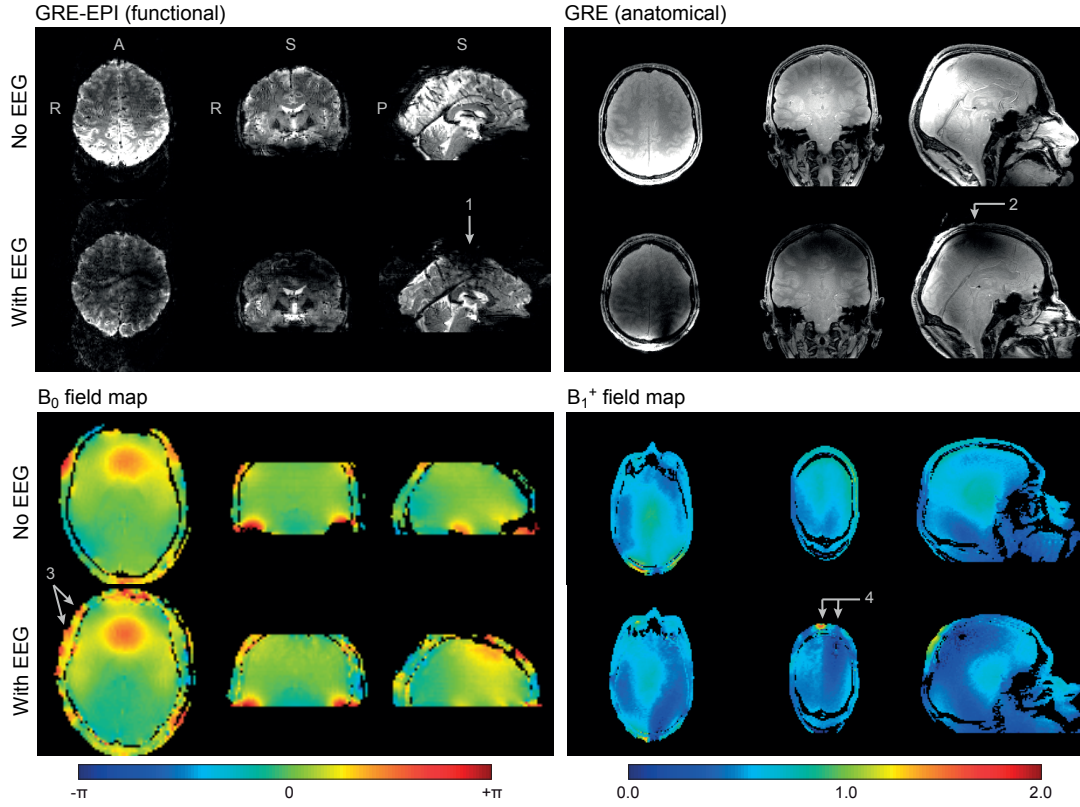


Figure 4.1: MRI data quality in a human subject scanned without (1st and 3rd rows) and with the EEG cap (2nd and 4th rows). The slices presented contain the most relevant differences between the two conditions. **Top-left:** GE-EPI image acquired with similar parameters to the functional runs (although with larger coverage). **Top-right:** GRE-based anatomical image. Arrows 1 and 2 indicate accentuated local signal drops. In both functional and anatomical images, the intensity scale is kept fixed between no-EEG and with-EEG conditions. **Bottom-left:** \vec{B}_0 field distribution, expressed as the phase shift relative to the nominal precession; local phase shifts appearing along the skin are indicated by arrow 3. **Bottom-right:** \vec{B}_1^+ field distribution, expressed as a fraction of the nominal flip angle; accentuated local field variations are indicated by arrow 4. Both \vec{B}_0 and \vec{B}_1^+ field maps here shown were masked to remove background regions in which there was no MR signal.

4.4 Discussion

The functional (GE-EPI) and anatomical (GRE) images acquired for data quality assessment (Fig. 4.2, 4.1) evinced artifacts caused by the introduction of the EEG system, notably an overall loss in spatial SNR and a few accentuated drops localized in superior regions. Temporal SNR losses were comparable to previous estimates at 7 T using a more standard EEG setup (Mullinger et al., 2008b), although here performed at a higher spatial resolution. Importantly, although significant, the losses observed in temporal SNR were considerably less severe than in spatial SNR, in good agreement with previous theoretical and experimental work (Luo and Glover, 2012). BOLD functional sensitivity is determined by its contrast-to-noise ratio, which

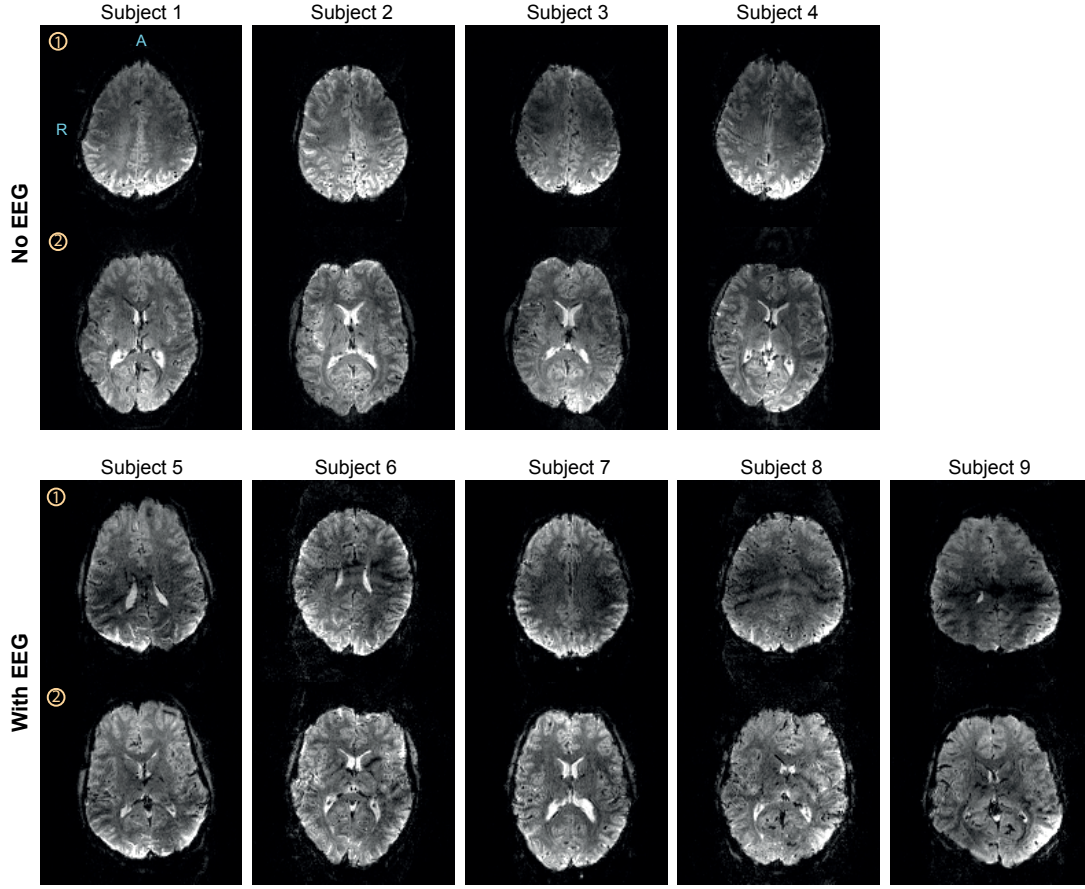


Figure 4.2: fMRI data quality in a group of subjects scanned either without (top) or with the EEG system in place (bottom). Two slices are shown per subject: a more inferior slice without focal SNR losses (2), and a superior slice with more pronounced focal losses (1). The slices shown were taken from the middle volume of each 4D dataset; image intensities were scaled from 0 to the 99th percentile of voxel intensities across the volume. Subject 6 is the subject who underwent additional field mapping and anatomical acquisitions, with and without EEG.

is in turn directly modulated by its temporal SNR (Luo and Glover, 2012, Eq. 1); therefore, the observed effects on temporal, compared to spatial SNR, indicate that functional sensitivity is in fact less affected by the introduction of EEG equipment than anatomical MR signals per se.

Also in agreement with previous studies (Bonmassar et al., 2001; Lazeyras et al., 2001; Mullinger et al., 2008b), the \vec{B}_0 maps exhibited local susceptibility artifacts along the skin, likely coinciding with EEG electrodes, but focal enough not to extend into actual brain regions, which remained largely unaffected in terms of \vec{B}_0 homogeneity. \vec{B}_1^+ maps, on the other hand, displayed clear alterations both globally and in specific regions, which were largely coincident with the more accentuated local SNR drops observed in functional and anatomical images. It is important to note that the central-superior regions where these stronger losses were observed lie essentially below a region of the cap where most EEG leads converge to a single

bundle, before leaving the cap surface (see Fig. 5.2c in Chapter 5). This area will thus contain a particularly high density of conductive material. Although it is hard to develop a consistent intuition for the effects of RF field disruption, and to confirm a causal relationship between the cap geometry and the observed artifacts, it is fairly likely that the two aspects may be strongly related. In fact, these local degradation effects had also been observed, with considerable similarity, in the EM simulations performed in Chapter 3, which employed a realistic model of the EEG cap geometry. Such simulations could thus present a useful platform to test and optimize novel EEG lead geometries, which may be able to minimize the observed local effects, or alternatively shift them towards other regions, according to specific research interests.

4.4.1 Conclusion

Overall, the results obtained in this study strengthen the growing view that the properties of modern EEG caps have managed to limit susceptibility artifacts to a satisfactory level, even at ultra-high field (Krakow et al., 2000; Lazeyras et al., 2001). RF pulse disruption, in contrast, stands as an important degradation effect that can significantly reduce the available SNR, as well as compromise the performance of brain segmentation and other image processing steps (Mullinger et al., 2008b). \vec{B}_1^+ inhomogeneity is already by itself a topic of intense research in ultra-high field MRI (Eggenschwiler et al., 2012). Aided by dedicated setup improvements, such as novel electrode and lead materials (Vasios et al., 2006), it is likely that EEG-related \vec{B}_1^+ degradation can be satisfactorily reduced in the future.

5 EEG-fMRI at 7T: EEG data quality

The deleterious interactions occurring between EEG and fMRI during simultaneous acquisitions can create important artifacts in the recordings of both modalities, most of which increase with \vec{B}_0 field strength. In particular, the artifacts induced on EEG recordings can surpass the signals of interest by several orders of magnitude and severely compromise data quality, especially at 7 T. For this reason, EEG artifact characterization and reduction has become a fundamental aspect of EEG-fMRI studies, and accordingly comprises the largest part of this thesis. The work here described was mainly focused on two aspects: signal transmission from the EEG cap to the amplifiers, and artifacts due to head motion in \vec{B}_0 .

In the first study, the **signal transmission** stage between the EEG cap and amplifiers was studied and optimized, so as to minimize artifact contamination at this level of the setup. The effects of EEG cable length and geometry for signal transmission were assessed in a phantom model, with specific attention to noise contributions from the MR scanner coldheads. Cable shortening (down to 12 cm from cap to amplifiers) and bundling effectively reduced environment noise by up to 84% in average power and 91% in inter-channel power variability. With the optimized setup, simultaneous EEG-fMRI acquisitions were performed on healthy volunteers undergoing two visual paradigms: an eyes-open/eyes-closed task, and a VEP paradigm using reversing-checkerboard stimulation. EEG data exhibited clear occipital alpha modulation and average VEPs, respectively, with concomitant BOLD signal changes. On a single-trial level, alpha power variations could be observed with relative confidence on all trials; VEP detection was more limited, although statistically significant responses could be detected in more than 50% of trials for every subject.

In the second study, a novel approach for **head motion** artifact detection was developed and integrated in the optimized EEG setup. This approach is based on a simple modification of

Parts of this chapter were adapted from:

Simultaneous EEG-fMRI at ultra-high field: artifact prevention and safety assessment, J. Jorge, F. Grouiller, Ö. Ipek, R. Stoermer, C. M. Michel, P. Figueiredo, W. van der Zwaag, R. Gruetter, 2015, Neuroimage 105, p.132–144.

Towards high-quality simultaneous EEG-fMRI at 7 T: Detection and reduction of EEG artifacts due to head motion, J. Jorge, F. Grouiller, R. Gruetter, W. van der Zwaag, P. Figueiredo, 2015, Neuroimage 120, p.143–153.

the EEG cap, in which four electrodes are non-permanently adapted to record only magnetic induction effects. EEG-fMRI data were acquired with this setup, at 7 T, from healthy volunteers undergoing a reversing-checkerboard visual stimulation paradigm. Data analysis assisted by the motion sensors revealed that, after gradient artifact correction, EEG signal variance was largely dominated by pulse artifacts (81–93%), but contributions from spontaneous motion (4–13%) were still comparable to or even larger than those of actual neuronal activity (3–9%). Multiple approaches were tested to determine the most effective procedure for denoising EEG data incorporating motion sensor information. Optimal results were obtained by applying an initial pulse artifact correction step (AAS-based), followed by motion artifact correction (based on the motion sensors) and ICA denoising. On average, motion artifact correction (after AAS) yielded a 61% reduction in signal power and a 62% increase in VEP trial-by-trial consistency. Combined with ICA, these improvements rose to a 74% power reduction and an 86% increase in trial consistency. Overall, the improvements achieved were well appreciable at single-subject and single-trial levels, and set encouraging perspectives for simultaneous EEG-fMRI at ultra-high field.

5.1 Introduction

Simultaneous EEG-fMRI acquisitions at ultra-high field suffer from various undesirable interactions that can degrade data quality and potentially compromise subject safety (Dempsey et al., 2001; Neuner et al., 2014). Safety concerns have been effectively moderated through a number of modifications in hardware and acquisition guidelines (Lemieux et al., 1997; Noth et al., 2012), and acquisitions thereafter have been confirmed safe, even at 7 T (as discussed in Chapter 3). Moreover, as observed and discussed in Chapter 4, although EEG components can reduce the SNR of MR images, numerous studies have found that losses in temporal SNR remain acceptable for fMRI, even at ultra-high field strengths with fairly high electrode densities (Mullinger et al., 2008b; Luo and Glover, 2012). In contrast, the artifacts induced in EEG recordings by the magnetic fields used in fMRI can surpass the signals of interest by several orders of magnitude, and severely compromise data quality (Allen et al., 2000; Debener et al., 2008). This is currently the most limiting obstacle for high-quality EEG-fMRI acquisitions, particularly at higher field strengths such as 7 T.

5.1.1 Gradient and pulse artifacts

EEG artifacts are mainly created by electromagnetic induction in the loops formed by the EEG leads and the head, which occurs whenever the existing magnetic field changes in time, or when loop geometry is changed relative to the field (Yan et al., 2009). The strongest contributions are generally due to the fast-switching **gradient fields** applied for image encoding (Allen et al., 2000). **Cardiac activity** can also cause large artifacts through various mechanisms, including bulk head motion prompted by the arrival of the ejected blood, scalp expansion due to arterial pulsation, and Hall effects occurring in the moving blood – altogether known as

pulse artifacts, or "ballistocardiogram" artifacts (Yan et al., 2010; Mullinger et al., 2013a).

Given their importance, a considerable amount of work has been dedicated to the study of gradient and pulse artifacts, and the development of strategies for their minimization (Mullinger and Bowtell, 2011). The inherent reproducibility of gradient artifacts across volumes and slices renders them suitable for correction based on **average artifact subtraction** (AAS) (Allen et al., 2000), guided by image acquisition triggers obtained from the scanner, and possibly complemented with **optimal basis set** (OBS) methods (Niazy et al., 2005). AAS corrects each artifact instance (an fMRI volume or slice) by subtracting a template created from the average of its N closest neighboring instances. The underlying assumption of this approach is that the morphology of artifact instances varies slowly with time, and thereby local averaging should provide an adequate template for correction of each instance. OBS can be considered an extension of the AAS approach, which aims to correct each artifact by fitting a linear model composed not only of the average artifact template, but also of the M most important principal components extracted from a population of artifact instances (typically from the whole timecourse), through principal component analysis (PCA). OBS can, in principle, overcome more complex variability patterns across artifact instances than AAS; on the other hand, its higher flexibility may also result in overfitting effects.

Cardiac activity is also cyclic in nature, which has motivated a widespread use of AAS and OBS-based approaches for pulse artifact correction, in this case guided by triggers from a separate cardiac trace such as the ECG (Allen et al., 1998; Niazy et al., 2005). Naturally, the variability of pulse artifacts across time is considerably higher than that of gradient artifacts, making its correction more challenging, which has motivated the development of various other correction techniques. **ICA**, for instance, has often been explored to separate the data into true EEG components and pulse artifact-related components, following specific selection criteria (Srivastava et al., 2005; Liu et al., 2012). The two types of components (pulse and non pulse-related) are expected to be statistically independent from each other, and thus suitable for ICA decomposition. On the other hand, this approach must be considered with some caution, since ICA requires that the underlying components to be separated have stationary spatial distributions, whereas the pulse artifact is, in fact, known to be non-stationary in its scalp topography, especially at higher field strengths, thereby violating this assumption and potentially leading to ineffective decompositions (Debener et al., 2008).

5.1.2 Environment noise

Given their dependence on Faraday's law of induction, many EEG artifact contributions scale with the amplitude of \vec{B}_0 . The pulse artifact has been shown to increase with field strength, not only in amplitude but also in spatial variability (Debener et al., 2008). Gradient artifacts depend more directly on the specified slew-rates than on \vec{B}_0 itself, but since spatial resolution is typically higher, slew-rates tend to be pushed as well to quickly achieve the necessary gradient strengths. Furthermore, besides gradient and pulse contributions, other previously

less relevant artifact sources can also attain important roles in data degradation at 7 T. These include **mechanical vibrations** propagated from the scanner environment, particularly due to the He compression systems (Mullinger et al., 2008a) and patient ventilation (Nierhaus et al., 2013). Compared to gradient and pulse artifacts, considerably less work has been devoted to these contributions.

Vibration-induced noise can be avoided by switching off the associated sources during acquisition, when possible (Mullinger et al., 2008a; Nierhaus et al., 2013). The periodic structure of He coldhead contributions, in particular, has motivated a few novel data-based correction approaches as well (Rothlubbers et al., 2013; Kim et al., 2014). While EEG noise correction algorithms are currently indispensable, reducing noise contributions during acquisition is undoubtedly the most desirable way to improve data quality, especially at ultra-high field. This can be done, for instance, by reducing the total areas formed by electrode leads between each channel and the reference, thereby reducing magnetic induction effects. Accordingly, in the first study within this chapter, the importance of EEG cable length and geometry on noise sensitivity was assessed, at the level of transmission between the cap and amplifiers. The benefits of shorter signal chains have previously been observed at lower fields (Assecon-di et al., 2013), as has the importance of cable geometry (Chowdhury et al., 2012). Here, on a phantom model, the effects of different cable lengths and geometries on EEG recordings were for the first time assessed together, at 7 T, with specific attention given to He coldhead contributions. An optimized EEG setup with ultra-short bundled cables (approximately 12 cm from cap to amplifiers) was implemented (Fig. 5.1), and employed for simultaneous EEG-fMRI acquisitions on healthy volunteers under two visual paradigms: an eyes-open/eyes-closed task and a VEP run using reversing-checkerboard stimulation.

5.1.3 Head motion artifacts

Besides environment noise, **spontaneous head motion** in \vec{B}_0 can likewise become highly problematic at higher field strengths, with visible artifact contributions even for experienced, steady subjects, and very limiting data degradation for less compliant subjects. In contrast with He coldhead contributions, spontaneous head motion is highly unpredictable, and while periods of large movement can often be identified by visual inspection and excluded, more subtle and widespread contributions can prove very hard to discern from true EEG patterns, even on simplified data decompositions such as those given by ICA (Debener et al., 2007; Arrubla et al., 2013). To address this challenge, a few groups have instead explored the use of dedicated motion sensors, recorded along with EEG-fMRI, which can be used to estimate and remove motion artifacts from the EEG data (Hill et al., 1995). At 1.5 T, Bonmassar et al. used a piezoelectric transducer to record motion information, and applied an adaptive denoising technique based on Kalman filtering to reduce both spontaneous motion and the motion-related component of the pulse artifact (Bonmassar et al., 2002). In a later study at 3 T, Masterton et al. (2007) proposed the use of multiple sensors based on carbon **wire loops**, distributed over the EEG cap and sensitive to magnetic induction effects (Masterton

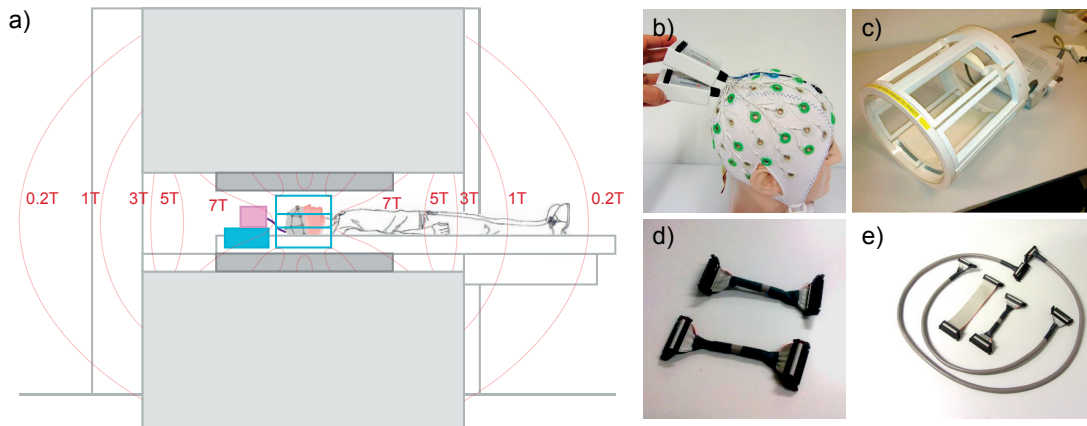


Figure 5.1: The custom EEG-fMRI setup developed in this work. **a)** A schematic representation of the custom setup, including the 7 T magnet (light grey), static field distribution (red), gradient system (dark grey), custom EEG cap (grey, shown in detail in **b)**), short bundled cables (purple, shown in detail in **d)**), RF coil and gateway box (blue, shown in detail in **c)**), and EEG amplifiers (pink). **e)** Examples of the ribbon cable configurations tested for noise sensitivity in the first study, which included three different lengths (100, 50 and 12 cm) and two different geometries (flat and bundled). All components are shown with permission from the respective manufacturers.

et al., 2007). These sensors were shown to provide richer information for motion and pulse artifact estimation, with clear benefits for the identification of epileptiform activity (Abbott et al., 2014). More recently, so-called **reference layer** methods have been explored, where EEG-like electrodes are distributed on a conductive layer on top of the EEG cap, but isolated from the scalp, recording only induction effects. These approaches aimed at both motion and pulse artifacts (Luo et al., 2014) and even gradient artifacts (Chowdhury et al., 2014), at the cost of requiring larger numbers of sensors. Alternatively, some studies have also explored the use of optical head motion tracking devices to correct for spontaneous and pulse-related motion artifacts; although subtle, these head movements were shown to be adequately tracked, allowing for an effective reduction of the resulting artifacts (LeVan et al., 2013).

While the use of dedicated sensors for artifact monitoring and reduction has shown clear benefits for EEG data quality (Flanagan et al., 2009; Chowdhury et al., 2014; Luo et al., 2014), these approaches have so far not achieved widespread use. This is possibly due to the need for additional recording equipment for the sensors (including amplification, synchronization with EEG acquisition, etc.), as well as other customized elements (electrodes, gel layers), altogether increasing the cost and complexity of acquisition setups. This is a rather unfavorable situation given the unique potential of these approaches for motion artifact reduction, with crucial importance at higher field strengths. Accordingly, in the second study of this chapter, a novel approach for motion artifact recording and EEG data denoising is proposed, and its benefits for simultaneous EEG-fMRI at 7 T are assessed. Artifact detection was performed with a simple and non-permanent modification of the EEG cap, where four electrodes were isolated from the

scalp and connected to the reference electrode via added resistors, measuring only magnetic induction effects. Several analysis approaches were investigated for optimal use of the sensor recordings in EEG signal correction, including: (I) a study of the combination of motion and pulse artifact correction techniques, (II) the development of different techniques for offline motion artifact correction, along with an assessment of artifact contributions at 7 T, and (III) the integration of motion artifact correction with ICA-based denoising. Throughout each part, data quality improvements were evaluated in terms of EEG power reduction and of increases in sensitivity to VEPs, particularly at a single-trial level.

5.2 Theory

Here, the mechanisms underlying EEG artifact generation are described, to provide a theoretical basis for the development of effective reduction strategies.

5.2.1 EEG artifact generation

As discussed in Chapter 1, the presence of a temporally-varying magnetic field \vec{B} will induce electromotive forces in the EEG loops according to **Faraday's law of induction** (Yan et al., 2010), as approximated by Eq. 1.5. This is the mechanism underlying gradient artifact generation. Reciprocally, when the loops move in space relative to a static field, such as \vec{B}_0 , electromotive forces will be generated as well – this is the mechanism behind motion-related artifacts, such as due to vibration propagation, spontaneous head motion, and at least part of pulse artifact contributions.

Although Eq. 1.5 is only accurate for a pure wire loop (it does not account for the complex current paths traversing the head, between the electrodes (Yan et al., 2009)), the importance of reducing the exposed area within the loops to minimize artifact contamination becomes evident. While a certain spatial separation between electrodes at the scalp is necessary for EEG signal measurements, any loop areas formed between each channel and the reference at the level of transmission between the cap and the amplifiers can and should be minimized. This can be done by **shortening** the transmission cables, and/or by **bundling** the respective wires closer together, thereby reducing their spatial separation. In the first case, some care must be taken to ensure that the EEG amplifiers, being brought closer to the head, can withstand the increased gradient field strength and RF power deposition without being damaged.

5.2.2 Motion artifact generation

As previously discussed, EEG artifacts due to head motion in the static field \vec{B}_0 can be described by Faraday's law of induction. For an EEG channel C_i and reference channel C_{Ref} , Eq. 1.5

becomes:

$$\xi_i(t) = -\frac{d\Phi_\Sigma}{dt}(t) = -\frac{d}{dt} \int_\Sigma \vec{B}_0(\vec{r}, t) \cdot \vec{N}(\vec{r}, t) d\Sigma \quad (5.1)$$

where ξ_i is the induced eletromotive force, Φ_Σ is the magnetic flux through the surface Σ enclosed by the loop (Fig. 5.2), and \vec{N} is the unitary normal vector to the surface, at each position \vec{r} and instant t . As before, the current path between C_i and C_{Ref} is treated as a linear path along the scalp surface (a more rigorous approximation would involve modeling the volume conduction properties of the head). Additionally, flux contributions from wire segments leaving the cap surface are assumed to be minimal, as a result of cable optimization during the first study here reported. If \vec{B}_0 is spatially homogenous, stationary and parallel to the z -axis, and assuming rigid-body motion, Eq. 5.1 can be simplified to:

$$\xi_i(t) = -B_0 \int_\Sigma \frac{d}{dt} N_z(\vec{r}, t) d\Sigma \quad (5.2)$$

where N_z is the z -component of the surface normal vector. It follows from Eq. 5.2 that only rotations along the x - and y -axis can produce induction effects, as $N_z(\vec{r}, t)$ does not change with translations or with rotations along the z -axis. Under the rigid-body assumption, the evolution of $N_z(\vec{r}, t)$ with x - and y -axis head rotations (globally described by angles ϕ and θ , respectively) can be written as:

$$N_z(\vec{r}, t) = \sin(\theta) N_x^0(\vec{r}) - \sin(\phi) \cos(\theta) N_y^0(\vec{r}) + \cos(\phi) \cos(\theta) N_z^0(\vec{r}) \quad (5.3)$$

where N_x^0 , N_y^0 , N_z^0 are the original components of the normal vector. Inserting this decomposition in Eq. 5.2 and applying the temporal derivative, we obtain an expression of the form:

$$\xi_i(t) = F_i(\phi(t), \theta(t)) \frac{d\phi}{dt}(t) + G_i(\phi(t), \theta(t)) \frac{d\theta}{dt}(t) \quad (5.4)$$

where F_i and G_i are surface integrals of linear combinations of sine and cosine functions of ϕ and θ , weighted by N_x^0 , N_y^0 , N_z^0 at each position \vec{r} . The potential difference created between C_i and C_{Ref} will then be proportional to ξ_i , and is measured in addition to the true, physiological EEG signal.

The structure of Eq. 5.4 suggests that this contribution can be approximated by a linear model with two degrees of freedom, $d\phi/dt$ and $d\theta/dt$, weighted by temporally-varying coefficients, $F(\phi, \theta)$ and $G(\phi, \theta)$. While the coefficients are channel-specific, the two rotations are common to all loops in the rigid body. This thus motivates the use of loop-based motion sensors, sensitive to similar induction effects, and the use of adaptive linear models to combine their timecourses and estimate the artifact contributions affecting actual EEG channels.

5.2.3 Motion artifact correction

We consider a recorded signal $y = s + m$, where s is the EEG signal of interest and m is a motion artifact timecourse. The two components are assumed to be uncorrelated. Based on a set of motion sensor signals x_i , recorded along with y , the timecourse m is then modeled as a linear combination of the sensors, weighted by time-varying coefficients w_i :

$$m(t) = \sum_i w_i(t) x_i(t) \quad (5.5)$$

The channels x_i capture only EM induction-related artifacts, and thus their measured signals are expected to be proportional to the electromotive forces ξ_i induced in the corresponding loops, depending on $d\phi/dt$ and $d\theta/dt$ as described above. The coefficients $w_i(t)$ can be estimated through various approaches, as described below.

Linear regression with basis set coefficients (BLS): the model described by Eq. 5.5 can be made parametric by defining the coefficients w_i as linear expansions of appropriate basis functions b_j (Huang et al., 2002):

$$w_i(t) = \sum_j a_{i,j} b_j(t) \quad (5.6)$$

The introduction of Eq. 5.6 in Eq. 5.5 leads to a new linear model with fixed coefficients $a_{i,j}$ for each product $b_j x_i$, which can then be estimated analytically using an ordinary least-squares approach.

Sliding-window weighted least squares (WLS): in the model described by Eq. 5.5, the coefficients w_i can be determined at each instant t by considering a local time window of the data centered on t , V_t , and applying weighted least-squares linear regression to that segment (Hoover et al., 1998; Fan and Zhang, 2000). In this sense, the least-squares cost function to minimize is defined as:

$$E(w, t) = \sum_{\tau \in V_t} \Omega(\tau - t) \left(y(\tau) - \sum_i w_i x_i(\tau) \right)^2 \quad (5.7)$$

where Ω is a weight function that can be chosen to attribute more importance to instants closer to t .

Multi-channel recursive least squares (M-RLS): originally proposed for active noise control in audio applications (Bouchard and Quednau, 2000), multi-channel recursive least-squares (M-RLS) is a real-time estimation method based on Kalman filtering, which has already been successfully applied to EEG data with loop-based motion sensors (Masterton et al., 2007). In this method, the linear model includes the original sensor timecourses x_i along with time-shifted versions, forming a finite impulse response (FIR) filter. For each instant t , the fitting weights w_i are updated from $t-1$ to produce the best estimate of $m(t)$, combining FIR-filtering, regressor decorrelation and least-squares fitting within the same update. A scalar parameter λ

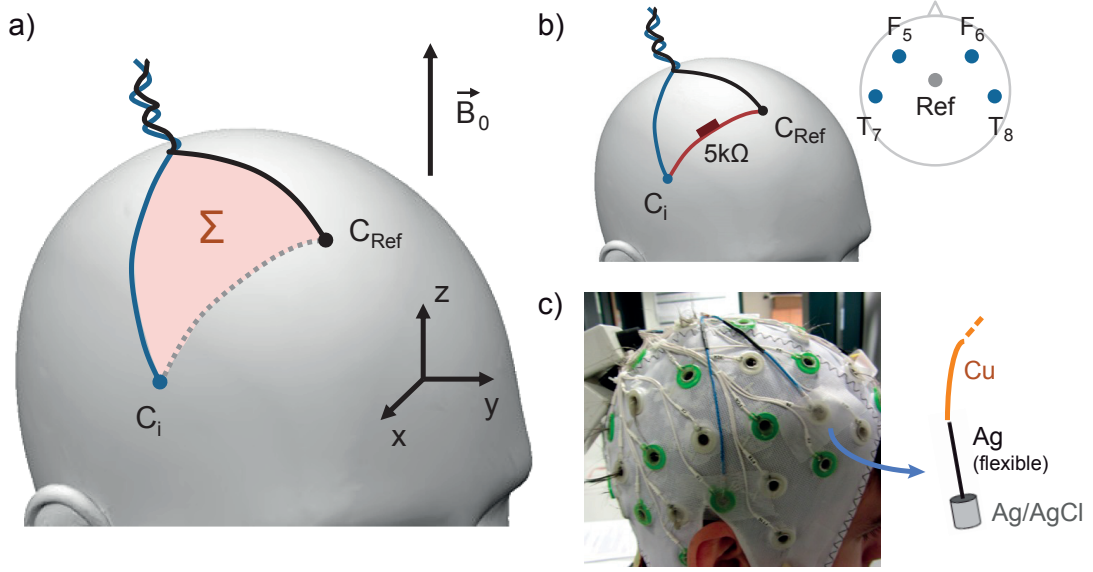


Figure 5.2: Schematics of EEG motion artifact generation and detection. **a)** Representation of a loop formed by a given EEG channel C_i with the reference C_{Ref} , covering an area Σ on the scalp surface; the static magnetic field \vec{B}_0 is depicted along the z -direction. **b)** Representation of the non-permanent cap modifications employed for motion artifact detection: each of the selected channels (T7, T8, F5 and F6) was isolated from the scalp and given a direct connection to the reference via a 5 k Ω resistor. **c)** The modified cap after preparation on a human subject; schematic details of the Ag/AgCl electrodes used to dip in the ring electrodes of the EEG cap are also shown, along with their flexible Ag termination, which was soldered to a copper wire for connecting to the reference.

controls the adaptability of the algorithm.

5.3 Methods: signal transmission

5.3.1 MRI system

All measurements were performed on an actively-shielded Magnetom 7 T head-only scanner (Siemens, Erlangen, Germany), with ultra-short bore length (Magnex Scientific, Oxford, UK) and 680 mm bore diameter (Fig. 5.1a). The scanner was equipped with an AC84 head gradient set (max. slew-rate 333 T/m/s) and a single-channel transmit/8-channel receive head RF loop array (Rapid Biomedical, Rimpf, Germany; Fig. 5.1c) was used.

5.3.2 Signal transmission optimization

Here, EEG noise sensitivity was assessed depending on the length and geometry of the ribbon cables (Fig. 5.1e). EEG recordings were performed with an agar gel phantom, with no concurrent MRI acquisition. Patient ventilation, room and bore lights, and the scanner host

remained switched off at all times. Recordings were performed both with and without the scanner coldheads in operation.

EEG acquisition: EEG data were recorded using a single 32-channel BrainAmp MR Plus amplifier (Brain Products, Munich, Germany) connected via a ribbon cable to an MR-compatible signal tester box. This signal tester, where each channel is directly linked to the reference via a 5 k Ω resistor, was then tightly fixed to the top (head side) of the agar gel phantom. This approach avoided the use of an actual EEG cap, so as to capture strictly cable-related noise contributions. EEG signals were recorded for approximately 2 min for each configuration, with a 500 Hz sampling frequency, hardware bandpass filtering of 0.016–250 Hz, and 0.5 μ V amplitude resolution.

Cable configurations: a total of 6 different ribbon cables were tested, comprising 3 different lengths (100, 50, and 12 cm) and 2 different geometries: (i) the typical flat ribbon configuration, with the reference channel running approximately in the middle, and (ii) a bundled configuration where all channels are tightly bunched together in a cylindrical shape (Fig. 5.1d–e). For the shortest cable length (12 cm), the EEG amplifier was placed on top of the RF coil gateway box; for longer cable lengths, the amplifier was suspended on a wooden support mechanically isolated from the bed, maintaining a similar position relative to the central axis of the scanner bore.

EEG data analysis: following acquisitions, EEG noise contamination was assessed and compared across different cable configurations. A qualitative comparison relied on visual inspection of channel timecourses and channel-averaged noise spectra, estimated via fast Fourier transform over a 30s period. For a quantitative comparison between configurations, an average full-spectrum noise power estimate was computed for each channel in each condition, based on the mean of the squared signal over 30s. These estimates were then statistically analyzed via a 3-way ANOVA, incorporating the factors of cable length, cable geometry, and He coldhead state.

5.3.3 Optimized EEG setup

Following the transmission tests, an optimized setup was implemented for tests in human volunteers: EEG data were recorded using two 32-channel BrainAmp MR Plus amplifiers and a customized BrainCap MR model (EasyCap, Herrsching, Germany). The cap contained 64 Ag/AgCl ring-type electrodes ("multitrodes"), arranged according to an extended 10-20 system, and was designed with shortened electrode leads terminating in two connectors at approximately 1–3 cm from the cap surface (Fig. 5.1b). Each copper electrode lead contained a 5 k Ω resistor near the electrode and another inside the connector. One of the 64 electrodes was placed on the back of the subject for ECG recording. The cap connectors were linked to the EEG amplifiers via two 12 cm bundled cables (Fig. 5.1d). The two amplifiers rested on top of each other just outside the head array, on the RF gateway box (Fig. 5.1a). After bandpass filtering (0.016–250 Hz) and digitization (0.5 μ V resolution), the EEG signals were

transmitted to the control room via two fiber optic cables. EEG sampling was performed at 5 kHz, synchronized with the scanner 10 MHz clock. Scanner triggers marking the onset of each fMRI volume were also recorded. In both phantom and human recordings, Abralyte gel (EasyCap) was used to reduce electrode impedances. The scanner He coldheads were kept in operation at all times.

5.3.4 Human acquisitions

Human tests comprised the final stage of this study, intended to assess BOLD and EEG data quality using the optimized setup, particularly in terms of functional sensitivity and potential use for single-trial studies. A total of 5 healthy male volunteers (20 ± 2 years old) participated in this study, having provided written informed consent. The study had been previously approved by the institutional review board of the local ethics committee (Commission d'Éthique de la Recherche sur l'Être Humain du Canton de Vaud). Volunteers were asked to remain as still as possible during the acquisitions, and foam pads were placed between the head and the RF coil to further constrain motion. Due to time constraints, one of the volunteers did not undergo the eyes-open/eyes-closed run.

Functional paradigms: volunteers underwent two functional runs: (i) an eyes-open/eyes-closed run mediated by auditory cues, and (ii) a VEP run applying reduced-field reversing-checkerboard stimuli. The eyes-open/closed run comprised eight blocks of 15s eyes-closed followed by 15s eyes-open periods. Instructions were given to the subjects from the control room via the patient communication system, with the room lights kept ON throughout the experiment. For the VEP run, checkerboards were presented during eight 10s blocks at a reversal frequency of approximately 4 Hz (totaling 39 reversals per block), followed by 20s of rest (fixation). A red cross was shown at the center of the FOV at all times, with slight shifts in color occurring twice per block at random time delays. Subjects were instructed to remain focused on the cross and report color shifts via a button press. Checkerboards were presented at 50% contrast, maintaining an equivalent average luminance to the rest periods. The stimulation FOV was limited to approximately 7° , a fairly selective central-field stimulus (ACNS, 2006). This was both due to technical limitations (the images were projected from the back of the bore, with the EEG amplifiers partially obstructing the FOV), and intentionally in order to assess sensitivity for a weaker stimulus, especially on a single-trial scale. As the stimulation was performed using an LCD projector, a StimTracker box (Cedrus Corporation, San Pedro CA, USA) equipped with a photodiode sensor was used to record the precise timing of checkerboard reversals. Room lights were kept OFF for this run. The two 4-minute runs were presented in counter-balanced order across subjects, separated by a short pause for communication with the subject and pre-scanning adjustments.

EEG-fMRI acquisition: simultaneous acquisitions were performed with the optimized EEG setup described in section 5.3.3, using a multislice 2D GE-EPI sequence (25 axial slices, $1.5 \times 1.5 \times 1.5 \text{ mm}^3$ spatial resolution with 1.5 mm interslice gaps, $TR/TE = 2000/25 \text{ ms}$, α

= 78°, 2×-GRAPPA acceleration, 7/8 partial Fourier imaging and sinusoidal readout). The EPI volume slab was placed in an axial-oblique orientation fit to contain as much of the primary visual cortex as possible. Volume triggers were received from the scanner at the start of each EPI volume and recorded along with the EEG traces. Bore lights and the patient ventilation system were kept OFF throughout the sessions, with no discomfort reported by the subjects.

EEG data analysis: data analysis was performed in Matlab using routines developed in-house. For each run, based on the recorded volume triggers, slice triggers were produced by splitting each volume interval in 25 equal segments. The resulting slice triggers were then fine-tuned by maximizing inter-slice correlations, in a 10×-upsampled EEG channel (Niazy et al., 2005). Gradient artifacts were then corrected slice-by-slice via AAS and OBS techniques (Allen et al., 2000; Niazy et al., 2005). For AAS, each slice was subtracted of an average over 50 slice samples (25 from the preceding and 25 from the following slices), with randomly-jittered steps of 4–6 slices separating the selected samples. With this spacing, the samples selected for averaging were thus spread over a period of approximately 20s (250 slices) centered on the slice to be corrected. Step jittering was applied to mitigate the removal of EEG activity of interest, especially for VEP data, where stimulation (250 ms period) was phase-locked with slice acquisition (80 ms) every 25 slices. Furthermore, the LCD projector used for checkerboard presentation had a variable delay of 0–17 ms (which was monitored with a photodiode for VEP triggering), providing an additional jitter to the acquisition-stimulation timing relationship.

Cardiac triggers were estimated from the ECG channel through a sliding-window correlation approach, in which a representative cardiac cycle was first manually segmented, and then correlated in time with the full ECG trace. The local maxima of the resulting correlation timecourse were selected as cardiac triggers, and then fine-tuned by another correlation-maximization approach, using a combination of EEG channels where pulse artifacts were most prominent. Based on these triggers, pulse artifacts were reduced via OBS, using the 3–5 most important principal components, depending on the stability of this artifact throughout each run. Data were then downsampled to 500 Hz, and bad channels were identified (1–5 per dataset) and replaced by weighted averages of 3–4 neighboring electrodes. For the eyes-open/closed run, data were re-referenced to the average reference, decomposed via ICA, and then reconstructed by manual selection of the components exhibiting differences in alpha power (8–12 Hz) between eyes-open and eyes-closed conditions. For the VEP run, data were bandpass filtered to 4–30 Hz, re-referenced to the average reference, and decomposed via ICA. The datasets were then reconstructed by manual selection of components displaying non-artifactual, potentially VEP-related dynamics, based on their topography, trial average response and trial-by-trial variability (Arrubla et al., 2013; Neuner et al., 2013). Component selection was always performed by the same operator (J.J.), using similar criteria.

fMRI data analysis: data analysis was performed using custom routines implemented in Matlab. For both runs, fMRI data underwent motion correction, slice-timing adjustments, brain segmentation, spatial smoothing (2 mm FWHM) and temporal de-trending (Smith et al., 2004b). The datasets were then analyzed voxel by voxel with a GLM approach (Worsley and

Friston, 1995). Here, a "boxcar" timecourse was designed for each experiment (1's during eyes-closed periods and 0's during eyes-open periods, for the eyes-open/closed run, and 1's during checkerboard stimulation and 0's during fixation, for the VEP run). These binary timecourses were then convolved with a (double-gamma) canonical HRF. Motion parameters were also included as confounds.

5.4 Methods: head motion

This study was approved by the institutional review board of the local ethics committee, and involved the participation of 6 healthy volunteers (20 ± 2 years old), who provided written informed consent. Volunteers were asked to remain as still as possible during the acquisitions, and foam pads were placed between the head and the RF coil to further constrain motion.

5.4.1 Data acquisition

Simultaneous EEG-fMRI acquisitions were performed on a Magnetom 7 T head scanner as described in section 5.3.1. The scanner He coldheads were kept in function at all times, while patient ventilation and room lights were switched off. Functional images were acquired with a multislice 2D GE-EPI sequence, as described in section 5.3.4. EEG data were recorded using the optimized setup described in section 5.3.3. All EEG artifact corrections were performed offline, after acquisition.

Motion sensors: in this setup, four of the EEG electrodes (T7, T8, F5 and F6) were adapted to serve as motion artifact sensors. For this set, each electrode was isolated from the scalp and given a direct connection to the reference electrode (FCz) via a copper wire fitted with a non-magnetic 5 k Ω resistor (Vishay, Malvern PA, USA) (Fig. 5.2b). Connections were performed in a non-permanent way: the selected electrodes were isolated from the scalp by placing plastic tape underneath, and then filled with gel within the ring; the connecting wires terminated in small Ag/AgCl probes (Warner Instruments, Hamden CT, USA) that were dipped in the gel (Fig. 5.2c), allowing conduction between the four electrodes and the reference electrode (which was not isolated and kept functioning as normal). Given the high input impedance of the amplifiers, current flows along the wires due to neuronal activity can be considered negligible (Yan et al., 2009), and as such the electric potential measured by each of the adapted electrodes will be equal to the potential at the reference, added by magnetically-induced fluctuations occurring in the loop. As the system records EEG signals as the difference in potential between each channel and the reference, by design, these four channels will then monitor essentially magnetic induction effects – including gradient, pulse, vibration and spontaneous motion artifacts. The channels employed for this modification were chosen in order to cover different areas of the scalp in lateral and frontal regions; occipital regions were avoided because these are pressed down against the bed when the subject is lying in the scanner. For each subject, the sensor connections were placed after minimizing the impedances for the other electrodes, adding approximately 5 minutes of preparation time.

Functional paradigm: each of the 6 volunteers underwent a 5-minute VEP run using reversing-checkerboard stimuli. Checkerboards were presented during ten 10s blocks at a reversal frequency of 3.35 Hz (totaling 33 reversals per block), followed by 20s of rest (fixation). The 7°-wide field of view featured a red cross at its center at all times, with slight shifts in color occurring twice per block at random time delays. Subjects were instructed to focus on the cross and report color shifts via a button press. Checkerboards were presented at 50% contrast, with an equivalent average luminance to the fixation periods. A StimTracker box with a photodiode sensor was used to record the timing of checkerboard reversals.

5.4.2 fMRI data analysis

The fMRI data acquired concurrently with EEG was analyzed to determine the white matter temporal SNR obtained with the current optimized setup, with added motion sensors. For each subject, the fMRI data were first motion-corrected; temporal SNR was then calculated for each voxel as the mean timecourse amplitude divided by the timecourse standard deviation, and finally averaged within a frontal white matter region ($7 \times 7 \times 7$ voxels), similar to the approach followed in Chapter 4.

5.4.3 EEG data analysis

Data analysis was performed in Matlab using routines developed in-house. All functional runs underwent an initial preprocessing pipeline, and were then studied in three distinct parts, addressing (I) the integration of motion and pulse artifact correction, (II) the optimization and comparison of motion correction approaches, and (III) the integration of motion correction with ICA denoising.

Data preprocessing: all recorded channels, including the motion sensors, underwent the same preprocessing routine. For each run, based on the recorded fMRI volume triggers, slice triggers were obtained and fine-tuned as described in section 5.3.4. Gradient artifacts were then corrected slice-by-slice via AAS (Allen et al., 2000); each slice was corrected by subtracting an average over 100 slice samples (50 from the preceding and 50 from the following slices), with jittered steps of 8–13 slices separating the selected samples. These steps permitted sufficient spacing between samples to avoid removing lower-frequency EEG activity (Niazy et al., 2005), and yielded a balanced distribution of samples relative to the visual stimulation cycle (3.35 Hz), mitigating phase-locking effects.

Cardiac triggers were estimated from the ECG channel and fine-tuned as described in section 5.3.4. Based on these triggers, pulse artifacts were reduced via AAS, subtracting each instance of an average over the closest 50 pulse samples (25 of the preceding and 25 of the following cardiac cycles). AAS was chosen for this step because each artifact instance is corrected with a fixed linear combination of its neighbors, which is the same for every channel (both EEG and motion sensors), thus preserving the linearity relationships of Eq. 5.4. This would not

hold for certain approaches such as OBS, where each instance is corrected by a local fit (not a subtraction) of basis functions, which is differently biased by the ongoing motion artifacts and EEG fluctuations of each channel (see section 5.1.1 for details on both approaches).

Following gradient and pulse artifact correction, EEG data were downsampled to 250 Hz, and bad channels were identified (2–5 per subject) and replaced by weighted averages of 3–4 of the neighboring electrodes. Each functional run was also inspected based on its GFP timecourse, obtained as the standard deviation of signal amplitudes across the scalp at each instant in time. Periods displaying strong GFP peaks, likely caused by large abrupt motion, were manually excluded from all subsequent analyses (a total of approximately 20–40s per 5-minute run). These periods were excluded as they would likely cause very fast variations in the linear coefficients $F(\phi, \theta)$ and $G(\phi, \theta)$, described in section 5.2.2, for which the proposed models would possibly not yield an accurate estimation.

Part I – pulse and motion artifact correction: previous studies have assumed the pulse artifact to be mainly caused by bulk head motion, relying on sensor information to correct both pulse and spontaneous motion artifacts (Bonmassar et al., 2002; Masterton et al., 2007). Here, the potential benefits of combining motion artifact correction with a dedicated pulse artifact correction step (AAS-based, as described above), at 7 T, were investigated. The original data were preprocessed in two versions, one with and another without pulse artifact correction. Both datasets underwent temporal highpass-filtering (1 Hz) and then motion artifact correction with M-RLS, implemented exactly as proposed in Masterton et al. (35 shifts for the FIR kernel with $2\times$ -downsampling, $\lambda = 1 - 10^{-8}$).

Part II – optimization of motion artifact correction: this part focused on the comparison of different approaches for optimal sensor-based motion artifact correction. Based on the results from part I, pulse artifact correction was included in data preprocessing. Temporal bandpass filtering was also applied, set at 2–120 Hz for EEG data and 2–30 Hz for the motion sensors. The choice of a highpass cutoff of 2 Hz was motivated by preliminary tests showing that increasing the cutoff frequency improved motion artifact estimation, likely due to reduced biases from slow-drift contributions; this compromise comes at the cost of excluding EEG information from part of the delta band, but did not affect VEP morphology (Widmann et al., 2015). The choice of a lowpass cutoff of 30 Hz for the motion sensors was again based on insights from part I, pointing that this is the relevant frequency band for motion contributions. Motion correction was based on the linear model of Eq. 5.5, and explored the three approaches introduced in section 5.2.3: BLS, sliding-window WLS and M-RLS. In all cases, the model regressors x_i included the 4 original sensors and a set of shifted versions of their timecourses, to produce a subject-specific FIR kernel (Bonmassar et al., 2002). The number and spacing of the shifts were optimized by testing multiple models with linear fits to the data (assuming constant weights w_i), and then comparing the respective adjusted coefficients of determination (R_{adj}^2), as well as the impact on visual response amplitude. R_{adj}^2 is a goodness-of-fit measure that is independent of the number of regressors in a model, and is thus particularly suitable for model comparison (Jorge et al., 2013). As a model (in this case, the kernel) is improved with

additional regressors (in this case, shifts), R^2_{adj} is expected to increase, until the point where adding more regressors does not explain more variance than would otherwise be achieved by simply adding random regressors; after this point, the model R^2_{adj} will begin to decrease. As all approaches were designed for offline correction, both positive and negative shifts could be included in the models – this was confirmed to produce better results than including only shifts from the past, as in real-time correction.

BLS: for this approach, three basis sets were tested to model the time-varying coefficients w_i , all designed to model smooth fluctuations: (i) a discrete cosine transform expansion (DCT), (ii) a full Fourier series expansion with an initial linear slope term, and (iii) a cardinal cubic B-spline set (Huang et al., 2002). The optimal expansion degree for each case was estimated by a similar empirical procedure to the one used for FIR kernel optimization.

Sliding-window WLS: for this approach, a Gaussian distribution was chosen as weight function for the sliding window, with its full width at half maximum (FWHM) controlling the temporal adaptability of the estimation. Preliminary tests yielded a value of 60s as a good compromise between adaptability and robustness.

Offline M-RLS (oM-RLS): this approach was based on the method described by Masterton et al. (2007), with a number of modifications that took advantage of the choice for post-acquisition data correction: (i) both forward and backward shifts were included in the FIR kernel, optimized as described above; (ii) the coefficients w_i were updated for every time instant; and (iii) the coefficient timecourses were estimated with a double pass, where the iterations were first performed forwards in time (each $w_i(t)$ was updated from $w_i(t-1)$, from the beginning to the end of the timecourse), and then backwards (each $w_i(t)$ was updated from $w_i(t+1)$, from the end to the beginning). This yielded a cleaner estimation for the starting periods, where the initial pass is not accurate since the coefficients take a certain time to converge from the initial set value ($w_i(0) = 0$) to the least-squares solution (see Fig. 5.3 for an example). The adaptability parameter λ was kept at a value of $1 - 10^{-8}$ (Masterton et al., 2007).

Besides the comparison of the three correction approaches, an additional characterization of the different artifact contributions to EEG signal power was performed in this part, based on the results from oM-RLS correction. For each subject, the EEG data resulting from three stages of the correction pipeline were considered: gradient artifact-corrected, gradient + pulse artifact-corrected, and finally gradient + pulse + motion artifact-corrected. At each stage, an estimate of the signal variance was obtained for each channel, and then averaged across channels. The decreases in variance across stages were then computed, as an estimate of the fraction of total signal variance expressed by each of the targeted sources (assuming all sources are uncorrelated).

Part III – motion artifact correction and ICA: as discussed in Chapter 1, section 1.3.3, ICA is a powerful exploratory technique that is often used in EEG data denoising. In this last section, we compared the performance of motion artifact correction based on motion sensors with

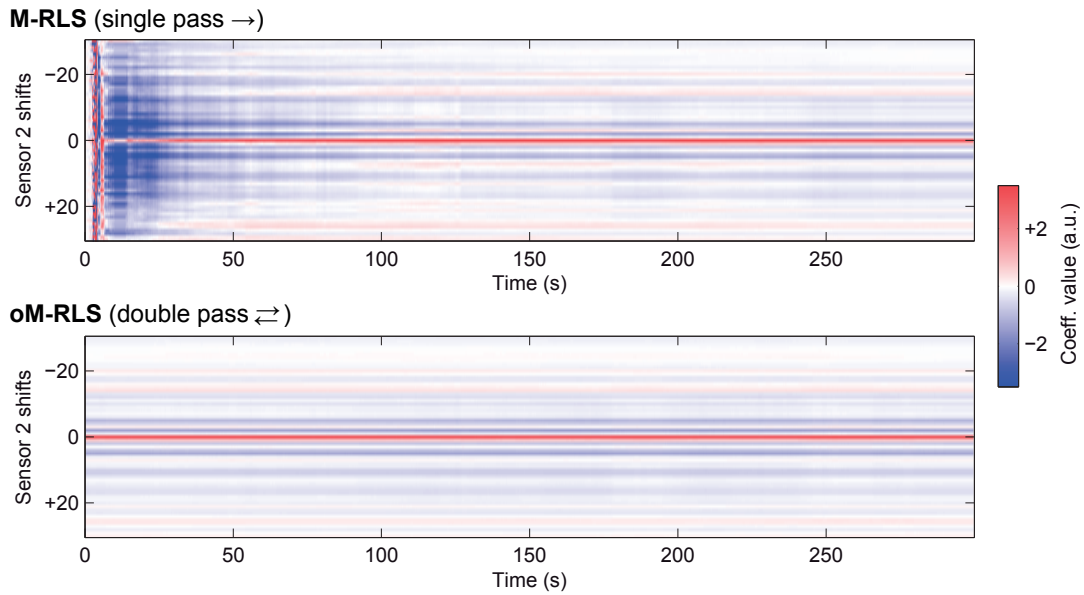


Figure 5.3: Coefficient timecourses estimated by M-RLS and oM-RLS for the FIR kernel of one motion sensor during the 5-minute functional run of a single subject. The second pass applied in oM-RLS corrects the initial period of coefficient convergence, retaining only the smooth variations attributed to changes in head position. The position-related variations were found to be relatively small compared to the range of values across the kernel, and thus appear to be almost constant with this color scale.

an approach based on ICA denoising, and investigated the potential benefits of combining the two techniques. As in part II, data preprocessing included pulse artifact correction and temporal bandpass filtering (2–120 Hz for EEG data, 2–30 Hz for the motion sensors). Data were then corrected based on the motion sensors, ICA, or a combination of motion artifact correction followed by ICA denoising. The approach here chosen for motion artifact correction was oM-RLS (as discussed in section 5.7.5). ICA decomposition was performed with the extended infomax algorithm (Lee et al., 1999), imposing statistical independence in the temporal dimension. The resulting components were then reviewed based on their topography, trial-average response and trial-by-trial consistency (Arrubla et al., 2013). Components found to be clearly not related to the visual response (pulse and motion artifacts/residuals, eye-movement artifacts, etc.) were marked and excluded from subsequent data reconstruction. Additionally, an alternative ICA-based approach was tested where the motion sensor timecourses were included as additional channels in the ICA decomposition, and reconstruction was performed after manually rejecting components with strong projection weights in the motion channels. This approach guided by motion information was termed motion-integrated ICA (miICA).

Performance measures: for the three main parts of data analysis (I–III), the performance of the different correction approaches under study was assessed based on EEG signal power and VEP single-trial consistency. EEG power was computed for each channel via fast Fourier transform of the entire timecourse, and estimated for the full frequency band (1–125 Hz), as

well as for specific bands delta (1–4 Hz), theta (4–8 Hz), alpha (8–12 Hz), beta (12–30 Hz) and gamma (30–100 Hz), in part I. For part I, relative power reductions obtained with correction were also estimated in dB as $10\log_{10}(P_f/P_i)$ (with P_i and P_f being the power before and after correction, respectively), for direct comparison with results from Masterton et al. (2007) at 3 T. VEP trial consistency was estimated after bandpass filtering (3–40 Hz) and re-referencing to the channel average, and involved computing the trial-average response in each channel, and then performing a least-squares fit of the average to each single trial. This yielded a Z-score of the fit per trial and per channel; the scores of all trials from occipital channels (Oz,1,2 and POz,3,4,7,8) were then averaged together, to yield a single Z-score per subject. The more restrictive filtering range of 3–40 Hz employed for this estimation was previously confirmed not to affect the average VEP morphology, while leading to more accurate single-trial fits. While signal power provides a more direct measure of the impact of denoising approaches on signal variability, VEP trial consistency is more informative of changes in response sensitivity due to artifact reduction, including potential effects of over-correction (since, under the assumption that the motion timecourses are uncorrelated with the visual responses, over-corrections will affect the different trials differently, and thereby reduce trial consistency). It should nevertheless be noted that this measure is only intended to monitor the effects of artifact correction, as it does not differentiate the natural variability of brain responses (Debener et al., 2006) from the variability introduced by the artifacts. For both measures, the values obtained with each correction approach were then compared via paired t-tests across subjects, assuming a maximum p-value of 0.05 for statistical significance. Relative variations in power and trial consistency reported in the text are shown as average \pm standard error across subjects. In part III, the quality improvements obtained with the optimal correction approach were further analyzed by direct observation of its effects on the trial-average and single-trial responses of individual subjects.

5.5 Results: signal transmission

5.5.1 EEG cable noise contributions

Based on preliminary tests, the scanner electronic hardware, room and bore lights, and host computer were found to have a negligible effect on EEG signal quality. The patient ventilation system produced relevant noise contributions at frequencies below 30 Hz, but could be switched off throughout all recordings without relevant consequences. With the scanner coldheads in function, using a 100 cm conventional (flat) ribbon cable, most EEG channels clearly displayed a stationary noise pattern of high frequency oscillations, with a fundamental period of approximately 1s (Fig. 5.4, left). This pattern disappeared upon switching off the coldheads. In the setup used for this study, channel numbers were attributed in sequence according to the position of each wire lane running along the cable, with the reference channel running approximately in the middle (between channels 16 and 17, and most distant from channels 1 and 32). A progressive increase in noise amplitude was clearly seen for channels running farther away from the reference, as would be expected from an artifact generated

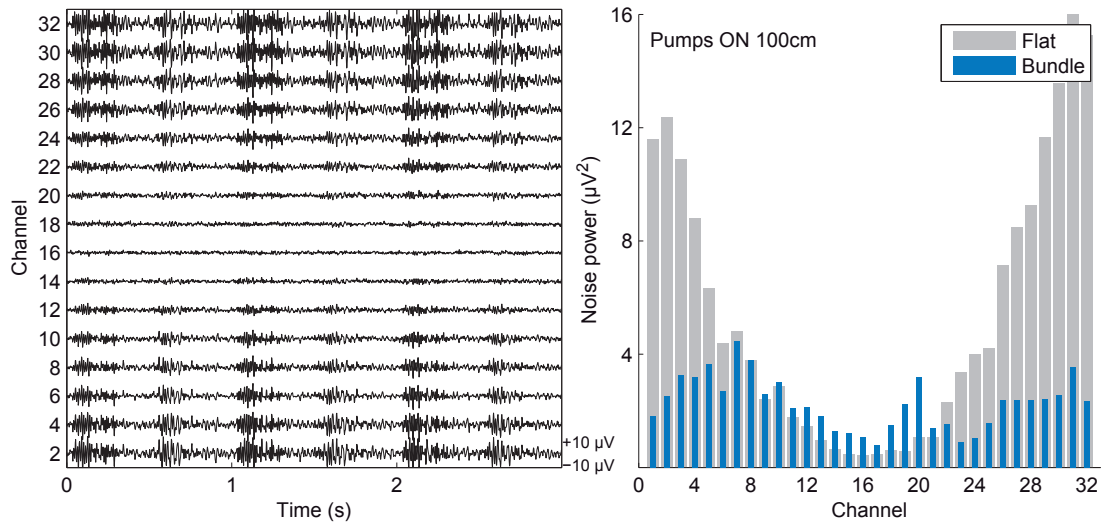


Figure 5.4: Channel-by-channel noise sensitivity of EEG ribbon cables depending on the distance relative to the reference channel, which runs along the middle of the cable. **Left:** EEG channel timecourses during a 3s window acquired with a 100 cm conventional (flat) ribbon cable, with the He coldheads in function; only even-numbered channels are shown in order to limit the figure size. **Right:** average noise power in each channel over a 30s period, for both flat and bundled ribbon cables, 100 cm long, with the coldheads in function.

by magnetic induction. This trend was quantified by computing full-spectrum noise power estimates for each channel and then comparing these values with results obtained with a similar configuration but using a bundled cable (Fig. 5.4, right). The dependence of channel noise power on the distance to the reference was evident for the flat type, but became greatly attenuated in the bundled configuration. Over all channels, for this cable length of 100 cm, the bundled type yielded a reduction of 58% in channel-averaged total noise power, and an 81% reduction in inter-channel noise power variability.

To compare the different cables tested, channel-averaged noise spectra were computed for each configuration. Different cable lengths and geometries displayed distinct overall power amplitudes, along with some differences in spectral distribution (Fig. 5.5). The scanner coldheads showed a major impact on noise amplitudes in the range of 20 up to 150 Hz, producing a considerable fraction of total noise power. The source(s) of the remaining noise could not be experimentally identified, but were confirmed not to be caused by the patient ventilation system, room or bore lights, scanner hardware or the host computer.

For a quantitative comparison between cable configurations, a full-spectrum noise power estimate was computed for each channel in each condition. Channel-averaged results are presented in Fig. 5.6. The influence of cable length and geometry on noise power was found highly statistically significant, as was the impact of coldhead contributions (all 3 effects with $p < 0.01$). Over all tested lengths, bundled cables yielded reductions of 0.2–69% in total noise power relative to flat cables, with the coldheads switched OFF, and of 43–63% with

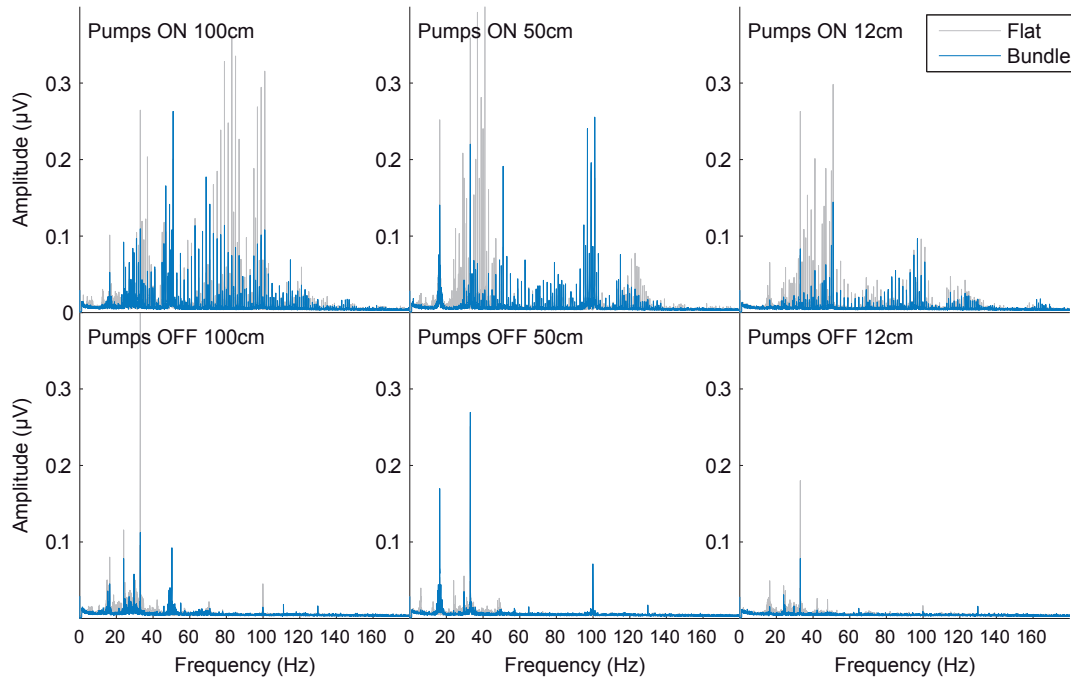


Figure 5.5: Channel-averaged EEG noise spectra for different ribbon cable configurations, with the He coldheads turned on (upper row) as well as off (lower row). All spectra were estimated from 30s periods of data.

the coldheads ON. Inter-channel variability was reduced by 18–88% with the coldheads OFF and by 47–81% with the coldheads ON when using bundled cables, compared to flat cables. Conversely, over the two geometry types, shortening from 100 to 12 cm yielded reductions of 44–70% in total noise power with the coldheads OFF and of 58–62% with the coldheads ON. Inter-channel variability was reduced by 59–83% with the coldheads OFF and by 52–63% with the coldheads ON, through cable shortening. Overall, the combination of cable bundling and shortening (from 100 to 12 cm) led to a reduction of 84% in total noise power and of 91% in inter-channel noise power variability, with the coldheads in operation.

5.5.2 Simultaneous acquisitions in humans

The feasibility of simultaneous EEG-fMRI at 7 T using the proposed setup was evaluated in 5 healthy volunteers, none of whom reported any unusual skin heating effects. Likewise, the EEG amplifiers operated normally throughout all runs, without heating-related impairments.

EEG data: gradient and pulse artifact correction steps produced strong changes on the original data (Fig. 5.7). Across all subjects and paradigms, full-spectrum (1–250 Hz) EEG power was reduced by $99.6 \pm 0.1\%$ with AAS-based gradient artifact correction, subsequently by $1.9 \pm 0.4\%$ with OBS-based residual gradient artifact correction, and finally by $64.3 \pm 5.9\%$ with OBS-based pulse artifact correction (each reduction estimated relative to the data from the preceding

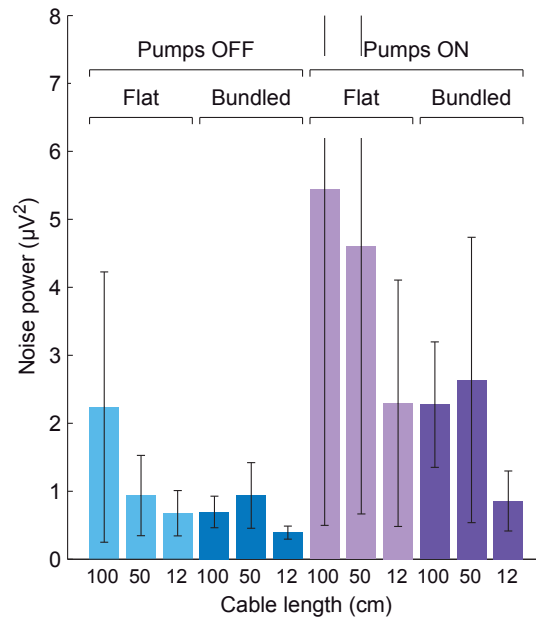


Figure 5.6: Average EEG noise power for different ribbon cable configurations, with the He cold-heads turned on as well as off. For each channel, noise power estimates were obtained from 30s periods. Bar heights represent channel averages, and error bars represent the standard deviation across channels.

correction step). Following ICA decomposition, 5–7 sources per subject were selected as relevant from the eyes-open/closed data, and 4–6 sources were selected from the VEP data. The ICA-reconstructed EEG data from the eyes-open/closed run revealed accentuated alpha modulation in occipital channels (Fig. 5.8a). Alpha power increases could be clearly observed in single-channel timecourses during most of the eyes-closed blocks, compared to eyes-open periods (Fig. 5.8b). The 4th subject did not show any task-related alpha power variations, consistent with the absence of significant task-related BOLD signal changes – it is thus likely that the subject did not properly follow the auditory cues for eyes-closing/opening.

For the VEP run, all 5 subjects exhibited an average response in occipital regions dominated by a positive peak occurring approximately 100 ms after stimulus onset (checkerboard reversal), commonly known as the P100 component (Bonmassar et al., 1999; Mahajan and McArthur, 2012). Over the scalp, the P100 peak reflected an anterior-posterior dipole (Fig. 5.9a), dominating the average GFP response at the same latency (Fig. 5.9b), in good agreement with previous reports (Skrandies, 2005; Bucher et al., 2006). On a single-trial scale, occipital responses were considerably noisier, with only a moderate fraction of the trials exhibiting a clear response pattern consistent with the average VEP (Fig. 5.9c). Nevertheless, a trial-by-trial regression analysis using a 2-regressor model, comprising the average VEP and its temporal derivative (to allow for variability in visual response latencies), showed that statistically significant responses ($p < 0.05$) were found in 164–177 trials out of 312 for this group of 5 subjects. The trials where VEPs were significantly detected were generally well spread across the paradigm timecourse,

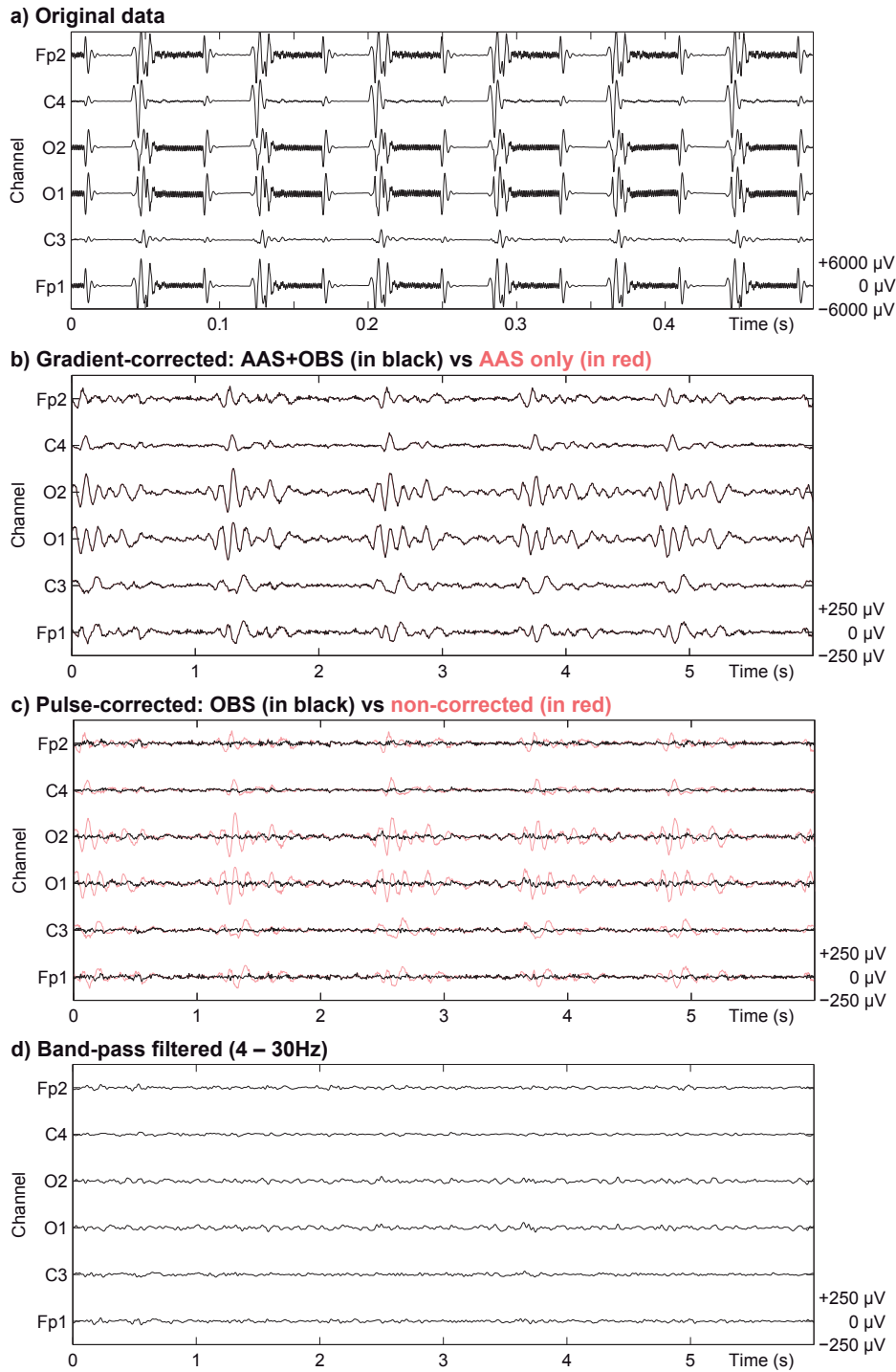


Figure 5.7: EEG channel timecourses before and after gradient and pulse artifact correction, selected from a representative dataset. **a)** Original EEG data. **b)** EEG data following gradient artifact correction with AAS (red) and AAS+OBS (black); the two outcomes are visually similar as OBS-based correction yielded relatively moderate improvements, most relevant above 100 Hz (frequencies not shown). **c)** EEG data before (red) and after (black) OBS-based pulse artifact correction. **d)** Bandpass filtered data (4–30 Hz) after artifact correction. Data presented in b) and c) are also shown bandpass filtered (1–100 Hz) for clearer visualization.

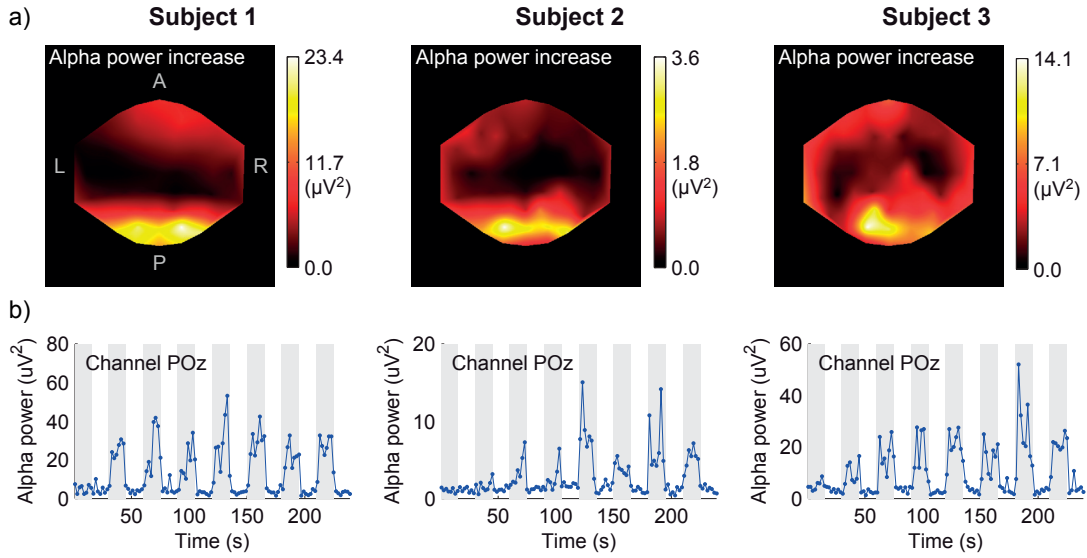


Figure 5.8: Alpha power variations in 3 human volunteers undergoing an eyes-open/eyes-closed task, as captured by EEG during simultaneous EEG-fMRI acquisitions. **a)** Average increases in alpha power over the scalp comparing an eyes-open to an eyes-closed state. **b)** Alpha power fluctuations during the full run, in a relevant occipital channel (POz); grey-shaded intervals mark the periods where subjects were instructed to have their eyes closed. The 4th subject did not show task-related alpha power variations, likely due to improper compliance with the task, and is therefore not shown. All results presented are derived from the reconstructed EEG datasets following ICA decomposition and source selection.

suggesting that habituation effects did not play a significant role in response sensitivity.

fMRI data: in the eyes-open/closed run, statistically significant negative BOLD signal changes were detected for eyes-closed periods in occipital regions in the same 3 out of 4 subjects showing significant EEG responses (Fig. 5.10a). Across these subjects, average Z-scores within significantly active regions ($Z < -3.5$) ranged from -5.6 to -4.4, with percent signal changes of -3.9% to -3.7%. Peak Z-scores ranged from -11.1 to -9.4. For the VEP run (Fig. 5.10b), statistically significant positive signal changes, correlated with checkerboard stimulation periods, were detected in occipital regions for all 5 subjects. Average Z-scores within significantly active regions ($Z > +3.5$) ranged from +4.9 to +5.2, with percent signal changes of +3.0% to +3.8%. Peak Z-scores ranged from +10.4 to +13.5.

5.6 Results: head motion

Tests conducted with the motion sensors showed no discernible contamination of the motion timecourses with neuronal activity. In particular, for EEG recordings performed outside the scanner on a volunteer at rest, signal power in the motion channels was below $1.4 \mu V^2$, compared to an average across the scalp of $41 \pm 28 \mu V^2$ for the EEG channels. A power peak

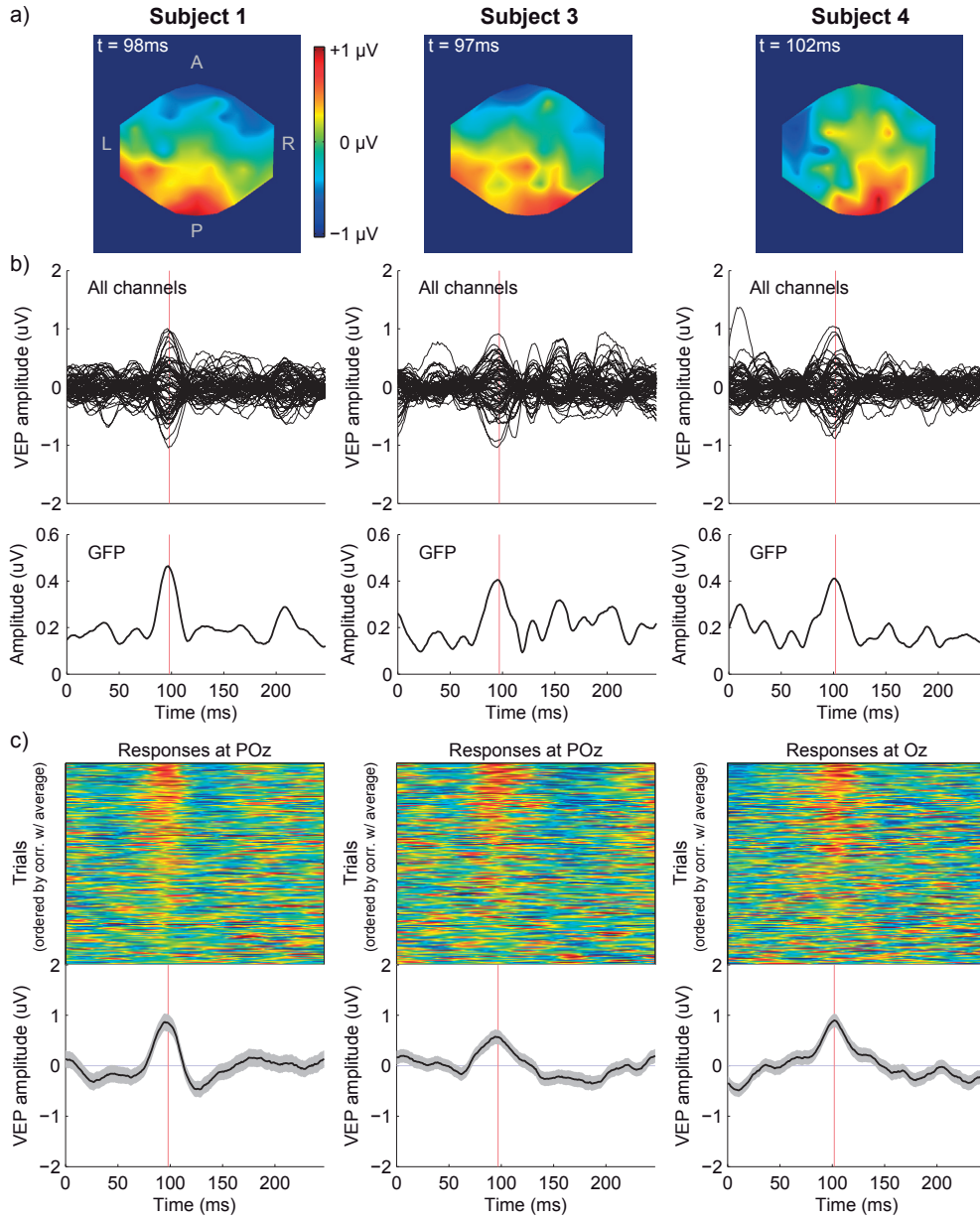


Figure 5.9: Responses to reduced-field reversing checkerboard stimulation in 3 human volunteers, as captured by EEG during simultaneous EEG-fMRI acquisitions. **a)** Scalp potential maps at the timing of the expected P100 peak. **b)** Trial-averaged responses of all 63 EEG channels, and the corresponding GFP response. **c)** Average and single-trial responses in a relevant occipital channel (POz or Oz), aligned at the onset of checkerboard reversal ($t = 0$ ms); single trial responses are ordered from top to bottom according to their correlation with the average response; only the 200 best trials (out of 312) are displayed. All results shown are derived from the reconstructed EEG datasets following ICA decomposition and source selection. The 3 subjects shown exhibited the clearest response patterns of the group.

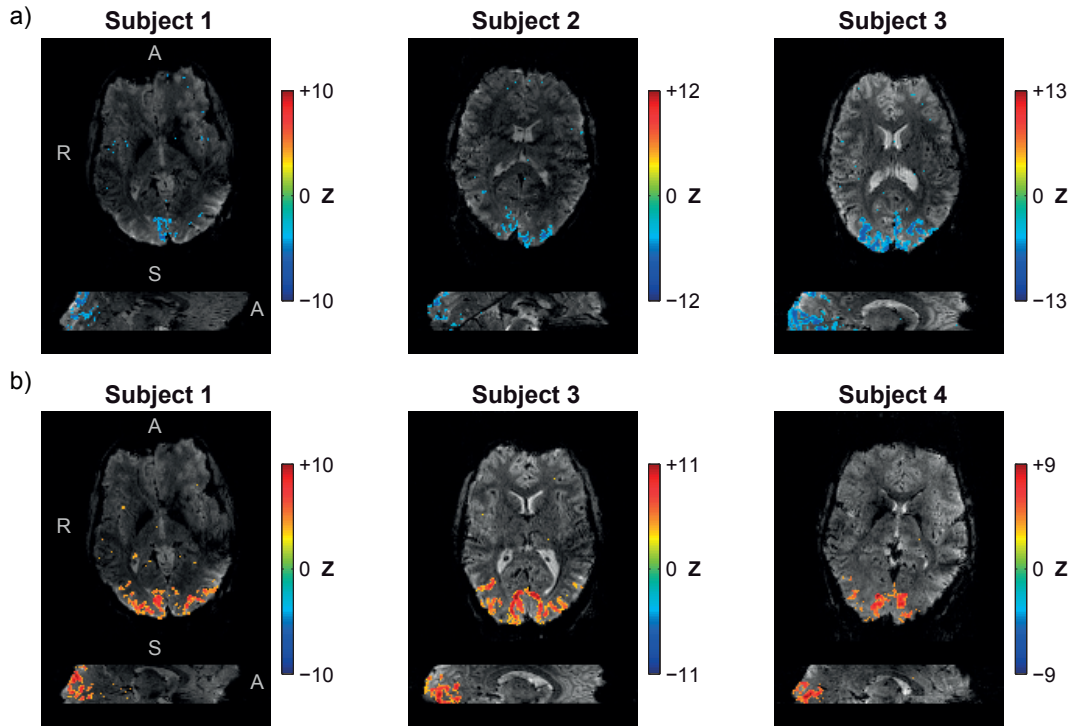


Figure 5.10: BOLD responses to (a) an eyes-open/eyes-closed task and (b) a reduced-field reversing checkerboard stimulation run, expressed as Z-score statistical maps, for the same subjects presented in Fig. 5.8 and Fig. 5.9. **a)** Negative values reflect negative BOLD signal changes during eyes-closed periods; maps were thresholded at $Z = -3.5$. **b)** Positive values reflect positive signal changes during checkerboard stimulation periods; maps were thresholded at $Z = +3.5$. Color bar ranges were manually restricted for clearer visualization.

in the alpha band was clearly identifiable in most EEG channels, including those adjacent to the reference electrode (Fz, Cz, FC1, FC2), but not on the motion sensors; accordingly, the temporal correlation between motion timecourses and EEG timecourses was, on average, 0.04 ± 0.02 . The impact of the sensor modification on fMRI data quality was found negligible, adding no visible susceptibility artifacts to the images; a white matter temporal SNR of 19 ± 1 was estimated for this subject group, whereas a value of 17 ± 1 had been obtained in previous work, described in Chapter 3, with a group of similar size and the same MRI acquisition parameters, using a non-modified EEG setup.

5.6.1 Part I: pulse and motion artifact correction

The impact of motion artifact correction with M-RLS was clearly visible in both the temporal and spectral domains of each subject dataset, even when pulse artifact correction had been applied beforehand with AAS (see Fig. 5.11 for an example). The three correction approaches (AAS, M-RLS and AAS+M-RLS) also brought appreciable changes to VEP morphologies across the scalp for each subject.

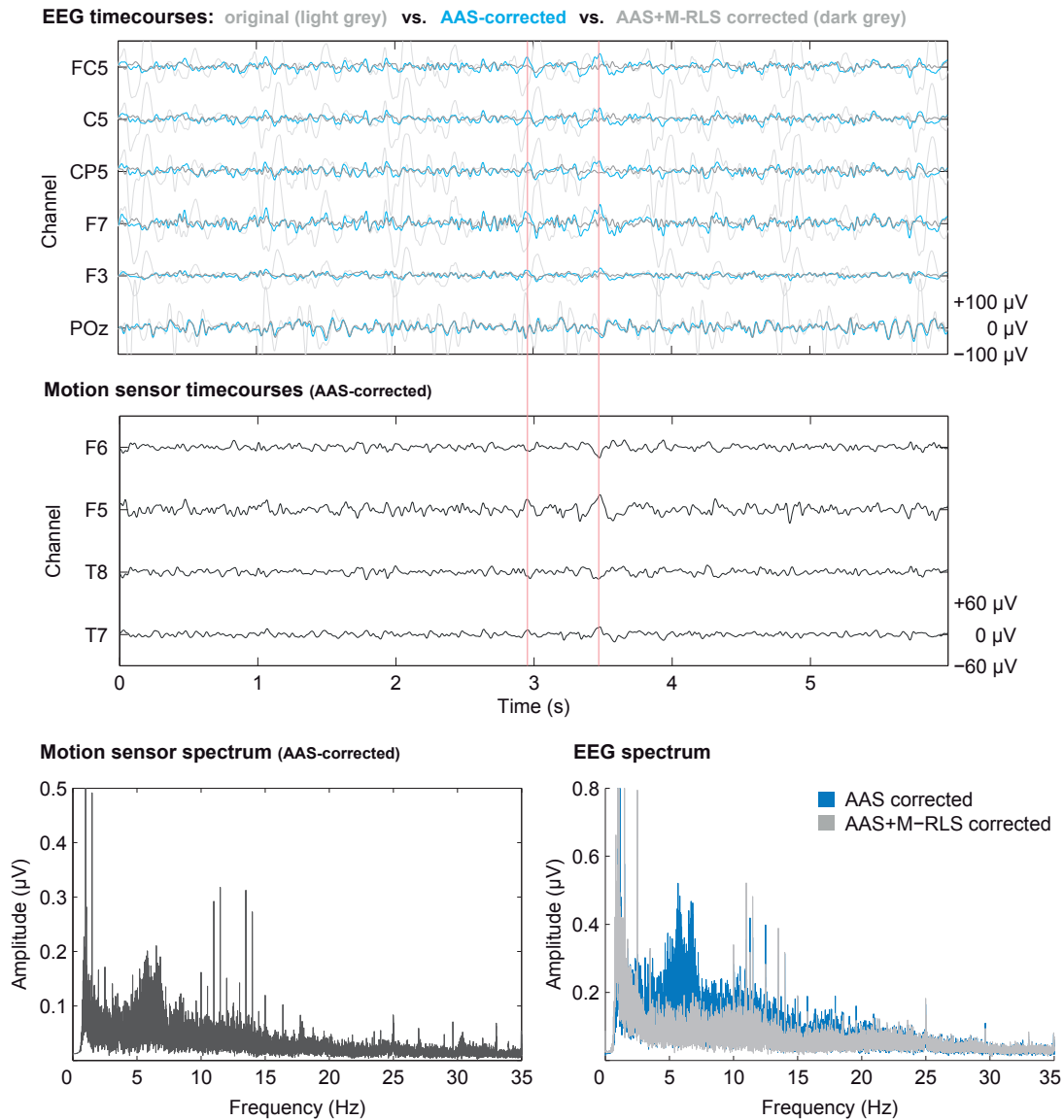


Figure 5.11: The impact of AAS and M-RLS artifact correction on EEG data from one representative subject, in the temporal and spectral domains. The timecourses shown correspond to EEG channels close to motion sensors F5 and T7, along with an occipital channel (POz). The impact of motion correction in the channels close to F5 and T7 is visibly consistent with the fluctuations observed in the motion timecourses (examples are marked by red lines). The spectra shown correspond to the average spectrum in motion sensors and in EEG channels, respectively, across the whole timecourse; as in the time domain, the impact of M-RLS is clearly visible and consistent with the profile of the motion sensor spectrum.

To evaluate the impact of AAS, M-RLS and AAS+M-RLS, the corrected and uncorrected data were compared in terms of signal power and VEP trial consistency. Across delta, theta, alpha and beta bands, all three approaches produced statistically significant reductions in signal

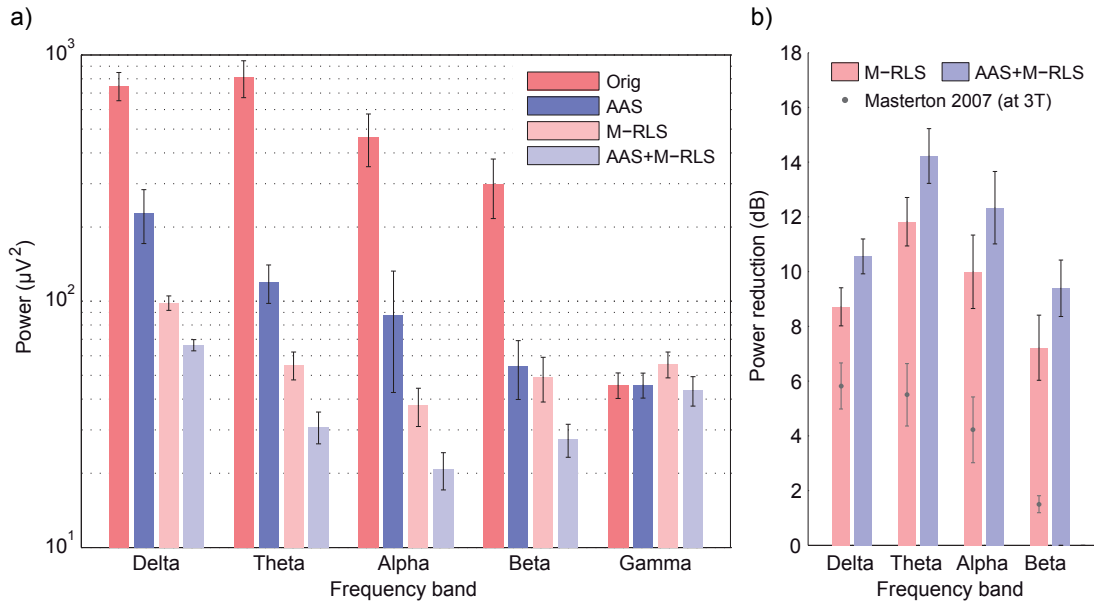


Figure 5.12: The impact of AAS-based pulse artifact correction and M-RLS motion artifact correction on EEG signal power, after gradient artifact correction. **a)** Average EEG power per frequency band, before correction and after AAS, M-RLS, or AAS followed by M-RLS. **b)** Relative power reduction achieved with M-RLS or with AAS followed by M-RLS, relative to pre-processed, uncorrected data; values obtained in a previous study using M-RLS at 3 T (Masterton et al., 2007), without prior AAS, are included for comparison. Bar heights represent averages across channels and subjects, and error bars represent the standard error across subjects; frequency band definitions are reported in section 5.4.3.

power, with M-RLS performing more effectively than AAS, but the combination of AAS followed by M-RLS achieving the largest power reductions (Fig. 5.12a). For the gamma band, no significant changes in power were found for any of the approaches. Compared to results obtained at 3 T using a similar M-RLS implementation (Masterton et al., 2007), the power attenuation achieved (without prior pulse correction) was approximately $1.5\times$ larger in the delta band, $2.3\times$ larger in the theta and alpha bands, and $4.8\times$ larger in the beta band, at 7 T (Fig. 5.12b).

Across subjects, full-band EEG signal power achieved its lowest average value with the combination of AAS and M-RLS, corresponding to a $91 \pm 1\%$ reduction relative to the uncorrected data (Fig. 5.13a). The power achieved with the combined approach was significantly lower than with each method separately. An equivalent outcome was found for VEP trial consistency, with the combination of AAS and M-RLS yielding an average increase of $55 \pm 5\%$ in consistency Z-score (Fig. 5.13b). The value achieved was significantly higher than with AAS alone, and also superior to M-RLS alone, although not reaching significance ($p = 0.12$). Regarding full-band power distributions across the scalp, the original (preprocessed) data exhibited a strong concentration of power at the most lateral electrodes, along with a more moderate presence at occipital electrodes (Fig. 5.13c). Across the scalp, the use of AAS appeared to have

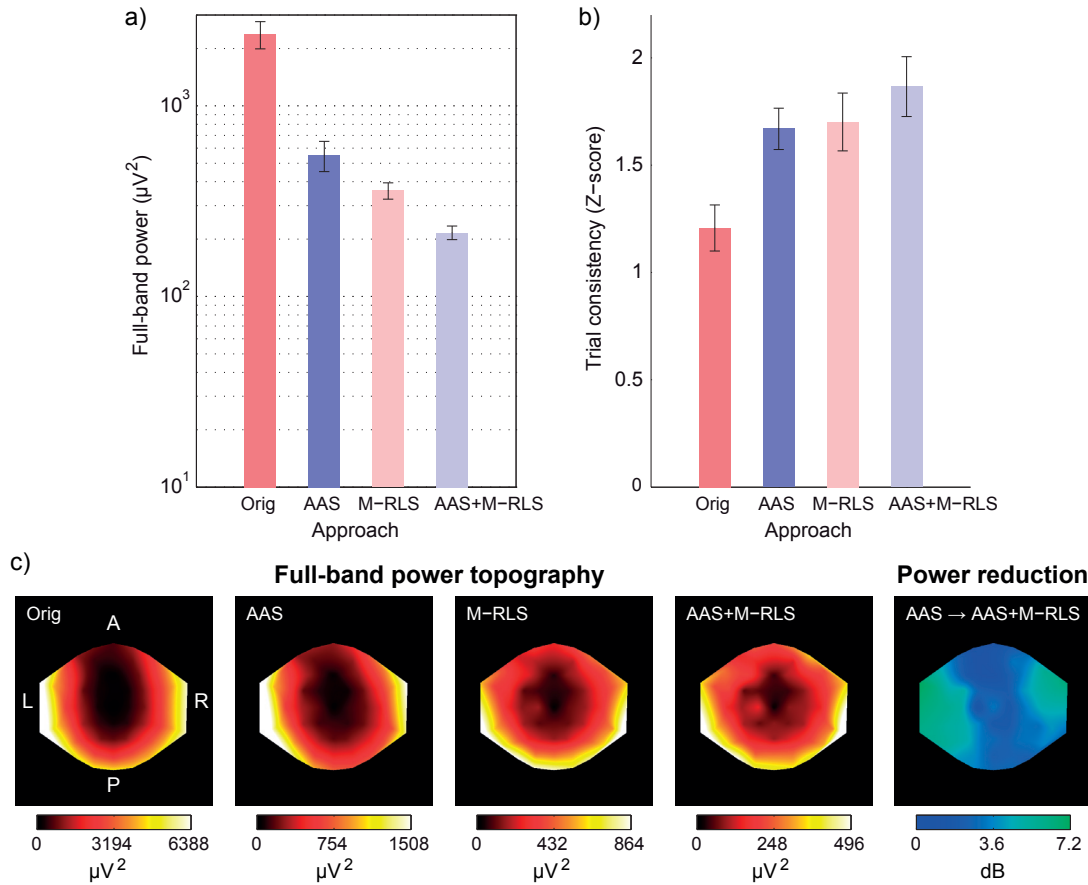


Figure 5.13: The impact of AAS-based pulse artifact correction and M-RLS motion artifact correction on **a)** EEG signal power and **b)** VEP trial consistency, after gradient artifact correction. Bar heights represent averages across channels and subjects, and error bars represent the standard error across subjects. **c)** Subject-averaged full-band power topographies before (Orig) and after corrections (AAS, M-RLS, AAS+M-RLS), and the relative power reduction achieved with M-RLS after AAS correction (please note different scales on the color bars).

a higher impact on occipital electrodes, while M-RLS produced stronger changes in more lateral electrodes. The combination of both approaches led to the most balanced, radial power distribution (centered at the reference electrode). The power attenuation achieved by M-RLS, after AAS correction, was confirmed to be strongest at more lateral regions (Fig. 5.13c, right).

5.6.2 Part II: optimization of motion artifact correction

Regarding model optimization, the preliminary tests performed for each subject, iterated in steps of 5 added shifts, indicated optimal kernel sizes of 11–61 regressors per motion sensor (41, 11, 61, 41, 61 and 21 for subjects 1–6, respectively), centered at $\Delta t = 0$ and spanning both positive and negative shifts in steps of 4 time samples (i.e. -80, -64, -48, -32, -16, 0, +16, +32, +48, +64, +80 ms for subject 2, for example). Regarding the BLS approach, the three bases

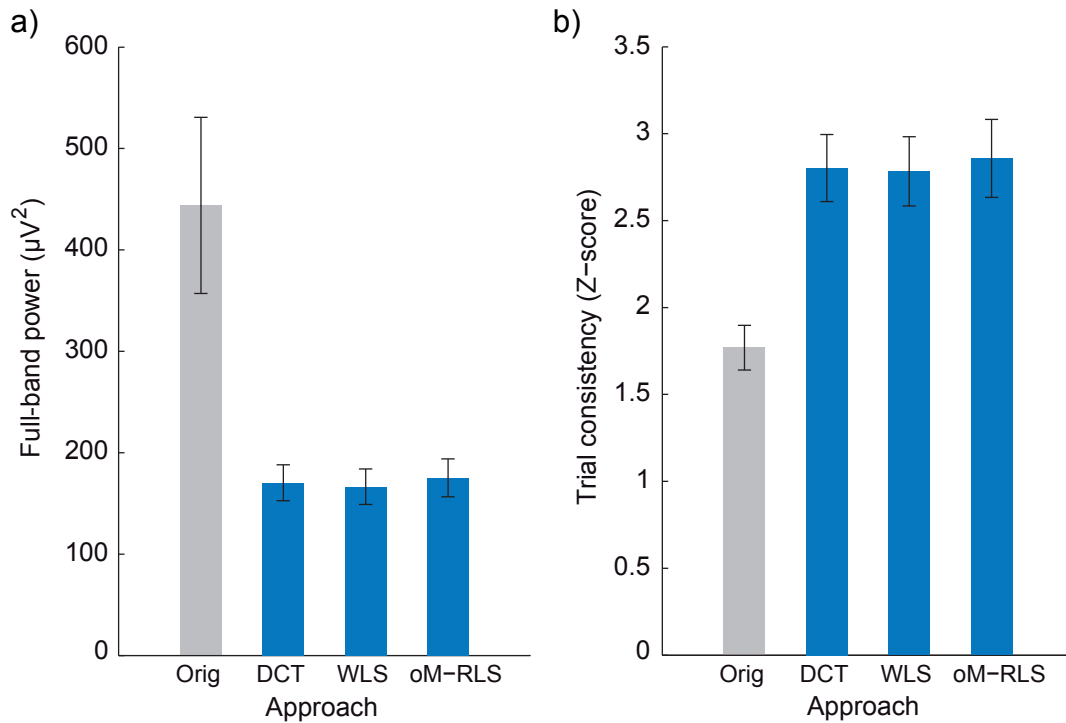


Figure 5.14: The impact of motion artifact correction on **a)** EEG signal power and **b)** VEP trial consistency, after gradient and AAS-based pulse artifact correction. The techniques tested included DCT-based BLS, sliding-window WLS and oM-RLS. Bar heights represent averages across channels and subjects, and error bars represent the standard error across subjects.

tested yielded very similar results for this subject group, and as such only the simplest, DCT, was considered for further comparisons. For this basis set, an expansion up to 2nd degree (cosine period equal to the total timecourse length) showed a good compromise between temporal adaptability and model size.

Following optimization, the different approaches developed for motion artifact correction (DCT-based BLS, WLS and oM-RLS) were applied to the data and then compared in terms of signal power and trial consistency. All three approaches achieved statistically significant power reductions of $62 \pm 4\%$ (DCT), $63 \pm 4\%$ (WLS) and $61 \pm 4\%$ (oM-RLS), relative to the preprocessed, pulse-corrected data (Fig. 5.14a). Analogously, in trial consistency, these approaches led to significant improvements of $58 \pm 15\%$ (DCT), $57 \pm 14\%$ (WLS) and $62 \pm 17\%$ (oM-RLS) in consistency Z-score (Fig. 5.14b). No significant differences between the three correction approaches were found for either measure. Alongside group-average effects, motion artifact correction produced clear improvements on visual response quality at the level of individual subjects – a detailed description is given below in part III (section 5.6.3 and Fig. 5.17).

The characterization of signal variance contributions yielded consistent results across the subject group, with pulse artifact contributions explaining 81–93% of the total variance, while

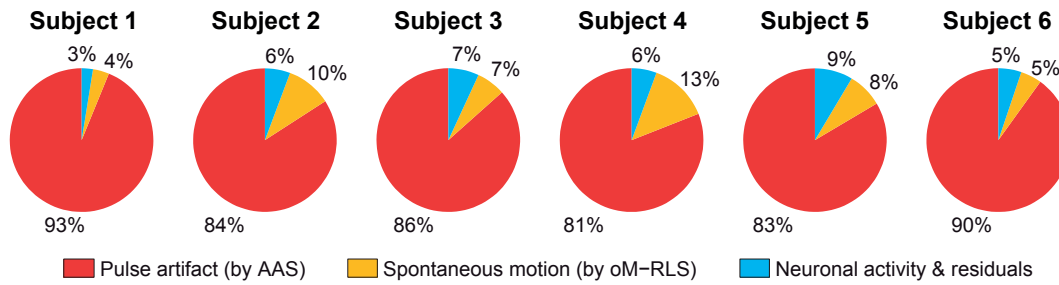


Figure 5.15: EEG signal power distribution after gradient artifact correction, based on AAS pulse artifact correction and oM-RLS motion artifact correction. The percentages shown for each subject correspond to averages across EEG channels. As should be noted, these estimates were obtained based on the outcome of the artifact correction procedures, and as such are not perfect; in particular, the estimates for spontaneous motion contributions are expected to contain residuals of pulse artifacts, and vice versa.

spontaneous motion artifacts and actual neuronal activity (plus residual artifacts) expressed more moderate contributions of 4–13% and 3–9%, respectively (Fig. 5.15). Overall, spontaneous motion contributions were comparable or superior to neuronal contributions in this subject group.

5.6.3 Part III: motion artifact correction and ICA

To evaluate the performance of ICA, miICA and oM-RLS artifact correction, the corrected and uncorrected data of all subjects were analyzed in terms of signal power and VEP trial consistency. On average, full-band EEG power was reduced by $53 \pm 5\%$ with miICA, $60 \pm 4\%$ with ICA, $61 \pm 4\%$ with oM-RLS, and $74 \pm 3\%$ with oM-RLS followed by ICA, relative to the preprocessed pulse-corrected data (Fig. 5.16a). The EEG power achieved with the combined approach was significantly lower than with individual methods. Regarding VEP trial consistency, the average Z-score was increased by $12 \pm 11\%$ with miICA, $37 \pm 15\%$ with ICA, $62 \pm 17\%$ with oM-RLS, and $86 \pm 19\%$ with oM-RLS followed by ICA (Fig. 5.16b). The value achieved with the combined approach was significantly higher than with miICA and oM-RLS alone, and tended to be superior to ICA as well ($p = 0.06$). The outcome of oM-RLS alone was significantly superior to that of miICA and, on average, also tended to be superior to ICA.

Besides group-average effects, motion artifact correction also yielded clear improvements on visual response quality for each individual subject (Fig. 5.17). In several cases, oM-RLS effectively enabled the recovery of the main expected features of the VEP response, including the larger P100 component and even the more subtle N75 and N140 components. Scalp topographies at the timing of the P100 component were also improved considerably, showing a clearer anterior-posterior dipole and minimal left-to-right asymmetries. While trial-average responses were more drastically corrected in lateral channels, single-trial responses were still visibly improved in occipital channels, allowing for the detection of P100, N75 and N140

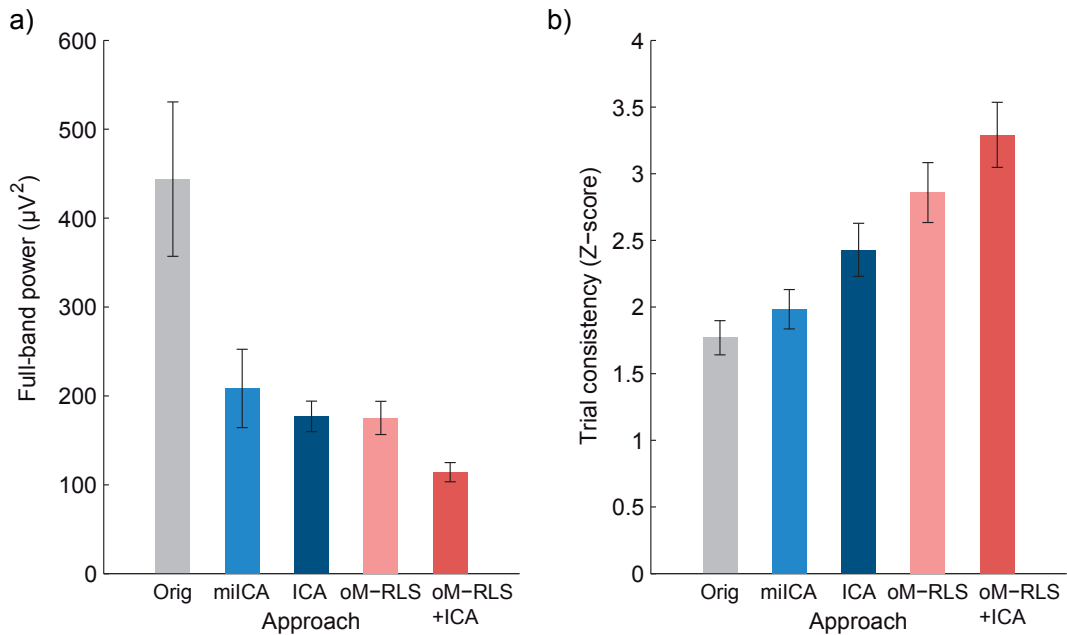


Figure 5.16: The impact of ICA denoising and oM-RLS motion artifact correction on **a)** EEG signal power and **b)** VEP trial consistency, after gradient and AAS-based pulse artifact correction. The approaches tested comprised ICA, with and without including the motion sensor time-courses (miICA, ICA), oM-RLS, and oM-RLS followed by ICA. Bar heights represent averages across channels and subjects, and error bars represent the standard error across subjects.

components in a large fraction of trials. The use of ICA after oM-RLS further added smaller, yet important benefits to signal quality, especially at a single-trial level (Fig. 5.17).

5.7 Discussion

The work presented in this chapter, devoted to the assessment and improvement of EEG data quality acquired concurrently with fMRI, at 7 T, was organized in two main studies. The first study demonstrates clear benefits in EEG cable shortening and bundling for artifact prevention, at the level of signal transmission between collection (EEG cap) and amplification (after which the signals are digitized). An optimized acquisition setup with ultra-short bundled transmission cables was implemented, and tested in simultaneous acquisitions on a group of 5 volunteers. The resulting data were analyzed to assess trial-average and single-trial response detection sensitivity.

In the second study, a novel technique for online measurement of EEG head motion artifacts was developed and implemented for simultaneous EEG-fMRI at 7 T. Data were collected from 6 healthy subjects, and several aspects of post-processing artifact reduction methodology were analyzed, aiming for optimal data quality improvements using the motion information. The impact of spontaneous motion artifacts on EEG data at 7 T was for the first time quantitatively

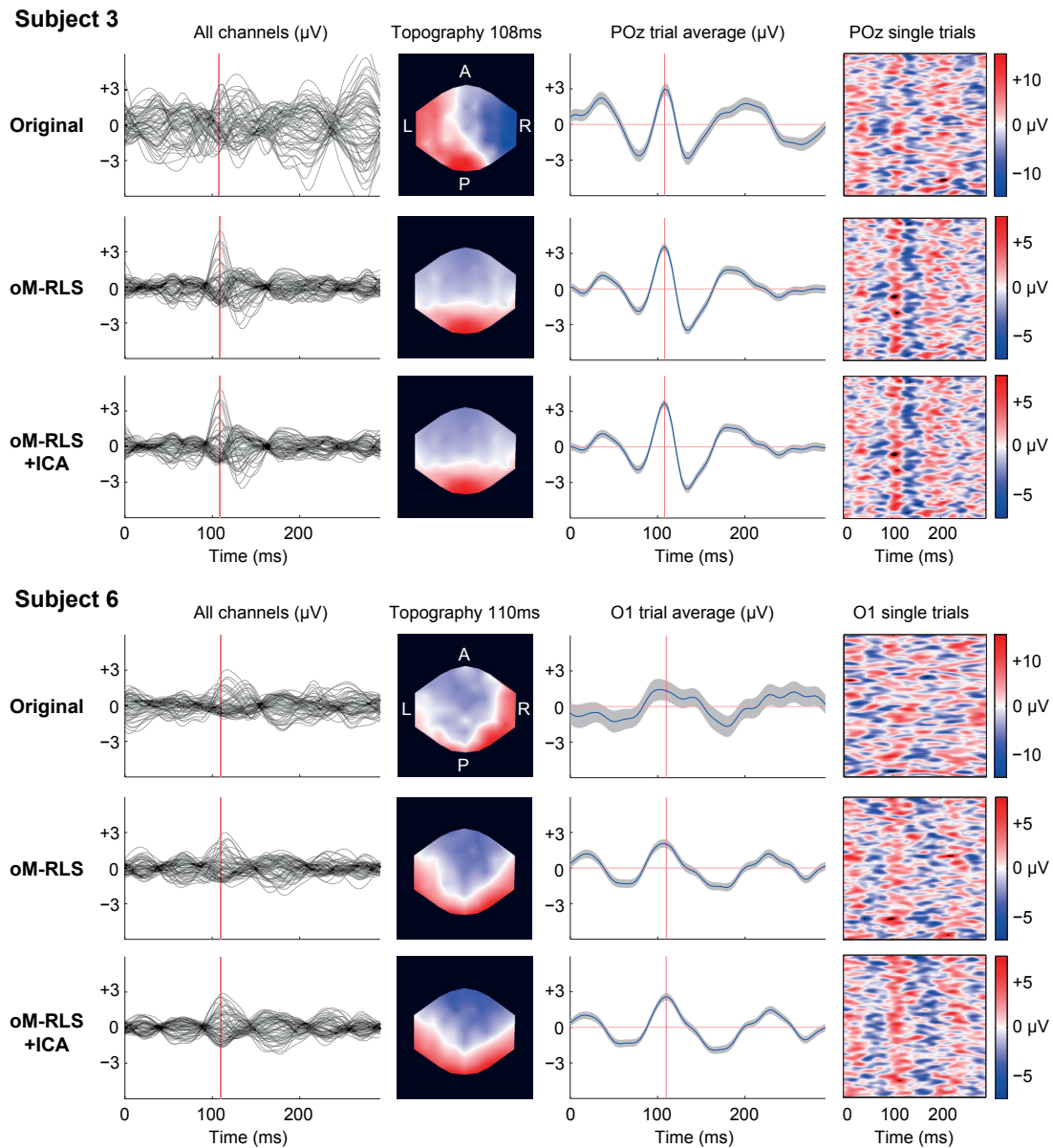


Figure 5.17: EEG responses to visual stimulation with reversing checkerboards, in two subjects, before and after correction with oM-RLS, and with oM-RLS followed by ICA. These subjects were chosen for illustration because in Subject 3, motion artifact correction provided the largest quality improvements, while in Subject 6 the benefits added by ICA were also considerably relevant. The scalp topographies shown correspond to the P100 component of the VEP, and are presented in a blue-white-red color scale centered at 0 V, with symmetric limits. The shaded margins in single-channel trial-averaged responses (3rd column) indicate the standard error across trials; the channel displayed was selected for having the largest average P100 amplitude amongst the occipital channels. All 330 single-trial responses are shown, with Gaussian smoothing across trials ($\sigma = 3$ trials).

assessed, and significant improvements in visual response sensitivity were achieved with artifact reduction.

5.7.1 EEG signal transmission optimization

The noise measurements performed in the first study provide clear insights into the importance of EEG setup optimization. Consistent with previous studies (Mullinger et al., 2008a), the He coldheads were shown to have a major impact on EEG recordings performed at 7 T, producing the largest noise contributions in the absence of gradient, pulse, and subject motion artifacts. Spanning a wide range of frequencies, well within the relevant EEG domain, coldhead-related contributions exhibited complex spectral profiles that are likely to depend on a multitude of properties of the overall mechanical system linking the coldheads, EEG amplifiers, patient bed and the patient itself. While these contributions can be fully avoided by switching off the compression systems during acquisition (Mullinger et al., 2008a; Ritter et al., 2010), this procedure is simply not allowed in many clinical and research sites, and becomes increasingly prohibitive as He availability decreases worldwide (Nuttall et al., 2012).

While initial developments have been presented to reduce vibration-related artifacts via post-acquisition data analysis (Rothlubbers et al., 2013), these approaches remain largely unexplored. Notably low coldhead-related contributions have been reported for a 9.4 T human scanner in which the coldheads are mounted on extended turrets and not directly on the magnet vessel (Neuner et al., 2014). While highly advantageous, this configuration is currently also rather unique. In this work, we directed our focus to the EEG acquisition system. The clear dependence of noise power on channel loop areas (Fig. 5.4) provided yet another indication that electromagnetic induction is the fundamental mechanism mediating coldhead-related noise propagation, and possibly of other environment sources. By reducing loop areas along the EEG transmission cables, significant improvements in signal quality were achieved through relatively simple modifications, which are inexpensive compared to the long-term costs of scanning with the coldheads switched off, or even modifying their placement. Furthermore, although not directly assessed in this work, gradient artifacts and a part of pulse artifacts are likewise strongly thought to be caused by magnetic induction effects on the EEG wire loops (Allen et al., 1998, 2000; Chowdhury et al., 2012; Mullinger et al., 2013a). As such, cable bundling is also likely to have significantly reduced the impact of these important noise sources at the level of EEG transmission cables. The effects of cable shortening, while probably also favorable for pulse artifact reduction, are more complex for gradient artifacts, as longer cables may in some scanners reach a point where the gradient profile has become inverted, and thus benefit to some extent from flux cancellation effects.

Naturally, given the site-specificity of vibration-related noise contributions, the results obtained in this study cannot be directly translated to other EEG-fMRI setups, which may differ in coldhead configuration, scanner and patient bed architecture, \vec{B}_0 field distribution, and even surrounding equipment that may propagate vibrations to the scanner room. Likewise,

the variations seen within this study are likely to have been affected not only by differences in cable length and geometry but also by properties such as stiffness and mass (for example, bundled cables tended to be stiffer than flat cables). This may explain some of the differences in spectral distribution (apart from overall power) observed for different cable configurations (Fig. 5.5). Another aspect of great importance is the extent to which the EEG setup can actually be shortened without affecting the operation of the amplifiers. As reported in Chapter 3, for this particular setup, using shielded amplifiers and a head-only MRI system, equipped with short gradients and a Tx/Rx head RF array, it was possible to conduct simultaneous acquisitions at 7 T with the amplifiers placed just outside the RF coil, even with spin-echo EPI. While the \vec{B}_0 field extent does not significantly influence amplifier heating, and many imaging centers are equipped with head Tx/Rx arrays for imaging, short gradients are less common and may play an important role in this setup – although the EEG amplifiers were actually positioned already inside the gradient region (Fig. 5.1). In general, it is likely that each particular EEG-MRI system configuration will require specific cable shortening tests prior to human studies, with gradual amplifier repositioning, or gradual increases in gradient slew-rates and RF power.

Finally, it is important to note that the noise reductions reported in the present study, while considerably large, are ascribed only to the contributions arising from the cables themselves. Loop areas formed by the leads on the cap surface remain at play and will still contribute to noise. Nonetheless, minimizing cable contributions is an important achievement by itself, and a potentially valuable step to improve the validity of various noise modeling and correction techniques already proposed in the literature, as well as the motion correction approaches proposed in the second study, which focus mainly on the cap and assume negligible contributions from the following connection cables (Masterton et al., 2007; Yan et al., 2010).

5.7.2 Optimized EEG-fMRI acquisitions

In addition to this work, only a handful of studies so far have conducted simultaneous EEG-fMRI acquisitions in humans above 4 T (Vasios et al., 2006; Mullinger et al., 2008a; Brookes et al., 2009). Following prior safety assessments on phantom and numerical models, human recordings proceeded without any indication of heating. Clear average EEG responses were observed for most subjects over both eyes-open/closed and VEP runs, coherent with the patterns expected for the respective paradigms (Pfurtscheller and Lopes da Silva, 1999; Skrandies, 2005).

At a single-trial level, response detection sensitivity was considerably different for the two runs: in the eyes-open/closed task, alpha power variations could be clearly observed over most blocks in 3 of the 4 subjects, while for the VEP run only approximately half of the trials in each run/subject exhibited statistically significant responses. These discrepancies in sensitivity may be related to the nature of the elicited responses: alpha power modulation via eyes-closing tasks is known to be a strong and robust effect, which has been successfully observed at

fields up to 9.4 T (Neuner et al., 2013). In contrast, the checkerboard stimuli used in this study were presented with a reduced FOV, likely to elicit weaker responses which are harder to decouple from artifacts and ongoing neuronal activity (ACNS, 2006). On the other hand, alpha fluctuations occur at a frequency range (8–12 Hz) which lies above the major part of pulse artifact contributions and below the major part of gradient artifact contributions, a factor which may have also favored this difference. Also worthy of note, visual stimulation in the VEP paradigm was phase-locked with slice acquisition every 25 slices, rendering gradient artifact correction potentially more susceptible to remove VEP signal. This was addressed with a fairly EEG-conservative AAS approach, using fixed gaps between averaged slices of 400 ms to mitigate the reduction of correlated EEG activity (Niazy et al., 2005), combined with random jittering to reduce phase locking with the VEP. The adopted spacing in turn required averaging over relatively large time windows (approximately 20s), leading to a certain compromise in adaptability to changes in the artifact profile. This limitation was potentially relevant in cases where the artifact was less stationary, such as due to frequent subject motion, although artifact residuals were still further reduced by OBS and temporal bandpass filtering, and were not found to be problematic in these data.

It is also important to note that the use of ICA for denoising in these datasets, while undeniably valuable, can be compromised by the fact that motion artifacts, including residual pulse artifacts and spontaneous subject movements, are not truly stationary sources, especially at high field (Debener et al., 2008), and thus may not be adequately separable from true neuronal sources. Given the importance of response sensitivity at a single-trial level for simultaneous EEG-fMRI, it is desirable to further explore this question in future work, for example by comparing responses to checkerboards of different FOV/contrast, and exploring alternative denoising techniques such as iterative ICA (Iyer and Zouridakis, 2007), wavelet-based approaches (Quiñero Quiroga and Garcia, 2003), or beamformer methodologies (Brookes et al., 2009).

Data from fMRI acquisitions exhibited clear responses in both functional runs for all but one subject, with significant paradigm-related signal changes arising, as expected, in visual areas (Fig. 5.10). In the eyes-open/closed run, the 4th subject showed neither task-related alpha power variations nor BOLD signal changes, suggesting non-compliance with the task. In general, the robustness of the elicited responses suggests that the \vec{B}_1^+ disruption effects observed in Chapter 3, while clearly reducing image SNR in the parietal lobe, did not hinder BOLD sensitivity in the occipital cortex. This discrepancy may be due to the distinct spatial localization of the two regions, but may also be related to the inherent differences between spatial SNR and functional sensitivity (temporal SNR), as previously mentioned, especially given the importance of signal-dependent physiological noise contributions at higher fields. In any case, this outcome follows the trend observed in various other studies at lower fields, with diverse types of stimuli, reporting little to no effects of the presence of the EEG system on BOLD sensitivity (Bonmassar et al., 2001; Lazeyras et al., 2001; Luo and Glover, 2012).

5.7.3 Motion artifact detection

The impact of spontaneous head motion on EEG recordings performed in strong magnetic fields is a well-known problem in EEG-fMRI studies (Flanagan et al., 2009; Jansen et al., 2012), most often addressed simply by excluding affected periods from data analysis, and in the worst cases discarding entire datasets. This approach incurs losses in acquisition time and costs, and tends to become less effective in acquisitions performed at higher magnetic fields. As discussed here (sections 5.1.3 and 5.2.2) and in previous studies (Debener et al., 2008; Yan et al., 2010), motion artifacts are based on magnetic induction effects that scale with \vec{B}_0 . In this work, at 7 T, it was estimated that contributions to signal variance from spontaneous motion artifacts are comparable to or even larger than those of actual neuronal activity (Fig. 5.15). The main artifact contributions were associated with the MRI gradients and the cardiac cycle, but while these contributions are approximately periodic, and thus more suited to temporal segmentation for averaging and subtraction, spontaneous motion does not follow regular patterns, and can thus highly benefit from an external monitoring system.

Several approaches for head motion detection have been proposed, including the use of highly sensitive optical systems (Maclaren et al., 2012), piezoelectric sensors (Bonmassar et al., 2002), and conductive wire loops (Masterton et al., 2007). Loop-based sensors were chosen in this work since they share similar mechanisms of artifact generation with EEG loops, and can be directly incorporated in linear regression models for EEG signal correction (as shown in section 5.2.2). Similar to Masterton et al. (2007), the present approach used multiple conductive loops distributed across the scalp, but while their approach uses a separate acquisition and recording system for the loops, these sensors were here implemented by adapting a number of electrodes from the EEG cap. This approach is not limited for use at 7 T, and requires neither additional amplification, gel layers or other recording equipment, nor modifications to the existing amplifiers, which are often the most expensive component of the EEG setup. While the cap adaptations, as implemented in this study, were non-permanent and set in place during each cap preparation, there should be no impediments in the design of new cap models with these modifications permanently integrated. In particular, based on the tests conducted with the current implementation, a modification with a similar number of sensors and resistor types is expected to have a negligible impact on either EEG or fMRI data quality. As a benefit, a permanent modification would not only save preparation time but also allow for a more geometrically optimal placement of the sensors (Abbott et al., 2014), which here was limited to the positions of the existing EEG electrodes. It should be noted that these sensors are connected to the reference electrode, and are thus not electrically isolated from the scalp. As such, an additional resistor was included in each connection to ensure subject safety, resulting in a total resistance of 25 k Ω for each motion loop (considering the two 5 k Ω resistors inserted in each channel lead), not including the resistance of gel interfaces between the electrodes and the skin. It is also important that the input impedance of the amplifiers is sufficiently high to ensure that currents in the leads created by true neuronal activity are effectively negligible, so that the potential difference measured between each motion sensor and the reference will effectively comprise only magnetic induction effects.

Finally, since under certain assumptions EEG artifacts due to rigid-body head motion only depend on two degrees of freedom (head rotations, as described in section 5.2.2), it should be pointed out that motion artifact reduction could potentially be performed using only two independent sensors. Nevertheless, here, as in previous studies (Masterton et al., 2007; Luo et al., 2014), an "overdetermined" detection approach was adopted instead, to ensure more robust estimations and for a higher sensitivity to eventual non-rigid motion effects – with the disadvantage of leaving less electrodes for actual EEG recording. Future studies may focus on the optimization of both the number and position of motion loops, possibly based on numerical simulations (Yan et al., 2010; Mullinger et al., 2014a), towards the design of optimally effective motion sensor loops. The importance of minimizing noise contributions at the transmission stage between the cap and amplifiers should also be stressed, as these sources do not follow rigid-body properties. In the current, optimized setup, such contributions have been minimized by appropriate cable shortening and bundling, as described in the first study of this chapter.

5.7.4 Motion artifact correction

Motion information can be used in various ways for data analysis, a simple and direct option being to use the sensor timecourses as an independent measure of head motion, which can guide epoch exclusion and help determining whether particular fluctuations can effectively be attributed to neuronal activity (Abbott et al., 2014). Here, the sensor timecourses were used to reduce motion contributions throughout the EEG timecourses. The linear relationships between the artifacts captured by loop sensors and EEG channels (as described in section 5.2.2) render them particularly suitable for linear regression methods, which were systemically explored in this work, in line with previous studies (Masterton et al., 2007; Luo et al., 2014). It should be noted that this type of approach relies on the assumption that motion artifacts are uncorrelated with neuronal activity (which forms the residuals of the linear fit). This assumption may become compromised in studies involving motor tasks, painful stimulation or attention modulations, for example, where subject motion may be more strongly correlated with the paradigm. Also important, as the weights of the linear relationships depend on the current head position (Eq. 5.4), these linear models incorporated temporally-adaptive coefficients (Eq. 5.5). The approaches here tested assume these coefficients to vary smoothly, and are thus less precise in the presence of large abrupt motion. Conversely, if the coefficients are allowed to adapt too quickly, the estimation may instead become significantly biased by neuronal activity. It was here opted to circumvent this compromise by rejecting the periods of most abrupt motion from data analysis, based on GFP fluctuations. The denoising of such periods would possibly require the use of other methods such as reference layer subtraction, where each electrode has a "copy" placed in the same position but connected to a reference layer, and denoising is performed with a direct signal subtraction, instead of a fit (Chowdhury et al., 2014). This could also be a potentially effective alternative for studies in which motion is expected to strongly correlate with brain activity. On the other hand, this approach requires twice as many recording channels, along with an additional gel layer, and residuals may

still persist due to differences in the current paths across the scalp and across the reference layer; the additional (conductive) components are also more likely to affect MRI data quality (Mullinger et al., 2008b).

An important question investigated in this work regarded the combination of motion and pulse artifact correction (part I). In the acquired subject group, the use of an AAS-based pulse artifact correction step followed by a motion sensor-based correction step was found to be more effective than either of the two techniques alone (Fig. 5.13). Consistent with this, while several studies have assumed the pulse artifact to be mainly caused by bulk head rotation, proposing to reduce both artifact types with motion sensors (Bonmassar et al., 2002; Masterton et al., 2007; Luo et al., 2014), substantial evidence exists for additional contributions to the pulse artifact, including local scalp dilations due to arterial pulsation, and the Hall effect occurring in charged particles carried by the blood as it flows in \vec{B}_0 (Tenforde et al., 1983; Debener et al., 2008). In particular, the Hall effect has evinced more important contributions to pulse artifact variability than head rotation per se, at 3 T (Mullinger et al., 2013a), and all three contributions are expected to scale with field strength. The results obtained here suggest that the additional sources of the pulse artifact do create important contributions at 7 T, which should be addressed with a dedicated correction step. At lower fields, some caution should be taken with this approach, since the prior reduction of pulse artifacts leaves the linear fitting essentially dependent on spontaneous motion fluctuations alone, which at such field strengths may not be sufficiently strong for a robust, unbiased fit (given that brain activity does not scale with \vec{B}_0 , and its correlation with motion is never exactly null). The choice of a dedicated correction should thus be carefully considered depending on the field strength and the performance of each subject group.

Having settled for including a dedicated pulse artifact correction step, the study then focused on determining optimal methods to tackle the contributions from spontaneous motion (part II). The three approaches tested led to similar outcomes in data denoising (Fig. 5.14), but do differ from each other in several aspects. Regarding computational speed, for comparison purposes, in the particular system and implementations used (no parallelization added), BLS took less than 2s to process each 5 min-long, 59-channel dataset, while oM-RLS took approximately 40 min, and WLS took more than 2h. BLS is by far the fastest method and thus most suitable for exploratory tests and model optimization (the FIR kernel, for example); on the other hand, being based on parametric modeling, its adaptability depends on particular dataset properties such as the timecourse length. Sliding-window WLS avoids that limitation and relies on an intuitive adaptability parameter (the window FWHM), but was found to be considerably slower (although parallelization techniques could be applied both across channels and time). Finally, oM-RLS is a non-parametric technique based on a previously validated method for EEG data correction (Masterton et al., 2007), and provided a good compromise between versatility and computational speed, thus motivating some preference for this method. Additionally, the original M-RLS can be used for real-time correction.

5.7.5 Motion artifacts and ICA

The third part of this study compared the performance of motion sensor-based correction with that of ICA denoising, and investigated the benefits of combining the two techniques. ICA is often employed for EEG data analysis and denoising, both in pure EEG studies (Makeig et al., 1996; Onton et al., 2006) and with EEG-fMRI (Marques et al., 2009; Arrubla et al., 2013). In the second case, however, a number of authors have obtained suboptimal results with this approach, especially at fields above 1.5 T (Debener et al., 2007). Similarly, the tests performed here with ICA denoising alone systematically showed inferior results to those obtained with ICA after oM-RLS (Fig. 5.16), even with prior pulse correction applied in both cases. Without oM-RLS, the ICA component explaining the most variance was consistently found to be motion-related, with a left-to-right dipolar topography and low stimulus-locked periodicity. Furthermore, the components associated with visual responses had considerably lower SNR than those obtained after oM-RLS, appearing to be still significantly contaminated with motion artifact contributions. Analogous results were found with miICA, where components attributed to the visual responses frequently exhibited appreciable projections on the motion channels. These issues are currently thought to be due to a violation of source stationarity, one of ICA's most important assumptions: while neuronal sources are measured as stationary (as long as the electrodes retain their positions on the scalp), motion-related artifacts are not. The pulse artifact, for instance, has been shown to increase in both amplitude and spatial variability with field strength (Debener et al., 2008), and the theoretical bases of motion artifacts (section 5.2.2) clearly show their dependence on the current head position, thus varying their topography as head position drifts in time.

Despite the suboptimal performance obtained with ICA alone, its application following oM-RLS did improve data quality. This is not unexpected since motion artifact correction does not cover other typical EEG artifacts (ocular movements, for example), which ICA can effectively isolate. Overall, for the 7 T datasets analyzed in this work, the combination of AAS-based pulse artifact correction, oM-RLS motion artifact correction and ICA denoising yielded optimal improvements in EEG data quality, with well appreciable benefits for visual response sensitivity. These were not only indicated by signal power and trial consistency measures, but also confirmed by direct observation of single subject results, both at trial-average and single-trial levels (Fig. 5.17). Motion artifact correction had a stronger impact on more lateral electrodes (namely FT7–10, TP7–10, F7–8, T7–8, P7–8; Fig. 5.13c), as could be expected since the respective loops have the largest projection areas relative to \vec{B}_0 . Nevertheless, occipital channels still exhibited crucial improvements at a single-trial level.

5.7.6 Conclusion

The results obtained in the first study of this chapter demonstrate important benefits of careful optimization of the EEG signal chain for simultaneous EEG-fMRI. Focusing on the transmission stage between the EEG cap and amplifiers, it was confirmed that both cable

shortening and bundling effectively help reducing cable noise contributions to large extents. Based on human recordings performed under eyes-open/closed tasks and checkerboard stimulation, it can be concluded that alpha-wave modulation, VEPs and the concomitant BOLD signal changes can be detected with adequate sensitivity. The second study builds on the previously optimized setup, and demonstrates clear improvements in EEG data quality through the minimization of motion-induced artifacts using information from independent loop sensors. Three distinct methods for the estimation and correction of motion artifacts were proposed, with generally comparable outcomes, but important differences in speed and adaptability. At 7 T, spontaneous motion contributions to EEG signal variance were found to be comparable to or even larger than those of neuronal activity, and their removal led to strong improvements in the detection of visual responses, particularly at a single-trial level.

6 Conclusions

The results obtained throughout this work offer optimistic perspectives for the implementation of EEG-fMRI at ultra-high fields. This work addressed three main aspects: subject safety, MRI data quality, and EEG data quality – all three essential for the implementation of this multimodal technique. This work was preceded by a pure-fMRI study aiming to characterize human positive and negative BOLD responses to visual stimulation, focusing on visual and auditory negative responses. The observed trends suggested the presence of a highly dynamic system of visual-auditory interactions, sensitive to stimulus contrast and duration. The neuronal correlates of these interactions could not be addressed in higher detail with fMRI alone, yet could potentially be clarified in future work with combined EEG-fMRI.

From the results obtained throughout the EEG-fMRI development work, overall, it can be concluded that simultaneous EEG-fMRI acquisitions can be safely performed in humans at 7 T, and with appropriate modifications in acquisition hardware and data analysis, the quality of the acquired data can be significantly improved, with marked benefits for the detection of relevant functional features at a single-subject, single-trial level.

For the EEG-MRI setup used in this work, the assessment of subject safety and MRI data quality revealed, in both cases, acceptable conditions for human studies. Based on both EM simulations and real temperature measurements, no significant safety concerns were found for the setup tested, using either a volume or a surface head RF coil. The stronger heating effects observed on EEG amplifiers are worthy of note, and possibly arose as a consequence of the compact setup optimization applied to the EEG system. On the other hand, the use of head coils for RF transmission, as opposed to full body coils, is likely to have countered the trend for increased heating to some extent, and overall, the temperature increases remained well within acceptable operating ranges. While the benefits of head-only RF transmission were not systematically assessed in this work, this is likely to be an important factor to prevent EEG hardware damage, and is therefore highly recommended instead of full-body RF transmission.

Regarding MRI data quality when acquired together with EEG, the results obtained show that magnetic susceptibility effects are currently not problematic for fMRI, the associated

signal drops being sufficiently small to remain essentially outside the brain region. In contrast, the disruption of RF field distributions caused by the conductive EEG materials resulted in significant signal losses, especially for central-superior brain regions, and therefore arises as the main cause of EEG-related MR image degradation. Nevertheless, for occipital areas, this effect did not prevent the detection of responses to visual stimulation with relatively high sensitivity (high Z-scores), in agreement with previous studies conducted at lower fields.

In contrast with safety and MRI data quality, EEG data revealed highly-compromising artifact contamination effects that could not be satisfactorily addressed with existing standard approaches, and thus required considerably more attention. An initial study focused on signal transmission between the EEG cap and amplifiers demonstrated important benefits of careful optimization of the EEG signal chain. Its results confirm that both cable shortening and bundling effectively help reducing cable noise contributions to large extents. The use of this setup in human recordings demonstrated favorable sensitivity for alpha-wave modulation and average VEP estimations, albeit with more limited outcomes at a single-trial level. A second study was focused on artifacts created by subject head motion. Building on the previously optimized setup, and integrating information obtained from added loop sensors, the minimization of motion-induced artifacts yielded clear improvements in EEG data quality. At lower fields, the large majority of studies have focused on improving gradient and pulse artifact minimization, with other sources such as motion and environment noise remaining less explored. At 7 T, spontaneous motion contributions to EEG signal variance were found to be comparable to or even larger than those of neuronal activity, and their removal led to strong improvements in the detection of visual responses, particularly at a single-subject, single-trial level. It can thus be concluded that a thorough reduction of exposed loops in signal transmission, and the use of independent sensors for artifact monitoring and reduction, can significantly improve EEG data quality in simultaneous EEG-fMRI, and are therefore highly recommended. It can further be noted that, although especially important at higher field strengths, these modifications can likewise be of significant benefit for studies at lower fields, particularly when probing more subtle EEG features, or dealing with less compliant subjects.

6.1 Outlook

The level of data quality that has currently been achieved appears to be favorable for the start of new acquisitions, more applied to the study of human brain function. Accordingly, we have recently started acquisitions on epilepsy patients, in collaboration with neurologists, with some preliminary results already confirming the feasibility of epileptic source detection at 7 T (Grouiller et al., 2015). Patients with drug-resistant epilepsy often need to undergo surgical interventions, aiming to remove the problematic sources of epileptic activity. The high functional sensitivity and spatial resolution offered by 7 T fMRI could provide crucial improvements in source/network localization, leading to better-informed pre-surgical planning, and thereby potentially more successful outcomes. Preliminary tests have also been directed to the study of resting-state activity, another major application of simultaneous

EEG-fMRI. The added benefits of ultra high-field imaging for resting-state analysis have so far remained relatively little explored, although the increased spatial resolution has proved to yield superior intra-network correlations in certain brain regions (Newton et al., 2012) and more accurate spatial co-registrations for group analysis (De Martino et al., 2011b). On the other hand, the increased functional sensitivity could facilitate the investigation of particular features at a single-subject level, and their comparison to group data (Laumann et al., 2015). Another promising application lies in the study of negative BOLD; as discussed in Chapter 2, the investigation of the electrophysiological correlates of negative BOLD responses may bring crucial insights into the nature and dynamics of these phenomena, their dependence on stimulus intensity and duration, and their interactions with positively-responding regions.

Alongside new applications, as previously mentioned, further developments in various aspects of data acquisition and denoising could still bring additional improvements in data quality. Regarding MRI data, the problem of \vec{B}_1 disruption could potentially be mitigated through the optimization of EEG lead materials (Vasios et al., 2006), resistivity (Angelone et al., 2006), and their geometrical arrangement over the cap. The use of accessory pads composed of dielectric materials, which can significantly alter \vec{B}_1 distributions created in the head (Yang et al., 2006), could also potentially bring relevant improvements. Conveniently, all these factors can be included and tested in EM simulations analogous to those performed in this work. This approach is highly practical for systematic testing and optimization of particular technical aspects, and also advantageous in terms of safety control, since SAR distributions are estimated together with \vec{B}_1^+ for all tested conditions. Moving on to in vivo tests, the field disruption effects, and potential improvements, could then be more thoroughly assessed with data acquired during motor or somatosensory paradigms, for example, where BOLD responses are expected to occur very close to the most affected (central-superior) brain regions, when using the present type of EEG cap and volume RF coil. Compared to visual studies, this would allow a more direct evaluation of worst-case losses in functional sensitivity, and eventual gains with the aforementioned modifications.

Regarding EEG data quality, while significant improvements have been achieved, it is very likely that further advances can still offer important gains in artifact reduction. In fact, despite more than twenty years of methodological developments, which the work described in this thesis has built upon, EEG data recorded during fMRI is still notably inferior in quality to data recorded outside the scanner. This clearly reflects the complexity of EEG artifact reduction in simultaneous EEG-fMRI, especially at higher field strengths. Gradient and pulse artifacts have received considerable attention since the first reports of the technique, and awareness for environment noise and head motion has grown considerably with the pursuit of higher field strengths. An aspect of great importance is the interdependence between gradient and pulse artifacts and head motion artifacts: when motion occurs, specific fluctuations are imposed on the signals, while at the same time, the change in orientation leads to changes in morphology for both gradient and pulse artifacts. While most studies so far have tackled the different artifact types individually, this coupling suggests that a more unified correction approach could be pursued, aiming to deal with all artifact types together while exploiting their

Chapter 6. Conclusions

interdependence, for a more accurate estimation. The ability to monitor head motion during acquisition, as pursued in this work, would likely be an essential step towards this goal. In general, the combination of specific hardware modifications to reduce artifact contamination, together with improved data processing methods for artifact correction, should steadily aid to bring simultaneous EEG-fMRI to satisfactory standards of signal quality, robustness and sensitivity, thereby allowing for the full exploit of the benefits offered by high-field imaging.

Bibliography

- D. F. Abbott, R. A. Masterton, J. S. Archer, S. W. Fleming, A. E. Warren, and G. D. Jackson. Constructing carbon fiber motion-detection loops for simultaneous EEG-fMRI. *Front Neurol*, 5:260, 2014.
- ACNS. Guideline 9b: Guidelines on visual evoked potentials, 2006.
- P. J. Allen, G. Polizzi, K. Krakow, D. R. Fish, and L. Lemieux. Identification of EEG events in the MR scanner: the problem of pulse artifact and a method for its subtraction. *Neuroimage*, 8(3):229–39, 1998.
- P. J. Allen, O. Josephs, and R. Turner. A method for removing imaging artifact from continuous EEG recorded during functional MRI. *Neuroimage*, 12(2):230–9, 2000.
- L. P. Andrade-Valenca, F. Dubeau, F. Mari, R. Zelman, and J. Gotman. Interictal scalp fast oscillations as a marker of the seizure onset zone. *Neurology*, 77(6):524–31, 2011.
- L. M. Angelone, A. Potthast, F. Segonne, S. Iwaki, J. W. Belliveau, and G. Bonmassar. Metallic electrodes and leads in simultaneous EEG-MRI: specific absorption rate (sar) simulation studies. *Bioelectromagnetics*, 25(4):285–95, 2004.
- L. M. Angelone, C. E. Vasios, G. Wiggins, P. L. Purdon, and G. Bonmassar. On the effect of resistive EEG electrodes and leads during 7T MRI: simulation and temperature measurement studies. *Magn Reson Imaging*, 24(6):801–12, 2006.
- J. Arrubla, I. Neuner, D. Hahn, F. Boers, and N. J. Shah. Recording visual evoked potentials and auditory evoked p300 at 9.4t static magnetic field. *PLoS One*, 8(5):e62915, 2013.
- O. J. Arthurs, T. Donovan, D. J. Spiegelhalter, J. D. Pickard, and S. J. Boniface. Intracortically distributed neurovascular coupling relationships within and between human somatosensory cortices. *Cereb Cortex*, 17(3):661–8, 2007.
- S. Assecon, P. Ferrari, and J. Jovicich. A compact setup to improve the quality of EEG data recorded during fMRI. In *Proceedings of the 21st Annual ISMRM Meeting*, Salt Lake City, USA, 2013.
- D. Attwell, A. M. Buchan, S. Charpak, M. Lauritzen, B. A. Macvicar, and E. A. Newman. Glial and neuronal control of brain blood flow. *Nature*, 468(7321):232–43, 2010.

Bibliography

- K. A. Awada, D. R. Jackson, J. T. Williams, D. R. Wilton, S. B. Baumann, and A. C. Papanicolaou. Computational aspects of finite element modeling in EEG source localization. *IEEE Trans Biomed Eng*, 44(8):736–52, 1997.
- A. Babajani and H. Soltanian-Zadeh. Integrated MEG/EEG and fMRI model based on neural masses. *IEEE Trans Biomed Eng*, 53(9):1794–801, 2006.
- A. Babajani-Feremi and H. Soltanian-Zadeh. Multi-area neural mass modeling of EEG and MEG signals. *Neuroimage*, 52(3):793–811, 2010.
- F. Babiloni, D. Mattia, C. Babiloni, L. Astolfi, S. Salinari, A. Basilisco, P. M. Rossini, M. G. Marciani, and F. Cincotti. Multimodal integration of EEG, MEG and fMRI data for the solution of the neuroimage puzzle. *Magn Reson Imaging*, 22(10):1471–6, 2004.
- F. Babiloni, F. Cincotti, C. Babiloni, F. Carducci, D. Mattia, L. Astolfi, A. Basilisco, P. M. Rossini, L. Ding, Y. Ni, J. Cheng, K. Christine, J. Sweeney, and B. He. Estimation of the cortical functional connectivity with the multimodal integration of high-resolution EEG and fMRI data by directed transfer function. *Neuroimage*, 24(1):118–31, 2005.
- P. A. Bandettini, K. K. Kwong, T. L. Davis, R. B. Tootell, E. C. Wong, P. T. Fox, J. W. Belliveau, R. M. Weisskoff, and B. R. Rosen. Characterization of cerebral blood oxygenation and flow changes during prolonged brain activation. *Hum Brain Mapp*, 5(2):93–109, 1997.
- M. Barth and D. G. Norris. Very high-resolution three-dimensional functional MRI of the human visual cortex with elimination of large venous vessels. *NMR Biomed*, 20(5):477–84, 2007.
- R. Becker, M. Reinacher, F. Freyer, A. Villringer, and P. Ritter. How ongoing neuronal oscillations account for evoked fMRI variability. *J Neurosci*, 31(30):11016–27, 2011.
- C. G. Benar, D. Schon, S. Grimault, B. Nazarian, B. Burle, M. Roth, J. M. Badier, P. Marquis, C. Liegeois-Chauvel, and J. L. Anton. Single-trial analysis of oddball event-related potentials in simultaneous EEG-fMRI. *Hum Brain Mapp*, 28(7):602–13, 2007.
- M. Bianciardi, M. Fukunaga, P. van Gelderen, S. G. Horovitz, J. A. de Zwart, K. Shmueli, and J. H. Duyn. Sources of functional magnetic resonance imaging signal fluctuations in the human brain at rest: a 7T study. *Magn Reson Imaging*, 27(8):1019–29, 2009.
- M. Bianciardi, M. Fukunaga, P. van Gelderen, J. A. de Zwart, and J. H. Duyn. Negative BOLD-fMRI signals in large cerebral veins. *J Cereb Blood Flow Metab*, 31(2):401–12, 2011.
- B. Biswal, F. Z. Yetkin, V. M. Haughton, and J. S. Hyde. Functional connectivity in the motor cortex of resting human brain using echo-planar MRI. *Magn Reson Med*, 34(4):537–41, 1995.
- C. Bledowski, D. Prvulovic, K. Hoechstetter, M. Scherg, M. Wibral, R. Goebel, and D. E. Linden. Localizing p300 generators in visual target and distractor processing: a combined event-related potential and functional magnetic resonance imaging study. *J Neurosci*, 24(42):9353–60, 2004.

- F. Bloch. Nuclear induction. *Physical Review*, 70(7-8):460–474, 1946.
- M. Boly, E. Balteau, C. Schnakers, C. Degueldre, G. Moonen, A. Luxen, C. Phillips, P. Peigneux, P. Maquet, and S. Laureys. Baseline brain activity fluctuations predict somatosensory perception in humans. *Proc Natl Acad Sci U S A*, 104(29):12187–92, 2007.
- G. Bonmassar, K. Anami, J. Ives, and J. W. Belliveau. Visual evoked potential (vep) measured by simultaneous 64-channel EEG and 3t fMRI. *Neuroreport*, 10(9):1893–7, 1999.
- G. Bonmassar, N. Hadjikhani, J. R. Ives, D. Hinton, and J. W. Belliveau. Influence of EEG electrodes on the BOLD fMRI signal. *Hum Brain Mapp*, 14(2):108–15, 2001.
- G. Bonmassar, P. L. Purdon, I. P. Jaaskelainen, K. Chiappa, V. Solo, E. N. Brown, and J. W. Belliveau. Motion and ballistocardiogram artifact removal for interleaved recording of EEG and eps during MRI. *Neuroimage*, 16(4):1127–41, 2002.
- L. Boorman, A. J. Kennerley, D. Johnston, M. Jones, Y. Zheng, P. Redgrave, and J. Berwick. Negative blood oxygen level dependence in the rat: a model for investigating the role of suppression in neurovascular coupling. *J Neurosci*, 30(12):4285–94, 2010.
- M. Bouchard and S. Quednau. Multichannel recursive-least-square algorithms and fast-transversal-filter algorithms for active noise control and sound reproduction systems. *Speech and Audio Processing, IEEE Transactions on*, 8(5):606–618, 2000.
- M. Brass, M. Ullsperger, T. R. Knoesche, D. Y. von Cramon, and N. A. Phillips. Who comes first? the role of the prefrontal and parietal cortex in cognitive control. *J Cogn Neurosci*, 17(9):1367–75, 2005.
- J. Britz, D. Van De Ville, and C. M. Michel. BOLD correlates of EEG topography reveal rapid resting-state network dynamics. *Neuroimage*, 52(4):1162–70, 2010.
- M. J. Brookes, J. Vrba, K. J. Mullinger, G. B. Geirsdottir, W. X. Yan, C. M. Stevenson, R. Bowtell, and P. G. Morris. Source localisation in concurrent EEG/fMRI: applications at 7T. *Neuroimage*, 45(2):440–52, 2009.
- G. D. Brown, S. Yamada, and T. J. Sejnowski. Independent component analysis at the neural cocktail party. *Trends Neurosci*, 24(1):54–63, 2001.
- K. Bucher, T. Dietrich, V. L. Marcar, S. Brem, P. Halder, S. Boujraf, P. Summers, D. Brandeis, E. Martin, and T. Loenneker. Maturation of luminance- and motion-defined form perception beyond adolescence: a combined erp and fmri study. *Neuroimage*, 31(4):1625–36, 2006.
- N. A. Busch, J. Dubois, and R. VanRullen. The phase of ongoing EEG oscillations predicts visual perception. *J Neurosci*, 29(24):7869–76, 2009.
- R. B. Buxton. Dynamic models of BOLD contrast. *Neuroimage*, 62(2):953–61, 2012.

Bibliography

- R. B. Buxton, E. C. Wong, and L. R. Frank. Dynamics of blood flow and oxygenation changes during brain activation: the balloon model. *Magn Reson Med*, 39(6):855–64, 1998.
- R. B. Buxton, K. Uludag, D. J. Dubowitz, and T. T. Liu. Modeling the hemodynamic response to brain activation. *Neuroimage*, 23 Suppl 1:S220–33, 2004.
- G. Buzsáki. *Rhythms of the brain*. Oxford University Press, New York, 1st edition, 2006.
- C. Caballero-Gaudes, D. Van de Ville, F. Grouiller, R. Thornton, L. Lemieux, M. Seeck, F. Lazeyras, and S. Vulliemoz. Mapping interictal epileptic discharges using mutual information between concurrent EEG and fMRI. *Neuroimage*, 68:248–62, 2013.
- V. D. Calhoun, J. Liu, and T. Adali. A review of group ica for fMRI data and ica for joint inference of imaging, genetic, and erp data. *Neuroimage*, 45(1 Suppl):S163–72, 2009.
- J. L. Cantero, M. Atienza, R. M. Salas, and C. M. Gomez. Brain spatial microstates of human spontaneous alpha activity in relaxed wakefulness, drowsiness period, and rem sleep. *Brain Topogr*, 11(4):257–63, 1999.
- D. W. Carmichael, S. Vulliemoz, R. Rodionov, M. Walker, K. Rosenkranz, A. McEvoy, and L. Lemieux. Simultaneous intracranial EEG-fMRI in humans suggests that high gamma frequencies are the closest neurophysiological correlate of BOLD fMRI. In *Proceedings of the 19th Annual ISMRM Meeting*, Montreal, Canada, 2011.
- M. Chowdhury, K. Mullinger, and R. Bowtell. Simultaneous EEG-fMRI: evaluating the effect of the cabling configuration on the gradient artefact. In *Proceedings of the 20th Annual ISMRM Meeting*, Melbourne, Australia, 2012.
- M. E. Chowdhury, K. J. Mullinger, P. Glover, and R. Bowtell. Reference layer artefact subtraction (rlas): a novel method of minimizing EEG artefacts during simultaneous fMRI. *Neuroimage*, 84:307–19, 2014.
- A. Christ, W. Kainz, E. G. Hahn, K. Honegger, M. Zefferer, E. Neufeld, W. Rascher, R. Janka, W. Bautz, J. Chen, B. Kiefer, P. Schmitt, H. P. Hollenbach, J. Shen, M. Oberle, D. Szczerba, A. Kam, J. W. Guag, and N. Kuster. The virtual family—development of surface-based anatomical models of two adults and two children for dosimetric simulations. *Phys Med Biol*, 55(2):N23–38, 2010.
- N. M. Correa, T. Eichele, T. Adali, Y. O. Li, and V. D. Calhoun. Multi-set canonical correlation analysis for the fusion of concurrent single trial erp and functional MRI. *Neuroimage*, 50(4):1438–45, 2010.
- C. B. Cunningham, B. G. Goodyear, R. Badawy, F. Zaamout, D. J. Pittman, C. A. Beers, and P. Federico. Intracranial EEG-fMRI analysis of focal epileptiform discharges in humans. *Epilepsia*, 53(9):1636–48, 2012.
- A. M. Dale and E. Halgren. Spatiotemporal mapping of brain activity by integration of multiple imaging modalities. *Curr Opin Neurobiol*, 11(2):202–8, 2001.

- A. M. Dale and M. I. Sereno. Improved localization of cortical activity by combining EEG and MEG with MRI cortical surface reconstruction: a linear approach. *J Cogn Neurosci*, 5(2): 162–176, 1993.
- A. M. Dale, A. K. Liu, B. R. Fischl, R. L. Buckner, J. W. Belliveau, J. D. Lewine, and E. Halgren. Dynamic statistical parametric mapping: combining fMRI and MEG for high-resolution imaging of cortical activity. *Neuron*, 26(1):55–67, 2000.
- T. T. Dang-Vu, S. M. McKinney, O. M. Buxton, J. M. Solet, and J. M. Ellenbogen. Spontaneous brain rhythms predict sleep stability in the face of noise. *Curr Biol*, 20(15):R626–7, 2010.
- J. Daunizeau, C. Grova, J. Mattout, G. Marrelec, D. Clonda, B. Goulard, M. Pelegrini-Issac, J. M. Lina, and H. Benali. Assessing the relevance of fMRI-based prior in the EEG inverse problem: A bayesian model comparison approach. *Ieee Transactions on Signal Processing*, 53(9):3461–3472, 2005.
- J. Daunizeau, C. Grova, G. Marrelec, J. Mattout, S. Jbabdi, M. Pelegrini-Issac, J. M. Lina, and H. Benali. Symmetrical event-related EEG/fMRI information fusion in a variational bayesian framework. *Neuroimage*, 36(1):69–87, 2007.
- T. L. Davis, K. K. Kwong, R. M. Weisskoff, and B. R. Rosen. Calibrated functional MRI: mapping the dynamics of oxidative metabolism. *Proc Natl Acad Sci U S A*, 95(4):1834–9, 1998.
- F. De Martino, A. W. de Borst, G. Valente, R. Goebel, and E. Formisano. Predicting EEG single trial responses with simultaneous fMRI and relevance vector machine regression. *Neuroimage*, 56(2):826–36, 2011a.
- F. De Martino, F. Esposito, P. F. van de Moortele, N. Harel, E. Formisano, R. Goebel, K. Ugurbil, and E. Yacoub. Whole brain high-resolution functional imaging at ultra high magnetic fields: an application to the analysis of resting state networks. *Neuroimage*, 57(3):1031–44, 2011b.
- J. C. de Munck, S. I. Goncalves, L. Huijboom, J. P. Kuijer, P. J. Pouwels, R. M. Heethaar, and F. H. Lopes da Silva. The hemodynamic response of the alpha rhythm: an EEG/fMRI study. *Neuroimage*, 35(3):1142–51, 2007.
- J. C. de Munck, S. I. Goncalves, R. Mammoliti, R. M. Heethaar, and F. H. Lopes da Silva. Interactions between different EEG frequency bands and their effect on alpha-fMRI correlations. *Neuroimage*, 47(1):69–76, 2009.
- S. Debener, C. Kranczioch, C. S. Herrmann, and A. K. Engel. Auditory novelty oddball allows reliable distinction of top-down and bottom-up processes of attention. *Int J Psychophysiol*, 46(1):77–84, 2002.
- S. Debener, M. Ullsperger, M. Siegel, K. Fiehler, D. Y. von Cramon, and A. K. Engel. Trial-by-trial coupling of concurrent electroencephalogram and functional magnetic resonance imaging identifies the dynamics of performance monitoring. *J Neurosci*, 25(50):11730–7, 2005.

Bibliography

- S. Debener, M. Ullsperger, M. Siegel, and A. K. Engel. Single-trial EEG-fMRI reveals the dynamics of cognitive function. *Trends Cogn Sci*, 10(12):558–63, 2006.
- S. Debener, A. Strobel, B. Sorger, J. Peters, C. Kranczioch, A. K. Engel, and R. Goebel. Improved quality of auditory event-related potentials recorded simultaneously with 3-t fMRI: removal of the ballistocardiogram artefact. *Neuroimage*, 34(2):587–97, 2007.
- S. Debener, K. J. Mullinger, R. K. Niazy, and R. W. Bowtell. Properties of the ballistocardiogram artefact as revealed by EEG recordings at 1.5, 3 and 7T static magnetic field strength. *Int J Psychophysiol*, 67(3):189–99, 2008.
- D. K. Deelchand, P. F. Van de Moortele, G. Adriany, I. Iltis, P. Andersen, J. P. Strupp, J. T. Vaughan, K. Ugurbil, and P. G. Henry. In vivo 1h nmr spectroscopy of the human brain at 9.4 t: initial results. *J Magn Reson*, 206(1):74–80, 2010.
- A. Delorme and S. Makeig. EEGLab: an open source toolbox for analysis of single-trial EEG dynamics including independent component analysis. *J Neurosci Methods*, 134(1):9–21, 2004.
- M. F. Dempsey and B. Condon. Thermal injuries associated with MRI. *Clin Radiol*, 56(6):457–65, 2001.
- M. F. Dempsey, B. Condon, and D. M. Hadley. Investigation of the factors responsible for burns during MRI. *J Magn Reson Imaging*, 13(4):627–31, 2001.
- J. A. Detre, W. Zhang, D. A. Roberts, A. C. Silva, D. S. Williams, D. J. Grandis, A. P. Koretsky, and J. S. Leigh. Tissue specific perfusion imaging using arterial spin labeling. *NMR Biomed*, 7(1-2):75–82, 1994.
- A. Devor, P. Tian, N. Nishimura, I. C. Teng, E. M. Hillman, S. N. Narayanan, I. Ulbert, D. A. Boas, D. Kleinfeld, and A. M. Dale. Suppressed neuronal activity and concurrent arteriolar vasoconstriction may explain negative blood oxygenation level-dependent signal. *J Neurosci*, 27(16):4452–9, 2007.
- J. H. Duyn. The future of ultra-high field MRI and fMRI for study of the human brain. *Neuroimage*, 62(2):1241–8, 2012.
- W. A. Edelstein, G. H. Glover, C. J. Hardy, and R. W. Redington. The intrinsic signal-to-noise ratio in nmr imaging. *Magn Reson Med*, 3(4):604–18, 1986.
- F. Eggenschwiler, T. Kober, A. W. Magill, R. Gruetter, and J. P. Marques. Sa2rage: a new sequence for fast b1+ -mapping. *Magn Reson Med*, 67(6):1609–19, 2012.
- T. Eichele, K. Specht, M. Moosmann, M. L. Jongsma, R. Q. Quiroga, H. Nordby, and K. Hugdahl. Assessing the spatiotemporal evolution of neuronal activation with single-trial event-related potentials and functional MRI. *Proc Natl Acad Sci U S A*, 102(49):17798–803, 2005.

- T. Eichele, V. D. Calhoun, M. Moosmann, K. Specht, M. L. Jongsma, R. Q. Quiroga, H. Nordby, and K. Hugdahl. Unmixing concurrent EEG-fMRI with parallel independent component analysis. *Int J Psychophysiol*, 67(3):222–34, 2008.
- T. Ernst and J. Hennig. Observation of a fast response in functional MR. *Magn Reson Med*, 32(1):146–9, 1994.
- Jianqing Fan and Wenyang Zhang. Simultaneous confidence bands and hypothesis testing in varying-coefficient models. *Scandinavian Journal of Statistics*, 27(4):715–731, 2000.
- D. J. Felleman and D. C. Van Essen. Distributed hierarchical processing in the primate cerebral cortex. *Cereb Cortex*, 1(1):1–47, 1991.
- D. Flanagan, D. F. Abbott, and G. D. Jackson. How wrong can we be? the effect of inaccurate mark-up of EEG/fMRI studies in epilepsy. *Clin Neurophysiol*, 120(9):1637–47, 2009.
- M. D. Fox and M. E. Raichle. Spontaneous fluctuations in brain activity observed with functional magnetic resonance imaging. *Nat Rev Neurosci*, 8(9):700–11, 2007.
- A. F. Frangi, W. J. Niessen, K. L. Vincken, and M. A. Viergever. Multiscale vessel enhancement filtering. *Medical Image Computing and Computer-Assisted Intervention - Miccai'98*, 1496:130–137, 1998.
- K. J. Friston, P. Fletcher, O. Josephs, A. Holmes, M. D. Rugg, and R. Turner. Event-related fMRI: characterizing differential responses. *Neuroimage*, 7(1):30–40, 1998.
- K. J. Friston, A. Mechelli, R. Turner, and C. J. Price. Nonlinear responses in fMRI: the balloon model, volterra kernels, and other hemodynamics. *Neuroimage*, 12(4):466–77, 2000.
- M. Fuchs, J. Kastner, M. Wagner, S. Hawes, and J. S. Ebersole. A standardized boundary element method volume conductor model. *Clin Neurophysiol*, 113(5):702–12, 2002.
- G. Garreffa, M. Bianciardi, G. E. Hagberg, E. Macaluso, M. G. Marciani, B. Maraviglia, M. Abbafati, M. Carni, I. Bruni, and L. Bianchi. Simultaneous EEG-fMRI acquisition: how far is it from being a standardized technique? *Magn Reson Imaging*, 22(10):1445–55, 2004.
- J. S. Gati, R. S. Menon, K. Ugurbil, and B. K. Rutt. Experimental determination of the BOLD field strength dependence in vessels and tissue. *Magn Reson Med*, 38(2):296–302, 1997.
- J. Goense, H. Merkle, and N. K. Logothetis. High-resolution fMRI reveals laminar differences in neurovascular coupling between positive and negative BOLD responses. *Neuron*, 76(3):629–39, 2012.
- R. I. Goldman, J. M. Stern, Jr. Engel, J., and M. S. Cohen. Acquiring simultaneous EEG and functional MRI. *Clin Neurophysiol*, 111(11):1974–80, 2000.
- R. I. Goldman, J. M. Stern, Jr. Engel, J., and M. S. Cohen. Simultaneous EEG and fMRI of the alpha rhythm. *Neuroreport*, 13(18):2487–92, 2002.

Bibliography

- S. I. Goncalves, J. C. de Munck, P. J. Pouwels, R. Schoonhoven, J. P. Kuijer, N. M. Maurits, J. M. Hoogduin, E. J. Van Someren, R. M. Heethaar, and F. H. Lopes da Silva. Correlating the alpha rhythm to BOLD using simultaneous EEG/fMRI: inter-subject variability. *Neuroimage*, 30(1):203–13, 2006.
- Javier Gonzalez-Castillo, Colin W. Hoy, Daniel A. Handwerker, Vinai Roopchansingh, Souheil J. Inati, Ziad S. Saad, Robert W. Cox, and Peter A. Bandettini. Task dependence, tissue specificity, and spatial distribution of widespread activations in large single-subject functional MRI datasets at 7T. *Cerebral Cortex*, 2014.
- J. Gotman and P. Gloor. Automatic recognition and quantification of interictal epileptic activity in the human scalp EEG. *Electroencephalogr Clin Neurophysiol*, 41(5):513–29, 1976.
- J. Gotman and F. Pittau. Combining EEG and fMRI in the study of epileptic discharges. *Epilepsia*, 52-4:38–42, 2011.
- M. A. Griswold, P. M. Jakob, R. M. Heidemann, M. Nittka, V. Jellus, J. Wang, B. Kiefer, and A. Haase. Generalized autocalibrating partially parallel acquisitions (grappa). *Magn Reson Med*, 47(6):1202–10, 2002.
- F. Grouiller, L. Vercueil, A. Krainik, C. Segebarth, P. Kahane, and O. David. Characterization of the hemodynamic modes associated with interictal epileptic activity using a deformable model-based analysis of combined EEG and functional MRI recordings. *Hum Brain Mapp*, 31(8):1157–73, 2010.
- F. Grouiller, R. C. Thornton, K. Groening, L. Spinelli, J. S. Duncan, K. Schaller, M. Siniatchkin, L. Lemieux, M. Seeck, C. M. Michel, and S. Vulliemoz. With or without spikes: localization of focal epileptic activity by simultaneous electroencephalography and functional magnetic resonance imaging. *Brain*, 134:2867–2886, 2011.
- F. Grouiller, J. Jorge, F. Pittau, P. Martelli, W. van der Zwaag, C. M. Michel, S. Vulliemoz, M. I. Vargas, and F. Lazeyras. Mapping epileptic networks using simultaneous EEG-MRI at ultra-high field. In *Proceedings of the 23rd Annual ISMRM Meeting*, Toronto, Canada, 2015.
- R. Gruetter. Automatic, localized in vivo adjustment of all first- and second-order shim coils. *Magn Reson Med*, 29(6):804–11, 1993.
- A. Guyton and J. Hall. *Textbook of medical physiology*. Elsevier Saunders, Philadelphia, 11th edition, 2006.
- E. Haacke, R. Brown, M. Thompson, and R. Venkatesan. *Magnetic resonance imaging: physical principles and sequence design*. Wiley-Liss, New York, 1st edition, 1999.
- F. Hamzei, C. Dettmers, R. Rzanny, J. Liepert, C. Buchel, and C. Weiller. Reduction of excitability ("inhibition") in the ipsilateral primary motor cortex is mirrored by fMRI signal decreases. *Neuroimage*, 17(1):490–6, 2002.

- B. M. Harvey, M. J. Vansteensel, C. H. Ferrier, N. Petridou, W. Zuiderbaan, E. J. Aarnoutse, M. G. Bleichner, H. C. Dijkerman, M. J. van Zandvoort, F. S. Leijten, N. F. Ramsey, and S. O. Dumoulin. Frequency specific spatial interactions in human electrocorticography: V1 alpha oscillations reflect surround suppression. *Neuroimage*, 2012.
- H. J. Heinze, G. R. Mangun, W. Burchert, H. Hinrichs, M. Scholz, T. F. Munte, A. Gos, M. Scherg, S. Johannes, H. Hundeshagen, and et al. Combined spatial and temporal imaging of brain activity during visual selective attention in humans. *Nature*, 372(6506):543–6, 1994.
- D. Hermes, K. J. Miller, M. J. Vansteensel, E. J. Aarnoutse, F. S. Leijten, and N. F. Ramsey. Neurophysiologic correlates of fMRI in human motor cortex. *Hum Brain Mapp*, 33(7): 1689–99, 2012.
- C. S. Herrmann and S. Debener. Simultaneous recording of EEG and BOLD responses: a historical perspective. *Int J Psychophysiol*, 67(3):161–8, 2008.
- R. A. Hill, K. H. Chiappa, F. Huang-Hellinger, and B. G. Jenkins. EEG during MR imaging: differentiation of movement artifact from paroxysmal cortical activity. *Neurology*, 45(10): 1942–3, 1995.
- A. Hillebrand and G. R. Barnes. The use of anatomical constraints with MEG beamformers. *Neuroimage*, 20(4):2302–13, 2003.
- E. M. Hillman. Coupling mechanism and significance of the BOLD signal: A status report. *Annu Rev Neurosci*, 37:161–81, 2014.
- A. Hirata, H. Sugiyama, and O. Fujiwara. Estimation of core temperature elevation in humans and animals for whole-body averaged sar. *Progress in Electromagnetics Research-Pier*, 99: 53–70, 2009.
- Y. Hlushchuk and R. Hari. Transient suppression of ipsilateral primary somatosensory cortex during tactile finger stimulation. *J Neurosci*, 26(21):5819–24, 2006.
- R. D. Hoge, J. Atkinson, B. Gill, G. R. Crelier, S. Marrett, and G. B. Pike. Stimulus-dependent BOLD and perfusion dynamics in human v1. *Neuroimage*, 9(6 Pt 1):573–85, 1999.
- Donald R. Hoover, John A. Rice, Colin O. Wu, and Li-Ping Yang. Nonparametric smoothing estimates of time-varying coefficient models with longitudinal data. *Biometrika*, 85(4): 809–822, 1998.
- S. G. Horowitz, B. Rossion, P. Skudlarski, and J. C. Gore. Parametric design and correlational analyses help integrating fMRI and electrophysiological data during face processing. *Neuroimage*, 22(4):1587–95, 2004.
- X. Hu and E. Yacoub. The story of the initial dip in fMRI. *Neuroimage*, 62(2):1103–8, 2012.

Bibliography

- Jianhua Z. Huang, Colin O. Wu, and Lan Zhou. Varying-coefficient models and basis function approximations for the analysis of repeated measurements. *Biometrika*, 89(1):111–128, 2002.
- C. H. Im, H. K. Jung, and N. Fujimaki. fMRI-constrained MEG source imaging and consideration of fMRI invisible sources. *Hum Brain Mapp*, 26(2):110–8, 2005.
- J. R. Ives, S. Warach, F. Schmitt, R. R. Edelman, and D. L. Schomer. Monitoring the patient's EEG during echo planar MRI. *Electroencephalogr Clin Neurophysiol*, 87(6):417–20, 1993.
- D. Iyer and G. Zouridakis. Single-trial evoked potential estimation: comparison between independent component analysis and wavelet denoising. *Clin Neurophysiol*, 118(3):495–504, 2007.
- K. Jann, T. Dierks, C. Boesch, M. Kottlow, W. Strik, and T. Koenig. BOLD correlates of EEG alpha phase-locking and the fMRI default mode network. *Neuroimage*, 45(3):903–16, 2009.
- B. H. Jansen and V. G. Rit. Electroencephalogram and visual evoked potential generation in a mathematical model of coupled cortical columns. *Biol Cybern*, 73(4):357–66, 1995.
- M. Jansen, T. P. White, K. J. Mullinger, E. B. Liddle, P. A. Gowland, S. T. Francis, R. Bowtell, and P. F. Liddle. Motion-related artefacts in EEG predict neuronally plausible patterns of activation in fMRI data. *Neuroimage*, 59(1):261–70, 2012.
- C. Janz, S. P. Heinrich, J. Kornmayer, M. Bach, and J. Hennig. Coupling of neural activity and BOLD fMRI response: new insights by combination of fMRI and vep experiments in transition from single events to continuous stimulation. *Magn Reson Med*, 46(3):482–6, 2001.
- M. Jenkinson, P. Bannister, M. Brady, and S. Smith. Improved optimization for the robust and accurate linear registration and motion correction of brain images. *Neuroimage*, 17(2):825–41, 2002.
- P. Jezzard, P. Matthews, and S. Smith. *Functional MRI : an introduction to methods*. Oxford University Press, New York, 2001.
- J. Jorge, P. Figueiredo, W. van der Zwaag, and J. P. Marques. Signal fluctuations in fMRI data acquired with 2d-epi and 3d-epi at 7 tesla. *Magn Reson Imaging*, 31(2):212–20, 2013.
- A. Kastrup, J. Baudewig, S. Schnaudigel, R. Huonker, L. Becker, J. M. Sohns, P. Dechent, C. Klingner, and O. W. Witte. Behavioral correlates of negative BOLD signal changes in the primary somatosensory cortex. *Neuroimage*, 41(4):1364–71, 2008.
- C. Kayser, C. I. Petkov, and N. K. Logothetis. Visual modulation of neurons in auditory cortex. *Cereb Cortex*, 18(7):1560–74, 2008.

- Jr. Kelly, R. E., G. S. Alexopoulos, Z. Wang, F. M. Gunning, C. F. Murphy, S. S. Morimoto, D. Kanellopoulos, Z. Jia, K. O. Lim, and M. J. Hoptman. Visual inspection of independent components: defining a procedure for artifact removal from fMRI data. *J Neurosci Methods*, 189(2):233–45, 2010.
- P. Khader, T. Schicke, B. Roder, and F. Rosler. On the relationship between slow cortical potentials and BOLD signal changes in humans. *International Journal of Psychophysiology*, 67(3):252–261, 2008.
- J. M. Kilner, J. Mattout, R. Henson, and K. J. Friston. Hemodynamic correlates of EEG: a heuristic. *Neuroimage*, 28(1):280–6, 2005.
- H. C. Kim, S. S. Yoo, and J. H. Lee. Recursive approach of EEG-segment-based principal component analysis substantially reduces cryogenic pump artifacts in simultaneous EEG-fMRI data. *Neuroimage*, 2014.
- C. M. Klingner, C. Hasler, S. Brodoehl, and O. W. Witte. Dependence of the negative BOLD response on somatosensory stimulus intensity. *Neuroimage*, 53(1):189–95, 2010.
- C. M. Klingner, R. Huonker, S. Flemming, C. Hasler, S. Brodoehl, C. Preul, H. Burmeister, A. Kastrup, and O. W. Witte. Functional deactivations: multiple ipsilateral brain areas engaged in the processing of somatosensory information. *Hum Brain Mapp*, 32(1):127–40, 2011.
- T. Koenig, D. Lehmann, M. C. Merlo, K. Kochi, D. Hell, and M. Koukkou. A deviant EEG brain microstate in acute, neuroleptic-naïve schizophrenics at rest. *Eur Arch Psychiatry Clin Neurosci*, 249(4):205–11, 1999.
- P. J. Koopmans, M. Barth, and D. G. Norris. Layer-specific BOLD activation in human v1. *Hum Brain Mapp*, 31(9):1297–304, 2010.
- K. Krakow, P. J. Allen, M. R. Symms, L. Lemieux, O. Josephs, and D. R. Fish. EEG recording during fMRI experiments: image quality. *Hum Brain Mapp*, 10(1):10–5, 2000.
- G. Kruger, A. Kastrup, and G. H. Glover. Neuroimaging at 1.5 t and 3.0 t: comparison of oxygenation-sensitive magnetic resonance imaging. *Magn Reson Med*, 45(4):595–604, 2001.
- F. Kruggel, C. J. Wiggins, C. S. Herrmann, and D. Y. von Cramon. Recording of the event-related potentials during functional MRI at 3.0 tesla field strength. *Magn Reson Med*, 44(2):277–82, 2000.
- J. P. Lachaux, P. Fonlupt, P. Kahane, L. Minotti, D. Hoffmann, O. Bertrand, and M. Baciau. Relationship between task-related gamma oscillations and BOLD signal: new insights from combined fMRI and intracranial EEG. *Hum Brain Mapp*, 28(12):1368–75, 2007.
- H. Laufs. A personalized history of EEG-fMRI integration. *Neuroimage*, 62(2):1056–67, 2012.

Bibliography

- H. Laufs, J. L. Holt, R. Elfont, M. Krams, J. S. Paul, K. Krakow, and A. Kleinschmidt. Where the BOLD signal goes when alpha EEG leaves. *Neuroimage*, 31(4):1408–18, 2006.
- H. Laufs, M. C. Walker, and T. E. Lund. Brain activation and hypothalamic functional connectivity during human non-rapid eye movement sleep: an EEG/fMRI study—its limitations and an alternative approach. *Brain*, 130(Pt 7):e75; author reply e76, 2007.
- T. O. Laumann, E. M. Gordon, B. Adeyemo, A. Z. Snyder, S. J. Joo, M. Y. Chen, A. W. Gilmore, K. B. McDermott, S. M. Nelson, N. U. Dosenbach, B. L. Schlaggar, J. A. Mumford, R. A. Poldrack, and S. E. Petersen. Functional system and areal organization of a highly sampled individual human brain. *Neuron*, 2015.
- P. J. Laurienti, J. H. Burdette, M. T. Wallace, Y. F. Yen, A. S. Field, and B. E. Stein. Deactivation of sensory-specific cortex by cross-modal stimuli. *J Cogn Neurosci*, 14(3):420–9, 2002.
- M. Lauritzen and L. Gold. Brain function and neurophysiological correlates of signals used in functional neuroimaging. *J Neurosci*, 23(10):3972–80, 2003.
- M. Lauritzen, C. Mathiesen, K. Schaefer, and K. J. Thomsen. Neuronal inhibition and excitation, and the dichotomic control of brain hemodynamic and oxygen responses. *Neuroimage*, 62(2):1040–50, 2012.
- F. Lazeyras, I. Zimine, O. Blanke, S. H. Perrig, and M. Seeck. Functional MRI with simultaneous EEG recording: feasibility and application to motor and visual activation. *J Magn Reson Imaging*, 13(6):943–8, 2001.
- T. W. Lee, M. Girolami, and T. J. Sejnowski. Independent component analysis using an extended infomax algorithm for mixed subgaussian and supergaussian sources. *Neural Computation*, 11(2):417–441, 1999.
- D. Lehmann, H. Ozaki, and I. Pal. EEG alpha map series: brain micro-states by space-oriented adaptive segmentation. *Electroencephalogr Clin Neurophysiol*, 67(3):271–88, 1987.
- X. Lei, D. Ostwald, J. Hu, C. Qiu, C. Porcaro, A. P. Bagshaw, and D. Yao. Multimodal functional network connectivity: an EEG-fMRI fusion in network space. *PLoS One*, 6(9):e24642, 2011.
- Marco Leite, Alberto Leal, and Patricia Figueiredo. Transfer function between EEG and BOLD signals of epileptic activity. *Frontiers in Neurology*, 4, 2013.
- L. Lemieux, P. J. Allen, F. Franconi, M. R. Symms, and D. R. Fish. Recording of EEG during fMRI experiments: patient safety. *Magn Reson Med*, 38(6):943–52, 1997.
- L. Lemieux, A. Salek-Haddadi, O. Josephs, P. Allen, N. Toms, C. Scott, K. Krakow, R. Turner, and D. R. Fish. Event-related fMRI with simultaneous and continuous EEG: description of the method and initial case report. *Neuroimage*, 14(3):780–7, 2001.

- M. Lenz, M. Musso, Y. Linke, O. Tuscher, J. Timmer, C. Weiller, and B. Schelter. Joint EEG/fMRI state space model for the detection of directed interactions in human brains—a simulation study. *Physiol Meas*, 32(11):1725–36, 2011.
- O. Leontiev and R. B. Buxton. Reproducibility of BOLD, perfusion, and cmro2 measurements with calibrated-BOLD fMRI. *Neuroimage*, 35(1):175–84, 2007.
- P. LeVan, J. Maclaren, M. Herbst, R. Sostheim, M. Zaitsev, and J. Hennig. Ballistocardiographic artifact removal from simultaneous EEG-fMRI using an optical motion-tracking system. *Neuroimage*, 75:1–11, 2013.
- A. L. Lin, P. T. Fox, Y. Yang, H. Lu, L. H. Tan, and J. H. Gao. Time-dependent correlation of cerebral blood flow with oxygen metabolism in activated human visual cortex as measured by fMRI. *Neuroimage*, 44(1):16–22, 2009.
- P. Lin, U. Hasson, J. Jovicich, and S. Robinson. A neuronal basis for task-negative responses in the human brain. *Cereb Cortex*, 21(4):821–30, 2011.
- T. T. Liu, L. R. Frank, E. C. Wong, and R. B. Buxton. Detection power, estimation efficiency, and predictability in event-related fMRI. *Neuroimage*, 13(4):759–73, 2001.
- Z. Liu and B. He. fMRI-EEG integrated cortical source imaging by use of time-variant spatial constraints. *Neuroimage*, 39(3):1198–214, 2008.
- Z. Liu, C. Rios, N. Zhang, L. Yang, W. Chen, and B. He. Linear and nonlinear relationships between visual stimuli, EEG and BOLD fMRI signals. *Neuroimage*, 50(3):1054–66, 2010.
- Z. Liu, J. A. de Zwart, P. van Gelderen, L. W. Kuo, and J. H. Duyn. Statistical feature extraction for artifact removal from concurrent fMRI-EEG recordings. *Neuroimage*, 59(3):2073–87, 2012.
- N. K. Logothetis. The neural basis of the blood-oxygen-level-dependent functional magnetic resonance imaging signal. *Philos Trans R Soc Lond B Biol Sci*, 357(1424):1003–37, 2002.
- N. K. Logothetis. What we can do and what we cannot do with fMRI. *Nature*, 453(7197):869–78, 2008.
- N. K. Logothetis and B. A. Wandell. Interpreting the BOLD signal. *Annu Rev Physiol*, 66:735–69, 2004.
- N. K. Logothetis, J. Pauls, M. Augath, T. Trinath, and A. Oeltermann. Neurophysiological investigation of the basis of the fMRI signal. *Nature*, 412(6843):150–7, 2001.
- H. Lu, X. Golay, J. J. Pekar, and P. C. Van Zijl. Functional magnetic resonance imaging based on changes in vascular space occupancy. *Magn Reson Med*, 50(2):263–74, 2003.
- H. Lu, X. Golay, J. J. Pekar, and P. C. Van Zijl. Sustained poststimulus elevation in cerebral oxygen utilization after vascular recovery. *J Cereb Blood Flow Metab*, 24(7):764–70, 2004.

Bibliography

- M. Luessi, S. D. Babacan, R. Molina, J. R. Booth, and A. K. Katsaggelos. Bayesian symmetrical EEG/fMRI fusion with spatially adaptive priors. *Neuroimage*, 55(1):113–32, 2011.
- Q. Luo and G. H. Glover. Influence of dense-array EEG cap on fMRI signal. *Magn Reson Med*, 68(3):807–15, 2012.
- Q. Luo, X. Huang, and G. H. Glover. Ballistocardiogram artifact removal with a reference layer and standard EEG cap. *J Neurosci Methods*, 233:137–49, 2014.
- J. Maclaren, B. S. Armstrong, R. T. Barrows, K. A. Danishad, T. Ernst, C. L. Foster, K. Gumus, M. Herbst, I. Y. Kadashevich, T. P. Kusik, Q. Li, C. Lovell-Smith, T. Prieto, P. Schulze, O. Speck, D. Stucht, and M. Zaitsev. Measurement and correction of microscopic head motion during magnetic resonance imaging of the brain. *PLoS One*, 7(11):e48088, 2012.
- Y. Mahajan and G. McArthur. Maturation of visual evoked potentials across adolescence. *Brain Dev*, 34(8):655–66, 2012.
- S. Makeig, A. J. Bell, T. P. Jung, and T. J. Sejnowski. Independent component analysis of electroencephalographic data. *Advances in Neural Information Processing Systems 8*, 8: 145–151, 1996.
- H. Mandelkow, P. Halder, P. Boesiger, and D. Brandeis. Synchronization facilitates removal of MRI artefacts from concurrent EEG recordings and increases usable bandwidth. *Neuroimage*, 32(3):1120–6, 2006.
- J. B. Mandeville, J. J. Marota, C. Ayata, G. Zaharchuk, M. A. Moskowitz, B. R. Rosen, and R. M. Weisskoff. Evidence of a cerebrovascular postarteriole windkessel with delayed compliance. *J Cereb Blood Flow Metab*, 19(6):679–89, 1999.
- D. Mantini, M. G. Perrucci, S. Cugini, A. Ferretti, G. L. Romani, and C. Del Gratta. Complete artifact removal for EEG recorded during continuous fMRI using independent component analysis. *Neuroimage*, 34(2):598–607, 2007a.
- D. Mantini, M. G. Perrucci, C. Del Gratta, G. L. Romani, and M. Corbetta. Electrophysiological signatures of resting state networks in the human brain. *Proc Natl Acad Sci U S A*, 104(32): 13170–5, 2007b.
- J. P. Marques, J. Rebola, P. Figueiredo, A. Pinto, F. Sales, and M. Castelo-Branco. Ica decomposition of EEG signal for fMRI processing in epilepsy. *Hum Brain Mapp*, 30(9):2986–96, 2009.
- A. Martinez, L. Anllo-Vento, M. I. Sereno, L. R. Frank, R. B. Buxton, D. J. Dubowitz, E. C. Wong, H. Hinrichs, H. J. Heinze, and S. A. Hillyard. Involvement of striate and extrastriate visual cortical areas in spatial attention. *Nat Neurosci*, 2(4):364–9, 1999.
- R. Martuzzi, M. M. Murray, R. A. Meuli, J. P. Thiran, P. P. Maeder, C. M. Michel, R. Grave de Peralta Menendez, and S. L. Gonzalez Andino. Methods for determining frequency- and

- region-dependent relationships between estimated lfps and BOLD responses in humans. *J Neurophysiol*, 101(1):491–502, 2009.
- R. A. Masterton, D. F. Abbott, S. W. Fleming, and G. D. Jackson. Measurement and reduction of motion and ballistocardiogram artefacts from simultaneous EEG and fMRI recordings. *Neuroimage*, 37(1):202–11, 2007.
- R. A. Masterton, G. D. Jackson, and D. F. Abbott. Mapping brain activity using event-related independent components analysis (eica): Specific advantages for EEG-fMRI. *Neuroimage*, 70:164–174, 2013.
- S. D. Mayhew, D. Ostwald, C. Porcaro, and A. P. Bagshaw. Spontaneous EEG alpha oscillation interacts with positive and negative BOLD responses in the visual-auditory cortices and default-mode network. *Neuroimage*, 76:362–72, 2013.
- G. McGibney, M. R. Smith, S. T. Nichols, and A. Crawley. Quantitative evaluation of several partial fourier reconstruction algorithms used in MRI. *Magn Reson Med*, 30(1):51–9, 1993.
- M. J. McKeown and T. J. Sejnowski. Independent component analysis of fMRI data: examining the assumptions. *Hum Brain Mapp*, 6(5-6):368–72, 1998.
- R. S. Menon. Postacquisition suppression of large-vessel BOLD signals in high-resolution fMRI. *Magn Reson Med*, 47(1):1–9, 2002.
- L. Meyer, J. Obleser, S. J. Kiebel, and A. D. Friederici. Spatiotemporal dynamics of argument retrieval and reordering: an fmri and EEG study on sentence processing. *Front Psychol*, 3: 523, 2012.
- M. C. Meyer, E. S. van Oort, and M. Barth. Electrophysiological correlation patterns of resting state networks in single subjects: A combined EEG-fMRI study. *Brain Topogr*, 26(1):98–109, 2013.
- C. M. Michel, M. M. Murray, G. Lantz, S. Gonzalez, L. Spinelli, and R. Grave de Peralta. EEG source imaging. *Clin Neurophysiol*, 115(10):2195–222, 2004.
- B. Mijovic, K. Vanderperren, N. Novitskiy, B. Vanrumste, P. Stiers, B. V. Bergh, L. Lagae, S. Sunaert, J. Wagemans, S. V. Huffel, and M. D. Vos. The "why" and "how" of jointica: results from a visual detection task. *Neuroimage*, 60(2):1171–85, 2012.
- H. Mizuhara, L. Q. Wang, K. Kobayashi, and Y. Yamaguchi. Long-range EEG phase synchronization during an arithmetic task indexes a coherent cortical network simultaneously measured by fMRI. *Neuroimage*, 27(3):553–63, 2005.
- M. Moosmann, P. Ritter, I. Krastel, A. Brink, S. Thees, F. Blankenburg, B. Taskin, H. Obrig, and A. Villringer. Correlates of alpha rhythm in functional magnetic resonance imaging and near infrared spectroscopy. *Neuroimage*, 20(1):145–58, 2003.

Bibliography

- R. Mukamel, H. Gelbard, A. Arieli, U. Hasson, I. Fried, and R. Malach. Coupling between neuronal firing, field potentials, and fmri in human auditory cortex. *Science*, 309(5736): 951–4, 2005.
- C. Mulert and L. Lemieux. *EEG-fMRI : physiological basis, technique, and applications*. Springer-Verlag, Berlin, Heidelberg, 1st edition, 2010.
- C. Mulert, L. Jager, S. Propp, S. Karch, S. Stormann, O. Pogarell, H. J. Moller, G. Juckel, and U. Hegerl. Sound level dependence of the primary auditory cortex: Simultaneous measurement with 61-channel EEG and fMRI. *Neuroimage*, 28(1):49–58, 2005.
- C. Mulert, G. Leicht, P. Hepp, V. Kirsch, S. Karch, O. Pogarell, M. Reiser, U. Hegerl, L. Jager, H. J. Moller, and R. W. McCarley. Single-trial coupling of the gamma-band response and the corresponding BOLD signal. *Neuroimage*, 49(3):2238–47, 2010.
- K. Mullinger and R. Bowtell. Combining EEG and fMRI. *Methods Mol Biol*, 711:303–26, 2011.
- K. Mullinger, M. Brookes, C. Stevenson, P. Morgan, and R. Bowtell. Exploring the feasibility of simultaneous electroencephalography/functional magnetic resonance imaging at 7T. *Magn Reson Imaging*, 26(7):968–77, 2008a.
- K. Mullinger, S. Debener, R. Coxon, and R. Bowtell. Effects of simultaneous EEG recording on MRI data quality at 1.5, 3 and 7 tesla. *Int J Psychophysiol*, 67(3):178–88, 2008b.
- K. J. Mullinger, J. Havenhand, and R. Bowtell. Identifying the sources of the pulse artefact in EEG recordings made inside an MR scanner. *Neuroimage*, 71:75–83, 2013a.
- K. J. Mullinger, S. D. Mayhew, A. P. Bagshaw, R. Bowtell, and S. T. Francis. Poststimulus under-shoots in cerebral blood flow and BOLD fMRI responses are modulated by poststimulus neuronal activity. *Proc Natl Acad Sci U S A*, 110(33):13636–41, 2013b.
- K. J. Mullinger, M. E. Chowdhury, and R. Bowtell. Investigating the effect of modifying the EEG cap lead configuration on the gradient artifact in simultaneous EEG-fMRI. *Front Neurosci*, 8:226, 2014a.
- K. J. Mullinger, S. D. Mayhew, A. P. Bagshaw, R. Bowtell, and S. T. Francis. Evidence that the negative BOLD response is neuronal in origin: a simultaneous EEG-BOLD-cbf study in humans. *Neuroimage*, 94:263–74, 2014b.
- M. Negishi, M. Abildgaard, I. Laufer, T. Nixon, and R. T. Constable. An EEG (electroencephalogram) recording system with carbon wire electrodes for simultaneous EEG-fMRI (functional magnetic resonance imaging) recording. *J Neurosci Methods*, 173(1):99–107, 2008.
- I. Neuner, T. Warbrick, J. Arrubla, J. Felder, A. Celik, M. Reske, F. Boers, and N. J. Shah. EEG acquisition in ultra-high static magnetic fields up to 9.4 t. *Neuroimage*, 68:214–20, 2013.

- I. Neuner, J. Arrubla, J. Felder, and N. J. Shah. Simultaneous EEG-fMRI acquisition at low, high and ultra-high magnetic fields up to 9.4t: Perspectives and challenges. *Neuroimage*, 102(1): 71–79, 2014.
- A. T. Newton, B. P. Rogers, J. C. Gore, and V. L. Morgan. Improving measurement of functional connectivity through decreasing partial volume effects at 7T. *Neuroimage*, 59(3):2511–7, 2012.
- R. K. Niazy, C. F. Beckmann, G. D. Iannetti, J. M. Brady, and S. M. Smith. Removal of fmri environment artifacts from EEG data using optimal basis sets. *Neuroimage*, 28(3):720–37, 2005.
- E. Niedermeyer and F. H. Lopes da Silva. *Electroencephalography: basic principles, clinical applications, and related fields*. Lippincott Williams and Wilkins, Philadelphia, 5th edition, 2005.
- T. Nierhaus, C. Gundlach, D. Goltz, S. D. Thiel, B. Pleger, and A. Villringer. Internal ventilation system of MR scanners induces specific EEG artifact during simultaneous EEG-fMRI. *Neuroimage*, 74:70–6, 2013.
- J. Niessing, B. Ebisch, K. E. Schmidt, M. Niessing, W. Singer, and R. A. Galuske. Hemodynamic signals correlate tightly with synchronized gamma oscillations. *Science*, 309(5736):948–51, 2005.
- U. Noth, H. Laufs, R. Stoermer, and R. Deichmann. Simultaneous electroencephalography-functional MRI at 3 t: an analysis of safety risks imposed by performing anatomical reference scans with the EEG equipment in place. *J Magn Reson Imaging*, 35(3):561–71, 2012.
- N. Novitski, I. Anourova, S. Martinkauppi, H. J. Aronen, R. Naatanen, and S. Carlson. Effects of noise from functional magnetic resonance imaging on auditory event-related potentials in working memory task. *Neuroimage*, 20(2):1320–8, 2003.
- P. Nunez and R. Srinivasan. *Electric fields of the brain*. Oxford University Press, New York, 2nd edition, 2006.
- P. L. Nunez and R. B. Silberstein. On the relationship of synaptic activity to macroscopic measurements: does co-registration of EEG with fMRI make sense? *Brain Topogr*, 13(2): 79–96, 2000.
- W. J. Nuttall, R. H. Clarke, and B. A. Glowacki. Resources: Stop squandering helium. *Nature*, 485(7400):573–5, 2012.
- S. Ogawa, T. M. Lee, A. R. Kay, and D. W. Tank. Brain magnetic resonance imaging with contrast dependent on blood oxygenation. *Proc Natl Acad Sci U S A*, 87(24):9868–72, 1990.
- S. Ogawa, D. W. Tank, R. Menon, J. M. Ellermann, S. G. Kim, H. Merkle, and K. Ugurbil. Intrinsic signal changes accompanying sensory stimulation: functional brain mapping with magnetic resonance imaging. *Proc Natl Acad Sci U S A*, 89(13):5951–5, 1992.

Bibliography

- S. Ogawa, R. S. Menon, D. W. Tank, S. G. Kim, H. Merkle, J. M. Ellermann, and K. Ugurbil. Functional brain mapping by blood oxygenation level-dependent contrast magnetic resonance imaging. a comparison of signal characteristics with a biophysical model. *Biophys J*, 64(3): 803–12, 1993.
- J. Onton, M. Westerfield, J. Townsend, and S. Makeig. Imaging human EEG dynamics using independent component analysis. *Neurosci Biobehav Rev*, 30(6):808–22, 2006.
- D. Ostwald, C. Porcaro, and A. P. Bagshaw. Voxel-wise information theoretic EEG-fMRI feature integration. *Neuroimage*, 55(3):1270–86, 2011.
- B. N. Pasley, B. A. Inglis, and R. D. Freeman. Analysis of oxygen metabolism implies a neural origin for the negative BOLD response in human visual cortex. *Neuroimage*, 36(2):269–76, 2007.
- M. R. Patel, A. Blum, J. D. Pearlman, N. Yousuf, J. R. Ives, S. Saeteng, D. L. Schomer, and R. R. Edelman. Echo-planar functional MR imaging of epilepsy with concurrent EEG monitoring. *AJNR Am J Neuroradiol*, 20(10):1916–9, 1999.
- L. Pauling and C. D. Coryell. The magnetic properties and structure of hemoglobin, oxyhemoglobin and carbonmonoxyhemoglobin. *Proc Natl Acad Sci U S A*, 22(4):210–6, 1936.
- G. Pfurtscheller and F. H. Lopes da Silva. Event-related EEG/MEG synchronization and desynchronization: basic principles. *Clin Neurophysiol*, 110(11):1842–57, 1999.
- R. Quian Quiroga and H. Garcia. Single-trial event-related potentials with wavelet denoising. *Clin Neurophysiol*, 114(2):376–90, 2003.
- M. E. Raichle and D. A. Gusnard. Intrinsic brain activity sets the stage for expression of motivated behavior. *J Comp Neurol*, 493(1):167–76, 2005.
- A. Rauch, G. Rainer, and N. K. Logothetis. The effect of a serotonin-induced dissociation between spiking and perisynaptic activity on BOLD functional MRI. *Proc Natl Acad Sci U S A*, 105(18):6759–64, 2008.
- C. Regenbogen, M. De Vos, S. Debener, B. I. Turetsky, C. Mossnang, A. Finkelmeyer, U. Habel, I. Neuner, and T. Kellermann. Auditory processing under cross-modal visual load investigated with simultaneous EEG-fMRI. *PLoS One*, 7(12):e52267, 2012.
- J. J. Riera and A. Sumiyoshi. Brain oscillations: ideal scenery to understand the neurovascular coupling. *Curr Opin Neurol*, 23(4):374–81, 2010.
- J. J. Riera, X. Wan, J. C. Jimenez, and R. Kawashima. Nonlinear local electrovascular coupling. i: A theoretical model. *Hum Brain Mapp*, 27(11):896–914, 2006.
- Petra Ritter, Robert Becker, Frank Freyer, and Arno Villringer. *EEG Quality: The Image Acquisition Artefact*, chapter 9, pages 153–171. Springer Berlin Heidelberg, 2010.

- A. K. Roopun, S. J. Middleton, M. O. Cunningham, F. E. LeBeau, A. Bibbig, M. A. Whittington, and R. D. Traub. A beta2-frequency (20-30 Hz) oscillation in nonsynaptic networks of somatosensory cortex. *Proc Natl Acad Sci U S A*, 103(42):15646–50, 2006.
- M. J. Rosa, J. Daunizeau, and K. J. Friston. EEG-fMRI integration: a critical review of biophysical modeling and data analysis approaches. *J Integr Neurosci*, 9(4):453–76, 2010a.
- M. J. Rosa, J. Kilner, F. Blankenburg, O. Josephs, and W. Penny. Estimating the transfer function from neuronal activity to BOLD using simultaneous EEG-fMRI. *Neuroimage*, 49(2):1496–509, 2010b.
- P. Roschmann. Radiofrequency penetration and absorption in the human body: limitations to high-field whole-body nuclear magnetic resonance imaging. *Med Phys*, 14(6):922–31, 1987.
- S. Rothlubbers, V. Relvas, A. Leal, and P. Figueiredo. Reduction of EEG artefacts induced by vibration in the MR-environment. *Conf Proc IEEE Eng Med Biol Soc*, 2013:2092–5, 2013.
- S. Sadaghiani, K. Ugurbil, and K. Uludag. Neural activity-induced modulation of BOLD poststimulus undershoot independent of the positive signal. *Magn Reson Imaging*, 27(8):1030–8, 2009.
- G. Salimi-Khorshidi, G. Douaud, C. F. Beckmann, M. F. Glasser, L. Griffanti, and S. M. Smith. Automatic denoising of functional MRI data: combining independent component analysis and hierarchical fusion of classifiers. *Neuroimage*, 90:449–68, 2014.
- G. Sammer, C. Blecker, H. Gebhardt, P. Kirsch, R. Stark, and D. Vaitl. Acquisition of typical EEG waveforms during fMRI: Ssvep, lrp, and frontal theta. *Neuroimage*, 24(4):1012–24, 2005.
- C. J. Scarff, A. Reynolds, B. G. Goodyear, C. W. Ponton, J. C. Dort, and J. J. Eggermont. Simultaneous 3-T fMRI and high-density recording of human auditory evoked potentials. *Neuroimage*, 23(3):1129–42, 2004.
- D. L. Schacter. EEG theta waves and psychological phenomena: a review and analysis. *Biol Psychol*, 5(1):47–82, 1977.
- R. Scheeringa, M. C. Bastiaansen, K. M. Petersson, R. Oostenveld, D. G. Norris, and P. Hagoort. Frontal theta EEG activity correlates negatively with the default mode network in resting state. *Int J Psychophysiol*, 67(3):242–51, 2008.
- R. Scheeringa, P. Fries, K. M. Petersson, R. Oostenveld, I. Grothe, D. G. Norris, P. Hagoort, and M. C. Bastiaansen. Neuronal dynamics underlying high- and low-frequency EEG oscillations contribute independently to the human BOLD signal. *Neuron*, 69(3):572–83, 2011.
- F. Schick. Whole-body MRI at high field: technical limits and clinical potential. *Eur Radiol*, 15(5):946–59, 2005.

Bibliography

- T. Schicke, L. Muckli, A. L. Beer, M. Wibral, W. Singer, R. Goebel, F. Rosler, and B. Roder. Tight covariation of BOLD signal changes and slow erps in the parietal cortex in a parametric spatial imagery task with haptic acquisition. *Eur J Neurosci*, 23(7):1910–8, 2006.
- M. L. Scholvinck, A. Maier, F. Q. Ye, J. H. Duyn, and D. A. Leopold. Neural basis of global resting-state fMRI activity. *Proc Natl Acad Sci U S A*, 107(22):10238–43, 2010.
- J. Schummers, H. Yu, and M. Sur. Tuned responses of astrocytes and their influence on hemodynamic signals in the visual cortex. *Science*, 320(5883):1638–43, 2008.
- A. Shmuel, E. Yacoub, J. Pfeuffer, P. F. Van de Moortele, G. Adriany, X. Hu, and K. Ugurbil. Sustained negative BOLD, blood flow and oxygen consumption response and its coupling to the positive response in the human brain. *Neuron*, 36(6):1195–210, 2002.
- A. Shmuel, M. Augath, A. Oeltermann, and N. K. Logothetis. Negative functional MRI response correlates with decreases in neuronal activity in monkey visual area v1. *Nat Neurosci*, 9(4):569–77, 2006.
- M. Singh, S. Kim, and T. S. Kim. Correlation between BOLD-fMRI and EEG signal changes in response to visual stimulus frequency in humans. *Magnetic Resonance in Medicine*, 49(1):108–114, 2003.
- W. Skrandies. Brain mapping of visual evoked activity–topographical and functional components. *Acta Neurol Taiwan*, 14(4):164–78, 2005.
- A. T. Smith, A. L. Williams, and K. D. Singh. Negative BOLD in the visual cortex: evidence against blood stealing. *Hum Brain Mapp*, 21(4):213–20, 2004a.
- S. M. Smith. Fast robust automated brain extraction. *Hum Brain Mapp*, 17(3):143–55, 2002.
- S. M. Smith, M. Jenkinson, M. W. Woolrich, C. F. Beckmann, T. E. Behrens, H. Johansen-Berg, P. R. Bannister, M. De Luca, I. Drobnjak, D. E. Flitney, R. K. Niazy, J. Saunders, J. Vickers, Y. Zhang, N. De Stefano, J. M. Brady, and P. M. Matthews. Advances in functional and structural MR image analysis and implementation as fsl. *Neuroimage*, 23(1):S208–19, 2004b.
- R. C. Sotero and N. J. Trujillo-Barreto. Modelling the role of excitatory and inhibitory neuronal activity in the generation of the BOLD signal. *Neuroimage*, 35(1):149–65, 2007.
- R. C. Sotero and N. J. Trujillo-Barreto. Biophysical model for integrating neuronal activity, EEG, fMRI and metabolism. *Neuroimage*, 39(1):290–309, 2008.
- G. Srivastava, S. Crottaz-Herbette, K. M. Lau, G. H. Glover, and V. Menon. Ica-based procedures for removing ballistocardiogram artifacts from EEG data acquired in the MRI scanner. *Neuroimage*, 24(1):50–60, 2005.
- B. Stefanovic, J. M. Warnking, and G. B. Pike. Hemodynamic and metabolic responses to neuronal inhibition. *Neuroimage*, 22(2):771–8, 2004.

- M. Steriade, D. Contreras, F. Amzica, and I. Timofeev. Synchronization of fast (30-40 hz) spontaneous oscillations in intrathalamic and thalamocortical networks. *J Neurosci*, 16(8): 2788–808, 1996.
- S. C. Strother. Evaluating fMRI preprocessing pipelines. *IEEE Eng Med Biol Mag*, 25(2):27–41, 2006.
- C. Tallon-Baudry, O. Bertrand, F. Peronnet, and J. Pernier. Induced gamma-band activity during the delay of a visual short-term memory task in humans. *J Neurosci*, 18(11):4244–54, 1998.
- J. Tamminen, J. D. Payne, R. Stickgold, E. J. Wamsley, and M. G. Gaskell. Sleep spindle activity is associated with the integration of new memories and existing knowledge. *J Neurosci*, 30(43):14356–60, 2010.
- T. S. Tenforde, C. T. Gaffey, B. R. Moyer, and T. F. Budinger. Cardiovascular alterations in macaca monkeys exposed to stationary magnetic fields: experimental observations and theoretical analysis. *Bioelectromagnetics*, 4(1):1–9, 1983.
- D. J. Thomson. Spectrum estimation and harmonic-analysis. *Proceedings of the Ieee*, 70(9): 1055–1096, 1982.
- C. Triantafyllou, R. D. Hoge, G. Krueger, C. J. Wiggins, A. Potthast, G. C. Wiggins, and L. L. Wald. Comparison of physiological noise at 1.5 t, 3 t and 7T and optimization of fMRI acquisition parameters. *Neuroimage*, 26(1):243–50, 2005.
- R. Turner. How much cortex can a vein drain? downstream dilution of activation-related cerebral blood oxygenation changes. *Neuroimage*, 16(4):1062–7, 2002.
- R. Turner, P. Jezzard, H. Wen, K. K. Kwong, D. Le Bihan, T. Zeffiro, and R. S. Balaban. Functional mapping of the human visual cortex at 4 and 1.5 tesla using deoxygenation contrast epi. *Magn Reson Med*, 29(2):277–9, 1993.
- L. Tyvaert, C. Hawco, E. Kobayashi, P. LeVan, F. Dubeau, and J. Gotman. Different structures involved during ictal and interictal epileptic activity in malformations of cortical development: an EEG-fMRI study. *Brain*, 131(8):2042–60, 2008.
- M. Ullsperger and D. Y. von Cramon. Subprocesses of performance monitoring: a dissociation of error processing and response competition revealed by event-related fMRI and erps. *Neuroimage*, 14(6):1387–401, 2001.
- K. Uludag. To dip or not to dip: reconciling optical imaging and fMRI data. *Proc Natl Acad Sci U S A*, 107(6):E23; author reply E24, 2010.
- M. S. Vafaei and A. Gjedde. Spatially dissociated flow-metabolism coupling in brain activation. *Neuroimage*, 21(2):507–15, 2004.

Bibliography

- W. van der Zwaag, S. Francis, K. Head, A. Peters, P. Gowland, P. Morris, and R. Bowtell. fMRI at 1.5, 3 and 7T: characterising BOLD signal changes. *Neuroimage*, 47(4):1425–34, 2009a.
- W. van der Zwaag, J. P. Marques, M. Hergt, and R. Gruetter. Investigation of high-resolution functional magnetic resonance imaging by means of surface and array radiofrequency coils at 7T. *Magn Reson Imaging*, 27(8):1011–8, 2009b.
- C. E. Vasios, L. M. Angelone, P. L. Purdon, J. Ahveninen, J. W. Belliveau, and G. Bonmassar. EEG/(f)MRI measurements at 7 tesla using a new EEG cap ("inkcap"). *Neuroimage*, 33(4):1082–92, 2006.
- S. Vulliemoz, D. W. Carmichael, K. Rosenkranz, B. Diehl, R. Rodionov, M. C. Walker, A. W. McEvoy, and L. Lemieux. Simultaneous intracranial EEG and fMRI of interictal epileptic discharges in humans. *Neuroimage*, 54(1):182–90, 2011.
- A. R. Wade. The negative BOLD signal unmasked. *Neuron*, 36(6):993–5, 2002.
- W. G. Walter, R. Cooper, V. J. Aldridge, W. C. McCallum, and A. L. Winter. Contingent negative variation: An electric sign of sensorimotor association and expectancy in the human brain. *Nature*, 203:380–4, 1964.
- X. Wan, J. Riera, K. Iwata, M. Takahashi, T. Wakabayashi, and R. Kawashima. The neural basis of the hemodynamic response nonlinearity in human primary visual cortex: Implications for neurovascular coupling mechanism. *Neuroimage*, 32(2):616–25, 2006.
- J. C. Whitman, L. M. Ward, and T. S. Woodward. Patterns of cortical oscillations organize neural activity into whole-brain functional networks evident in the fMRI BOLD signal. *Front Hum Neurosci*, 7:80, 2013.
- K. Whittingstall and N. K. Logothetis. Frequency-band coupling in surface EEG reflects spiking activity in monkey visual cortex. *Neuron*, 64(2):281–9, 2009.
- A. Widmann, E. Schroger, and B. Maess. Digital filter design for electrophysiological data - a practical approach. *J Neurosci Methods*, 250:34–46, 2015.
- C. H. Wolters, A. Anwander, X. Tricoche, D. Weinstein, M. A. Koch, and R. S. MacLeod. Influence of tissue conductivity anisotropy on EEG/MEG field and return current computation in a realistic head model: a simulation and visualization study using high-resolution finite element modeling. *Neuroimage*, 30(3):813–26, 2006.
- K. J. Worsley and K. J. Friston. Analysis of fMRI time-series revisited—again. *Neuroimage*, 2(3):173–81, 1995.
- E. Yacoub, A. Shmuel, J. Pfeuffer, P. F. Van De Moortele, G. Adriany, P. Andersen, J. T. Vaughan, H. Merkle, K. Ugurbil, and X. Hu. Imaging brain function in humans at 7 tesla. *Magn Reson Med*, 45(4):588–94, 2001.

- E. Yacoub, N. Harel, and K. Ugurbil. High-field fMRI unveils orientation columns in humans. *Proc Natl Acad Sci U S A*, 105(30):10607–12, 2008.
- W. X. Yan, K. J. Mullinger, M. J. Brookes, and R. Bowtell. Understanding gradient artefacts in simultaneous EEG/fMRI. *Neuroimage*, 46(2):459–71, 2009.
- W. X. Yan, K. J. Mullinger, G. B. Geirsdottir, and R. Bowtell. Physical modeling of pulse artefact sources in simultaneous EEG/fMRI. *Hum Brain Mapp*, 31(4):604–20, 2010.
- L. Yang, Z. Liu, and B. He. EEG-fMRI reciprocal functional neuroimaging. *Clin Neurophysiol*, 121(8):1240–50, 2010.
- Q. X. Yang, W. Mao, J. Wang, M. B. Smith, H. Lei, X. Zhang, K. Ugurbil, and W. Chen. Manipulation of image intensity distribution at 7.0 t: passive rf shimming and focusing with dielectric materials. *J Magn Reson Imaging*, 24(1):197–202, 2006.
- H. Yuan, T. Liu, R. Szarkowski, C. Rios, J. Ashe, and B. He. Negative covariation between task-related responses in alpha/beta-band activity and BOLD in human sensorimotor cortex: an EEG and fMRI study of motor imagery and movements. *Neuroimage*, 49(3):2596–606, 2010.
- H. Yuan, V. Zotev, R. Phillips, W. C. Drevets, and J. Bodurka. Spatiotemporal dynamics of the brain at rest - exploring EEG microstates as electrophysiological signatures of BOLD resting state networks. *Neuroimage*, 60(4):2062–2072, 2012.

List of Figures

1.1	Neuronal substrates of EEG	5
1.2	Potential generation and source modeling	7
1.3	Scalp EEG recording	10
1.4	Visual evoked potential	13
1.5	Nuclear magnetization of a nuclei sample	18
1.6	Spin excitation with a precessing magnetic field	20
1.7	2D MRI acquisition block diagram	23
1.8	BOLD response timecourse	25
1.9	Hardware for MRI data acquisition	26
1.10	EPI sequence diagram	28
1.11	Substrates of EEG, fMRI and behavior	32
1.12	EEG-fMRI data integration approaches	35
2.1	Functional paradigms	45
2.2	Data analysis outline	46
2.3	BOLD response functional localizer	48
2.4	Responses to contrast-varying stimulation	49
2.5	Responses to duration-varying stimulation	51
2.6	Large draining vein segmentation	52
2.7	Influence of large draining veins	53

List of Figures

2.8	Typical fMRI independent components	54
2.9	Impact of ICA-assisted denoising	55
3.1	Computational models	65
3.2	Electromagnetic simulation results	68
3.3	Validation of electromagnetic simulations	69
3.4	Temperature measurement results	70
3.5	Additional temperature measurement results	71
4.1	MRI data quality characterization	79
4.2	fMRI data quality	80
5.1	Compact EEG-fMRI setup	87
5.2	EEG motion artifact detection	91
5.3	M-RLS and oM-RLS coefficient timecourses	99
5.4	Noise sensitivity of ribbon cables	101
5.5	Noise spectra for different cable configurations	102
5.6	Noise power for different cable configurations	103
5.7	EEG timecourses with gradient and pulse artifact correction	104
5.8	Alpha power during eyes-open/eyes-closed	105
5.9	Evoked potentials during visual stimulation	106
5.10	Bold response to eyes-open/eyes-closed and visual stimulation	107
5.11	Impact of M-RLS in time and frequency	108
5.12	Impact of AAS and M-RLS on band-specific signal power	109
5.13	Impact of AAS and M-RLS on signal power and trial consistency	110
5.14	Impact of motion artifact correction	111
5.15	EEG signal power characterization	112
5.16	Impact of ICA denoising and motion artifact correction	113

5.17 Visual responses with artifact correction	114
--	-----

Publications arising from this thesis

Journal articles

Stimulus dependence of the negative BOLD response to visual stimulation in visual and auditory cortical regions at 7T, João Jorge, Patrícia Figueiredo, Rolf Gruetter, Wietske van der Zwaag; submitted

Towards high-quality simultaneous EEG-fMRI at 7 Tesla: detection and reduction of EEG artifacts due to head motion, João Jorge, Frédéric Grouiller, Rolf Gruetter, Wietske van der Zwaag, Patrícia Figueiredo; NeuroImage 120, 2015, pp.143-153

Simultaneous EEG-fMRI at ultra-high field: Artifact prevention and safety assessment, João Jorge, Frédéric Grouiller, Özlem Ipek, Robert Stoermer, Christoph M Michel, Patrícia Figueiredo, Wietske van der Zwaag, Rolf Gruetter; NeuroImage 105, 2015, pp.132-144

EEG-fMRI integration for the study of human brain function, João Jorge, Wietske van der Zwaag, Patrícia Figueiredo; NeuroImage 102, 2014, pp.24-34

Conference abstracts

Improving simultaneous EEG-fMRI acquisitions at 7 Tesla: detection, characterization and reduction of EEG artifacts due to head motion, João Jorge, Frédéric Grouiller, Rolf Gruetter, Wietske van der Zwaag, Patrícia Figueiredo; oral presentation at the 2nd bi-annual BaCI meeting, Utrecht, Netherlands, September 2015

Towards high-quality simultaneous EEG-fMRI acquisitions at 7 Tesla: detection and reduction of EEG artifacts due to head motion in B₀, João Jorge, Frédéric Grouiller, Wietske van der Zwaag, Rolf Gruetter, Patrícia Figueiredo; e-poster presentation at the 23rd Annual ISMRM Meeting, Toronto, Canada, May 2015

Contrast and duration dependence of the negative BOLD response to visual stimulation in visual and auditory cortical regions at 7T, João Jorge, Patrícia Figueiredo, Rolf Gruetter, Wietske van

Publications arising from this thesis

der Zwaag; poster presentation at the 23rd Annual ISMRM Meeting, Toronto, Canada, May 2015

Mapping epileptic networks using simultaneous EEG-MRI at ultra-high field, Frédéric Grouiller, João Jorge, Francesca Pittau, Pascal Martelli, Wietske van der Zwaag, Christoph M Michel, Serge Vulliémou, Maria I Vargas, François Lazeyras; poster presentation at the 23rd Annual ISMRM Meeting, Toronto, Canada, May 2015

RF safety assessment of simultaneous EEG-fMRI at 7T MR, Özlem Ipek, João Jorge, Frédéric Grouiller, Wietske van der Zwaag, Lijing Xin, Rolf Gruetter; poster presentation at the 23rd Annual ISMRM Meeting, Toronto, Canada, May 2015

An optimized setup for simultaneous EEG-fMRI at ultra-high field in a head-only 7T scanner, João Jorge, Frédéric Grouiller, Robert Stoermer, Christoph M Michel, Patrícia Figueiredo, Wietske van der Zwaag, Rolf Gruetter; poster presentation at the 22nd Annual ISMRM Meeting, Milan, Italy, May 2014

Intra and cross-modal negative BOLD responses in grey matter regions and large draining veins under contrast-varying visual stimulation, João Jorge, Patrícia Figueiredo, Rolf Gruetter, Wietske van der Zwaag; poster presentation at the Annual SfN Meeting, San Diego, USA, November 2013

Intra and cross-modal negative BOLD response to contrast-varying visual stimuli, João Jorge, Patrícia Figueiredo, Rolf Gruetter, Wietske van der Zwaag; oral presentation at the 29th Annual ESMRMB Scientific Meeting, Lisbon, October 2012

Curriculum Vitae

PERSONAL INFORMATION

João Pedro Forjaco Jorge

(41) 21 6930582

joao.jorge@epfl.ch

Sex Male | Date of birth 28/04/1987 | Nationality Portuguese

EDUCATION

Jul 2011 onwards

Doctoral Program in Biomedical Engineering
(not yet completed)

École Polytechnique Fédérale de Lausanne, Switzerland

Instituto Superior Técnico, Universidade de Lisboa, Portugal

- Functional magnetic resonance imaging, electroencephalography, neuroscience

2008 – 2010

Integrated Master in Biomedical Engineering (2nd Cycle)
Master's degree (final grade: 19 out of 20)

Instituto Superior Técnico, Universidade Técnica de Lisboa, Portugal

- Physics, mathematics, chemistry, biology, physiology, computer programming

2005 – 2008

Integrated Master in Biomedical Engineering (1st Cycle)
Bachelor's degree (final grade: 18 out of 20)

Instituto Superior Técnico, Universidade Técnica de Lisboa, Portugal

- Physics, mathematics, chemistry, biology, physiology, computer programming

WORK EXPERIENCE

Jan 2011 – Jun 2011

Researcher (Research Grant)

ISR – Department of Electrical and Computer Engineering, Instituto Superior Técnico

- Brain imaging, structural and functional MRI data processing

Mar 2009 – Dec 2010

Researcher (Scientific Initiation Grant)

ICIST – Department of Civil Engineering and Architecture, Instituto Superior Técnico

- MRI data processing, computational modelling, finite element analysis in biomechanics

PERSONAL SKILLS

Mother tongue

Portuguese

Other language(s)

English (fluent), French (basic)

Computer skills

- Familiarity with Matlab, C, Mathematica, and EEG and fMRI data processing tools such as EEGLab, FSL and SPM

Other skills

- Acoustic/electric guitar, as a hobby

Driving licence

- Categories B1 and B

PUBLICATIONS

Journal articles
(first author)

- *Stimulus dependence of the negative BOLD response to visual stimulation in visual and auditory cortical regions at 7T*, **Jorge J**, Figueiredo P, Gruetter R, van der Zwaag W, submitted
- *Towards high-quality simultaneous EEG-fMRI at 7 Tesla: detection and reduction of EEG artifacts due to head motion*, **Jorge J**, Grouiller F, Gruetter R, van der Zwaag W, Figueiredo P, NeuroImage 120, 2015, pp.143-153
- *Simultaneous EEG-fMRI at ultra-high field: Artifact prevention and safety assessment*, **Jorge J**, Grouiller F, Ipek Ö, Stoermer R, Michel CM, Figueiredo P, van der Zwaag W, Gruetter R, NeuroImage 105, 2015, pp.132-144
- *EEG-fMRI integration for the study of human brain function*, **Jorge J**, van der Zwaag W, Figueiredo P, NeuroImage 102, 2014, pp.24-34
- *Signal fluctuations in fMRI data acquired with 2D-EPI and 3D-EPI at 7 Tesla*, **Jorge J**, Figueiredo P, van der Zwaag W, Marques JP, Magnetic Resonance Imaging 31(2), 2013, pp.212-220
- *Finite element simulations of a hip joint with femoroacetabular impingement*, **Jorge JP**, Simões FM, Pires EB, Rego PA, Tavares DG, Lopes DS, Gaspar A, Computer Methods in Biomechanics and Biomedical Engineering 17(11), 2014, pp.1275-1284

Journal articles
(co-author)

- *Presurgical brain mapping in epilepsy using simultaneous EEG and functional MRI at ultra-high field: feasibility and first results*, Grouiller F, **Jorge J**, Pittau F, van der Zwaag W, Michel CM, Vulliémoz S, Gruetter R, Vargas MI, Lazeyras F, submitted
- *Fourier modelling of the BOLD response to a breath-hold task: optimization and reproducibility*, Pinto J, **Jorge J**, Sousa I, Vilela P, Figueiredo P, submitted
- *Ballistocardiogram artefact correction taking into account physiological signal preservation in simultaneous EEG-fMRI*, Abreu R, Leite M, **Jorge J**, Grouiller F, van der Zwaag W, Leal A, Figueiredo P, submitted
- *Physiological noise in human cerebellar fMRI*, van der Zwaag W, **Jorge J**, Buttica D, Gruetter R, MAGMA, DOI 10.1007/s10334-015-0483-6
- *Femoroacetabular impingement of the cam type: Finite element simulations and comparison with a non-cam hip*, Simões F, Tavares D, **Jorge J**, Pires E, Rego P, Journal of Biomechanics 45, 2012, pp.S270

Conference articles

- *Sources of signal fluctuations in functional magnetic resonance imaging at 7 Tesla*, **Jorge JPF**, Figueiredo P, van der Zwaag W, Marques JP, 1st Portuguese Meeting in Bioengineering (ENBENG), March 2011
- *Finite element studies of a hip joint with femoroacetabular impingement of the Cam type*, **João Jorge**, Fernando Simões, Eduardo Borges Pires, Daniel Lopes, Paulo Rego, 2010, 9th International Symposium Computer Methods in Biomechanics and Biomedical Engineering 2010
- *A three-dimensional geometric model of a hip joint presenting a femoral head deformity based on radial magnetic resonance arthrography images*, Daniel Lopes, **João Jorge**, Eduardo Borges Pires, Fernando Simões, Paulo Rego, 2009, VIPIMAGE 2009
- *Pressão de contacto intra-articular no conflito femuro-acetabular; estudo tridimensional por elementos finitos*, Paulo Rego, **João Jorge**, Fernando Simões, Eduardo Borges Pires, Daniel Lopes, P. Pinto, A. Spranger, F. Oliveira, A. Gaspar, Jacinto Monteiro, 2010, Revista Portuguesa de Ortopedia e Traumatologia, XXX Congresso Nacional de Ortopedia e Traumatologia

Conference participations

- *Improving simultaneous EEG-fMRI acquisitions at 7 Tesla: detection, characterization and reduction of EEG artifacts due to head motion*, **J Jorge**, F Grouiller, R Gruetter, W van der Zwaag, P Figueiredo. Oral presentation at the 2nd bi-annual BaCI meeting, Utrecht, Netherlands, September 2015
- *Towards high-quality simultaneous EEG-fMRI acquisitions at 7 Tesla: detection and reduction of EEG artifacts due to head motion in B₀*, **J Jorge**, F Grouiller, W van der Zwaag, R Gruetter, P Figueiredo. E-poster presentation at the 23rd Annual ISMRM Meeting, Toronto, Canada, May 2015
- *Contrast and duration dependence of the negative BOLD response to visual stimulation in visual and auditory cortical regions at 7T*, **J Jorge**, P Figueiredo, R Gruetter, W van der Zwaag. Poster presentation at the 23rd Annual ISMRM Meeting, Toronto, Canada, May 2015
- *Mapping epileptic networks using simultaneous EEG-MRI at ultra-high field*, F Grouiller, **J Jorge**, F Pittau, P Martelli, W van der Zwaag, C M Michel, S Vulliémoz, M I Vargas, and F Lazeyras. Poster presentation at the 23rd Annual ISMRM Meeting, Toronto, Canada, May 2015
- *RF safety assessment of simultaneous EEG-fMRI at 7T MR*, Ö Ipek, **J Jorge**, F Grouiller, W van der Zwaag, L Xin, and R Gruetter. Poster presentation at the 23rd Annual ISMRM Meeting, Toronto, Canada, May 2015
- *An optimized setup for simultaneous EEG-fMRI at ultra-high field in a head-only 7T scanner*, **J Jorge**, F Grouiller, R Stoermer, C M Michel, P Figueiredo, W van der Zwaag, R Gruetter. Poster presentation at the 22nd Annual ISMRM Meeting, Milan, Italy, May 2014
- *Intra and cross-modal negative BOLD responses in grey matter regions and large draining veins under contrast-varying visual stimulation*, **J Jorge**, P Figueiredo, R Gruetter, W van der Zwaag. Poster presentation at the Annual SfN Meeting, San Diego, USA, November 2013
- *Intra and cross-modal negative BOLD response to contrast-varying visual stimuli*, **J Jorge**, P Figueiredo, R Gruetter, W van der Zwaag. Oral presentation at the 29th Annual ESMRMB Scientific Meeting, Lisbon, October 2012
- *Improving the characterization of the BOLD response to breath-hold challenges*, **J Jorge**, P Vilela, W van der Zwaag, P Figueiredo. Poster presentation at the 18th Annual HBM Meeting, Beijing, June 2012
- *High temporal resolution and physiological noise removal improve BOLD detection in brainstem and auditory cortex at 7T*, W van der Zwaag, M Narsude, **J Jorge**, J Marques, R Gruetter. E-poster presentation at the 20th Annual ISMRM Meeting, Melbourne, Australia, May 2012
- *Correlated noise correction in 2D and 3D fMRI at 7 Tesla*, **J Jorge**, P Figueiredo, W van der Zwaag, M Narsude, J Marques. Poster presentation at the 17th Annual HBM Meeting, Quebec City, Canada, June 2011
- *Sources of signal fluctuations in single-shot 2D EPI and segmented 3D EVI acquisitions for fMRI at 7T*, **J Jorge**, P Figueiredo, W van der Zwaag, M Narsude, J Marques. E-poster presentation at the 19th Annual ISMRM Meeting, Montréal, Canada, May 2011

Article peer-reviewing

- NeuroImage
- Journal of Neuroscience Methods

Master's Thesis

- *Sources of signal fluctuations in fMRI at 7 Tesla* (grade: 20/20), 2010, Instituto Superior Técnico

Awards

- *Carlos Lima Award (honorable mention)* attributed to *Pressão de contacto intra-articular no conflito femuro-acetabular, estudo tridimensional por elementos finitos*, P. Rego, **J.P. Jorge**, F.M. Simões, E.B. Pires, D.S. Lopes, P. Pinto, A. Spranger, F. Oliveira, A. Gaspar, J. Monteiro, 2010, Revista Portuguesa de Ortopedia e Traumatologia, XXX Congresso Nacional de Ortopedia e Traumatologia
- *Study award scholarship* from Instituto Superior Técnico for exceptional academic performance in the academic year of 2007-2008
- *Study award scholarship* from Instituto Superior Técnico for exceptional academic performance in the academic year of 2005-2006

